Università degli Studi della Basilicata

SCUOLA DI INGEGNERIA

Dottorato di ricerca in Ingegneria per l'innovazione e lo sviluppo sostenibile

Curriculum Metodi e tecnologie per il monitoraggio e la tutela ambientale

Titolo della tesi

Geophysical techniques for urban environment monitoring

ICAR/09

Coordinatore del dottorato

Prof.ssa Aurelia Sole

Dottorando

Dr. Nicola Tragni

Tutor
Prof. Felice Carlo Ponzo

Co – Tutor
Dott.ssa Ing. *Maria Rosaria Gallipoli*

Co – Tutor
Dr. *Bojana Petrovic*

Co – Tutor
Dr. Ing. *Rocco Ditommaso*

Alla mia famiglia

Abstract

The research activities conducted in this thesis contributes, through the application of geophysical techniques, to the mitigation of seismic risk with the twofold objective of studying the interaction between the urban subsoil and the overlying-built heritage and carrying out a modal characterisation of a strategic infrastructure. The former objective was pursued by producing a map of the double soil-structure resonance levels of the Matera urban area, while the latter was achieved by setting up and applying an innovative multi-methodological geophysical approach on the Gravina Bridge.

As part of the first study, I performed 230 single-station ambient seismic noise measurements on the main lithologies (134) and on the main typology of buildings (96) in reinforced concrete (RC) and unreinforced load-bearing masonry buildings (URM) of the Matera urban area. The ambient seismic noise recorded on the soil 12 min time duration and on buildings 14 min time duration was recorded with a compact digital seismometer and processed using a non-reference site method, the Horizontal-to-vertical noise spectral ratio technique, HVNSR. The measurements taken on the ground and buildings allowed the resonance frequencies and relative amplitudes of the fundamental peaks of the soil and the first elastic frequency of vibration of the buildings to be estimated. A deterministic interpolator (Inverse Distance Weight, IDW) was used in GIS environment to derive the iso-frequency and iso-amplitude maps of the urban area by using as variables the resonance frequencies and amplitudes of the soil HV ratios. A linear period-to-height relationship for the buildings was derived from the experimental results, allowing the fundamental elastic frequency to be estimated for all buildings in the study area. An intersection approach between soil and building frequency bands was used for the first time to derive a map of double soil-structure resonance levels in the linear elastic domain for the whole urban area. Matera represents an important case study since the elastic frequency of vibration for most of the buildings is quite close to that of the foundation soils. In the study area, 21% of the buildings show a high susceptibility to the effect of double soil-building resonance, 63% of the buildings could be characterised by a medium level of double resonance, while 16% could exhibit a zero or very low resonance level. The proposed approach also makes it possible to locate the areas of the city characterised by these different levels of double resonance. Therefore, the first part of the thesis work provided a contribution in assessing the soil – structure interaction effect (SSI, influence of built structures in modifying the ground motion during earthquake shaking) between urban soil and all the overlying buildings in the city of Matera by characterising all the foundation soils of the urban area and all the overlying buildings.

A geo-database, the CLARA WebGIS portal (available at this link: https://smartcities-matera-clara.imaa.cnr.it/), for storing and sharing the data and results collected during my PhD activity has been implemented with 488 pre-existing geological, geotechnical, geophysical data. CLARA WebGIS is the first useful tool for predicting which and how many buildings could suffer higher damage due to the double soil-building resonance effect and is the first open geo-platform that shares the results of the double soil-building resonance from experimental data for an entire urban area. CLARA WebGIS addresses a wide range of end-users (local administrations, engineers, geologists, etc.) as support for the implementation of seismic risk mitigation strategies in terms of urban planning, seismic retrofit, and post-earthquake crisis management. The knowledge of the spatial distribution of the site effects (modifications of the ground motions due to changes in the shallow geological layers) in terms of amplification effect, the primary characteristics of buildings, and of soil-building resonance levels estimations, a three-part objective have been achieved: (i) through CLARA's WebGIS every citizen is aware of the characteristics of buildings and foundation soils, so this knowledge makes each individual citizen more resilient to the effects of a seismic event; (ii) preventing the potential losses in economic and social terms; (iii) reducing recovering phase time to facilitate the return of the urban system to equilibrium pre-existing conditions.

A deepening of this first study was made by specialising the linear period-height relationship derived from the experimental results as a function of the construction typology and foundation soil for unreinforced load-

bearing masonry buildings (URM) founded on rigid soil (Gravina calcarenite characterised by flat HVNSR curves). This relationship is more representative of the condition of a fixed-base masonry building. Variations in the dynamic response of masonry buildings due to soil-foundation-structure interaction at urban scale can be evaluated by simplified analytical approaches based on the traditional compliant-base oscillator model and on simplified assumptions about the geometry and mechanical properties of the soil and foundations. The experimental period-height relationship for URM buildings founded on Gravina calcarenite were integrated in a simplified analytical procedure extended to complex and more realistic stratified soils and irregular foundation geometry. The modified simplified procedure were applied at an urban scale to predict the fundamental period of seven masonry buildings studied in the historic centre of Matera, for which all soil and structural data necessary for the analytical model were available. The comparison of the fundamental periods obtained with the three approaches, traditional, simplified-modified, and experimental, shown that the adoption of the simplified-modified approach significantly improved the agreement between the experimental and analytical periods. This part of the thesis work therefore appears promising to encourage an extended application of the analytical and experimental techniques to other historic urban area characterised by similar characteristics of the built heritage and soil stratification.

In the second study of the thesis, has been implemented a multi-methodological approach that allowed to estimate the main modal parameters of the Gravina bridge by analysing short duration ambient noise signals (less than two hours) recorded by low-cost and non-invasive sensors and by performing dynamic tests. The Gravina is an arch bridge located on outcropping limestone in the city of Matera and spans 144 m along a steel-concrete deck suspended by two tubular steel arches. Ambient seismic noise was recorded using two acquisition configurations on the deck and inside the arch. The noise signal data were processed by applying: the standard spectral analysis (FFT), to examine frequencies and energy content distribution, a spectral ratio method with reference station, the Standard Spectral Ratio (SSR) technique, to check and validate eigenfrequencies, the Operational Modal Analysis (OMA) technique, i.e., the Frequency Domain Decomposition (FDD) method, to derive eigenfrequencies and mode shapes, and a seismic interferometric method, the Ambient Noise Deconvolution Interferometry (ANDI), to derive the propagation velocity of ambient noise in the infrastructure. Six eigenfrequencies have been estimated on the deck. The examination of the energy content distribution played a key role for the interpretation of the mode shapes. The variation of the eigenfrequencies of the infrastructure with the seasons as a function of temperature (°C) were monitored: the frequency variations are less than 5% and the behaviour of the structure do not exhibit degradation since the Gravina Bridge is a newly constructed road infrastructure. Deconvolution interferometry has been applied on the ambient noise signals recorded on the deck deriving the wave propagation velocity on the infrastructure. The results presented showed that the ANDI method is sensitive to the distribution of infrastructure stiffness. The multi-methodological approach used in this part of the thesis is promising for (i) evaluating the behaviour of standard structure like buildings and critical infrastructure like a bridge at different scales (global and local), (ii) examining variation of eigenfrequencies, mode shapes and ambient noise waves propagation velocities as a result of aging, degradation, and/or occurrence of potential damage, (iii) controlling and validating outcomes comparing the results obtained from different techniques, (iv) supporting at an early stage as a quick, non-invasive, low-cost tool applied without either diverting, blocking the traffic flow, or stopping the infrastructure service.

Introduction

In this thesis work, geophysical techniques were applied to monitor the urban environment. Specifically, the soil-structure interaction between the foundation soils and the overlying buildings of the urban area of the city of Matera were studied, and the modal characterisation of the Gravina Bridge was performed through a multi-methodological geophysical approach.

The first chapter is dedicated to the definition of models for characterising the seismic response of the soil. The discussion attempts to set out the models for the qualitative prediction of expected seismic motion at a site under so-called free-field conditions (in the absence of buildings). In this section, theoretical solutions related to increasingly complex geotechnical subsurface models are presented. A quick but necessary discussion of site effects is proposed. The built heritage represents an extremely important element in the urban areas, therefore models for characterising the structural response of structures and models for characterising the soil-structure interaction effect are discussed.

The second chapter presents geophysical methods for estimating local seismic amplification of the soil and structural response of buildings in the elastic-linear domain: Horizontal-to-Vertical Noise Ratio (HVSR), and Standard Spectral Ratio (SSR). Among the geophysical techniques used to characterise a structure, this chapter will discuss an Operationl Modal Analysis technique, the Frequency Domain Decomposition, introduced by **Brincker et al. (2001)**. It is a user-friendly technique for the modal identification of output-only systems, i.e., in the case where the modal parameters need to be estimated without knowing the input exciting the system will be discussed. In addition, I will discuss a seismic interferometry technique, deconvolution interferometry (e.g., **Snieder and Safak, 2006**), a method based on the comparison of recordings of the same impulse at different locations providing the propagator between the two locations. This technique is gaining popularity due to the possibility of deriving the modal parameter propagation velocity of recorded signals, noise, or earthquakes, in the structures where it is applied.

In the third chapter a study for the seismic characterisation of the urban soils together with the built environment is presented, with a holistic vision to mitigate seismic risk of the city of Matera. In the framework of the CLARA project (CLoud plAtform and smart underground imaging for natural Risk Assessment), funded by the Italian Ministry of University and Research, the interaction effects between near surface geology and all overlying buildings have been evaluated in the city of Matera (Southern Italy). 230 Single-station seismic ambient noise measurements performed on the main lytologies (134) and on the main building typologies (96) allowed estimating the fundamental frequency of urban soils and the first vibrational frequency of buildings. The results and all the collected data were digitally archived in CLARA WebGIS (available at this link: https://smartcities-matera-clara.imaa.cnr.it/). CLARA WebGIS is a useful tool to share the main results derived from the intersection of all geophysical and engineering data presented in this chapter: (1) the estimation of fundamental resonance frequency for all urban soils; (2) the main vibrational frequencies for all buildings in the urban area of Matera, which have been estimated from the height of each building and using the experimental period-height (T-H) relationship derived for the ambient vibration measurements in 96 buildings of the city; (3) the resonance effect of each building with respect to the relative foundation soil in the linear elastic domain, evaluated by means of matching the vibrational frequencies of the building stock as a whole with the interpolated frequencies map of the underlying soil. The results of this part of the thesis have been published in peer-reviewed scientific journal (**Gallipoli et al., 2019**; **Tragni et al., 2019, 2021**).

The second study presented in this **third chapter** validates a multidisciplinary approach, engineering and geophysical, applied to several masonry buildings in the urban centre of Matera (**Piro et al., 2022**). Since ambient noise measurements were performed on both the subsoil and the buildings and the principal geotechnical characteristics of the foundation soils have been evaluated, it was possible to compare the period values obtained from the simplified analytical procedure proposed by **Piro et al., 2020** with the experimental ones carried out in this thesis work. The analytically calculated frequencies are in good agreement with the experimental ones.

In the fourth chapter, the Ambient Noise Deconvolution Interferometry (ANDI) technique and the Frequency Domain Decomposition (FDD) were used to characterise the main modal properties of the Gravina Bridge (eigenfrequencies, mode shapes and propagation velocities) using ambient vibration recordings. This bridge is located in Southern Italy, near the city of Matera and is a 144m long bow-string bridge with an isolation system at its base, founded on outcropping calcarenite. The estimation of the main eigenfrequencies and mode shapes was done by an Operational Modal Analysis, OMA using the FDD method. The interferometric seismic approach was also applied to evaluate the deconvolved wave fields and estimate wave propagation velocities along the main directions of the deck (**Tragni et al., 2022**).

Chapter 1: Seismic characterisation of the built environment

1.1 Models for characterising the seismic response of the soil

Site effects result in both local amplifications due to litho-stratigraphic and morphological conditions and ground instability phenomena (e.g., collapse, and sometimes in movement of large masses of soil incompatible with the stability of structures, liquefaction, active and capable faults, differential soil subsidences, etc.). From a strictly physical point of view, **Lanzo and Silvestri, 1999** define the site effect (or local seismic response) as the set of changes in amplitude, duration, and frequency content, that the incoming wave field, that is the seismic motion related to a bedrock formation (R - Fig. 1.1), undergoes as it passes through the overlying soil layers to the surface (S). In fact, defining the phenomena of modification of the seismic motion characteristics only in terms of maximum amplitude changes may not be enough if changes in frequency content are not taken into account; indeed, since the soil acts as a filter, it precisely increases the amplitude of the ground motion at some frequencies, thus triggering the so-called local seismic amplification, and reducing or de-amplifying it for others, depending on many parameters. The existence of unfavourable site and soil conditions that can stress even very well-designed structures to withstand strong earthquakes, now well known in both the scientific and technical communities, can cause spatial variability in earthquake-induced damage and effects. Site effects can play an important role for damage to buildings and thus to humans, both because of the local amplification of seismic actions transmitted by the ground, and because double resonance phenomena can also occur between the vibration modes of the soils and those of the structure, i.e., whenever the oscillation frequency of a building is very close to the resonance frequency of the foundation soil. The effects of local geological conditions on building damage were noted as early as Mallet in reports during his mission to the territories affected by the Basilicata earthquake of 1857 (**Mallet, 1862**). **Lanzo and Silvestri (1999)** pointed out that the analyses of the effects on soils and buildings produced by the Irpinia earthquake of 1980 November 23 (M = 6.9) had an extreme variability of the level of damage in relation to the uneven morphological and stratigraphic conditions of the subsoil (**Rippa and Vinale, 1983**). Following the earthquake of September 19, 1985 (M = 8.1), Mexico City suffered very severe damage due to the phenomenon of amplification of seismic motion due to the peculiar geotechnical characteristics of the soils covering the valley on which the city is founded, despite the city was located hundreds of kilometres away from the epicentre (**Celebi et al., 1987**). Following the Loma Prieta (San Francisco, California, USA) earthquake of October 17, 1989 (M = 7.1), numerous examples of the influence of local conditions on seismic motion have emerged. For example, **Seed et al., 1991** showed that the peak acceleration values recorded at two accelerometer stations, Treasure Island and Yerba Buena, located at the same distance from the epicentre of the earthquake were completely different. Specifically, the value recorded at the Treasure Island station, whose subsurface consisted of a layer of soft soils resting on a rocky substrate, was found to be three times the recorded value at the Yerba Buena station located on an outcrop of the same substrate material. **Darragh and Shakal (1991)** verified that as the intensity of the earthquake increased, the natural frequencies and maximum amplification factors of the Treasure Island deposit decreased, further confirming the impact of nonlinear soil response on seismic signal modification. Further destructive events (Friuli 1976, Armenia 1988, Iran 1990, Philippines 1990, Northridge 1994, Kobe 1995, Umbria-Marche 1997, Kocaeli and Düzce, Turkey 1999, Athens 1999, Gujarat 2001, Sumatra 2004, Kashmir 2005, L'Aquila 2009, Haiti 2010, Central Italy 2016-2017, Afghanistan 2022), showed that the most severe damage was observed where particular site effects occurred. In the context of the evaluation and study of site effects, great advances have been made by the world of research. **Brax et al. (2016)** proposed a multi-step procedure for ground motion prediction in Beirut, coupling empirical Green’s functions, ground motion prediction equations and instrumental transfer functions. **Peruzzi et al. (2016)** presented a procedure to provide practitioners charged for seismic microzoning studies of a tool for assessing and quantifying seismic amplification phenomena induced by the local litho-stratigraphic configuration that could be applied in developing countries low seismicity areas or where extensive accelerometric databases are lacking. **Fiamingo et al. (2018)** examined the seismic performance of a building damaged by the 26 December 2018 earthquake in Italy, focusing on the role of soil in the structural response. **Mascandola et al. (2020)** presented a methodology intended for seismic microzonation studies and regional probabilistic seismic hazard assessments that account for site effects, aiming at the selection of accelerometric time histories as input for dynamic response analyses over vast areas. **Mori et al. (2020)** derived a large-scale Vs30 map for Italy started integrating a large amount of data from the Italian seismic microzonation dataset. **Fabozzi et al. (2021)** proposed the possible use of equivalent homogeneous subsoil models for 1D seismic response analyses in seismic microzonation studies. **Falcone et al. (2021)** proposed a methodology to perform seismic site response analyses at national scale in Italy based on site-specific microzonation dataset and one-dimensional numerical approach. **Gjorgjeska et al. (2022)** proposed a multi-method approach for seismic site characterization. **Ilhan and Zulfikar (2022)** performed a small-scale parametric study of several one-dimensional nonlinear and equivalent-linear ground response analyses using different medium stiff-to-stiff site profiles from the southern coast of Izmir city (Anatolia, Turkey) and a high number of motions to produce simulated amplification factors. **Mobarki et al. (2022)** investigated the site effects parameters in Algiers city using simulated accelerograms. **Jornet-Monteverde et al. (2022)** designed and implemented a wireless recorder system for site effects assessments through seismic noise array measurements in Alicante (southeast Spain). Therefore, the purpose of seismic microzonation studies is to define valid methodologies for the assessment of site effects even at the urban scale and the type of investigations and numerical analyses suitable for defining the values of engineering parameters for proper earthquake-resistant design.

The ground motion at a site generated by a seismic event, is the result of the elastic waves propagation from the source, through bedrock in depth and affected by generally loose soil formations at the surface (schematically illustrated in Figure 1.1). The variability of seismic motion on the outcropping surface is called local seismic response phenomenon and is related to the properties of the soil deposits. Before describing any of the ground response models, it is necessary to define several terms that are commonly used to describe the ground motion. The motion at the surface of a soil deposit (S) is called the free surface motion; the motion at the base of the soil deposit, i.e., the top of the bedrock (R) the bedrock motion, and the motion at a location where the bedrock is exposed at the ground surface (A) the rock outcropping motion (Fig. 1.1).

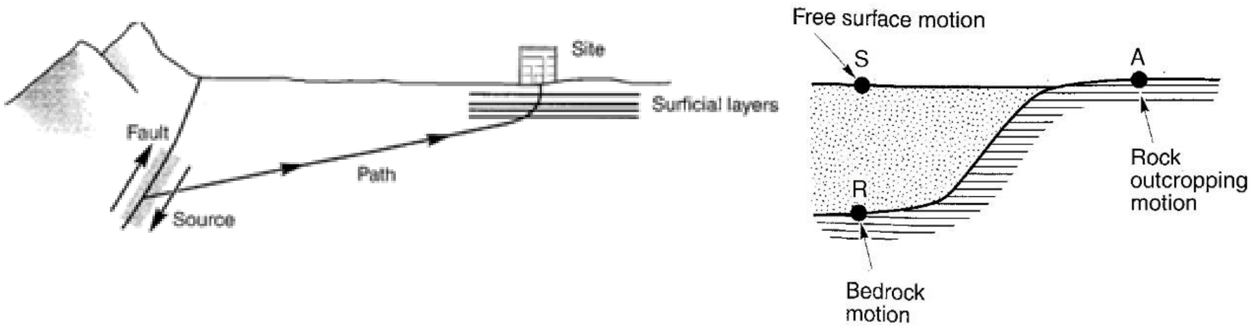

Fig. 1. 1 (Left) Scheme of seismic wave propagation from a source to a site producing near-vertical wave propagation near the ground surface); (right) Nomenclature of the ground response for soil overlying bedrock (Kramer, 1996)

In this section, theoretical solutions related to increasingly complex geotechnical subsurface models are presented.

1.1.1 Model of elastic homogeneous layer on rigid bedrock

The basic scheme is the one-dimensional problem represented by a homogeneous soil layer of thickness H, density ρ, shear wave propagation velocity V_S above a bedrock characterised by an infinite stiffness and considered as a perfectly reflecting boundary. The bedrock is considered excited by a harmonic oscillation with a shear wave S with frequency f, incident on the bedrock with vertical propagation direction.

In the simplest homogeneous layer model (Figure 1.2), soil with linear elastic constitutive relationship between the shear stress τ, shear modulus G, and shear strain γ ($\tau = G\gamma$) and hard bedrock is assumed. Due to the wave crossing, the solid soil element that have mass m will be subjected to displacements in the horizontal directions with an acceleration a that will cause an inertial force F_i ($F_i = ma$), and thus it will induce a distortion that will generate a change in the stress state along the height dz of the infinitesimal solid element in figure 1.2. Therefore, the dynamic equilibrium equation of motion can be written as:

$$-\tau(z,t) + [\tau(z,t) + \frac{\partial\tau(z,t)}{\partial z}] - F_i = 0 \qquad 1.\ 1$$

Equation (1.1) can be written in expanded form as:

$$\frac{\partial\tau(z,t)}{\partial z} - \rho\frac{\partial^2 u(z,t)}{\partial t^2} = 0 \qquad 1.\ 2$$

where u(z,t) is the horizontal displacement component.

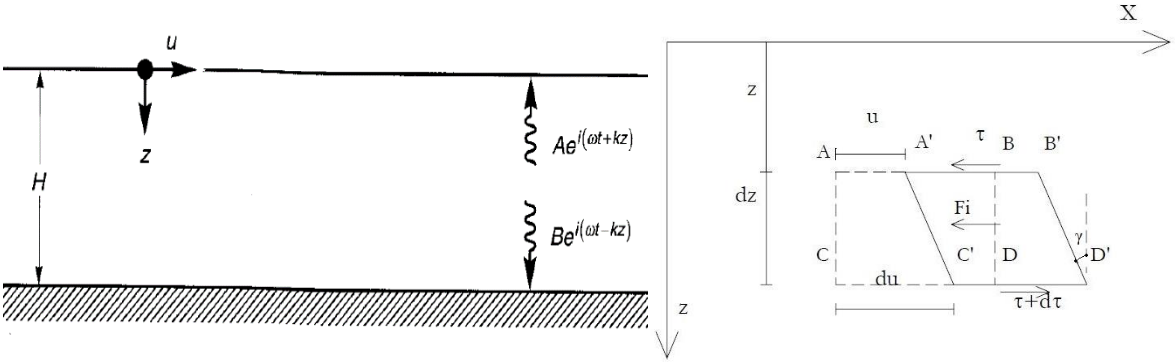

Fig. 1. 2 (Left) Linear elastic soil deposit of thickness H over rigid bedrock; (right) Thin solid element with height dz, mass m, at depth z, before (ABCD) and after (A'B'C'D') the application of x-horizontal shearing and consequent displacement u. Since a change in displacement is assumed along the height dz, and consequently a change (dτ) in the stress state, a tangential stress equal to τacts on the upper side of the solid thin element, while a different stress (τ+ dτ) acts on the lower side. Total resistance to shearing is given by the sum of an elastic component.

By combining the congruence equation ($\gamma = \partial u/\partial z$) and the constitutive equation ($\tau = G\gamma$) following relationship is obtained:

$$\tau(z,t) = G\gamma = G\frac{\partial u(z,t)}{\partial z} \qquad 1.\ 3$$

Substituting (1.3) into (1.2) yields the dynamic equilibrium differential equation that describes the phenomenon of one-dimensional wave propagation within the elastic layer and the horizontal vibration motion:

$$\rho\frac{\partial^2 u(z,t)}{\partial t^2} = G\frac{\partial^2 u(z,t)}{\partial z^2} \qquad 1.\ 4$$

For a harmonic stress with angular frequency $\omega = 2\pi f$, the solution $u(z,t)$ can be sought by variables decomposition in the form:

$$u(z,t) = p(z)e^{i\omega t} \qquad 1.5$$

where $p(z)$ is the shape function describing the distribution of displacement amplitudes with depth at each point, varying with the frequency being equal to the stress frequency, and $e^{i\omega t}$ is a harmonic-type function whose harmonic variation over time is expressed in Eulerian notation i (i = imaginary unit).

The derivatives of $u(z,t)$ with respect to z are defined as:

$$\frac{\partial u(z,t)}{\partial z} = \frac{\partial p(z)}{\partial z}e^{i\omega t}$$

$$\frac{\partial^2 u(z,t)}{\partial z^2} = \frac{\partial^2 p(z)}{\partial z^2}e^{i\omega t}$$

and with respect to t:

$$\frac{\partial u(z,t)}{\partial t} = i\omega e^{i\omega t}p(z)$$

$$\frac{\partial^2 u(z,t)}{\partial t^2} = -\omega^2 e^{i\omega t}p(z)$$

and substituting them in (1.4), we get:

$$G\frac{\partial^2 p(z)}{\partial^2 z}e^{i\omega t} + \rho\omega^2 e^{i\omega t}p(z) = 0 \qquad 1.6$$

whose solution is given by:

$$p(z) = Ae^{ikz} + Be^{-ikz} \qquad 1.7$$

where k is the wave number defined as $k = \omega/V_S = 2\pi f/V_S = 2\pi/\lambda$.

Substituting (1.7) into (1.5) gives the expression for horizontal displacement:

$$u(z,t) = Ae^{ikz}e^{i\omega t} + Be^{-ikz}e^{i\omega t} \qquad 1.8$$

where A and B are the amplitudes of two waves propagating upward and downward, respectively, within the layer.

Imposing as a boundary condition the absence of shear stress (eq 1.3) at the surface (z = 0) results in:

$$\tau(0,t) = G\gamma(0,t) = G\frac{\partial u(0,t)}{\partial z} = 0 \qquad 1.9$$

The derivation of (1.8) yields:

$$\frac{\partial u(z,t)}{\partial z} = ikAe^{ikz}e^{i\omega t} - ikBe^{-ikz}e^{i\omega t} \qquad 1.10$$

which becomes for z = 0:

$$\frac{\partial u(0,t)}{\partial z} = ikAe^{i\omega t} - ikBe^{i\omega t} \tag{1.11}$$

Substituting (1.11) into (1.9) gives:

$$Gike^{i\omega t}(A - B) = 0 \tag{1.12}$$

identically satisfied if A = B.

The transfer function $H_r(\omega)$ between surface ($z = 0$) and the base ($z = H$) of the layer has, in this case, expression (**Lanzo e Silvestri, 1999**):

$$H_r(\omega) = \frac{u(0,t)}{u(H,t)} \tag{1.13}$$

where

$$u(0,t) = Ae^{i\omega t} + Be^{i\omega t} = 2Ae^{i\omega t} \tag{1.14}$$

and $u(z,t)$ for z = H is given by:

$$\begin{aligned} u(z,t) &= Ae^{ikz}e^{i\omega t} + Ae^{-ikz}e^{i\omega t} = \\ &= Ae^{i\omega t}\left(e^{ikz} + e^{-ikz}\right) = \\ &= 2Ae^{i\omega t}\,\frac{\left(e^{ikz} + e^{-ikz}\right)}{2} = 2Ae^{i\omega t}\cos kz \end{aligned} \tag{1.15}$$

Which represents a stationary wave of amplitude $2A\cos(kz)$ from which:

$$u(z,H) = 2Ae^{i\omega t}\cos kH \tag{1.16}$$

Substituting (1.14) and (1.15) into (1.13) yields the transfer function as follows:

$$H_r(\omega) = \frac{2Ae^{i\omega t}}{2Ae^{i\omega t}\cos kH} = \frac{1}{\cos kH} = \frac{1}{\cos F} \tag{1.17}$$

where the dimensionless parameter $F = kH = \omega H/V_S$ is the frequency factor. The amplification function is the modulus of the transfer function:

$$A_r(\omega) = |A_r(\omega)| = \sqrt{\{\mathbb{R}[H_r(\omega)]\} + \{\mathfrak{I}[H_r(\omega)]\}} = \frac{1}{\left|cos\left(\frac{2\pi f H}{V_S}\right)\right|} \tag{1.18}$$

where $R[H_r(\omega)]$ and $I[H_r(\omega)]$ are the real and imaginary parts (zero in this case) of the amplification function, respectively.

The domain of existence of the function $A_r(\omega)$ is $0 \leq |cos\ (kH)| \leq 1$.

For $cos\ (kH) = 1$ the function $A_r(\omega) = 1$ thus draws the minimum value. The function A_f goes to infinity when $cos\ (kH) = 0$, that is, when $kH = \pi/2$. Since $kH = 2\pi fH/V_S$ we can write:

$$k_n H = \frac{(2\pi f_n)}{V_S} H = \frac{\pi}{2}(2n - 1) \tag{1.19}$$

Therefore, the plot of the amplification function (Figure 1.3) shows that it is periodic, always assuming values greater than or equal to unity, i.e., the amplitude of the displacement at the layer surface is always at least equal to that at the rock formation and becomes infinite for $F_n = k_nH = (2n-1)\pi/2$, i.e., at the following frequency values:

$$\begin{cases} \omega_n = \frac{V_s}{H}(2n-1)\frac{\pi}{2} \\ f_n = \frac{V_s}{4H}(2n-1) \end{cases} \qquad n = 1,2,\ldots\infty \qquad 1.20$$

and at periods T_n:

$$T_n = \frac{1}{f_n} = \frac{4H}{V_s(2_n-1)} \qquad n = 1,2,\ldots\infty \qquad 1.21$$

The frequencies (ω_n and f_n) corresponding to the maxima of the amplification function are called the natural vibration frequencies of the layer; their number is infinite, as is the number of degrees of freedom of the system, and they are uniformly distributed because $A_r(\omega)$ is periodic. Similarly, the periods T_n are called natural vibration periods of the layer. Since they are directly proportional to the thickness of the layer and inversely proportional to the velocity of the shear waves of the soil, they increase with the transverse deformability of the layer.

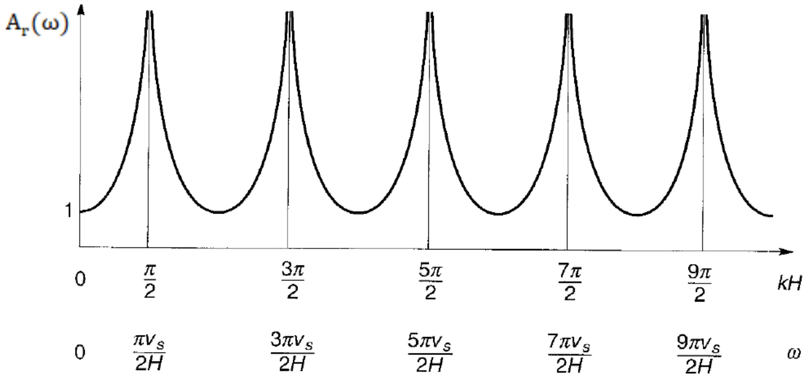

*Fig. 1. 3 Amplification function related to undamped elastic stratum on rigid bedrock (**Kramer, 1996**)*

Analysing function (1.15), the distribution of displacements with depth can be expressed in dimensionless form by relating u(z,t) to the maximum value at the surface ($u(0,t) = 2Ae^{i\omega t}$).

Introducing $k_n = \frac{(2\pi f_n)}{V_s} = \frac{\pi}{2H}(2n-1)$ in (1.15), it appears that each natural frequency is associated with a modal form $U_n(z)$:

$$U_n(z) = \frac{u(z,t)}{u(0,t)} = \frac{2Ae^{i\omega t}\cos(k_n z)}{2Ae^{i\omega t}} = \cos\left[(2n-1)\frac{\pi}{2}\frac{z}{H}\right] \qquad n = 1,2,\ldots\infty \qquad 1.22$$

The mode shapes U_n are plotted in Figure 1.4 for the first four vibration modes as a function of the dimensionless depth *z/H*. Note that when the soil is vibrating in the first mode (i.e., at the natural frequency of vibration, or fundamental frequency), the displacements have the same sign (i.e., are in phase) at every point in the layer. Conversely, for the higher vibration modes, the ground displacements occur partially in one direction and partially in the opposite direction.

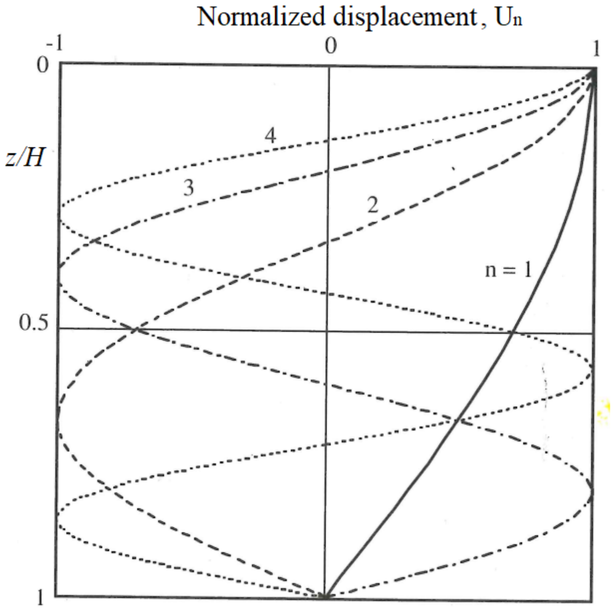

*Fig. 1. 4 Mode shapes of the first four modes of vibration of a homogeneous elastic layer over a rigid bedrock. The displacements are normalised by the maximum displacement at the fundamental frequency (**Kramer, 1996**)*

Assuming a homogeneous elastic-linear layer overlying an infinitely rigid bedrock, the downward propagating waves in the soil layer which are a result of the reflection at the soil surface, are completely reflected at the bedrock. The energy associated with the waves then remains completely trapped in the layer. Under this hypothesis, the response of a soil layer to harmonic excitation is strongly influenced by the frequency of the excitation: the frequencies at which the highest amplifications occur depend on the geometry (thickness) and the physical-mechanical characteristics (velocity of the shear waves V_S) of the soil layer.

The most dangerous condition in terms of amplification phenomena occurs when the frequency of harmonic excitation (ω) is equal to one of the fundamental frequencies of the layer (ω_n). When this condition occurs ($\omega=\omega_n$), the resonance of the layer sets in, and the amplification factor is theoretically infinite.

1.1.2 Model of elastic homogeneous layer on deformable bedrock

In the deformable substrate hypothesis, waves propagating downward through the layer are partly reflected within the layer and partly transmitted to the bedrock below. This form of dissipated energy is called geometric or radiation damping (**Roesset, 1970**). In reality, the bedrock is not a perfectly rigid medium, so a physically correct amplification function must account for radiation energy losses.

Considering the model shown in Figure 1.5, let E_R and F_R be the amplitudes of a harmonic wave of a given frequency with a vertical propagation direction in the rock formation propagating upward and downward, respectively, at both the outcrop (A) and the soil-rock interface (R), and E_S and F_S be the amplitudes of the incident and reflected waves at the soil surface (S). Assuming two local reference systems, then two vertical reference axes, the first (z_s) with origin at the soil surface, and the second (z_R) with origin at the soil-bedrock interface.

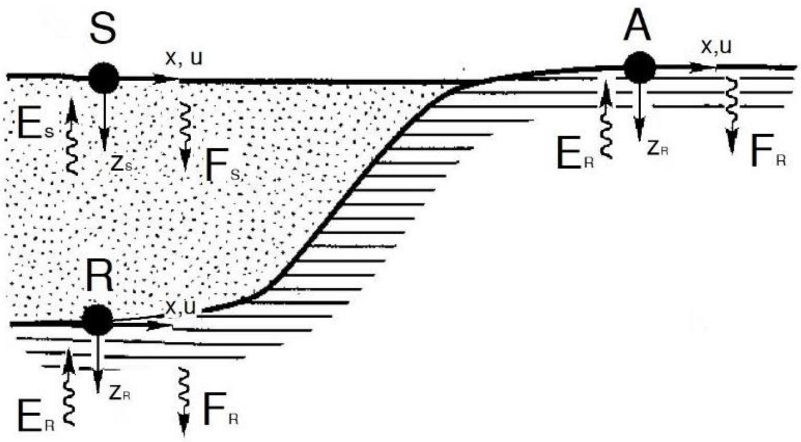

Fig. 1. 5 Nomenclature for determining the transfer function of a soil layer overlying a half-space of elastic rock.

The horizontal displacement of a generic point in the soil and bedrock can be written:

$$u_S(z_S,t) \ = \ E_S e^{ik_s z_s} e^{i\omega t} + F_S e^{-ik_s z_s} e^{i\omega t} \qquad 1.\,23$$

$$u_R(z_R,t) \ = \ E_R e^{ik_R z_R} e^{i\omega t} + F_R e^{-ik_R z_R} e^{i\omega t} \qquad 1.\,24$$

Since k_s and k_R are the wave numbers of the soil and rock formation, respectively:

$$\begin{cases} k_S \ = \ \dfrac{\omega}{V_S} \ = \ \omega\sqrt{\dfrac{\rho_S}{G_S}} \\ k_R \ = \ \dfrac{\omega}{V_R} \ = \ \omega\sqrt{\dfrac{\rho_R}{G_R}} \end{cases} \qquad 1.\,25$$

The boundary condition to be imposed is the absence of shear stress (eq 1.3) at the soil surface ($z_s = 0$) and the continuity of displacements (1.23 and 1.24) and stresses at the soil-bedrock interface, i.e.:

$$\tau_S(0,t) = G_S\gamma_S(0,t) = G_S\,\frac{\partial u_S(0,t)}{\partial z_S} = 0 \qquad 1.\,26$$

$$u_S(H,t) = u_R(0,t) \qquad 1.\,27$$

$$\tau_S(H,t) = G_S\gamma_S(H,t) = G_S\,\frac{\partial u_S(H,t)}{\partial z_S} = \tau_R(0,t) = G_R\gamma_R(0,t) = G_R\,\frac{\partial u_R(0,t)}{\partial z_R} \qquad 1.\,28$$

Substituting (1.23), for $z_s = 0$, in (1.26) yields:

$$E_S \ = \ F_S \qquad 1.\,29$$

Therefore, the ground displacement (eq 1.23) has the expression:

$$u_S(z_S,t) \ = \ E_S e^{ik_s z_s} e^{i\omega t} + E_S e^{-ik_s z_s} e^{i\omega t} \qquad 1.\,30$$

$$u_S(0,t) \ = \ 2E_S e^{i\omega t} \qquad 1.\,31$$

Substituting (1.30), and the displacement equations (1.24) for $z_R = 0$, into (1.27), yields:

$$E_S e^{ik_s z_s} e^{i\omega t} + E_S e^{-ik_s z_s} e^{i\omega t} = E_R e^{i\omega t} + F_R e^{i\omega t} \qquad 1.\,32$$

which is, for $z_S = H$, equal to

$$E_S(e^{ik_sH} + e^{-ik_sH}) = E_R + F_R \qquad 1.33$$

Introducing the derivation of the displacement equations (1.23 and 1.24) for $z_S = H$ and for $z_R = 0$ into eq. (1.28), gives:

$$G_S(ik_sE_Se^{ik_sH}e^{i\omega t}\text{-}iE_Se^{-ik_sH}e^{i\omega t}) = G_R(ik_RE_Re^{i\omega t}\text{-}ik_RF_Re^{i\omega t}) \qquad 1.34$$

and then:

$$G_sik_sE_se^{i\omega t}(e^{ik_sH}\text{-}e^{-ik_sH}) = G_Rik_Re^{i\omega t}(E_R\text{-}F_R) \qquad 1.35$$

which can be rewritten as:

$$(E_R\text{-}F_R) = \frac{G_sk_s}{G_Rk_R}\,E_s(e^{ik_sH}\text{-}e^{-ik_sH}) \qquad 1.36$$

where:

$$\frac{G_Sk_S}{G_Rk_R} = \frac{\omega G_SV_R}{\omega G_RV_S} = \frac{G_S}{G_R}\sqrt{\frac{G_R\rho_S}{\rho_RG_S}} = \frac{\rho_SV_S}{\rho_RV_R} = \mu \qquad 1.37$$

and μ is the impedance ratio or admittance.

Introducing (1.37) into (1.36), results in:

$$(E_R\text{-}F_R) = \mu\, E_s(e^{ik_sH}\text{-}e^{-ik_sH}) \qquad 1.38$$

which can be written as:

$$F_R = E_R - \mu\, E_s(e^{ik_sH}\text{-}e^{-ik_sH}) \qquad 1.39$$

Substituting (1.39) into (1.33), yields:

$$E_S(e^{ik_sH} + e^{-ik_sH}) = E_R + E_R - \mu E_S(e^{ik_sH} - e^{-ik_sH}) \qquad 1.40$$

this becomes:

$$2E_R = E_Se^{ik_sH} + E_Se^{-ik_sH} + \mu E_Se^{ik_sH} - \mu E_Se^{-ik_sH} \qquad 1.41$$

this is:

$$2E_R = E_Se^{ik_sH}(1 + \mu) + E_Se^{-ik_sH}(1 - \mu) \qquad 1.42$$

from which we can deduce:

$$E_S = \frac{2E_R}{e^{ik_sH}(1+\mu) + e^{-ik_sH}(1-\mu)} \qquad 1.43$$

Inserting (1.43) into (1.39), we get:

$$F_R = E_R - \mu\,\frac{2E_R(e^{ik_sH} - e^{-ik_sH})}{e^{ik_sH}(1+\mu) + e^{-ik_sH}(1-\mu)} \qquad 1.44$$

$$F_R = \frac{E_R e^{ik_sH} + \mu E_R e^{-ik_sH} + E_R e^{-ik_sH} - \mu E_R e^{-ik_sH} - 2\mu E_R e^{ik_sH} + 2\mu E_R e^{-ik_sH}}{e^{ik_sH}(1+\mu) + e^{-ik_sH}(1-\mu)} \qquad 1.45$$

$$F_R = E_R \frac{e^{ik_sH}(1-\mu) + e^{-ik_sH}(1+\mu)}{e^{ik_sH}(1+\mu) + e^{-ik_sH}(1-\mu)} \qquad 1.46$$

The transfer function $H_{db}(\omega)$ can be expressed as the ratio of the displacement amplitude at the soil surface $u_s(0,t)$ given by (1.31) to the displacement amplitude at the soil-bedrock interface given by (1.30) for $z_s = H$:

$$H_{db}(\omega) = \frac{u_s(0,t)}{u_s(H,t)} = \frac{2E_s e^{i\omega t}}{E_s e^{ik_sH} e^{i\omega t} + E_s e^{-ik_sH} e^{i\omega t}} = \frac{2}{e^{ik_sH} + e^{-ik_sH}} = \frac{1}{\cos k_sH} \equiv H_r(\omega) \qquad 1.47$$

which coincides with (1.17) obtained assuming the propagation of a harmonic wave in an elastic soil layer over a rigid substrate. Therefore, the transfer function $H_{db}(\omega)$ does not depend on the deformation characteristics of the bedrock.

If, on the other hand, the transfer function is calculated as the ratio between the displacement at the surface and the displacement at the outcropping bedrock, the boundary condition to be satisfied at the outcropping bedrock is the absence of shear stress (1.3) at the free surface ($z_R = 0$), i.e:

$$\tau_R(0,t) = G_R\gamma_R(0,t) = G_R \frac{\partial u_R(0,t)}{\partial z_R} = 0 \qquad 1.48$$

The derivation (1.24) gives:

$$\frac{\partial u_R(z_R,t)}{\partial z_R} = ik_R E_R e^{ik_R z_R} e^{i\omega t} - ik_R F_R e^{-ik_R z_R} e^{i\omega t} \qquad 1.49$$

which introduced in (1.48) for $z_R = 0$ is identically satisfied when $E_R = F_R$.

Therefore, by calculating the ratio between the displacement amplitude at the soil surface and that at the outcropping bedrock u_o, we obtain the transfer function $H_{daf}(\omega)$:

$$H_{da}(\omega) = \frac{u_s(0,t)}{u_R(0,t)} = \frac{2E_s e^{i\omega t}}{2E_R e^{i\omega t}} = \frac{E_s}{E_R} = \frac{2}{e^{ik_sH}(1+\mu) + e^{-ik_sH}(1-\mu)} =$$
$$\frac{2}{(e^{ik_sH} + e^{-ik_sH}) + \mu(e^{ik_sH} - e^{-ik_sH})} = \frac{2}{2\cos k_sH + 2\mu i\sin(k_sH)} =$$
$$= \frac{1}{\cos k_sH + \mu i\sin(k_sH)} \qquad 1.50$$

which takes into account the deformability of the bedrock due to the impedance ratio, and therefore, $H_{da}(\omega)$, unlike $H_{db}(\omega)$, can't disregard the assumption of a deformable substrate. Recalling (1.37), the ratio I between the seismic impedance of the bedrock ($\rho_R V_R$) and that of the soil ($\rho_s V_s$), is given as:

$$I = \frac{1}{\mu} = \frac{\rho_R V_R}{\rho_S V_S} \qquad 1.51$$

The amplification function $A_{da}(\omega)$, which is the modulus of the transfer function $H_{da}(\omega)$, is defined as:

$$A_d = \frac{1}{|cos\,(k_s H\,) + \,(k_s H)\,|} = \frac{1}{\sqrt{(k_s H\,)]^2 + \mu^2 [sin\,(k_s H)\,]^2}} =$$

$$= \frac{1}{\sqrt{(k_s H\,)]^2 + \frac{1}{I^2}[sin\,(k_s H)\,]^2}} \qquad 1.52$$

Assuming a deformable bedrock, the amplification function $A_d(\omega)$ depends not only on the mechanical properties of the soil, but also on those of the bedrock through the impedance ratio. Figure 1.6 shows the model of a linearly elastic soil layer over a deformable rock half-space, in which the amplification function $A_d(\omega)$ as a function of the frequency factor $F(=k_S H)$, is given for different values of the dynamic bedrock-soil impedance ratio I.

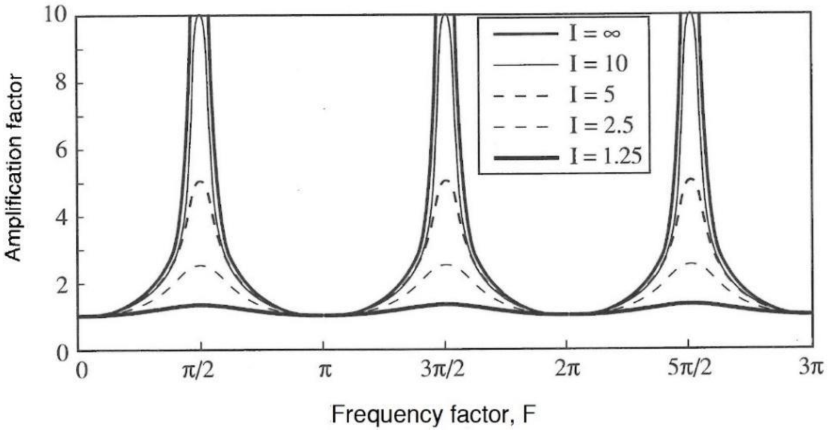

Fig. 1. 6 Amplification functions for different undamped soils (Figure re-drawn by ***Lanzo and Silvestri, 1999****).*

For comparison, the amplification function for the rigid substrate model (special case of (1.52) with $I = \infty$) is also shown. As for $A_r(\omega)$ (1.18), $A_d(\omega)$ is also periodic; the frequencies f_n (or the periods T_n) at which the maximum values of the amplification function occur are the same as those of the rigid substrate model and are expressed by the (1.20) and (1.21). For a given value of the ratio I, the maxima of the amplification function assume a finite value which is independent of the frequency:

$$(A_d)_{max} = \mathrm{I} = \frac{1}{\mu} \qquad 1.53$$

Since the peak value of the amplification function corresponds exactly to the impedance ratio I, the amplification phenomena of the seismic motion are directly proportional to the impedance contrast of the bedrock and that of the overlying soil layer.

1.1.3 Model of visco-elastic homogeneous layer on rigid bedrock

The amplification functions considered so far have been derived based on the assumption of linear elastic behaviour of the soil. In real materials, some of the elastic energy of a propagating wave is always converted to heat. This conversion is accompanied by a decrease in the amplitude of the wave. Viscous damping is often used to represent this dissipation of elastic energy because of its mathematical convenience. For viscoelastic wave propagation, soils are usually modelled as Kelvin-Voigt solids (i.e., materials whose resistance to shear deformation is the sum of an elastic part and a viscous part). Figure 1.7 illustrates a thin element of a Kelvin-Voigt solid.

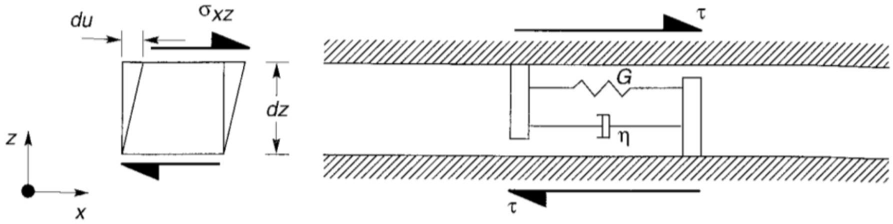

*Fig. 1. 7 Thin element of a kelvin – Voigt solid subjected to horizontal shear (**Kramer, 1996**). The total resistance to shear deformation is the sum of an elastic component (spring) and a viscous component (dashpot).*

The stress-strain relationship for a Kelvin – Voigt solid under shear, which is the constitutive equation of a viscoelastic material, can be expressed as follows:

$$\tau = G\gamma + \eta\dot{\gamma} = \; G\gamma + \eta\frac{\partial\gamma}{\partial t} \qquad 1.54$$

Where G is the shear modulus $G = \rho V_S^2$, $\tau = \sigma_{xz}$ is the shear stress, $\gamma = \partial u/\partial z$ is the shear strain, $\dot{\gamma}$ ($= \partial\gamma/\partial t$) is the shear strain velocity, and η is the viscosity of the material. Thus, the shear stress is the sum of an elastic part which is proportional to strain and a viscous part which is proportional to strain rate. A Kelvin – Voigt soil can be represented by a stack of infinitesimal elements of the type shown schematically in figure 1.7. for vertically propagating SH-waves Introducing the shear strain $\gamma = \partial u/\partial z$ into the constitutive equation for a thin element of a Kelvin – Voigt solid shear yields:

$$\tau(z,t) = G\gamma(z,t) + \eta\dot{\gamma}(z,t) = \; G\frac{\partial u}{\partial z} + \eta\frac{\partial^2 u}{\partial z\partial t} \qquad 1.55$$

Substituting (1.55) into (1.3), we obtain the dynamic equilibrium differential equation governing the phenomenon of one-dimensional vertically propagating SH-waves within the visco-elastic layer and describing the horizontal vibrational motion:

$$\rho\frac{\partial^2 u(z,t)}{\partial t^2} \; = G\frac{\partial^2 u(z,t)}{\partial z^2} + \eta\frac{\partial^3 u}{\partial z^2\partial t} \qquad 1.56$$

Recalling (1.6) in (1.56), we differentiate:

$$\frac{\partial u(z,t)}{\partial z} \; = \frac{\partial p(z)}{\partial z}e^{i\omega t}$$

$$\frac{\partial^2 u(z,t)}{\partial z^2} \; = \frac{\partial^2 p(z)}{\partial z^2}e^{i\omega t}$$

$$\frac{\partial u(z,t)}{\partial t} \; = i\omega e^{i\omega t}p(z)$$

$$\frac{\partial^2 u(z,t)}{\partial t^2} \; = -\omega^2 e^{i\omega t}p(z)$$

$$\frac{\partial^3 u(z,t)}{\partial z^2\partial t} \; = i\omega\frac{\partial^2 p(z)}{\partial z^2}e^{i\omega t}$$

and introducing them into (1.56), the ordinary differential equation is obtained:

$$-\rho\omega^2 p(z)e^{i\omega t} \; = G\frac{\partial^2 p(z)}{\partial z^2}e^{i\omega t} + \eta i\omega\frac{\partial^2 p(z)}{\partial z^2}e^{i\omega t} \qquad 1.57$$

which can be rewritten into the following form

$$\frac{\partial^2 p(z)}{\partial z^2}(G + \eta i\omega) + \rho\omega^2 p(z) = 0 \tag{1.58}$$

Applying the definition of the damping factor *D* (**Lanzo and Silvestri, 1999**) to the visco-elastic medium, it can be shown that for a harmonic stress cycle with frequency ω, the following relation holds:

$$D = \frac{\eta\omega}{2G} \tag{1.59}$$

By introducing the complex shear modulus *G**, the complex wave number *k**, and the complex shear wave velocity V_S*:

$$\begin{cases} G^* = G + i\omega\eta = G + 2GDi = G(1 + 2iD) \\ k^* = \frac{\omega}{V_s^*} = \frac{\omega}{\sqrt{\frac{G^*}{\rho}}} \end{cases} \tag{1.60}$$

the dynamic equilibrium equation is written as:

$$G^* \frac{\partial^2 p(z)}{\partial z^2} + \rho\omega^2 p(z) = 0 \tag{1.61}$$

whose solution is given by:

$$p(z) = Ae^{ik^* z} + Be^{-ik^* z} \tag{1.62}$$

and thus, the horizontal displacement $u(z,t)$ can be written as:

$$u(z,t) = Ae^{ik^* z}e^{i\omega t} + Be^{-ik^* z}e^{i\omega t} \tag{1.63}$$

Based on similar considerations as in the model of a homogeneous elastic layer over a rigid bedrock (**Kramer, 1996**), the expression of the complex transfer function $H_r^*(\omega)$ is evaluated as the ratio between the amplitude of the displacement at the surface of the soil layer and that at the interface between soil and bedrock (or at the outcropping bedrock assumed to be rigid):

$$H_r^*(\omega) = \frac{1}{\cos(k^* H)} = \frac{1}{\cos F^*} \tag{1.64}$$

Where the complex frequency factor *F* = k*H*. The complex shear wave velocity V_S*, can be written for low values of the damping factor (*D* <<< 1) as:

$$V_S^* = \sqrt{\frac{G^*}{\rho}} = \sqrt{\frac{G(1+2iD)}{\rho}} \approx \sqrt{\frac{G}{\rho}}(1 + iD) = V_S\,(1 + iD) \tag{1.65}$$

and thus, the complex wave number as:

$$k^* = \frac{\omega}{V_S^*} \approx \frac{\omega}{V_S(1+iD)} \approx \frac{\omega}{V_S}(1 - iD) = k\,(1 - iD) \tag{1.66}$$

Therefore, the transfer function has the expression:

$$H_r^*(\omega) \approx \frac{1}{\cos\cos\,[k\,(1 - iD)H]} = \frac{1}{\cos\,(kH - iDkH)} \tag{1.67}$$

and the amplification function is again obtained as the modulus of $H_r^*(\omega)$:

$$A_r^*(\omega) = \frac{1}{|\cos\,(kH - iDkH)|} \tag{1.68}$$

which, using the rule $|cos(x - iy)| = \sqrt{\cos^2 x + \sinh^2 y}$ and recalling that $sinh^2 x \approx x^2$ if x <<< 1 becomes:

$$A_r^*(\omega) = \frac{1}{\sqrt{cos^2(kH) + sinh^2(kDH)}} = \frac{1}{\sqrt{cos^2(kH) + (kDH)^2}} = \frac{1}{\sqrt{cos^2 F + (FD)^2}} \qquad 1.\ 69$$

The trend of the amplification function *A*$_r$**(ω)* with the frequency factor *F* is shown in Figure 1.8 for different values of the damping factor *D*.

For *D* = 0 (no internal soil damping), the plot of the amplification function is as shown in Figure 1.3 characterised by infinite maximum values; for *D* > 0, the function is not periodic and has finite maximum values since the denominator is always greater than zero.

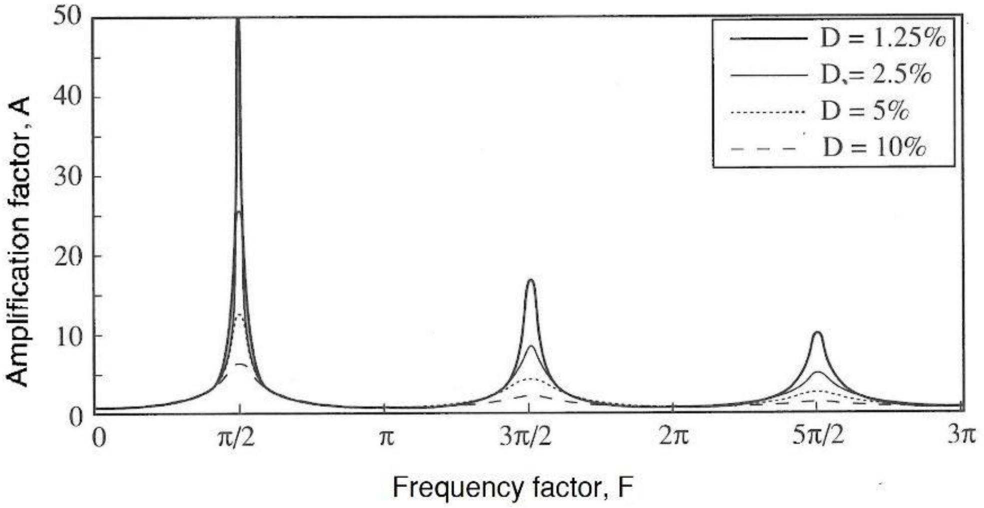

*Fig. 1. 8 Amplification function of damped linear elastic layer on rigid bedrock (**Lanzo and Silvestri, 1999**).*

The natural frequencies at which the amplification function reaches its maximum values are the same as for the previous models and can therefore be expressed by (1.20). The corresponding maximum amplification factors obtained by cancelling the derivative of (1.69) decrease with the order *n* of the vibration mode in the form:

$$(A_r^*)_{max,n} \approx \frac{2}{(2n-1)\pi D} \qquad n = 1,2,\ldots\infty \qquad 1.\ 70$$

The resonance peaks decrease with increasing frequency factor *F*, and the more so the higher *D* is. This effect is also well illustrated by the shape functions in Figure 1.9. At the first natural frequency (the so-called fundamental frequency of the site), setting *n* = 1 in (1.70), it gives:

$$(A_r^*)_{max,1} \approx \frac{2}{\pi D} \qquad 1.\ 71$$

Thus, for a homogeneous layer with linear visco-elastic behaviour over a rigid bedrock, the maximum value of the amplification at the fundamental frequency depends only on and is inversely proportional to the soil damping. The influence of internal damping phenomena on the amplification function then becomes more and more significant as f increases. At high values of *D*, seismic motion attenuation phenomena, rather than amplification may occur at high frequencies.

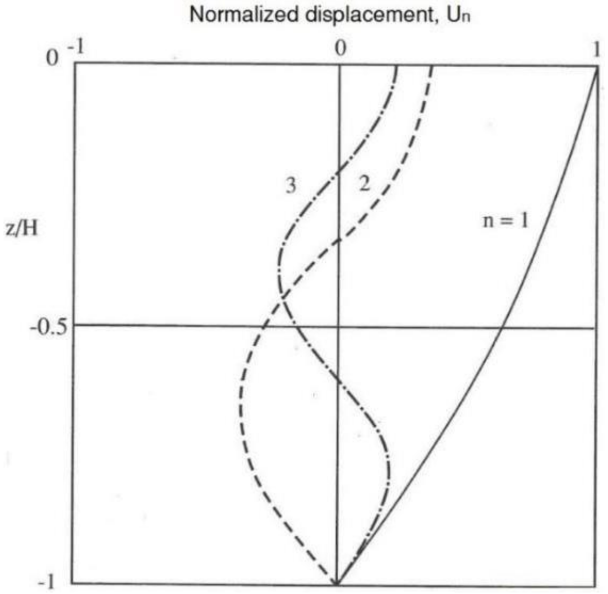

*Fig. 1. 9 Mode shapes for standing waves at fundamental (n = 1), second (n =2) and third (n = 3) natural frequencies for a soil layer with D = 5 % overlying rigid bedrock. Displacements are normalised by maximum displacement at the fundamental frequency (**Lanzo and Silvestri, 1999**).*

1.1.4 Model of visco-elastic homogeneous layer on deformable bedrock

The model of a soil layer with visco-elastic behaviour on a deformable bedrock represents the generalisation of all the models described above.

The transfer function $H_d^*(\omega)$, calculated as the ratio between the displacement amplitude at the soil surface and that at the outcropping bedrock, for the visco-elastic homogeneous layer on deformable bedrock model, has the expression (**Lanzo and Silvestri, 1999**):

$$H_d^*(\omega) = \frac{1}{cos\,(\frac{\omega H}{V_S^*}) + \mu {*} isin\,(\frac{\omega H}{V_S^*})} = \frac{1}{cos\,(F^*) + \frac{i}{I^*} sin\,(F^*)} \qquad 1.\,72$$

with the complex dynamic impedance ratio:

$$I^* = \frac{1}{\mu^*} = \frac{\rho_R V_R^*}{\rho_S V_S^*} \qquad 1.\,73$$

which is independent of *ω*.

The complex amplification function, the modulus of the transfer function, is a function of both the geometric damping related to μ, and the viscous (or mechanical) damping related to *D*, and cannot be expressed here in simple form; therefore, simply the expression of the peak values at natural frequencies is given (**Lanzo and Silvestri, 1999**):

$$(A_r^*)_{max,n} \approx \frac{1}{\mu + (2n-1)\frac{\pi}{2} D} \qquad n = 1,2,\ldots\infty \qquad 1.\,74$$

Relationship (1.74) shows that the peak values of the amplification function $A_d{}^*(\omega)$ at the natural frequencies of the layer depend exclusively on the impedance ratio μ and the viscous damping factor *D*. The maximum value obtained at the fundamental frequency for n = 1 is:

$$(A_r^*)_{max,1} = \frac{1}{\mu+\frac{\pi}{2}D} \qquad 1.75$$

and is plotted in Figure 1.10 as a function of the impedance ratio *I*, for different values of the damping factor *D*.

For *D* = 0, i.e., in the absence of mechanical soil damping, the amplification function reduces to (1.52), whereby the maximum peak amplification is equal to the impedance ratio *I*.

For a fixed value of *D* > 0, the maximum amplification increases as the dynamic impedance ratio I increases (i.e., as the admittance *μ* decreases). Similarly, for the same dynamic impedance ratio *I*, there is a decrease of the amplification peak as *D* increases.

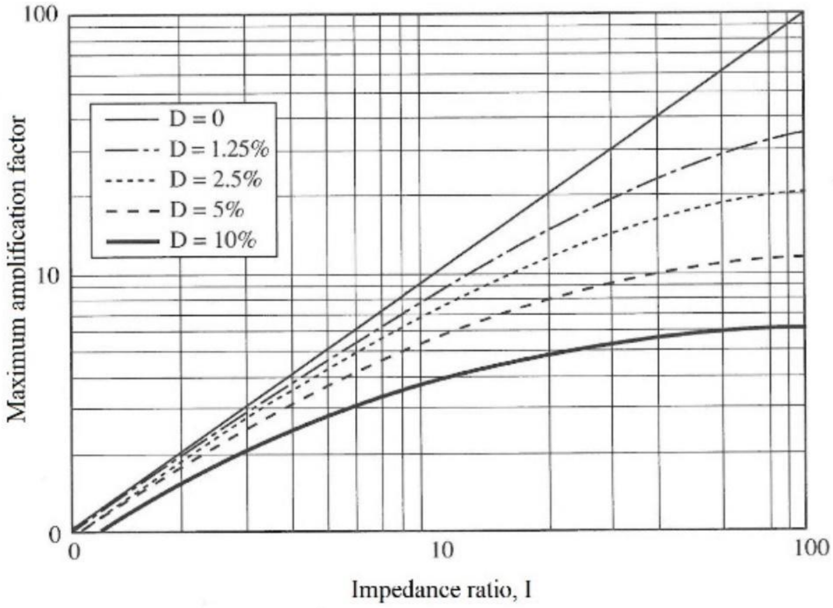

*Fig. 1. 10 Influence of dynamic impedance ratio I on maximum amplification factor relative to fundamental frequency in the case of a visco-elastic homogeneous layer over a deformable substrate (**Lanzo and Silvestri, 1999**)*

The impedance ratio *I* has a similar effect on the maximum amplification factor as the visco-mechanical damping of the soil. Therefore, it is possible to define an effective damping factor D_{ef} which is the sum of the terms:

$$D_{ef} = D + D_r = D + \frac{2}{\pi I} \qquad 1.76$$

The first term *D* represents the internal visco-mechanical damping of the soil, while the second term D_r depends on the impedance contrast between soil and bedrock and represents the damping associated with radiation energy loss.

The expression of the amplification peak with respect to the first fundamental frequency can thus be expressed in the more compact form as:

$$(A_d^*)_{max,1} \cong \frac{2}{\pi D_{ef}} \qquad 1.77$$

Which corresponds to the equation (1.71).
Also for this model, the values of the fundamental frequencies and periods are always provided by (1.20) and (1.21). Thus, the maximum value of the amplification function occurs at the fundamental frequency f_1:

$$f_1 = \frac{\omega}{2\pi} = \frac{V_S}{4H} \tag{1. 78}$$

And the corresponding vibration period, i.e., the fundamental period of the site, is obtained as:

$$T_1 = \frac{1}{f_1} = \frac{4H}{V_S} \tag{1. 79}$$

Expressions (1.77), (1.79), and (1.80), despite their simplicity, are particularly significant from an application point of view. Indeed, by assimilating a subsoil to an equivalent homogeneous layer (**Lanzo and Silvestri, 1999**), the expressions provide a first direct indication of the frequency ranges in which a significant site amplification effect can be expected, as well as the expected amplification factors.

1.1.5 Heterogeneity of the terrain

The dependence of the stiffness G_0 of the soil at very small strain on the state variables (mean effective stress $p' = \sum_i \sigma_i'/3$, plasticity index, degree of overconsolidation R_0 (= p'_p/p')) can be expressed with semi-empirical relations in the form (**Viggiani and Atkinson, 1995**):

$$\frac{G_0}{p_r} = A\left(\frac{p'}{p_r}\right)^n R_0^m \tag{1. 80}$$

where *A*, *m*, and *n* are dimensionless soil parameters, and p_r is a reference pressure (equal to 1kPa for simplicity). Therefore, the shear modulus *G* of a soil is proportional to a power of the mean effective stress, which is generally less than unity. Thus, even in the simple case of a subsoil with homogeneous lithology, the transverse stiffness varies proportionally with depth and so does the shear wave velocity. Closed-form analytical solutions exist in the literature that describe the local seismic response of a subsoil characterised by a continuous variation of shear stiffness (and hence V_S) with depth.

Ambraseys, 1959 treated the case of a constant density *ρ* and a modulus *G(z)* varying linearly with depth according to the expression:

$$\frac{G(z)}{G_H} = K^2 + \frac{1-K^2}{H} z \qquad \left(K^2 = \frac{G_0}{G_H} \Rightarrow K = \frac{V_0}{V_H}\right) \tag{1. 81}$$

where *H* is the thickness of the soil layer and K is a parameter that controls the variation of *G(z)*; $K = 1$ means *G* (or V_S) constant with z, while if $0 < K < 1$ then *G(z)* varies linearly with z. G_0 and G_H, V_0 and V_H denote the shear moduli and S-waves velocity at the surface and bedrock, respectively.

Idriss and Seed, 1968 and **Dobry et al. 1971** analysed the case of a horizontal deposit with constant density ρ, but with an increase in shear modulus with depth that varies with a power law:

$$\frac{G(z)}{G_H} = \left(\frac{z}{H}\right)^n \tag{1. 82}$$

where the exponent n can vary between 0 and 2. This model is closer to the constitutive relationship of the soil but has the disadvantage that the stiffness at the surface is infinitesimal or equal to zero.

To resolve this inconsistency, **Gazetas (1982)** and **Vinale and Simonelli (1983)** studied the case of a homogeneous soil layer with constant density ρ and modulus G that varies with depth according to the law:

$$G(z) = G_0(1 + \alpha \frac{z}{H})^{2m} \quad \Rightarrow V(z) = V_0(1 + \alpha \frac{z}{H})^m \qquad 1.83$$

Denoted by H the thickness of the horizontal soil layer, and with G_0 the stiffness at the surface, α and m are parameters that express the degree of heterogeneity, the combination of which can adequately interpret the average stiffness trend for soft alluvial soils, provided that the variation of the subsoil physical-mechanical properties with depth is sufficiently regular. The parameter α expresses the heterogeneity ratio and indicates the deviation from the ideal situation with a constant stiffness layer ($\alpha = 0$). In this model, the shear wave velocity increases with depth z.

Assuming a linear variation of shear wave velocity with depth ($m = 1$), (1.84) becomes:

$$\frac{G(z)}{G_0} = (1 + \alpha)^2 \qquad \Rightarrow \frac{V(z)}{V_0} = (1 + \alpha) \qquad 1.84$$

and the coefficient α expresses the heterogeneity ratio V_H/V_0.

In the model studied by **Gazetas (1982)**, the analytical solution of the equations of motion for m = 1 allows the derivation of the roots of Sn of the equation of motion:

$$S_n[ln\, ln\,(1 + \alpha)\,] + arctan(2S_n) = n\pi \qquad 1.85$$

and derive the modal shapes U_n and the natural periods T_n for each mode. In fact, given $\zeta = z/H$, yields:

$$U_n = \frac{1}{\sqrt{1+\alpha\zeta}} sin\left\{S_n ln\left[\frac{(1+\alpha)}{1+\alpha\zeta}\right]\right\} \qquad 1.86$$

$$T_n = \frac{4H}{V_0}\frac{\pi}{\alpha(4S_n^2+1)} \qquad n = 1,2,\ldots\infty \qquad 1.87$$

Figure 1.11 shows some of the results of the study in terms of the mode shapes U_n of the first four vibration modes, expressed for different values of the heterogeneity ratio V_H/V_0; for comparison, the mode shapes for the homogeneous subsoil model, corresponding to $V_H/V_0 = 1$ ($\alpha = 0$), are also shown. Figure 1.11 shows how the effect of heterogeneity leads to a significant change in mode shapes compared to the homogeneous subsoil case. As the heterogeneity ratio increases, the amplitude of the displacements of the mode shapes decreases more and more significantly with depth, and the maximum values are concentrated in the shallowest zone of the deposit.

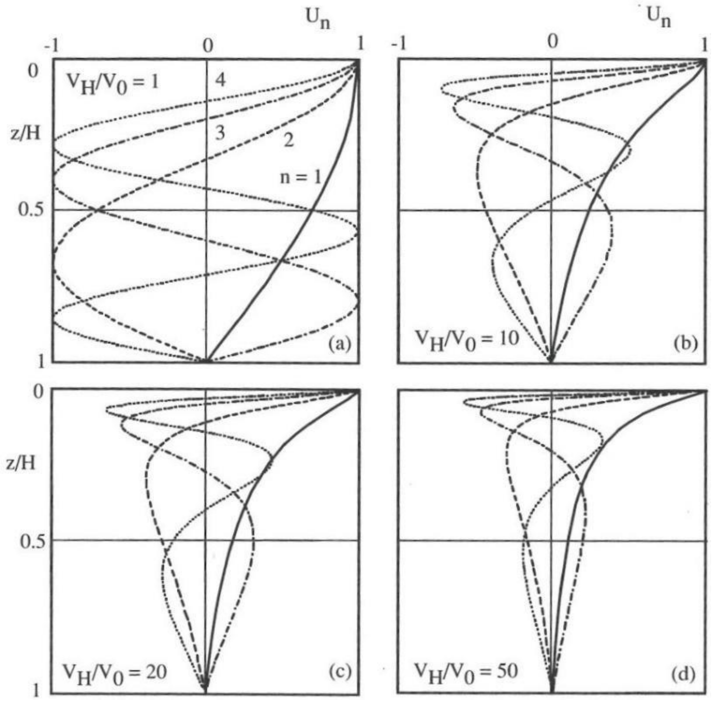

Fig. 1. 11 Mode shapes relative to the m = 1 case of linear variation of shear wave velocity with depth for increasing values of α. The mode shapes vary as the heterogeneity factor α varies. In (a) the case of visco-elastic homogeneous layer model on rigid bedrock with V_S *(or G) constant with depth z and thus* $V_H/V_0 = 1$ *(*V_S *= cost; α = 0) is plotted. The variation of α corresponds to the introduction of an increasingly significant variation with z of the* V_S *(and thus of the shear modulus G(z)) from (b)* $V_H/V_0 = 10$*, to (c)* $V_H/V_0 = 20$*, up to (d)* $V_H/V_0 = 50$*. Therefore, as α increases, the maximum displacement amplitudes are concentrated at the surface and decrease very rapidly with depth z. (**Vinale and Simonelli, 1983**)*

Relating the values of T_n expressed by (1.88) to the corresponding periods $\bar{T}_n$ of the homogeneous layer with a velocity equal to the average velocity of the heterogeneous soil deposit (Figure 1.12), we see that the heterogeneity reduces T_1 with respect to the corresponding $\bar{T}_1$. In contrast, for the higher modes there are values of $T_n/\bar{T}_n$ that are always greater than 1 and increase with V_H/V_0. Thus, the natural periods of the layer are always larger than those for the homogeneous case, the larger the heterogeneity ratio is.

By coupling the general solution of the equation of motion in the frequency domain, u(z,ω), with the boundary conditions, it is possible to obtain the transfer function *H(ω)* as ratio between the displacement *u(0,ω)* of the free surface of the soil deposit and the displacement at the base *u(H,ω)*. The solution of **Gazetas (1982)** expresses the transfer function. Considering a constant damping D with depth, in the general form the transfer function *H(ω)* yields:

$$H(\omega) = \frac{2q}{(-0.5+q)(1+\alpha)^{-0.5-q}+(0.5+q)(1+\alpha)^{-0.5+q}} \qquad 1.88$$

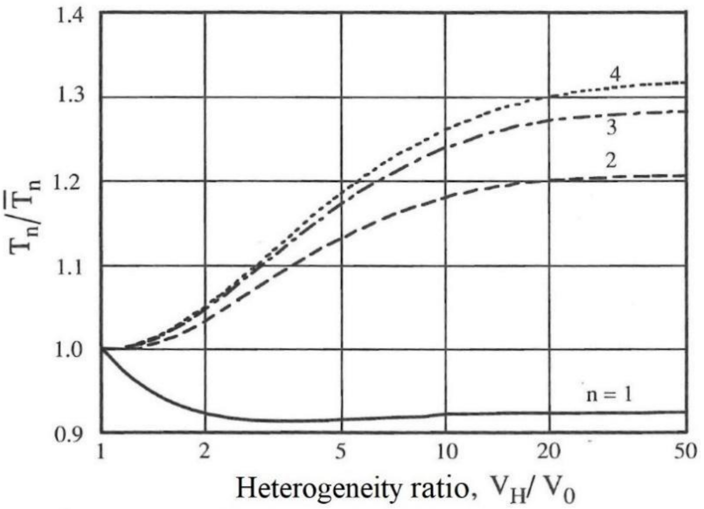

*Fig. 1. 12 Natural period for m = 1 as a variation of the heterogeneity ratio V_H/V_0 (**Vinale and Simonelli, 1983**). As the heterogeneity factor increases, i.e. as the variation of the shear modulus G (or shear wave propagation velocity VS) increases with depth z, it is observed that the ratio between the natural period Tn calculated with (1.88) and the period $\bar{T}_n$ relative to the case constant V_s with z (or G) decreases for the first vibration mode (n = 1), and increases for the subsequent modes (n=2,3,4); this implies that the fundamental frequency increases and the subsequent natural frequencies decrease, completely changing the amplification function.*

In (1.89), the frequency dependence is expressed by the dimensionless complex parameter q:

$$q = \sqrt{\frac{1}{4} - \frac{\omega^2 H^2}{V_0^2 \alpha^2 (1+2iD)}} = \sqrt{\frac{1}{4} - \frac{F^2}{\alpha^2 (1+2iD)}} \qquad 1.89$$

In Figure 1.13, the amplitude *A(F)* of the amplification function obtained from the modulus of eq. (1.89) is plotted with continuous line for a deposit with $\alpha = 0.5$ ($V_H = 1.5\ V_0$), for two damping values (D = 5%, D = 10%).

To show the influence of the degree of heterogeneity (represented by the parameter α), the figure 1.13 also shows the first peaks of the amplification functions for different values of α ($\alpha = 0$ corresponding to a homogeneous deposit, $\alpha = 2$ and $\alpha = 10$). As the degree of heterogeneity α increases, the plot shows both an increase in the first fundamental frequency (i.e., the decrease in period T_1 discussed earlier) and an increase in the amplification factor.

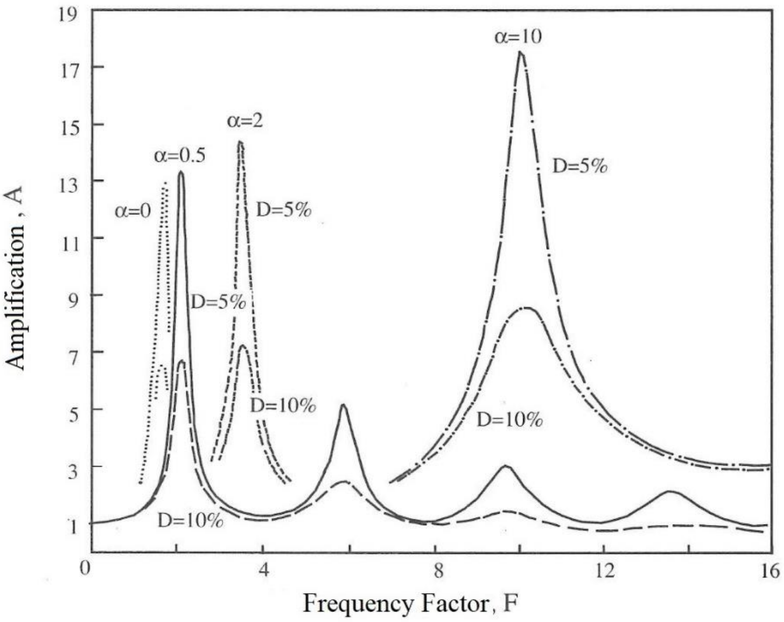

*Fig. 1. 13 Amplification function A for a layer with linearly increasing velocity and constant hysteretic damping, 5 percent or 10 percent (**Gazetas, 1982**). In the plot, each line type refers to a different heterogeneity factor α. With the same heterogeneity factor α, the amplitudes of the amplification function decrease as the damping factor D increases. On the contrary, fixed, for example, a value of damping factor D = 5%, as the heterogeneity factor α increases, i.e. as the variation of the shear modulus G (or shear wave propagation velocity V_S) with depth z increases, an increase in the amplitude of the peaks relative to the first natural frequency (or fundamental frequency) is observed. This is a direct consequence of the concentration of energy and thus displacements at the surface (Fig. 1.11), which results in larger peaks.*

The effect of the soil decomposition heterogeneity on the amplification function A is effectively illustrated by the example in Figure 1.14, taken from the analysis of the response of soft clays in Mexico City (1985 Mexico City earthquake, **Lanzo and Silvestri, 1999**). The amplification function related to the heterogeneous soil model, with shear wave velocities characterised by a parabolic distribution with increasing depth (~20 m/s at the surface; ~100 m/s at the base of the deposit), is compared with that corresponding to the homogeneous subsoil model, with constant average shear wave velocity V_S = 75 m/s throughout the layer. The comparison confirms what was expected from the theoretical function, namely that the effect of soil heterogeneity on the amplification function caused the fundamental frequencies of the deposit to move closer together and the amplification peaks to increase compared to the homogeneous subsoil model. The two factors combined mean that simplifying a subsoil (or layer) with stiffness properties that increase with depth to an equivalent homogeneous soil layer result in a significant underestimation of the potential amplification effects of the seismic motion.

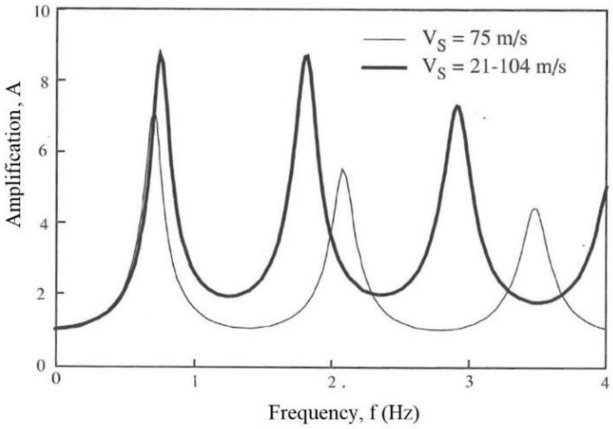

*Fig. 1. 14 Comparison of amplification functions for the assumption of homogeneous and a heterogeneous subsoil for Mexico City (**Lanzo and Silvestri, 1999**)*

1.1.6 Effect of the non-linearity of soil behaviour

The behaviour of soil is non-linear and dissipative even at very small deformation. This is evident from the trend of the experimental G-γ and D-γ curves of shear stiffness decrease and damping increase with increasing values of shear deformation induced in the soil element. An important step in obtaining a more reliable model of the soil layer affected by seismic wave propagation is to move away from the assumption of a linear constitutive relationship or at most a linear visco-elastic relationship, as assumed in previous cases. Recent research, carried out taking advantage of an extensive instrumental network, has made it possible to study the effects of non-linear behaviour on the seismic response of the site. The influence of the non-linearity of the soil behaviour on peak acceleration is qualitatively illustrated in Figure 1.15. The plot refers to a homogeneous soil layer on an horizontal bedrock, and subjected to seismic motion characterised by increasing values of peak acceleration at the bedrock $a_{max,r}$. The same figure shows the distributions of the maximum shear deformation γ_{max} (Figure 1.15 a), the shear modulus *G* (Figure 1.15 b), the damping factor *D* (Figure 1.15 c), and of peak acceleration a_{max} within the soil layer as a function of depth (Figure 1.15 d), when the peak acceleration at the bedrock $a_{max,r}$ varies.

When the latter increases, due to the non-linear behaviour of the soil, the maximum shear deformation increases and consequently the shear modulus decreases, and the mobilised damping factor increases. For low energy levels of the considered earthquake, the peak acceleration increases along the layer profile from the bedrock to the soil surface (curves 1 and 2 in Figure 1.15 d). This is because, the reduction of the stiffness properties of the soil due to the non-linear behaviour reduces the transmission of high frequencies, while the increase of the damping factor reduces the peak amplification of the displacement amplitudes.

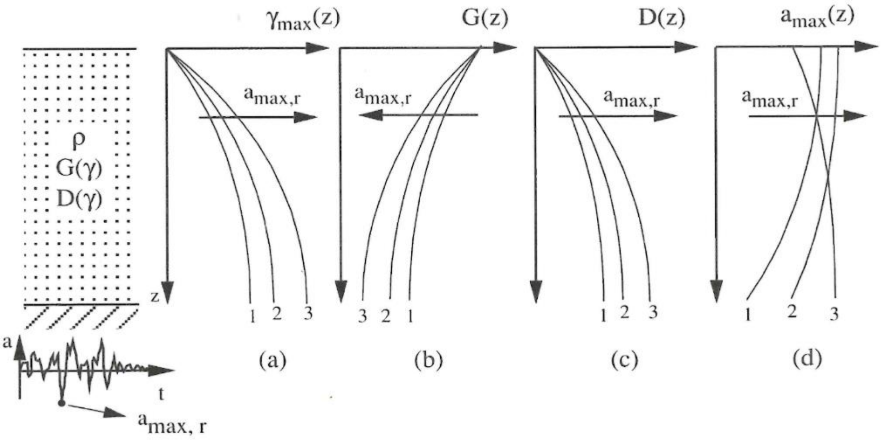

*Fig. 1. 15 Variation of maximum tangential strain profiles (a), shear modulus (b), and damping factor (c) m, and maximum acceleration (d) in soil as maximum acceleration on rock $a_{max,r}$ increases (**Lanzo and Silvestri, 1999**)*

Thus, in terms of the amplification factor (evaluated as the ratio between the peak acceleration at the soil surface and the peak acceleration at the rock), the non-linearity effect results in a decrease of the amplification factor as the level of acceleration at the rock increases. **Seed et al. (1976a)**, on the basis of statistical processing of numerous accelerometric recordings of seismic events, proposed the plot in Figure 1.16a; the average curves of peak acceleration at the surface versus peak acceleration at the bedrock are illustrated. Average curves are shown for three categories of deposits: stiff soils (consistent clays, thickened sands, and gravels), deep cohesionless soils (H>75 m), and soft to medium stiff clays and sands. When peak acceleration values on rock are less than about 0.1 g, all soils amplify seismic motion. As peak acceleration on rock increases above 0.1 g, maximum values at the surface decreases, with the decrease being greater for soft soils than for consistent soils. For peak acceleration values on rock greater than 0.2 g, average curves are obtained by extrapolating the available experimental data.

Idriss (1990) updated the empirical relationship between peak acceleration on rock and the surface, restricted to soft, cohesive soil deposits. The relationship shown in Figure 1.16b was based on accelerometric recordings from the Mexico City (1985) and Loma Prieta (1989) earthquakes for peak acceleration values on rock less than 0.2g; for values greater than 0.2 g, the results of numerical analyses of the local response were used because of the lack of empiric data. Comparison of the average curves for the more deformable deposits in Figures 1.16a,b shows the dramatic change that the empirical evaluation of the local seismic response to the surface of soft, cohesive soils has undergone in less than a decade: not only because the observed amplification factors are much larger, but also because of the much wider range of values (up to 0.4g) of the peak acceleration on rock in which sensitive amplification phenomena can occur.

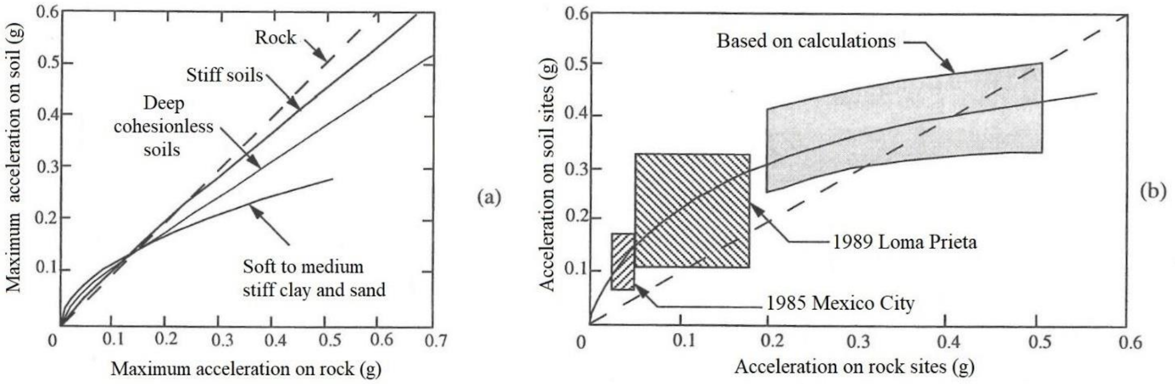

*Fig. 1.16 Variation of maximum acceleration on surface with maximum acceleration on rock for (a) on rock and other local site conditions (**Seed et al., 1976a**) and (b) soft cohesive soils (**Idriss, 1990**). In both plots the dotted line corresponds to the absence of amplification or de-amplification (a_{max}/a_{max}(rock) = 1).As the input acceleration increases, there is a shift from amplification to de-amplification effects. This effect is less pronounced for more consistent soils that amplify/deamplify less than the soft soils .*

Figure 1.17 illustrates the influence of the non-linearity of the soil behaviour on the amplification function of the clay deposits in Figure 1.15 (Mexico City subsoil). The plot of the amplification functions is related to the increasing energies of the reference seismic motion, to which correspond increasingly higher values of the shear deformation γ induced in the soil, and therefore varying stiffnesses and damping corresponding to the dependence of G and D on γ. However, this variation changes in reduction as a function of frequency, i.e. at high frequencies the reduction in frequency and amplitude is more pronounced than the variation at low frequencies, since high-frequency waves attenuate much faster than low-frequency waves.

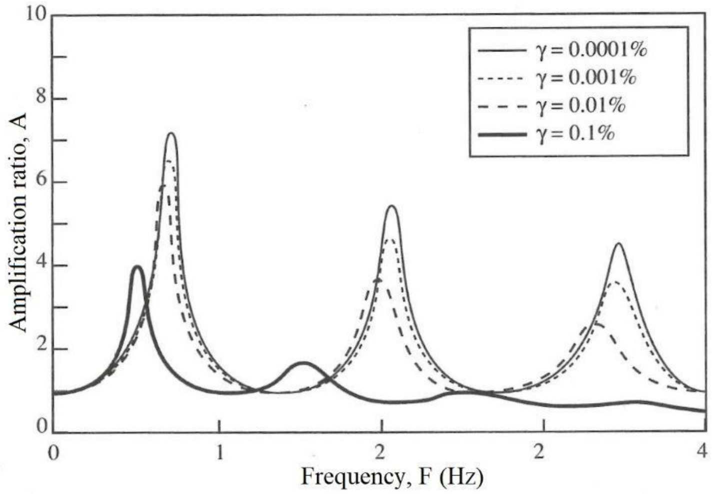

*Fig. 1. 17 Influence of non-linear soil behaviour on the amplification function (**Lanzo and Silvestri, 1999**). As the magnitude M of a seismic event increases, both the maximum acceleration a_{max} and the strain level γ increase; this leads to a reduction in the shear modulus G and an increase in the damping factor D, which result in a reduction of both the natural frequencies and their peaks. Therefore, the effect of non-linearity completely changes the amplification function.*

As the amount of mobilised deformation increases, the influence of the non-linearity of the soil behaviour leads to an attenuation of the amplification peak, which is inversely proportional to the damping. At the same time, the amplification peak shifts to lower frequencies (higher periods), which is due to the reduction of the shear modulus (and thus the increase of the impedance contrast). The figure also shows that at high energy levels of the reference earthquake on rock (curve $\gamma = 0.1\%$), the non-linearity effect tends to cause attenuation phenomena at high frequencies.

It can be seen that the amplification function depends on the combination of stratigraphic characteristics of the subsoil, amplitudes, and frequency content of the seismic motion, and the occurrence of the non-linear behaviour of the soil. Given the same expected earthquake and the same stratigraphic characteristics of the site, the local seismic response is strongly influenced by the susceptibility of the soils to high or low linear behaviour. However, the outcome of Figure 1.17 is valid for the model of non-linearity considered that very often was not confirmed by real data. Moreover, only in a few cases it has been observed that for very strong earthquakes, some soil types can show de-amplification effects due to non-linearity effects; for example, according to **Kokusho and Ishizawa (2021)** “soil nonlinearity during strong earthquakes has only a marginal effect even in soft soil sites on the amplification between surface and outcrop base except for ultimate soil liquefaction failure, while strong nonlinearity clearly appears in the vertical array amplification between surface and downhole base”.

1.1.7 Effects of basins geometry

Several studies in the 1980s highlighted the importance of the presence of alluvial valleys and sedimentary basins in the estimation of site response. The significant amplification phenomena that can occur on the surface of alluvial deposits in a valley can cause the duration and amplitude of the seismic motion to be increased compared to what is predicted by the one-dimensional theory relating to the propagation of shear waves in vertical direction (**Bard and Bouchon, 1985**; **Wirgin e Bard et al., 1996**). The understanding of these phenomena has been of primary importance for seismic risk studies of large urban areas (Mexico City, Los Angeles, Osaka, Tokyo) located right at alluvial valleys and in the analysis of the seismic vulnerability of the existing building stock there. In the case of a soil deposit, which can be assigned to a one-dimensional scheme, it has already been observed (**e.g. Lanzo and Silvestri, 1999**) that the main causes of the amplification of the motion are both the phenomenon of trapping S waves inside the deposit (favoured by the impedance contrast between the soil and the bedrock) and the resonance phenomenon determined by the proximity of the frequencies of motion of the bedrock with the natural vibration frequencies of the soil deposit.

In the case of an alluvial valley, in addition to the factors mentioned above, two other phenomena must be considered that induce edge effects related to the two-dimensional geometry of the problem.

The first effect is the focusing of the seismic waves in areas close to the edge of the valley as a result of the constructive interference between the reflected and refracted wave fields (Figure 1.18). This phenomenon explains the damage that occurred in several seismic events along strips of land at the edge of alluvial valleys (**Pitarka et al., 1996**). The second effect results from the incidence of seismic waves on the non-horizontal bedrock-soil interface at the edge of the valley, leading to the generation of surface waves with a horizontal propagation direction (**Aki and Larner, 1970**). In this case, with a high soil-bedrock impedance contrast, the generated surface waves remain confined to the valley and are reflected multiple times at the edges. The range of displacements that are generated by surface waves is limited only by internal soil damping. Typically, these surface waves have a relatively low propagation velocity (<1000 m/s) and periods between 0.5s and 5s (i.e., frequencies between 0.2 and 2 Hz). However, the distinctive feature of these waves is their long duration, which is generally several tens of seconds.

The previously described edge effects are illustrated in figure 1.18, where the cross section of an alluvial valley is represented, subject to S-waves incident at the edge of the alluvial basin. Qualitative seismograms of the horizontal component, which are recorded at two different locations, on the rock and on the soil, are indicated. The seismogram related to the alluvial deposit clearly shows the arrival of surface waves generated by the conversion of the incident S-waves.

Therefore, the use of the classical one-dimensional scheme, which does not take into account the generation of surface waves, may lead to a significant underestimation of the amplitude and duration of the seismic motion, especially for periods longer than 0.5 s (**Lanzo and Silvestri, 1999**). This can have important implications from an engineering perspective particularly with respect to the seismic vulnerability of bridges, dams, high-rise buildings, and other structures characterised by high natural periods of vibration.

In deep alluvial valleys, phenomena of interaction between volume and surface waves are much more complex than those of shallow valleys. Furthermore, the excited waves can produce significant differential motions causing a spatial variability in the seismic response (**Bard, 1998**).

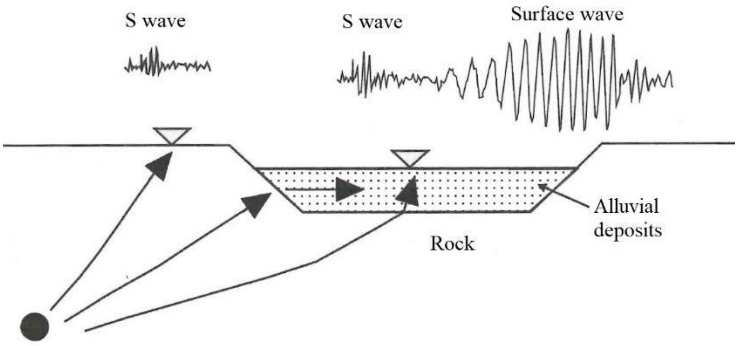

Fig. 1. 18 Schematic representation of the generation of surface wave by edge effects at the edge of an alluvial basin (**Lanzo and Silvestri, 1999**)

In recent decades, there has been considerable progress in the study of alluvial valley amplification phenomena, both from an experimental and modelling perspective.

Experimental observations of recent low- and high-intensity earthquakes, derived from seismic network records or, to a lesser extent, local arrays, have made it possible to highlight the geometric factors influencing the variation of the local seismic response at different stations located along cross-sections of a valley (e.g. **Jongmans and Campillo, 1993**) and to verify the presence of long-period surface waves generated at the edges (e.g. **Frankel, 1994**). Numerical studies have examined an extremely wide range of situations varying in relation to the geometric configuration of the valley, the type of incident wave, the angle of incidence, and the schematisation (2D or 3D) adopted in the model. An extensive review of the most commonly used modelling methods and the main results obtained can be found in **Aki (1988)** and **Bard (1994)**.

As an example, Figure 1.19 shows a comparison between the results of some 1D and 2D numerical simulations of simplified geometric models of alluvial valleys subject to SH incident waves (**Bard and Gariel, 1986**). The deposit models present two sediment-filled valleys A and B, with geometric characteristics expressed as a function of the H/L shape factor, where H is the maximum thickness of the deposit at the centre and L is the half-width of the valley. The numerical analyses refer to the shallow valley case (characterised by $H/L < 0.25$), with a shape factor $H/L = 0.1$, and the deep valley case (characterised by $H/L > 0.25$) with a shape factor $H/L = 0.4$. The numerical analyses performed are of three types: (a) one-dimensional with linear variation of shear wave velocity with depth (1D, V_S, increasing); (b) two-dimensional with constant value of shear wave velocity (2D, constant V_S); (c) two-dimensional with linear variation of shear wave velocity with depth (2D, increasing Vs). In each of the cases examined, the damping factor of the alluvial soil is 2.5%.

The modelling results are presented, for several stations located along the valley cross-section, in terms of the amplification factor variation with the dimensionless frequency f, i.e. the frequency f normalised with respect to the first resonance frequency f_1, of the one-dimensional model relative to the centre of the valley ($f_1 = V_S/4_H$). Figure 1.19a shows the results for the surface valley case model A (H/L = 0.1). The 1D model provides results that satisfactorily approximate those of the 2D model at the centre of the valley (station 8). Moving from the centre of the valley towards the edge, the difference in response between the 1D model and the 2D model becomes more and more sensitive (stations 6 and 4). Near the edge of the valley (station 2), where the interference phenomena between incident vertical waves and surface diffracted waves are marked, the local response of 2D model is broadband while the 1D model is characterised by an isolated maximum.

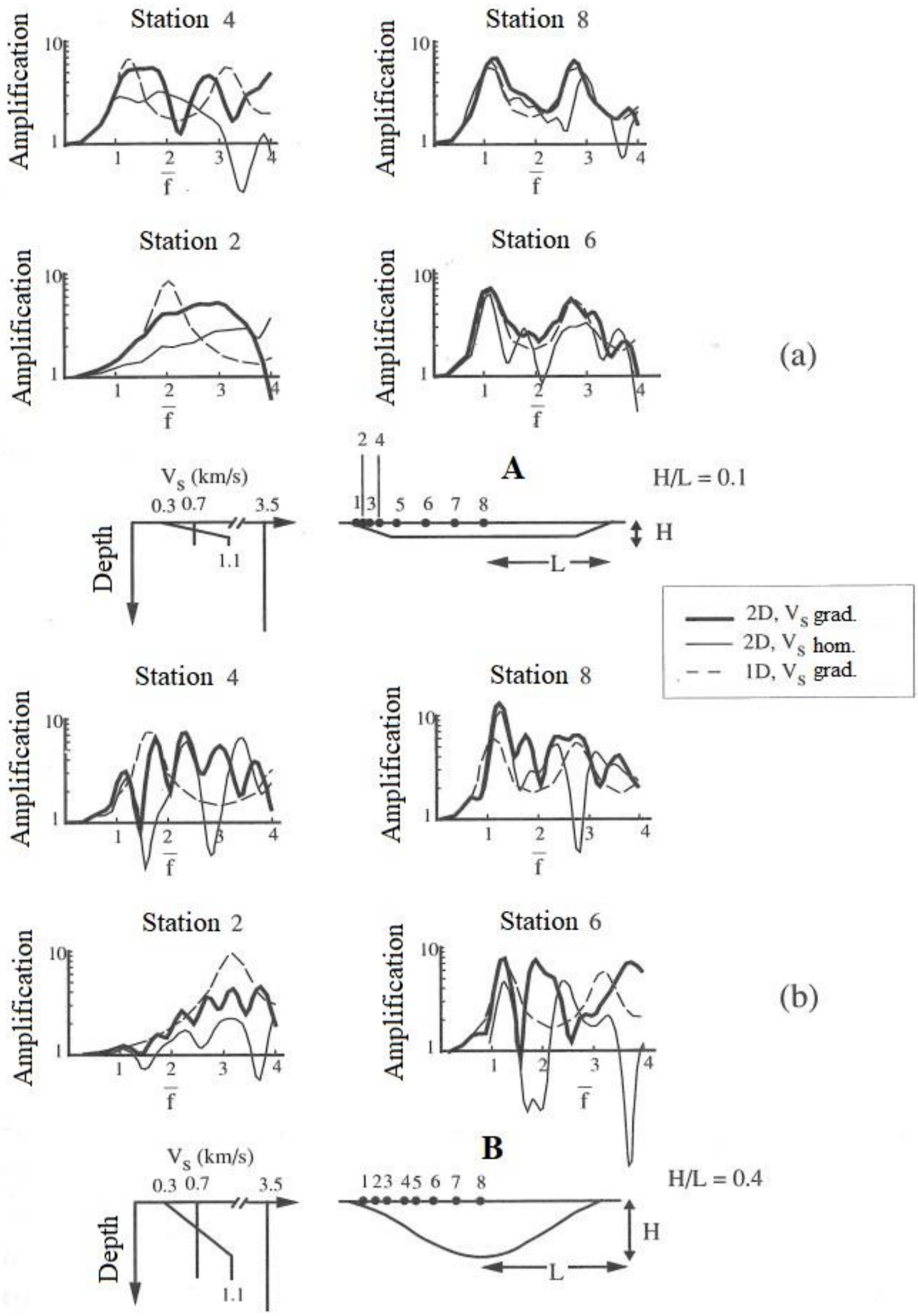

Fig. 1.19 Numerical modelling and analysis of the amplification produced by (a) shallow valley A model (H/L = 0.1) and (b) deep valley model B (H/L = 0.4) (Modified from **Lanzo and Silvestri, 1999**)

Figure 1.19b shows the results for the deep valley case model B (H/L = 0.4). The 2D model provides a significantly different response to that of the 1D model at all stations. The main difference is the oscillatory nature of the 2D model response, evidenced by the presence of different peaks in the amplification function. With regard to the magnitude of amplification, the 2D model underestimates amplification phenomena compared to the 1D model in proximity of the valley edge (station 2); on the contrary, as the distance from the edge increases (stations 4 and 6) toward the centre of the valley (station 8), the 2D model overestimates amplification phenomena at higher frequencies compared to the 1D model.

It follows from the above considerations that deep alluvial valleys are characterised by significantly more complex interaction phenomena between body and surface waves than shallow valleys. The reliability of 1D modelling is also limited at the valley centre for high values of shape factor; for such geometries it is appropriate, if not indispensable, to use 2D analysis (**Lanzo and Silvestri, 1999**). In both cases, however, it must be emphasised that the marked difference in response between the different locations can lead to differential ground movements with relevant implications for the anti-seismic design of structures with considerable linear development, such as dams. A more detailed analysis of the problem is offered by **Gazetas and Dakoulas (1992)**.

Other examples documenting complex 2D effects in alluvial valleys are provided in two areas near Thessaloniki (Greece) in the EUROSEISTEST experimental site (http://euroseis.civil.auth.gr) described by **Pitilakis et al. (1999)**, and in a study conducted by **Bindi et al. (2009)** in the Gubbio basin (Umbria, Central Italy). The EUROSEISTEST experimental site was deployed in a valley near Thessaloniki in the epicentral area of the strong 1978 Ms = 6.4 earthquake.

In a first study conducted at the EUROSEISTEST experimental site, **Raptakis et al. (2000)** reported the transverse direction recordings for each station of an example of a far-field event (Kozani earthquake Mw=6.5, R=100km) that is part of the database of ground motions recorded in surface and down-hole accelerographs. For each trace, the authors also report synthetic 1D SH wave models to enhance discrepancies between the 1D model and recorded motion. Therefore, **Raptakis et al. (2000)** first pointed out that the 1D model is inadequate to accurately simulate the recorded motion, especially in the central part of the valley. The reasons for these discrepancies have been discussed in detail in many studies (**Raptakis et al., 2000**; **Chavez-Garcia et al., 2000**; **Makra et al., 2001**; **Pitilakis et al., 2001**). Furthermore, the authors in the frequency domain, through the transfer functions of the P-, S- and Surface Waves (SW-waves) that make up the signal recorded both at the surface and in the down-hole in the centre of the valley, observed that up to 2Hz the amplitudes of the SW-waves are greater than the amplitudes of the S-wave window. Thus, **Raptakis et al. (2000)** emphasised that this trend shows that the surface waves influence the entire volume of the subsurface, at least in the central part of the valley, and all three components. Since surface waves were neither observed at the reference site located on outcropping gneiss basement nor at the edges of the valley, **Raptakis et al. (2000)** concluded that the observed strong surface wave traces are locally generated on the lateral geological discontinuities of the valley, which is a graben. Furthermore, **Raptakis et al. (2000)** pointed out that since the observed maxima in the S-wave and surface-wave parts appear at the same frequency (0.7 Hz), it implies that both upward-propagating S-waves and locally generated surface waves contribute to the spectral amplification of the fundamental peak. **Makra et al. (2001)** on the same site conducted a 2D numerical analysis, clearly indicating that the higher amplitudes of motion are not related to vertically propagating SH waves, since the synthetic seismograms calculated in their study are dominated by locally generated Love waves that converge towards the centre of the valley, resulting in large amplitudes and a consequent increase in duration. These phenomena are not observed outside the central part of the valley. Therefore, **Makra et al. (2001)** through numerical analysis of synthetic ground motions verified the same phenomenon observed experimentally by **Raptakis et al. (2000)**, i.e. the existence and importance of surface waves, which are generated locally at the valley edges and propagate towards the centre of the valley.

In a 2nd case study conducted in the city of Thessaloniki, **Raptakis et al. (2004a)** showed the examined complex effect of the lateral variations on ground motion studied on a 2D cross section that joins the coastline and the boundary between sediments and bedrock on which the city lies. The authors used three simultaneous recordings of a Mw= 4.8 event occurred on 1993 December 16th recorded by broadband seismometers along whose coordinate the cross-section had been drawn. From the experimental transfer functions calculated for the two stations located on the coastline and in the centre of the cross-section respectively, **Raptakis et al. (2004a)** inferred that the amplification of the fundamental peak of the transverse component is greater than the radial one and moreover shifted to lower frequencies, guessing that it is a strong indication of the appearance of diffracted Love waves and their pronounced role in the recorded ground motions. Furthermore, the authors point out that the greater amplification of the vertical component at the station furthest from the edges is an indication that Rayleigh waves are also generated at the edges and influence the vertical component. Thus, **Raptakis et al. (2004a)** found the same phenomenon observed at Euroseistest, i.e. that locally generated surface waves at the valley edges induce additional amplification to the propagation of 1D volume waves, particularly at the 1D fundamental frequency. **Raptakis et al. (2004b)** performed numerical analyses at the same site and found that 2D analyses using a finite difference or finite element model simulated the actual recordings much better, while the 1D model in their study proved to be rather inadequate to accurately describe the complicated pattern of site effects at the station furthest from the edges, which is dominated by the presence of surface waves generated at lateral geological discontinuities, i.e. at the valley edges.

In another study conducted in the Gubbio basin (Umbria, Central Italy), **Bindi et al. (2009)** analysed in both time and frequency domains the recordings of 140 local earthquakes ($1.2 \leq Ml \leq 4.7$) observed by two linear arrays installed along the longitudinal and perpendicular axis of the basin to determine the spatial variation of local site effects in the basin. The authors point out that the time series recorded in the Gubbio plain are characterised by locally generated waves affecting both horizontal and vertical components, which cause a significant increase in both the duration and amplitude of ground motion compared to a nearby rock site. **Bindi et al. (2009)** concluded that the spectral amplifications detected in the Gubbio basin are determined by a combination of 1D effects and lateral propagation, which cause a large amplification of the horizontal and vertical components of the motion over a wide frequency range that reaches maximum values in the centre of the valley, thus highlighting the contribution of 2D/3D effects in the Gubbio Plain response site. **Bindi et al. (2011)** highlighted how 2D–3D effects play an important role in determining the site amplification effects in Norcia; they performed time-frequency analysis on a station located inside the basin showing high spectral amplitudes after the S-wave phase, “not observed on a station located on the bedrock, suggesting the presence of locally generated wave trains”. **Di Giulio et al. (2020)** studied the heterogeneous distribution of the H/V curves in nearby points showing as it is an indication of the spatial variability of seismic ground motions in Norcia basin.

1.1.8 Effects of topography

Local effects attributable to the influence of topography have been observed several times during the past two decades in numerous seismic events (**Geli et al., 1988; Faccioli, 1991; Finn, 1991; Chavez-Garcia et al., 1996; 1997, LeBrun et al., 1999; Jibson, 1987**). Observation of the location of damage suggests that the influence of surface geometry is strongest at the top of a relief (**Celebi, 1987**; **Kawase and Aki, 1990**). The relevance of such phenomena in seismic events is documented, for example in Italy, by the extent of damage observed at the top of reliefs in the 1976 Friuli earthquake (**Brambati et al, 1980**), the 1980 Irpinia earthquake (**Siro, 1982**; **Rippa and Vinale, 1983**), the 2009 L'Aquila earthquake (**Gallipoli et al., 2013**), and the 2016 Central Italy earthquake (**Primofiore et al., 2020**, **Grelle et al., 2021**, **Sextos et al., 2018**).

From the application point of view, the change in the characteristics of seismic motion due to the surface geometry of the soil affects not only the assessment of seismic risk of the built environment, but also infrastructures such as road and river embankments, and dams made of loose materials, in topographically rugged areas (**Davis and West, 1973**; **Çelebi, 1991**; **Vessia et al., 2013, 2016**). “Topography can have significant effects on seismic waves when the incident wavelengths are comparable to the size of the topographic features and the topographic slopes are relatively steep" (**Boore, 1972**).

The physical phenomenon of amplification of motion at the top of a topographic relief is attributed to the focusing of seismic waves near the crest of the relief due to reflection from the free surface (Figure 1.20) and to the interaction between the incident and diffracted wave fields (**Bard, 1982**).

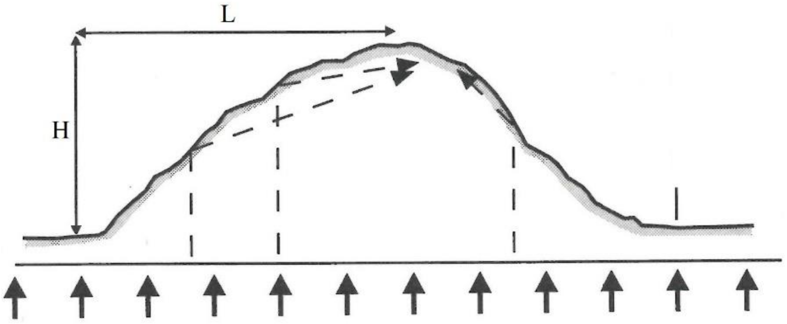

*Fig. 1. 20 Mechanism of focusing seismic waves at the top of a relief (**Lanzo and Silvestri, 1999**). L: semi-length; H: height of the topographic irregularity.*

A first approximate quantitative assessment of the topographic effects can be made using a simple topographic irregularity represented by an undefined wedge, assuming an elastic, homogeneous, and isotropic medium (e.g., **Aki, 1988**; **Faccioli, 1991**). The wedge is subjected to incident SH-waves that propagate vertically and move parallel to the longitudinal axis of the wedge (Figure 1.21a).

For this geometric scheme and with the assigned boundary conditions, a closed-form analytical solution is available (**Sanchez-Sesma, 1985, 1990**) in which the motion parameters are expressed as a function of the angle at the wedge vertex $\phi = \theta\pi$ ($0 < \theta \leq 2$). The horizontal soil surface corresponds to the case $\theta = 1$.

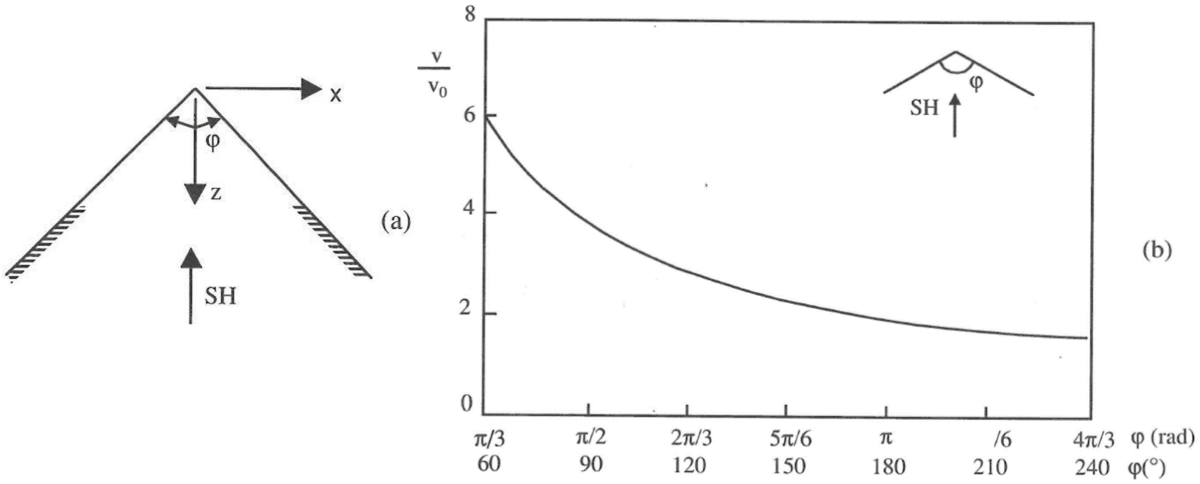

*Fig. 1. 21 (a) Characterisation of a simple topographic irregularity: notation for a triangular wedge excited by vertical SH waves with orthogonal displacements with respect to the plane; (b) variation of the amplification factor as a function of the angle at the vertex of the triangular wedge (**Sanchez-Sesma, 1990**)*

The amplification factor *A*, calculated as the ratio between the amplitude *v* of the displacement along the longitudinal axis at the vertex of the triangle, and the amplitude of the incident waves v_0, is:

$$A = \frac{v}{v_0} = \frac{2}{\theta} = \frac{2\pi}{\varphi} \qquad 1.90$$

Figure 1.20b shows the variation of the amplification factor as a function of the angle ϕ. It can be observed that even for relatively gentle topographies (e.g., $\phi \approx 120°$, corresponding to a slope of 1:2, which is characteristic of many earth structures), amplification factors of three times the amplitude of the incident SH waves can occur at the surface.

Thus, according to this simple model, the amplification of SH waves associated with a topographic irregularity depends only on the geometric shape and is not affected by other factors.

Numerical model and experimental studies (**Bard e Tucker, 1985**; **Jibson, 1987**; **Pedersen et al., 1994**; **Chavez-Garcia et al., 1997**) show that topography-related effects of seismic motion amplification must be considered in the seismic design of structures near the crest and sides of a natural or artificial slope.

The following is a summary of the most reliable evidence on the influence of topography on seismic motion, taken from the main experimental and theoretical studies in the literature (e.g., **Geli et al., 1988**; **Bard, 1994**; **Faccioli, 1991**; **Finn and Liam, 1991**):

- at the top of a topographic irregularity, seismic motion is amplified compared to that at the base;
- the amplification at the top of a topographic irregularity is due to its geometrical characteristics, since focusing phenomena occur when the incident wavelength λ is comparable to the semi-length L of the base of the irregularity (Figure 1.20);
- the entity of the amplification phenomena is correlated with the shape of the topographic irregularity: the larger the shape factor H/L (H: height; L: semi-length of the topographic irregularity), the stronger the amplification at the top;
- along the flanks of a topographic irregularity, the interaction between incident and diffracted waves leads to rapid changes in motion, amplitude, and frequency content; this generates a complex field of displacements with alternating amplification and attenuation phenomena that can result in pronounced differential motions;
- there is qualitative agreement between the results of the two-dimensional numerical modelling and the experimental observations regarding the amplification of ground motion at the top of a topographic irregularity and the complex phenomena of amplification and attenuation that occur along the flanks;
- However, there is no quantitative agreement between the modelling results and the experimental observations: In general, the measured amplification ratios are much larger than the theoretical values due to the sum of stratigraphic and topographic effects.

1.2 Models for characterising the structural response of structures

In the context of the dynamics of structures, the motion and state of stress of a mechanical-structural system that evolves over time is studied. In this paragraph is presented an approach that will lead to the formulation of mechanical models of the "deterministic" type and will therefore focus attention on dynamic systems with known features and subjected to variable conditions prescribed as a function of time. Starting from the structural problem, and in agreement with the principles of physics, the analyses are carried out in mathematical terms by schematizing the empirical reality by means of discrete models formulated appropriately.

The fundamental distinction between the behaviour of a dynamically loaded system compared to a static one can be described heuristically by means of the example schematized in Fig. 1.22. Therefore, let's imagine studying the structural response of a slender tower, represented for simplicity as a vertical shelf fixed to the soil and subjected to a constant static load *P*, as shown in the figure on the left, or variable over time *P(t)* as shown in right. In the first case the displacement field *u(z)* varies as a function of the height z and the deformation of the cantilever, as well as the internal actions, depend only on the value of the applied force *P* and are naturally assumed to be constant. If, on the other hand, there is a force *P(t)* varying over time, then the displacements *u(z,t)* also vary as a function of time t, and consequently there will be dynamic effects generated by the velocity fields *u(z,t)* and acceleration *ü(z,t)*.

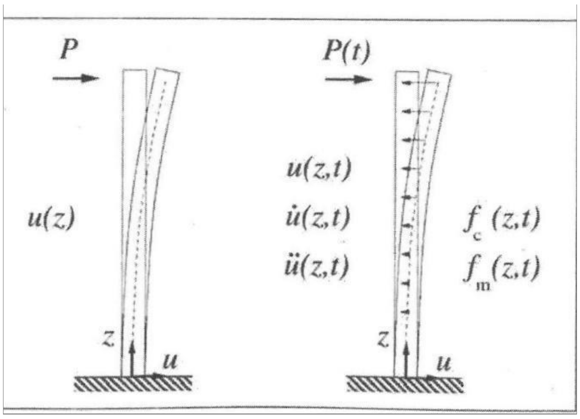

Fig. 1. 22 Statically and dynamically loaded tower scheme

These velocity and acceleration fields result in additional force fields. In the case in question, for example, the velocity field is usually associated with a distribution of viscous forces f_C(z,t) opposite to the movement of the structure, while the acceleration field is associated with a corresponding distribution of inertia forces f_m(z,t) opposite to the variation of the motion itself. Furthermore, in terms of energy balance, in addition to the work W of the external force P(t) applied at the top, and in addition to the energy V linked to the elastic deformation of the cantilever, it will be necessary to take into account both the work dissipated for the viscous effects W_c and kinematic energy T. The total work W_T is therefore: $W_T=W_P+V+Wc+T$.

To formulate a model that allows to obtain a good approximation of the dynamic behaviour of a structure it is necessary, first of all, to represent realistically both its elastic and inertial characteristics. To do this, two types of modelling are generally adopted: lumped parameter model, and a distributed parameter model. In both cases, the models adopted are always a compromise between the accuracy of the kinematic-static description and the adoption of the lowest possible number of degrees of freedom. The dissipative effects linked to viscous or internal friction actions are instead usually modelled in a second phase, by means of generalised parameters subsequently defined as a function of the inertial and elastic parameters.

1.2.1 Lumped parameter model

A building like the one in figure 1.23 (left) can be represented by a load-bearing structure consisting of two superimposed frames in reinforced concrete, therefore a very simple scheme, but effective from the point of view of the description of the global dynamic behavior, can be that the double shear-type shown on the right. In this scheme the mass of the building is concentrated in the two rigid beams with masses m_1, m_2, while all the flexural deformability is attributed to the columns considered axially rigid. In this way the scheme is reduced to a model with two degrees of freedom, which can be given for example by the displacements $u_1(t)$, u_2 (t) of the beams with respect to the ground.

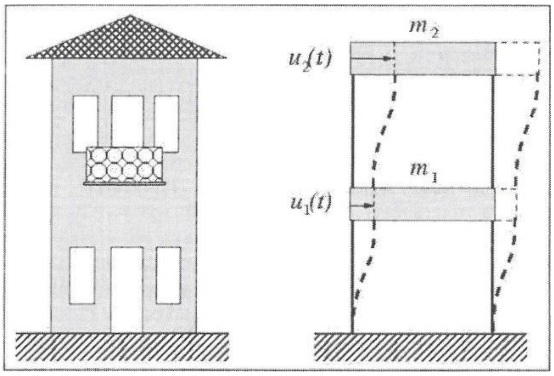

Fig. 1. 23 Schematic shear-type model with 2-mass concentrated in rigid beams, and flexibly deformable and axially rigid column

1.2.2 Distributed parameter model

A different but equally significant situation is represented in figure 1.24 and concerns the case of a slender structure, such as a reinforced concrete chimney, or a tower, subjected to a seismic stress. The effect of the ground movement is schematized as a relative movement between the reference system of axes (u, z) fixed with the soil and the absolute reference system of axes (r, s). In the case of a ground motion with a purely horizontal component, the history of the ground motion is given by s(t), while the corresponding accelerogram is defined by $\ddot{s}(t)$. It should be noted that the forces of inertia $f_\mu(z, t)$ that stress the structure are distributed along the height and result from the combination between the acceleration $\ddot{u}(z,t)$ variable with the height z of each point of the structure with respect to the ground, and of the soil acceleration $\ddot{s}(t)$ (constant along the height z) with respect to the absolute reference system. In this specific case, modelling with a single concentrated mass is not appropriate as neither the equivalent mass parameter m* nor the corresponding height h* are immediately definable. On the other hand, it is more appropriate to proceed in a different way, starting from the consideration that the seismic load is overall quite similar to a uniformly distributed load, especially in the most intense phase of the stress, that is when the term $\ddot{s}(t)$ is higher and more prevalent with respect to relative accelerations. The resulting displacement field will have a trend that is sufficiently well approximated by the shape function $\varphi(z)$ corresponding to the elastic line indicated in figure 1.24. It is therefore convenient to separate the variables and assume that the kinematics of the system is described by a displacement field given by the simple function: $u(t) = \eta(t)\varphi(z)$. The variable $\eta(t)$ then constitutes the generalised displacement of the system, which is therefore modelled as a single degree of freedom system having distributed mass and stiffness.

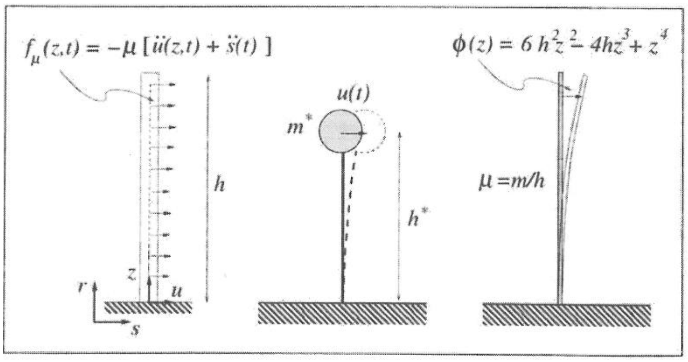

Fig. 1. 24 Schematic of concentrated mass model and SDOF idealisation of uniform flexural cantilever column

Once the mechanical model that schematizes the structure to be studied has been defined, it is necessary to formulate the system of equations of motion. These equations can be obtained directly by explaining the equilibrium conditions by means of the Principle of d'Alembert which states that a system of forces applied to a mechanical system is always in equilibrium, provided that the forces of inertia are also introduced into the account. Indeed, this principle is the extension of the concept of equilibrium valid in statics to the dynamic field. In other words, in the dynamic field, a mechanical system will move with accelerations that produce inertial effects such as to compensate exactly for the imbalance that would occur in the purely static field.

1.2.3 SDoF model

Figure 1.25 illustrates a single degree of freedom shear-type model, consisting of mass m constrained to the soil by means of two flexible columns.

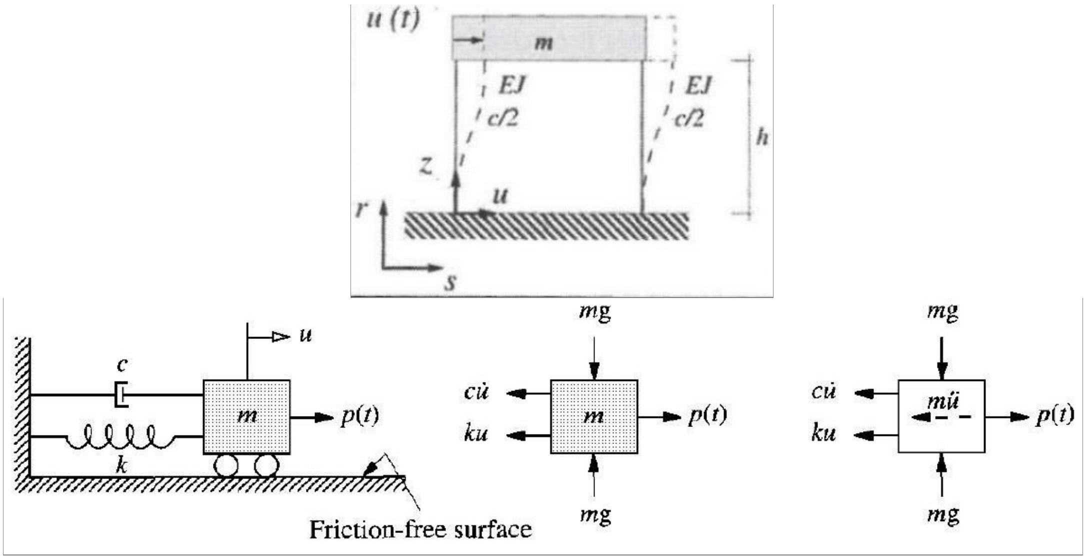

*Fig. 1. 25 (top) Basic SDOF dynamic system (**Clough and Penzien, 2003**); (bottom) Mass – spring – damper system (**Chopra, 1995**)*

The horizontal forces in this problem are the horizontal elastic pull-back force f_k, which corresponds to the internal shear action of the two columns due to the displacement at the top *u(t)*; the viscous force f_C proportional to the velocity $\dot{u}(t)$; the traverse inertia force f_m proportional to the absolute acceleration $\ddot{u}(t) + \ddot{s}(t)$, in agreement with Newton's law. The equilibrium equation for the forces in the horizontal direction of the beam therefore results:

$$f_m(t) + f_c(t) + f_k(t) = 0 \qquad 1.91$$

whose terms are given by:

$f_m(t) = -m\,[\ddot{u}(t) + \ddot{s}(t)]$

$f_c(t) = -c\,\dot{u}(t)$

$f_k(t) = -k\,u(t) = 2\,\frac{12EJ}{h^3}u(t)$

having indicated m as the total mass of the beam, c as the viscous damping coefficient and k as the elastic constant proportional to the total transverse stiffness of the two columns. Finally, the equation of motion of this single-degree-of-freedom model, SDoF, is given by:

$$m\ddot{u}(t) + c\dot{u}(t) + ku(t) = -m\ddot{s}(t) \qquad 1.92$$

This equation of motion has been obtained by directly imposing equilibrium; however, it must be considered that this procedure is in fact easy only in the case of elementary systems that can be described by means of models with a very limited number of degrees of freedom.

Considering the equation of motion (1.92) for the single-degree-of-freedom model subject to seismic stress at the base yields:

$$m\ddot{u} + c\dot{u} + ku = -m\ddot{s}(t) \equiv p(t) \qquad 1.93$$

1.2.3.1 Free vibrations

The differential equation (1.94) can be solved from the associated homogeneous equation, which governs the system in the case of free, unforced oscillations:

$$m\ddot{u} + c\dot{u} + ku = 0 \qquad 1.94$$

The particular solution can be in the form:

$$u(t) = \mathrm{C}e^{\alpha t} \qquad 1.95$$

with α and C constants belonging to the field of complex numbers.

Substituting (1.95) and its derivations:

$\dot{u}(t) = \alpha \mathrm{C}e^{\alpha t}$
$\ddot{u}(t) = \alpha^2 \mathrm{C}e^{\alpha t}$

into (1.94) yields:

$$(m\alpha^2 + c\alpha + k)Ce^{\alpha t} = 0 \qquad 1.96$$

Dividing the latter equation by $mCe^{\alpha t}$ finally results:

$$\alpha^2 + 2\xi\omega\alpha + \omega^2 = 0 \qquad 1.97$$

where

- $\omega = \sqrt{k/m}$ is called the natural pulsation of the oscillator
- $\xi = \frac{c}{2\omega m} = \frac{c}{2\sqrt{km}}$ is called the damping factor

The roots of (1.97) belong to the field of complex numbers.
In particular, $\alpha_{1,2} = \omega(-\xi \pm \sqrt{\xi^2 - 1})$. Depending on the value di $\sqrt{\xi^2 - 1}$, and thus of ξ, four systems can be derived:

$\xi = 0$ UNDAMPED FREE VIBRATIONS MODEL

$\xi = 1$ *CRITICALLY - DAMPED* MODEL

$\xi < 1$ *UNDERCRITICALLY - DAMPED* MODEL

$\xi > 1$ *OVERCRITICALLY-DAMPED* MODEL

1.2.3.2 Undamped free vibrations model ($\xi = 0$)

In the simplest case of an undamped oscillator, i.e. for $c = 0$, (1.97) becomes:

$$\alpha^2 + \omega^2 = 0 \qquad 1.98$$

from which $\alpha_{1,2} = \pm i\omega$ is directly derived. The general solution of the homogeneous equation (1.98) is therefore given by:

$$u(t) = C_1 e^{i\omega t} + C_2 e^{-i\omega t} \qquad 1.99$$

Using Euler relations:

$$\begin{gathered} e^{i\theta} = \cos\theta + i\sin\theta \\ e^{-i\theta} = \cos\theta - i\sin\theta \end{gathered} \qquad 1.100$$

thus, showing the real and imaginary parts of the constants $C_i = \mathbb{R}C_i + \Im C_i$, la (1.107) can be written in the form:

$$u(t) = (\mathbb{R}C_1 + \Im C_1)(\cos\omega t + i\sin\omega t) + (\mathbb{R}C_2 + \Im C_2)(\cos\omega t - i\sin\omega t) \qquad 1.101$$

which simplifying becomes:

$$\begin{aligned} u(t) = {} & (\mathbb{R}C_1 + \mathbb{R}C_2)\cos\omega t - (\Im C_1 - \Im C_2)(\sin\omega t) + \\ & + i[(\Im C_1 + \Im C_2)\cos\omega t + (\mathbb{R}C_1 + \mathbb{R}C_2)\sin\omega t] \end{aligned} \qquad 1.102$$

A solution in the real field can be obtained if the second term is null, therefore:

$$\mathbb{R}C_1 = \mathbb{R}C_2 \qquad 1.\ 103$$

$$\Im C_1 = -\Im C_2 \qquad 1.\ 104$$

i.e. the two constants C1 and C2 must be conjugated. At this point, the general solution can be rewritten in one of the two following equivalent forms:

$$u(t) = A \cos \omega t + B \sin \omega t \qquad 1.\ 105$$

$$u(t) = \rho \sin(\omega t - \theta) \qquad 1.\ 106$$

where $\rho = \sqrt{A^2 + B^2}$, $\theta = \arctan(B/A)$. The value of the integration constants A and B can be derived from the initial conditions on displacement $u(0) = u^0 = A$ and velocity $\dot{u}(0) = -\omega A \sin \omega t + \omega B \cos \omega t = \dot{u}^0 = \omega B$, obtaining:

$$A = u^0 \qquad B = \frac{\dot{u}^0}{\omega} \qquad 1.\ 107$$

The solution then becomes:

$$u(t) = u^0 \cos \omega t + \frac{\dot{u}^0}{\omega} \sin \omega t \qquad 1.\ 108$$

The oscillator then moves in simple harmonic motion (Figure 1.25).

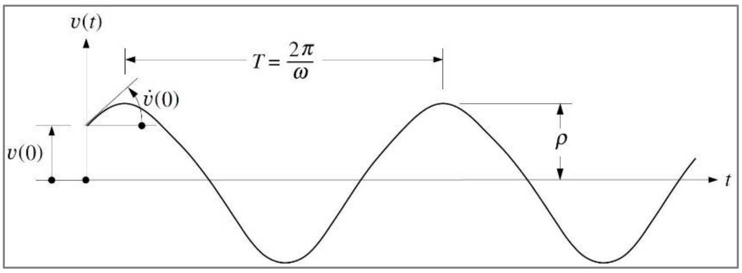

*Fig. 1. 26 Free vibration of a system without damping (**Clough and Penzien, 2003**)*

In addition to the pulsation ω, which is also called the *circular frequency*, certain quantities associated with the characteristics of motion can be defined:

- Frequency *f* defined as the number of cycles completed in the unit of time and measured in Hz;
- The period *T*, the inverse of frequency, defined as the time taken to complete an entire cycle and measured in seconds.

The relationships between the different quantities are as follows:

$$T = \frac{1}{f} = \frac{2\pi}{\omega} \qquad 1.\ 109$$

1.2.3.3 *Critically - damped model (ξ = 1)*

The model with $c = 2\omega m = 2\sqrt{km} = c_{cr}$, ovvero $\xi = 1$, results in a single solution:

$$\alpha_1 = \alpha_2 = -\omega \quad , \omega \in \mathbb{R} \qquad 1.110$$

The value c_{cr} is called the critical damping of the system and in this case the general solution of (1.94) is given by the following combination:

$$u(t) = (C_1 + C_2 t)e^{-\omega t} \qquad 1.111$$

Since $e^{-\omega t}$ is a real term, the two constants C_1 and C_2 are also, and can be derived directly from knowledge of the system's initial conditions $u(0) = u^0 = C_1$, $\dot{u}(0) = \dot{u}^0 = -\omega C_1 e^{-\omega t} + C_2 e^{-\omega t} = -\omega C_1 + C_2 = -\omega u^0 + C_2$ obtaining:

$$u(t) = [u^0(1 - \omega t) + \dot{u}^0 t]e^{-\omega t} \qquad 1.112$$

As can be seen from Figure 1.26, which represents the motion for positive values of u^0 e $\dot{u}^0$, in the case of critical damping with initial values of concordant sign there are no oscillations around the initial position and furthermore the system tends asymptotically to assume a null displacement: $\lim_{t \to \infty} u(t) = 0$. The critical damping value c_{cr} is the smallest for which the motion assumes this character.

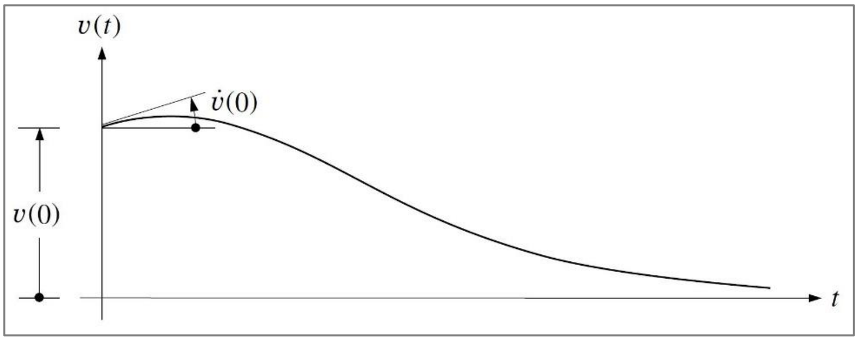

*Fig. 1. 27 Free-vibration response of critically damped system (**Clough and Penzien, 2003**)*

1.2.3.4 *Undercritically - damped model (ξ < 1)*

In the somewhat more realistic model corresponding to a non-zero damping value but below the critical value, i.e. the so-called subcritical model, the motion will have an intermediate character between those just described. It should be borne in mind that in earthquake engineering problems one typically assumes $\xi \in [0.02 - 0.05]$. Eq. (1.97) admits as a solution:

$$\alpha_{1,2} = \omega[-\xi \pm \sqrt{\xi^2 - 1}] \qquad 1.113$$

For $c < c_{cr}$, i.e. $\xi < 1$ the sub-root term in (1.113) assumes a negative value and it is therefore convenient to write the solution to eq. (1.97) in the form:

$$\alpha_{1,2} = -\xi\,\omega \pm \sqrt{\omega^2\xi^2 - \omega^2} = -\xi\,\omega \pm i\omega\sqrt{1-\xi^2} = -\xi\,\omega \pm i\omega_D \tag{1. 114}$$

where $\omega_D \in \mathbb{R}$

$$\omega_D = \omega\sqrt{1-\xi^2} \tag{1. 115}$$

Substituting the values of $\alpha_{1,2}$ into (1.95) yields the two particular integrals:

$$u_2(t) = e^{-\xi\,\omega t + \,i\omega_D} \tag{1. 116}$$

$$u_2(t) = e^{-\xi\,\omega t - \,i\omega_D} \tag{1. 117}$$

that through Euler's formulas

$$\begin{cases} e^{i\theta} = \cos\theta + i\sin\theta \\ e^{-i\theta} = \cos\theta - i\sin\theta \end{cases} \tag{1. 118}$$

Can be rewritten in the form:

$$\begin{cases} u_1(t) = e^{-\xi\,\omega t}\,(\cos\omega_D t + i\sin\omega_D t) \\ u_2(t) = e^{-\xi\,\omega t}\,(\cos\omega_D t - i\sin\omega_D t) \end{cases} \tag{1. 119}$$

and combined linearly:

$$\begin{cases} \dfrac{u_1(t) + u_2(t)}{2} = e^{-\xi\,\omega t}\,(\cos\omega_D t) \\ \dfrac{u_1(t) - u_2(t)}{2i} = e^{-\xi\,\omega t}\,(\sin\omega_D t) \end{cases} \tag{1. 120}$$

The general solution of the equation of motion is obtained as a linear combination of the above and, in analogy to the case of the oscillator with zero damping, can be written in trigonometric form:

$$u(t) = e^{-\xi\omega t}\,(C_1 \cos\omega_D t + C_2 \sin\omega_D t) \tag{1. 121}$$

Initial conditions noted $u_0 = 0$ and $\dot{u}_0 = 0$, developing in the

$$\begin{cases} u(t=0) = u_0 = C_1 \\ \dot{u}(t=0) = \dot{u}_0 = -\xi\omega e^{-\xi\omega t}\,C_1\cos\omega_D t - \omega_D e^{-\xi\omega t} C_1 \sin\omega_D t - \\ -\xi\omega e^{-\xi\omega t} C_2 \sin\omega_D t + \omega_D e^{-\xi\omega t} C_2\cos\omega_D t = \\ = \xi\omega e^{-\xi\omega t}(C_1\cos\omega_D t + C_2\sin\omega_D t) + \\ + e^{-\xi\omega t}(-\omega_D C_1\sin\omega_D t + \omega_D C_2 \cos\omega_D t) = \\ = -\xi\omega C_1 + \omega_D C_2 = \\ = -\xi\omega u_0 + \omega_D C_2 \end{cases} \tag{1.122}$$

introducing the constants $C_1 = u_0$ and $C_2 = \frac{\xi\omega u_0 + \dot{u}_0}{\omega_D}$ into (1.121) the solution becomes:

$$u(t) = [u^0 \cos(\omega_D t) + \frac{\dot{u}^0 + u^0 \xi\omega}{\omega_D} \sin(\omega_D t)] e^{-\xi\omega t} \qquad 1.123$$

Alternatively, this response can be written in the form:

$$u(t) = \rho \cos(\omega_D t + \theta) e^{-\xi\omega t} \qquad 1.124$$

in which

$$\begin{cases} \rho = \sqrt{u(0)^2 + (\frac{\dot{u}^0 + u^0 \xi\omega}{\omega_D})^2} \\ \theta = -\tan^{-1}(\frac{\dot{u}(0) + u(0)\xi\omega}{\omega_D u(0)}) \end{cases} \qquad 1.125$$

The character of the motion is therefore oscillatory, with period $T_D = 2\pi/\omega_D$, longer than the corresponding period of the undamped oscillator, while the amplitude of the oscillations decreases exponentially as a function of the damping coefficient ξ, as shown in Figure 1.27.

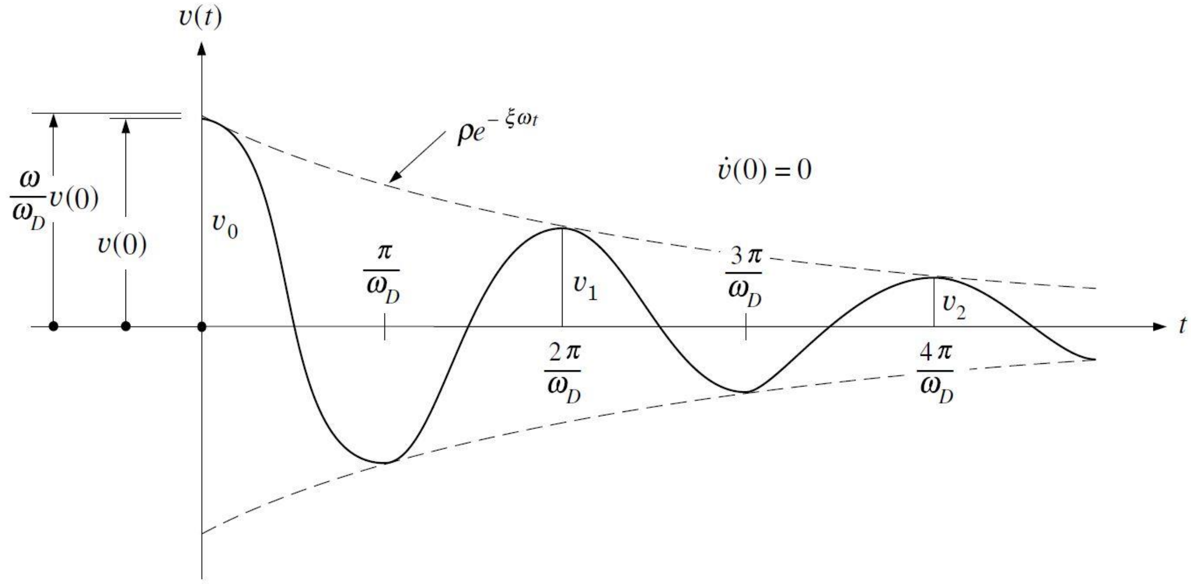

*Fig. 1. 28 Free-vibration response of undercritically-damped system (**Clough and Penzien, 2003**)*

1.2.3.5 Overcritically - damped systems ($\xi > 1$)

Although it is very unusual under normal conditions to have overcritically- damped structural systems, they do sometimes occur as mechanical systems; therefore, it is useful to carry out the response analysis of an overcritically - damped system to make this presentation complete. In this case having $\xi \equiv c/c_{cr} > 1$, indicating with $\gamma = \omega\sqrt{\xi^2 - 1}$, it is convenient to write the roots of the eq. (1.96) in the form:

$$\alpha_{1,2} = -\xi\omega \pm \omega\sqrt{\xi^2 - 1} = -\xi\omega \pm \gamma \qquad 1.126$$

Substituting the two values of α given by (1.126) into (1.95) leads to two particular integrals:

$$\begin{cases} u_1(t) = e^{-\xi\omega t}\, e^{-\gamma t} \\ u_2(t) = e^{-\xi\omega t}\, e^{\gamma t} \end{cases} \qquad 1.127$$

Considering the following linear combinations of the two particular integrals, so as to show hyperbolic functions, we obtain:

$$\begin{cases} \frac{u_1(t)+u_2(t)}{2} = e^{-\xi\omega t}\, \frac{e^{\gamma t}+e^{-\gamma t}}{2} = e^{-\xi\omega t} \cosh \gamma t \\ \frac{u_1(t)-u_2(t)}{2} = e^{-\xi\omega t}\, \frac{e^{\gamma t}-e^{-\gamma t}}{2} = e^{-\xi\omega t} \sinh \gamma t \end{cases} \qquad 1.128$$

The general integral is obtained as a linear combination of the above:

$$u(t) = e^{-\xi\omega t}(C_1 \cosh \gamma t + C_2 \sinh \gamma t) \qquad 1.129$$

in which the real constants C_1 and C_2 can be evaluated using the initial conditions $u(0)$ and $\dot{u}(0)$. It is easily shown from the form of (1.129) that the response of an overcritically - damped system is similar to the motion of a critically - damped system (Figure 1.29); however, the asymptotic return to the zero-displacement position is slower depending upon the amount of damping.

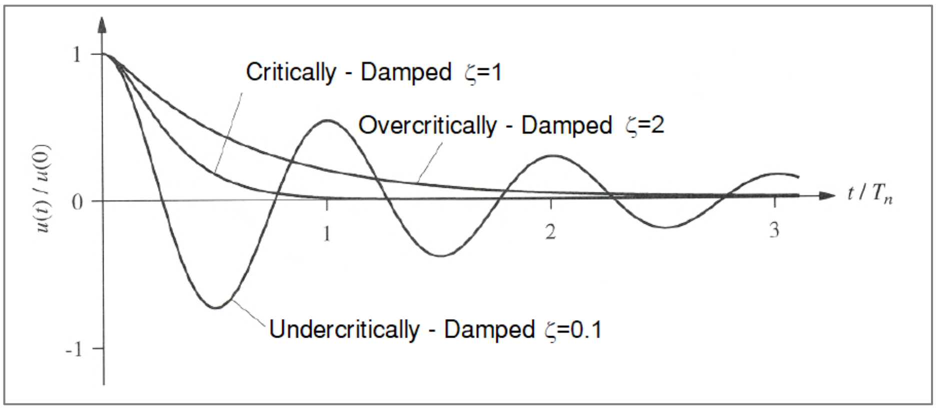

*Fig. 1.29 Free-vibration response of overcritically-damped system (**Chopra, 1995**)*

1.2.3.6 Forced vibrations (model with unit impulse forcing)

The equation of motion of a single-degree-of-freedom system in the absence of damping and subject to a time-varying initial perturbation is:

$$m\ddot{u}(t) + ku(t) = F(t) \qquad 1.130$$

The equation of motion of the forced oscillator is a second-order differential equation with constant coefficients, linear but not homogeneous. The particular solution can be considered as the superposition of the solution of the associated homogeneous equation and a particular integral, which depends on the specific form of the forcer and is therefore assumed to be in the form:

$$u(t) = u_{om}(t) + u_p(t) \qquad 1.131$$

In the case of the application of unit impulsive force F_1, the solution of (1.130) is given by the sum of the solution of the associated homogeneous (1.105) and the solution of the particular integral $u_p(t)$:

$$u(t) = C_1 \cos \omega t + C_2 \sin \omega t + \frac{F_1}{k} \qquad 1.132$$

From the initial conditions (t = 0) the integration constants C_1 e C_2 result:

$$\begin{cases} u(0) = u_0 \Rightarrow C_1 = -\frac{F_1}{k} \\ \dot{u}(0) = \dot{u}_0 = -\omega C_1 \sin \omega t + \omega C_2 \cos \omega t = 0 \Rightarrow C_2 = 0 \end{cases} \qquad 1.133$$

Therefore, introducing (1.133) into (1.132) the final form of the equation of motion in the case of impulsive forcing is given by:

$$u(t) = -\frac{F_1}{k} \cos \omega t + \frac{F_1}{k} = \frac{F_1}{k}(1 - \cos \omega t) \qquad 1.134$$

The ratio between $u(t)$ and the particular integral $u_p(t) = \frac{F_1}{k}$ is called dynamic load factor $DLF = \frac{u(t)}{u_p(t)} = 1 - \cos \omega t$. This function, the trend of which is shown in figure 1.30, gives an idea of how much the effects are amplified/worsened in the dynamic case compared to the static case; $DLF_{max} = 2$ when the trigonometric function is $\cos\omega t = -1$; therefore, if a constant force is applied impulsively to a linear elastic system, the displacement, and therefore the deformations, and oscillations, periodically are twice as great as those that the same force would produce if applied statically.

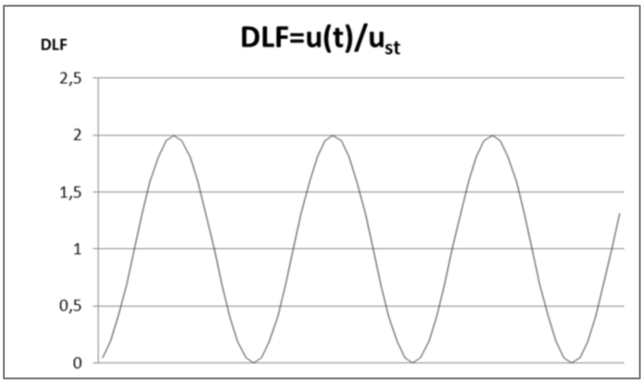

Fig. 1.30 Dynamic Load Factor

1.2.3.7 *Response to harmonic loading of undamped system*

Assume that the system of figure 1.25 is subjected to a harmonically varying load *p(t)* of sine-wave form having an amplitude p_0 and circular frequency Ω as shown by the equation of motion:

$$m\ddot{u}(t) + c\dot{u}(t) + ku(t) = p_0 \sin \Omega t \qquad 1.135$$

Before considering this viscously damped case, it is good to examine the behavior of an undamped system as controlled by

$$m\ddot{u}(t) + ku(t) = p_0 \sin \Omega t \qquad 1.136$$

The general solution must also include the particular solution which depends upon the form of dynamic loading. In this case of harmonic loading, it is reasonable to assume that the corresponding motion is harmonic and in phase with the loading; thus, the particular solution is:

$$u_p(t) = C\sin\Omega t \qquad 1.\,137$$

in which the amplitude C is to be evaluated. Substituting the derivative of (1.137)

$$\dot{u}_p(t) = \Omega C\cos\Omega t$$
$$\ddot{u}_p(t) = -\Omega^2 C\sin\Omega t$$

in (1.136) gives:

$$-\Omega^2 C\sin\Omega t + \omega^2 C\sin\Omega t = \frac{p_0}{m}\sin\Omega t \qquad 1.\,138$$

Dividing through by $\sin\Omega t$ (which is nonzero in general) and by k and noting that $k/m = \omega^2$, one obtains:

$$C(\omega^2 - \Omega^2) = \frac{p_0}{m} \qquad 1.\,139$$

from which:

$$C = \frac{p_0}{m}\frac{1}{(\omega^2-\Omega^2)} = \frac{p_0}{m\omega^2}\frac{1}{(1-\frac{\Omega^2}{\omega^2})} = \frac{p_0}{k}\frac{1}{(1-\frac{\Omega^2}{\omega^2})} \qquad 1.\,140$$

The general solution of (1.135) is now obtained by combining the complementary and particular solutions and making use of (1.140); thus, one obtains

$$u(t) = A\cos\omega t + B\sin\omega t + \frac{p_0}{k}\frac{1}{(1-\frac{\Omega^2}{\omega^2})}\sin\Omega t \qquad 1.\,141$$

For the system starting from rest, i.e., $u(0) = \dot{u}(0) = 0$, it is easily shown that A e B:

$$\begin{cases} u(0) = u_0 = 0 \Rightarrow A = 0 \\ \dot{u}(0) = \dot{u}_0 = -\omega A\sin\omega t + \omega B\cos\omega t + \\ + \Omega\frac{p_0}{k}\frac{1}{(1-\frac{\Omega^2}{\omega^2})}\cos\Omega t = 0 \Rightarrow B = -\frac{\Omega}{\omega}\frac{p_0}{k}\frac{1}{(1-\frac{\Omega^2}{\omega^2})} \end{cases} \qquad 1.\,142$$

in which case the response of (1.141) becomes

$$u(t) = \frac{p_0}{k}\left[\frac{1}{(1-\frac{\Omega^2}{\omega^2})}\right]\left(\sin\Omega t - \frac{\Omega}{\omega}\sin\omega t\right) \qquad 1.\,143$$

Equation (1.143) has been plotted for $\Omega/\omega = 0.2$, $u(0) = 0$, and $\dot{u} = \omega\, p_0/k$ as the solid line in figure 1.31. The $\sin\Omega t$ term in this equation is the particular solution of (1.137) and is shown by the dashed line. Equation (1.143) and fig. 1.31 show that $u(t)$ contains two distinct vibration components: (1) the $\sin\Omega t$ term, giving an oscillation at the forcing or exciting frequency; and (2) the $\sin\omega t$ $\cos\omega t$ terms, giving an oscillation at the natural frequency of the system. The first of these is the *forced vibration* or *steady-state vibration*, for it is present because of the applied force no matter what the initial conditions. The latter is the *transient vibration*, which depends on the initial displacement and velocity. The difference between the solid and dashed lines is the transient component, where it is seen to continue forever. This is only an academic point because the damping inevitably present in real systems makes the free vibration decay with time. It is for this reason that this component is called *transient vibration*.

The factor in brackets in (1.143) has been plotted in figure 1.32 against Ω/ω, the ratio of forcing frequency to the natural frequency. The *deformation* (or *displacement*) *response factor* R_d gives the ratio of the amplitude u_0 of the vibratory deformation to the static deformation $(u_{st})_0 = p_0/k$ due to the force p_0.

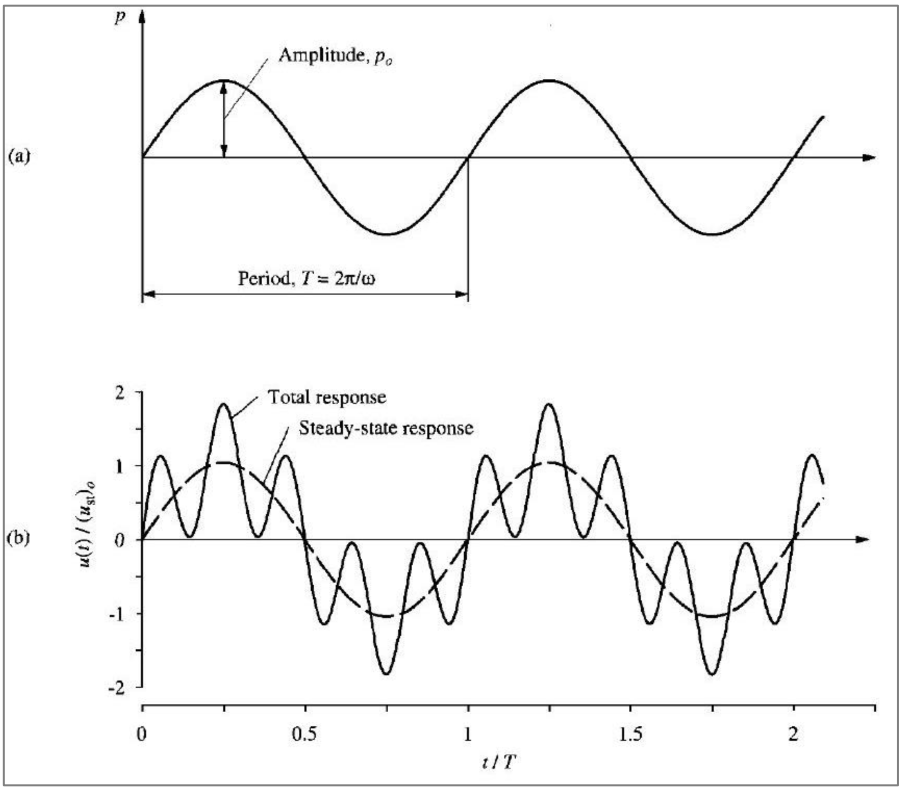

*Fig. 1.31 (a) Harmonic force; (b) response of undamped system to harmonic force; Ω/ω = 0.2, u(0) = 0, and $\dot{u}(0) = \omega p_0/k$ (**Chopra, 1995**)*

Figure 1.32, which shows the R_d plotted as a function of the frequency ratio Ω/ω, permits several observations. If Ω/ω is small (i.e., the force is "slowly varying"), R_d is only slightly larger than 1 and the amplitude of the vibratory deformation is essentially the same as the static deformation. If $\Omega/\omega > \sqrt{2}$ (i.e., Ω is higher than $\omega\sqrt{2}$), $R_d < 1$ and the deformation amplitude is less than the static deformation. As Ω/ω increases beyond $\sqrt{2}$, R_d become smaller and approaches zero as $\Omega/\omega \longrightarrow \infty$, implying that the vibratory deformation due to a "rapidly varying" force is very small. If Ω/ω is close to 1 (i.e., ω is close to Ω), R_d is many times larger than 1, implying that the deformation amplitude is much larger than the static deformation. The resonant frequency is defined as the forcing frequency at which R_d is maximum.

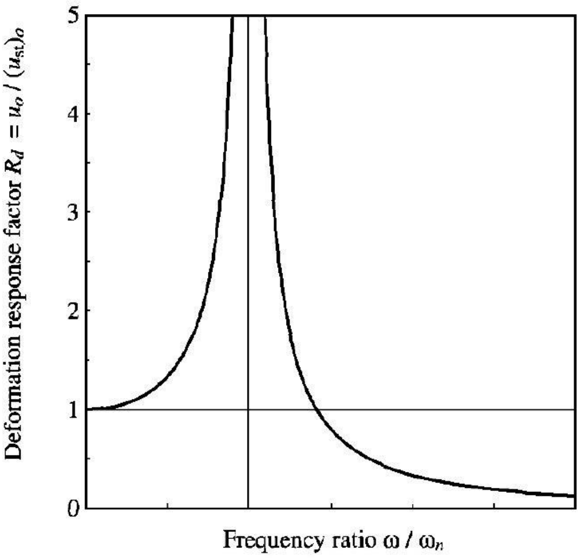

*Fig. 1.32 Deformation response factor for an undamped system excited by harmonic force (**Chopra, 1995**)*

This result is plotted in figure 1.33, which shows that the time taken to complete one cycle of vibrations is T_n (or natural period).

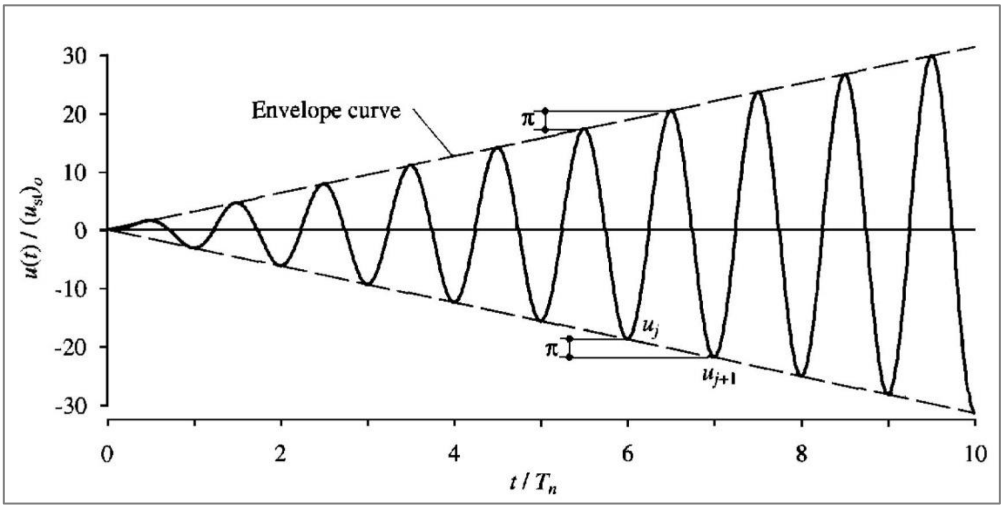

*Fig. 1.33 Response of undamped system to sinusoidal force of frequency $\Omega = \omega$; $u(0) = \dot{u}(0) = 0$ (**Chopra, 1995**)*

The deformation amplitude grows indefinitely, but it becomes infinite only after an in finitely long time. This is an academic result and should be interpreted appropriately for structures. As the deformation continues to increase, at some point in time the system would fail if it were brittle. On the other hand, the system would yield if it is ductile, its stiffness would decrease, and its "natural frequency" would no longer be equal to the forcing frequency, and figure 1.33 would no longer be valid.

1.2.3.8 Harmonic vibration with viscous damping

Including viscous damping the differential equation governing the response of SDoF systems to harmonic force is (1.135) whose complete solution is:

$$u(t) = [u_c(t)] + [u_p(t)] = [e^{-\xi\omega t}(A\cos\omega_D t + B\sin\omega_D t)] + [C\sin\omega t + D\cos\omega t] \qquad 1.\ 144$$

where $u_c(t)$ and $u_p(t)$ represent the complementary (the transient response) and the particular (the steady-state response) solutions respectively of the differential equation (1.135).

The constants *A*, *B*, *C*, and *D* can be determined by standard procedures:

$$A = u(0) \qquad 1.\ 145$$

$$B = \frac{\dot{u}(0)}{\omega} - \frac{p_0}{k}\frac{\Omega/\omega}{1-(\Omega/\omega)^2} \qquad 1.\ 146$$

$$C = \frac{p_0}{k}\frac{1-(\Omega/\omega)^2}{[1-(\Omega/\omega)^2]^2+[2\xi(\Omega/\omega)]^2} \qquad 1.\ 147$$

$$D = \frac{p_0}{k}\frac{-2\xi(\Omega/\omega)}{[1-(\Omega/\omega)^2]^2+[2\xi(\Omega/\omega)]^2} \qquad 1.\ 148$$

Equation 1.144 is plotted in figure 1.34 for Ω/ω = 0.2, ξ = 0.05, u(0) = 0, and $\dot{u}(0) = \omega p_0/k$; the total response is shown by the solid line and the steady - state response by the dashed line. The difference between the two is the transient response, which decays exponentially with time at a rate depending on Ω/ω, and ξ. After a while, essentially the forced response remains, and we therefore call it *steady-state response*. Figure 1.34 show that the largest deformation peak may occur before the system has reached steady state.

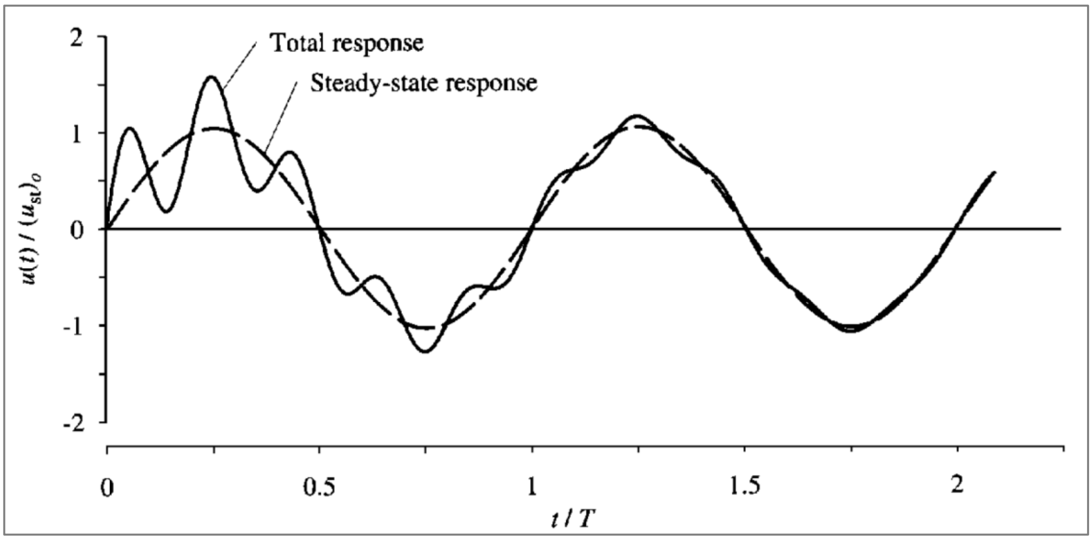

*Fig. 1.34 Response of damped system to harmonic force; Ω/ω= 0.2, ξ = 0.05, u(0) = 0, and $\dot{u}(0) = \omega p_0/k$ (**Chopra, 1995**)*

For $\omega = \Omega$ (1.147) gives *C* = 0 and *D* = $-(u_{st})_0/2\xi$; moreover, for zero initial conditions, the constants *A* and *B* in (1.144) can determined: *A* = $(u_{st})_0/2\xi$ and *B* = $(u_{st})_0/2\sqrt{1-\xi^2}$. With these solutions for *A, B, C,* and *D*, (1.144) becomes:

$$u(t) = \frac{(u_{st})_0}{2\xi}\ [e^{-\xi\omega t}(\cos\omega_D t + \frac{\xi}{\sqrt{1-\xi^2}}\sin\omega_D t) - \cos\omega t] \qquad 1.\ 149$$

This result is plotted in figure 1.35 for a system with ξ = 0.05. The damping lowers each peak and limits the response to the bounded value $u(t) = (u_{st})_0/2\xi$. The deformation varies with time as a cosine function, with its amplitude increasing with time according to the envelope function shown by dashed lines. The amplitude of the steady - state deformation of a system to a harmonic force with Ω = ω and the rate at which steady state is attained is strongly influenced by damping.

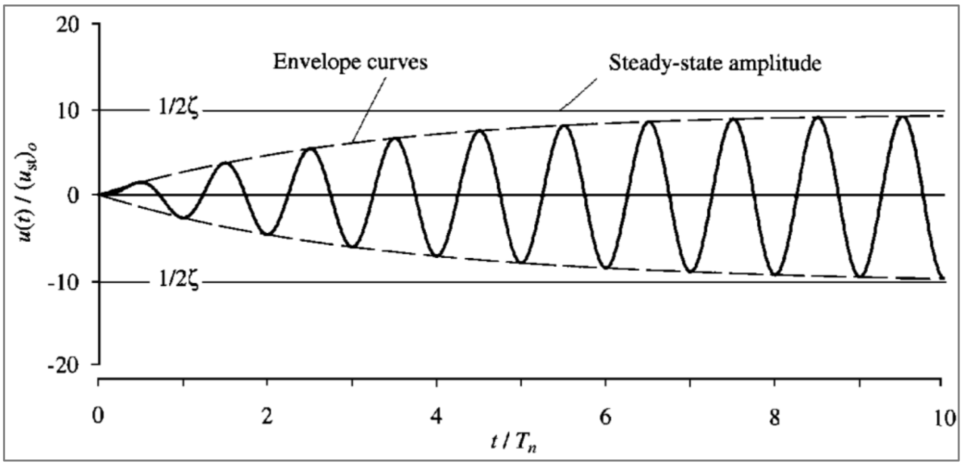

Fig. 1.35 Response of damped system with ξ = 0.05 to sinusoidal force of frequency $\Omega = \omega$; $u_0 = \dot{u}_0 = 0$ ***(Chopra, 1995)***

The important influence of the damping ratio on the amplitude is seen in figure 1.36, where the (1.149) is plotted for three damping ratios ξ = 0.01, 0.05, and 0.1.

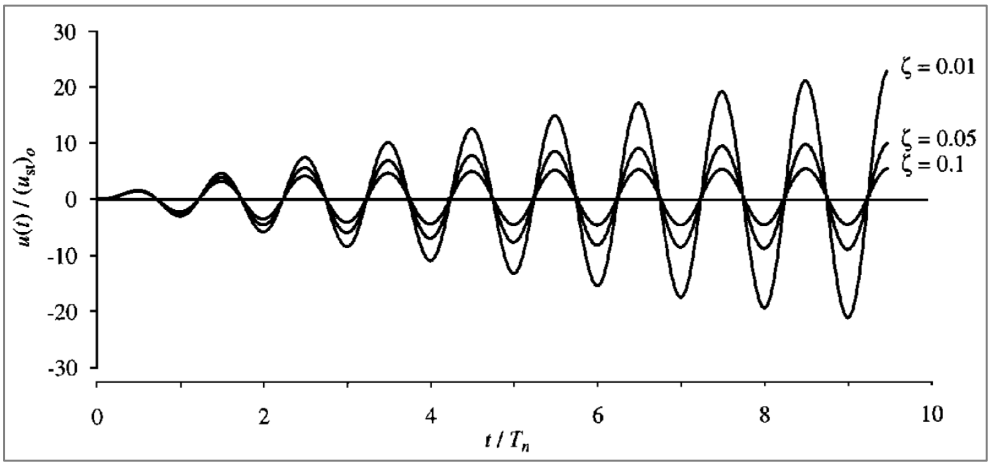

Fig. 1.36 Response of three systems - ξ = 0.01, 0.05, and 0.1 - to sinusoidal force of frequency $\Omega = \omega$; $u_0 = \dot{u}_0 = 0$ ***(Chopra, 1995)***

A plot of the amplitude of a response quantity against the excitation frequency is called a *frequency - response curve*. Such a plot for deformation *u* is given by figure 1.37, wherein $D = R_d$ is plotted as a function of $\beta = \Omega/\omega$ for a few values of ξ; all the curves are below the ξ = 0 curve in figure 1.31. Damping reduces D, and hence the deformation amplitude at all excitation frequencies. The magnitude of this reduction is strongly dependent on the excitation frequency.

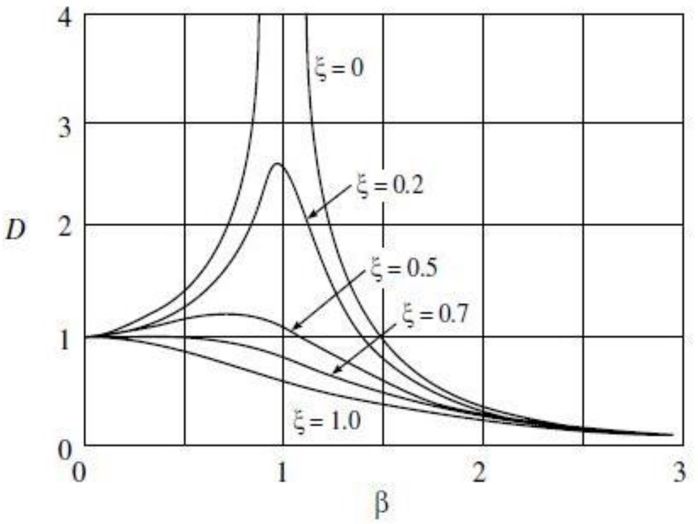

*Fig. 1.37 Variation of dynamic magnification factor with damping and frequency (**Clough and Penzien, 2003**)*

1.2.3.9 Vibrations with non-periodic forcing (Unit Impulse Response)

Consider the case in which an oscillator with subcritical damping is, initially, at rest and is then subjected to an impulsive stress starting at time $t = \tau$, with intensity equal to $f_\tau(t)$ and of very short duration ($\varDelta\tau = T$). It follows from Newton's law that the increase in momentum of the system corresponds to the impulse provided by the acting forces:

$$m[\dot{u}(\tau + \varDelta\tau) - \dot{u}(\tau)] = \int_{\tau}^{\tau+\varDelta\tau} [f_\tau(t) - c\dot{u}(t) - ku(t)]\, dt \qquad 1.150$$

Since the system is at rest until the instant $t = \tau$, if the duration of the impulse tends to be infinite, i.e. for $\varDelta\tau \rightarrow \delta\tau \rightarrow 0$, at the end of it the final conditions of the motion are:

$$u_\tau(\tau + \tau) = 0 \qquad 1.151$$

$$\dot{u}_\tau(\tau + \tau) = \frac{f_\tau^*}{m}\tau \qquad 1.152$$

At the end of the impulse, for subsequent instants $t > (\tau + \tau)$, the motion of the system will be governed by (1.123). Therefore, the system remains at rest until $t = \tau + \varDelta\tau$, and thereafter it will have a motion of a damped oscillatory character beginning at the instant $t = \tau + \varDelta\tau$ with null displacement and velocity given by the condition (1.152):

$$u_\tau(t) = \left\{\frac{f_\tau^* \tau}{m\omega_D} sin[\omega_D(t - \tau)]\right\} e^{-\xi\omega(t-\tau)} \qquad 1.153$$

In the case of a system on which a time-varying force $f(t)$ acts, it is possible to evaluate the response of an elastic-linear system by treating $f(t)$ as a succession of pulses of duration τ. If the forcing is a sufficiently regular function, then the response of the system to the single impulse will be given by eq. (1.153), and taking into account the linearity of the system, the overall response in an interval (0,t) is given by the combination of the responses to all the elementary stress impulses, i.e. the integral::

$$u(t) = \frac{1}{m\omega_D}\int_0^t f(\tau)\, sin[\omega_D(t-\tau)]\, e^{-\xi\omega(t-\tau)}d\tau \qquad 1.154$$

is the Duhamel integral which, for generic forcings, is generally solved numerically. In the case where the system is subjected to a seismic type forcing, represented by an accelerogram $\ddot{s}(t)$, then its response is given by:

$$u(t) = -\frac{1}{\omega_D}\int_0^t \ddot{s}(\tau)\, sin[\omega_D(t-\tau)]\, e^{-\xi\omega(t-\tau)}d\tau \qquad 1.155$$

1.2.3.10 Spectral response values

In many earthquake engineering applications, one is essentially interested in knowing the maximum values of a few more significant quantities. In practice, therefore, one does not require knowledge and analysis of the response for all values of the time variable t, as is obtained, for example, by solving the Duhamel integral. Is therefore indicated with S_v, called pseudo spectral velocity, the scalar representing the maximum of the absolute value of the following integral function, which derives from the Duhamel integral, simplified taking into account that for the limited damping values typical in the field of civil constructions one can assume that $\omega = \omega_D$:

$$S_v = max\left|\int_0^t \ddot{s}(t)\, sin[\omega(t-\tau)]e^{-\xi\omega(t-\tau)}\, dt\right| \qquad 1.156$$

The scalar S_d, called the spectral displacement, then indicates the absolute maximum of the relative displacement, given by the following ratio:

$$S_d = \frac{S_v}{\omega} \qquad 1.157$$

This expression implies that the scalar spectral pseudo-velocity S_v can be taken to be a reasonable approximation of the system's peak velocity, imagining that this peak is reached with a pulsation close to its own. Finally, the scalar $S_a = \omega Sv$ called pseudo-spectral acceleration is also defined in a similar way.
In general, for a given seismic excitation $\ddot{s}(t)$, one determines the values S_d, S_v, S_a for different pairs of values of the eigenperiod and the damping factor (ω, ξ) by referring to the responses of the corresponding linear single-degree-of-freedom systems. The corresponding diagrams, known as displacement, velocity, and acceleration response spectra, are then represented as a function of the oscillators' eigenperiod.

1.3 Models for characterising the soil-structure interaction effect

The dynamic response of a building during an earthquake can be influenced by the interaction with the soil, which can lead to an increase or decrease in the seismic demand due to the combination of structure and foundation soil characteristics (**Mylonakis and Gazetas 2000**; **Kausel 2010**). Indeed, on one hand the free-field motions are referred to as the condition in which ground motions are not influenced by the presence of structures, while when the response of the soil influences the motion of the structure, and the response of the structure influences the motion of the soil we speak of soil-structure interaction.

An extremely high stiffness solid rock subjected to an earthquake constrains its motion to be very close to the free-field motion. Structure founded on this kind of rock is considered to be fixed-base structure.

On the other hand, the same structure would respond differently if supported on a soft soil deposit. The soil-structure interaction can be related to two main causes: first, the motion of the base of the structure deviates from the free field motion due to the inability of the foundation to conform free field motion deformations; second, the dynamic response of the structure itself would induce deformation of the supporting soil.

Neglecting or not the soil-structure interaction effect on the dynamic response of structures and foundation systems depends on the details of the problem at hand and must be evaluated on a case-by-case basis **Wolf (1985)**.

The seismic assessment of building structures, generally, is conducted by adopting a system that is a combination of a rigid foundation element on a rigid base, the so-called fixed-base (FB) capacity models instead of soil-foundation-structure (SFS) in which the compliance (i.e., deformability or total flexibility) of both the foundation elements and the soil is considered.

Considering the case of the simple SDoF system mounted on a rigid, massless, L-shaped foundation (Figure 1.38a) representing a structure characterized by its mass, m, stiffness, k, and damping coefficient, c supported on an elastic soil deposit, if the material supporting the foundation is rigid, the natural frequency of the resulting fixed-base system would depend only on the mass and stiffness of the structure, that is, $\omega = \sqrt{k/m}$, and the hysteretic damping ratio would be $\xi = c\omega/2k$ (**Wolf, 1985**).

If the supporting material is compliant, however, the foundation can translate and rotate. The stiffness and damping characteristics of the compliant soil-foundation system can be represented by the translational and rotational springs and dashpots shown in Figure 1.38b. The foundation dashpots represent two sources of damping: material damping caused by inelastic behavior of the soil supporting the foundation, and radiation damping that occurs as dynamic forces in the structure cause the foundation to deform the soil, producing stress waves that travel away from the foundation. The amount of material damping will depend on the level of strain induced in the soil; if the strains are high, material damping can be substantial, but if they are low, the material damping may be negligible. In contrast, radiation damping is a purely geometric effect that exists at low as well as high strain amplitudes. For typical foundations, radiation damping is often much greater than material damping.

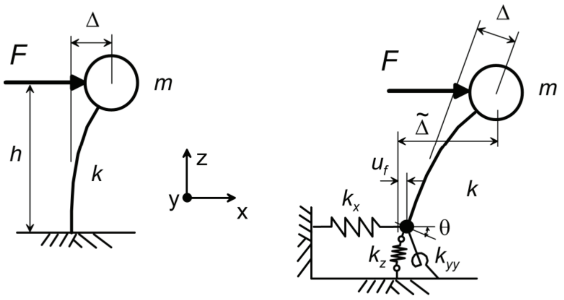

*Fig. 1.38 Schematic illustration of deflections caused by force applied to: (a) fixed-base structure; and (b) structure with vertical, horizontal, and rotational flexibility at its base (**NEHRP, 2012**)*

Soil structure interaction is caused by two phenomena: the inability of the foundation to match the free-field deformation (kinematic interaction) and the effect of the dynamic response of the structure-foundation system on the movement of the supporting soil (inertial interaction).

Kinematic interaction will occur whenever the stiffness of the foundation system impedes development of the free-field motions (Figure 1.39). Kinematic interaction can induce modes of deformation (e.g., rocking and torsion) that are not present in a free-field motion. The seismic motion transmitted from the foundation to the structure is modified from Free Field Motion (FFM) into Foundation Input Motion (FIM) because of the relative soil-foundation stiffness and the foundation embedment (**Elsabee and Murray 1977; Kramer, 1996**; **Kim and Stewart 2003**; **Conti et al., 2017**).

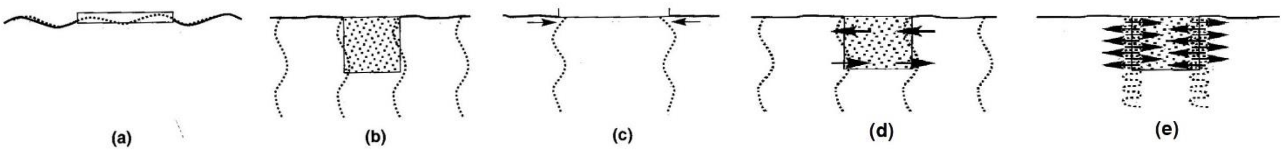

*Fig. 1.39 Kinematic interaction with free-field motions indicated by dashed lines: (a) flexural stiffness of surface foundation prevents it from following vertical component of free-field displacement; (b) rigidity of block foundation prevents it from following horizontal component of free-field displacement; (c) axial stiffness of surface foundation prevents immediately underlying soil from deforming incoherently; (d) Excitation of rocking vibrations in an embedded foundation by vertically propagating s-waves: at certain frequencies, the wavelength is such that unbalanced overturning moments cause rocking, even though the free-field motion is purely translational; (e) at other frequencies (and wavelength), rocking may be suppressed (**Kramer, 1996**)*

The effect of the mass of the structure-foundation system in terms of dynamic response on the movement of the supporting soil is called inertial interaction; if the supporting soil is compliant, the forces transmitted to it by the foundation will produce foundation movement that would not occur in a fixed-base structure. So, if the soil is compliance to the structure motion it produces the modification of the period and damping of the whole system, affecting the structural response in terms of displacements and/or accelerations, as well as inducing additional energy dissipation by means of wave radiation and hysteresis of soil (**Gazetas 1983**; **Wolf 1985**; **Mylonakis et al., 2006**; **Givens et al., 2016**).

Consider the responses of fixed-base (FB) and soil-foundation-structure (SFS) systems subjected to horizontal ground motion (Figure 1.40). The lateral displacement on top of the FB model is associated only to the structural deformation (u_{str}), being FFM ≡ FIM, and oscillation energy is not transmitted through the foundation to the underlying soil. The total horizontal displacement of the SFS model can be expressed as the sum of u_{str}, u_u (displacement for swaying, with the assumption of rigid soil), and u_θ (rocking oscillations of the base, with the assumption of rigid structure).

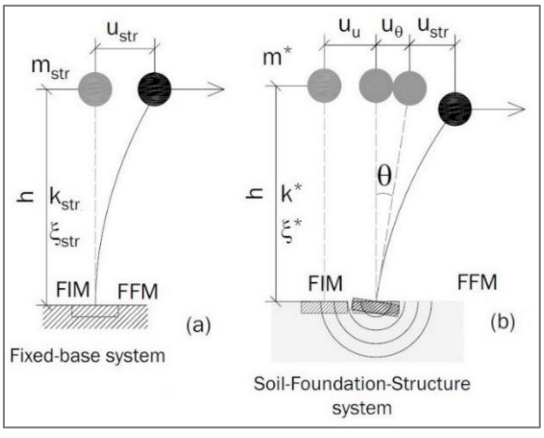

*Fig. 1.40 Comparison between seismic responses of FB (a) and SFS (b) systems (**Piro et al, 2020**)*

Since the low-rise URM buildings are the most recurrent class of structures for the Italian historical built heritage, the focus will be on this construction typology. The foundation stiffness of existing masonry buildings is often comparable to that of the soil, thus kinematic interaction can be neglected. With this in mind, the fundamental frequency decreases from f_0 (FB system value) to f^* (SFS value); the structural damping ratio reduces from ξ_{str} to ξ^*_{str}, while the damping ratio of the soil-foundation system is the sum $\xi^* = \xi_{str} + \xi_{rad} + \xi_{soil}$.

Figure 1.40 depicts the variation in pseudospectral acceleration in the first mode versus period in both linear and log scales. For low-rise URM buildings, the pseudo-spectral acceleration for a flexible-base structure, $\tilde{S}_a$, or the intensity of the seismic action transmitted to the base of the SFS, is usually expected to be increased by SSI.

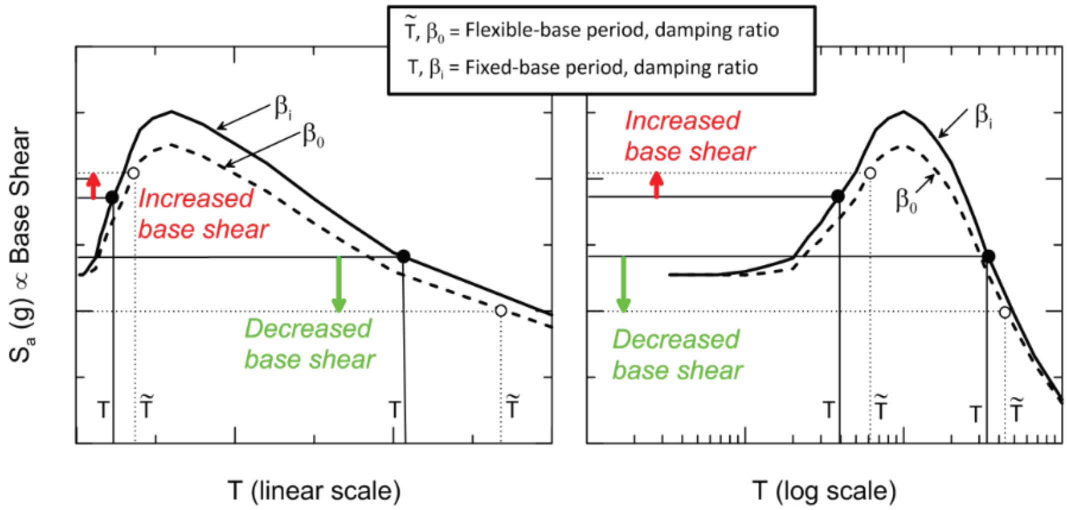

*Fig. 1.41 Illustration of inertial SSI effects on spectral acceleration (base shear) associated with period lengthening and change in damping (**NEHRP, 2012**).*

However, if the foundation is both embedded and stiffer with respect to the soil, the kinematic interaction cannot be neglected, since the FIM differs significantly from the FFM; the foundation can be considered as a filter of the signal transmitted to the structure (**Piro et al., 2020**).

In order to account for SSI effects in seismic performance assessment, more or less refined models of soil and structure have been proposed in the literature. Following **Veletsos and Meek (1974)**, if the subsoil is softer than the structure, the fundamental frequency of the soil-structure system decreases and part of the seismic energy is radiated through the subsoil, so flexural displacement and structural damping are reduced. These authors define a replace the SDoF model with a modified fixed – base replacement oscillator (RO – Figure 1.42), a fixed-base SDOF system with equivalent mass m^*, and lateral stiffness k^*, properly calibrated to achieve the same dynamic behaviour of a compliant-base SDOF system with frequency f^* and damping ratio ξ^* of the soil – structure system given by:

$$\frac{f^*}{f_0} = \frac{1}{\sqrt{1+\frac{k_{str}}{k'_u}\left(1+\frac{k'_u}{k'_e}h^2\right)}} \qquad 1.158$$

$$\xi^* = \left(\frac{f^*}{f_0}\right)\left[\xi_{str} + \frac{(2-\nu)\pi^4\delta}{2\sigma^3}\left(\frac{\beta_u}{\alpha_u^2}\frac{r^2}{h^2} + \frac{\beta_\theta}{\alpha_\theta^2}\right)\right] \qquad 1.\ 159$$

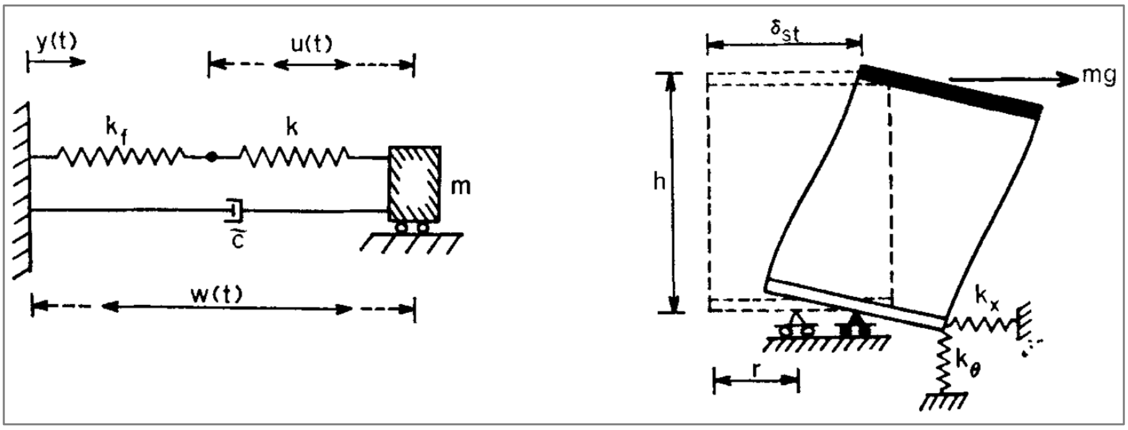

*Fig. 1.42 Replacement oscillator and its static deflection (**Veletsos and Meek, 1974**)*

In Figure 1.43, *f*/f0* and *ξ** are plotted against σ for three h/r values, related, respectively, to short (*h/r* = 1), squat (*h/r* = 2) and slender (*h/r* = 5) structures (*r* = is the radius of the foundation). Given the structure properties (*h*, *f*$_0$) and the *h/r* ratio, as the soil deformability increases *σ* reduces, so the influence of SSI increases, causing a reduction in the fundamental frequency. The same variation in σ produces an increase in radiation damping, which has a significant impact on short structures and negligible effects on slender structures.

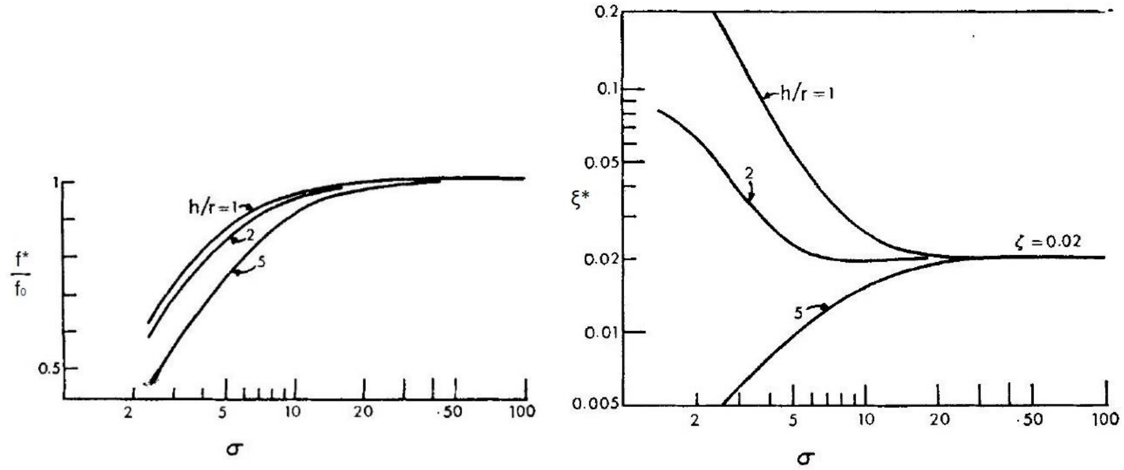

*Fig. 1.43 Natural frequency and damping factor for SDF oscillator (**Veletsos and Meek, 1974**)*

Wolf (1985) also highlighted the important effect of soil-structure interaction in reducing the natural frequency of the equivalent system with respect to that of the fixed – base structure. The natural frequency (ω_e) and the equivalent hysteretic damping ratio (ξ_e) of the equivalent model can be expressed as (**Wolf, 1985**):

$$\omega_e = \frac{\omega_0}{\sqrt{1+\frac{k}{k_h}+\frac{kh^2}{k_r}}} \tag{1.160}$$

$$\xi_e = \frac{\omega_e^2}{\omega_0^2}\xi + \left(1-\frac{\omega_e^2}{\omega_0^2}\right)\xi_g + \frac{\omega_e^2}{\omega_h^2}\xi_x + \frac{\omega_e^2}{\omega_r^2}\xi_\theta \tag{1. 161}$$

The reduction of the natural frequency of the soil-structure system to a value lower than that of the structure under fixed-base conditions as the stiffness ratio ($\bar{s} = \omega_0 h/V_s$) increases is shown in figure 1.44a. For the fixed-base condition ($\bar{s}$ = 0), the natural frequency of the equivalent system is equal to the fixed-base natural frequency. Another, important effect of soil-structure interaction is to increase the effective damping ratio of the equivalent system to a value greater than that of the structure itself (Figure 1.44b). For the fixed-base condition, the damping ratio of the equivalent system is equal to the structural damping ratio, but as the stiffness ratio increases, the effects of radiation and soil damping become more apparent. At high stiffness ratios, structural damping represents only a small part of the total damping of the system. Each curve refers to different value of the mass ratio $\bar{m}$ (= $m/\rho a^3$; a is characteristic length of the foundation; ρ is the mass density).

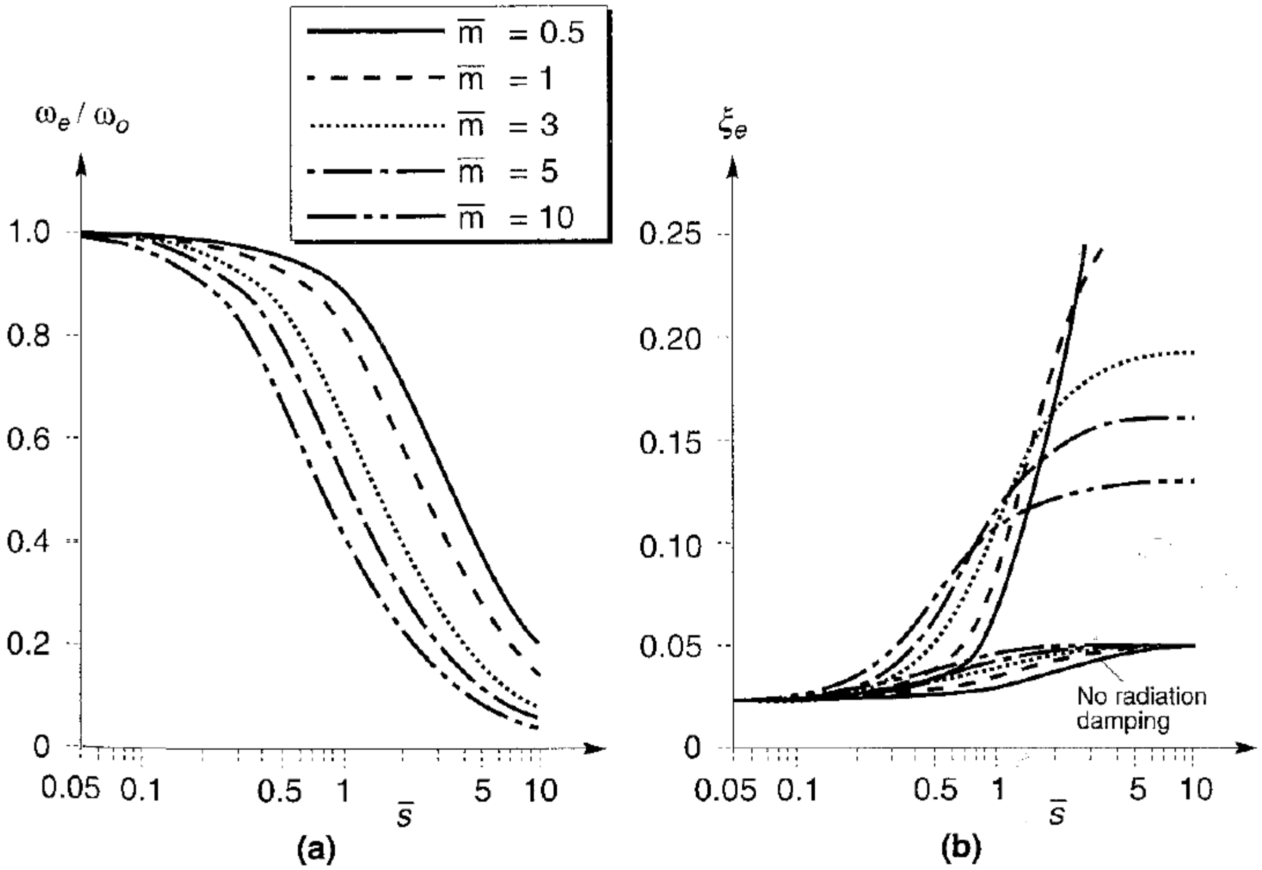

*Fig. 1.44 Effect of stiffness ratio and mass ratio on (a) natural frequency, and (b) damping ratio of soil-structure systems (h = 1, v = 0.33, ξ = 0.025, ξg = 0.05) **(Wolf, 1985)***

The effects of soil-structure interaction on displacements are illustrated in Figure 1.45, where *h* is the height of a straightforward structural model of a single-story building frame, *u* represents the amplitude of the relative displacement of the mass referred to the moving frame of reference attached to the rigid base and which is equal to the structural distortion, u_0 is the amplitude of the horizontal displacement of the base relative to the free field motion, and θ is the rotation. In this case, the effects of the soil-structure interaction were both to reduce the maximum structural distortion, $u_{\max}$, and to increase the overall displacement $(u + u_0 + h\theta)_{\max}$ (with respect to the free field) by an amount that increases with increasing stiffness ratio $\bar{s}$. Thus soil-structure interaction tends to reduce the demands on the structure, but because the foundation can translate and rotate, increase the overall displacement. These effects can be important for tall, slender structures or for closely spaced structures that may be subjected to *pounding* when relative displacements become large.

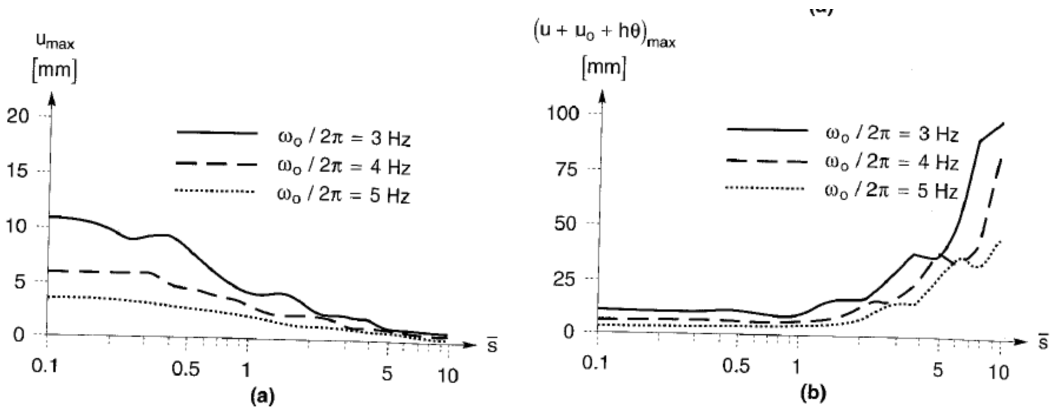

*Fig. 1.45 Response of equivalent soil-structure system to artificial time history: (a) maximum structural distortion; (b) maximum displacement of mass relative to free field (**Wolf, 1985**)*

A more recent solution for the evaluation of the frequency reduction (period elongation) is that proposed by **Maravas et al. (2014)**, which is based on the compliant-base SDOF. In that study, an exact analytical solution was proposed. The difference between the formulation by **Maravas et al. (2014)** and that proposed by **Veletsos and Meek (1974)** consists in the equation used to derive the exact solution for radiation damping.

Specifically, **Maravas et al. (2014)** introduce complex-valued and frequency-dependent impedances, and obtaining the following expression:

$$\xi^{*}=S\left[\frac{\xi_{u}}{\omega_{u}^{2}(1+4\xi_{x}^{2})}+\frac{\xi_{\theta}}{\omega_{\theta}^{2}(1+4\xi_{\theta}^{2})}+\frac{\xi_{str}}{\omega_{0}^{2}(1+4\xi_{str}^{2})}\right] \qquad 1.\ 162$$

where:

- ξ_u and ξ_θ are energy loss coefficients that are similar to viscous damping ratios
and equal to the ratio between the imaginary and two times the real parts of the impedance functions;

- ξ_{str} is the structural damping;

- ω_u, ω_θ and ω_0 are the uncoupled circular natural frequencies of the system, respectively under swaying oscillation of the base, rocking oscillation and oscillation of the fixed-base structure;

- S is a factor defined by (1.164) and it is used to calculate the fundamental frequency, f^*, as follows:

$$S=\left[\frac{1}{\omega_{u}^{2}(1+4\xi_{u}^{2})}+\frac{1}{\omega_{\theta}^{2}(1+4\xi_{\theta}^{2})}+\frac{1}{\omega_{0}^{2}(1+4\xi_{str}^{2})}\right] \qquad 1.\ 27$$

$$f^{*}=\frac{S}{2\pi(1+4\xi^{*2})} \qquad 1.\ 28$$

The formulations proposed above consider a shallow, circular, rigid foundation resting on a homogenous linear or viscoelastic/hysteretic half-space and permits to introduce the hysteretic damping ξ_{soil} into (1.159) and (1.162).

Chapter 2: Geophysical techniques for the characterisation of the urban environment

A site characterisation can be conducted through empirical approaches that can refer to spectral ratios of seismic event signals (weak and strong motion) or ambient noise recordings called microtremors. During my PhD work activity, two main experimental configurations were used: a reference site technique, i.e., the Standard Spectral Ratio method (SSR) to analyse seismic noise and a non-reference site method with single-station configuration to record and analyse seismic noise, i.e., the Horizontal to Vertical Noise Spectral Ratio technique (HVNSR). In this chapter, only empirical methods with a reference station (Standard Spectral Ratio, SSR) and without a reference station (Horizontal-to-Vertical Spectral Ratio, HVSR) will be described for site characterisation through the determination of spectral ratios of seismic noise data.

2.1 Seismic noise

The Earth's surface is subject to continuous oscillations in the seismic frequency range (0.01-100 Hz). These oscillations are called microseisms or microtremors or seismic noise, they are characterised by modest amplitudes (generally between 10^{-4} and 10^{-2} mm) and are imperceptible to humans. In the study of earthquakes, microtremors represent a source of noise that can mask the signal of distant seismic sources.

Although studies of seismic noise have been carried out since the mid-19th century (**Ferrari et al., 2000**), it was not until the 1950s that instruments capable of recording and analysing seismic noise became available. Some scientists, such as **Kanai et al. (1954)**, **Aki (1957)**, and **Akamatsu (1961)**, pointed out that microtremors contained valuable information about soil characteristics and site response to a seismic event. However, although techniques for collecting and analysing microtremor data have advanced over time, several open questions about the nature of seismic noise persist.

Research on the sources of microtremors shows that they are partly related to human activity (e.g., industry, traffic, etc.) and partly related to natural phenomena (e.g., the flow of water in a river, rain, wind, pressure variations, ocean waves, etc.); therefore, due to the human component, microtremors are not a purely natural phenomenon. Since human activity and natural phenomena vary in time and space, microtremors take on extremely complex, irregular, and unrepeatable forms. However, when microtremors are measured simultaneously by various stations located at different points on the earth's surface, signals containing coherent waves (i.e., waves that have the same phase both in time and space domain) are revealed, i.e. microtremors that present a superposition of waves travelling in different directions. **Toksös and Lacoss (1968)** demonstrated through data collected by a large aperture seismic antenna (LASA) that microtremors are the superposition of volume and surface waves.

2.1.1 Origin and nature of noise

The research carried out over the years (**Gutenberg, 1958**; **Asten, 1978**; **Asten and Henstridge, 1984**; **Bonnefoy-Claudet et al., 2004**) while emphasising the existence of many types of noise sources, show how they can be classified into two types: natural and anthropic. Table 2.1 summarises the results of the studies of **Gutenberg (1958)**, **Asten (1978)**, and **Asten and Henstridge (1984)** that state how different noise sources affect different frequencies (oceanic effects and large-scale weather conditions < 0.5 Hz, effect of wind and local weather conditions ~ 1 Hz, human activity, i.e., vehicular traffic and industrial activities for frequencies > 0.5 Hz).

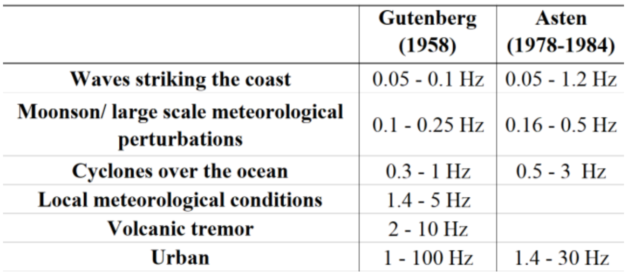

	Gutenberg (1958)	Asten (1978-1984)
Waves striking the coast	0.05 - 0.1 Hz	0.05 - 1.2 Hz
Moonson/ large scale meteorological perturbations	0.1 - 0.25 Hz	0.16 - 0.5 Hz
Cyclones over the ocean	0.3 - 1 Hz	0.5 - 3 Hz
Local meteorological conditions	1.4 - 5 Hz	
Volcanic tremor	2 - 10 Hz	
Urban	1 - 100 Hz	1.4 - 30 Hz

Tab. 2. 1 Seismic noise sources at different frequencies according to ***Gutenberg (1958)****,* ***Asten (1978)****,* ***Asten and Henstridge (1984)*** *studies.*

In summary, the following can be deduced from the aforementioned studies:

- noise below 0.5 Hz is mainly due to natural sources, is generally stable, has high coherence (i.e., composed of the superposition of waves that have the smallest phase differences in the time and space domains) and is essentially composed of surface waves;
- noise in the 0.5 - 1 Hz frequency range is generated by both anthropogenic and natural sources (meteorological conditions); the noise is less stable and consists of a variable percentage of surface waves;
- noise characterised by frequencies above 1 Hz is produced by human activity; since anthropogenic sources exhibit great variability, the noise is very unstable both in amplitude and in the ratio between surface and body waves.

The above-mentioned authors agree to set a frequency limit of 1 Hz to divide low-frequency noise due to natural causes (microseisms) from high-frequency noise due to anthropogenic factors (microtremors).

In recent decades, research has been carried out to understand the nature of noise. Several studies summarised in the SESAME project (report **WP08, 2004**), identified three useful ratios to characterise the nature of noise:

- ratio between the energy of body waves and surface waves;
- ratio between the energy of Rayleigh waves and Love waves;
- ratio between the energy of the fundamental Rayleigh mode and the higher modes.

Douze (1964, 1967) carried out studies on the relationship between the energy of body waves and surface waves by measuring the magnitude of noise in deep wells and comparing the theoretical and experimental relationship between deep and surface noise with the following conclusions:

- at 0.5 Hz, although not clearly, the noise seems to be given by the superposition of P-waves and Rayleigh waves (third mode);
- the noise at 1 Hz is given by the superposition of P waves and Rayleigh waves (first mode);
- noise at 2 Hz is the result of superposition of P-waves and Rayleigh waves (third mode; **Lai (1998)** showed that for each frequency there is a number M of oscillation modes that can be finite or infinite depending on the dependence of the properties of the medium and the frequency of excitation with depth z).

Li et al. (1984) compared the experimentally determined propagation velocity of seismic waves with the theoretical wave velocity in a known ground; the authors concluded that for frequencies above 1 Hz the noise is superposition of body waves and Rayleigh waves (higher modes).

Horike (1985) pointed out that in the range 0.5 - 0.9 Hz the noise is Rayleigh waves, while for frequencies compre between 0.9 and 3 Hz the noise is given by the superposition of various modes of Rayleigh waves.

Subsequent studies by **Yamanaka (1994)** in the Kanto Plain (Japan) showed that microseisms with frequencies between 0.1 - 1 Hz consist of Rayleigh waves.

Bormann and Wielandt (2013) carried out studies in boreholes that provided insight into the contribution of surface waves in seismic noise: Figure 2.2 shows an exponential decrease in noise amplitude with depth.

In addition, **Bormann and Wielandt (2013)** points out that the noise at 300 m depth, compared to that at the surface (Figure 2.3), is reduced by:

- 10 dB for frequencies of 0.5 Hz;
- 20 dB for frequencies of 1 Hz;
- 35 dB for frequencies of 10 Hz .

The findings of **Bormann and Wielandt, 2013** are in agreement with the nature of surface waves for microtremors.

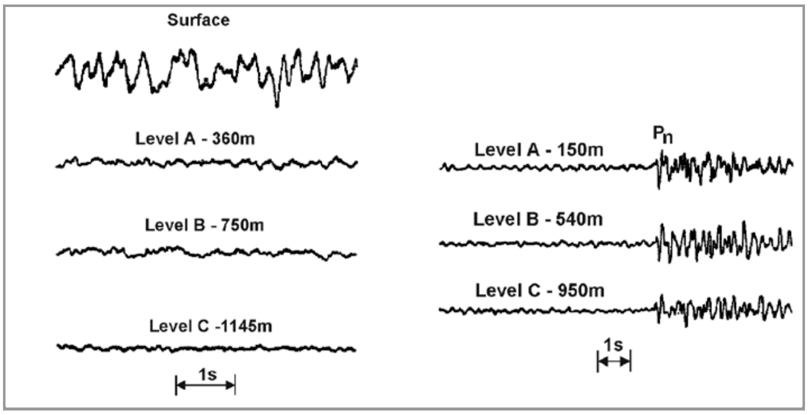

Fig. 2. 1 Recording of short-period seismic noise (left) and signals (right) at the surface and at different depth levels of a borehole seismic array. Note the significantly larger Pn amplitude closer to the surface. It is due to the surface amplification effect which may reach a factor of two for vertical incident waves. (Figure re-drawn from ***Bormann and Wielandt, 2013****)*

Thus, it appears that at low frequencies (<1 Hz), the noise consists essentially of Rayleigh waves in the fundamental mode; although there is not complete agreement, it appears that at frequencies above 1 Hz, the noise is characterised by the superposition of P-waves and S-waves with the various modes of Rayleigh waves.

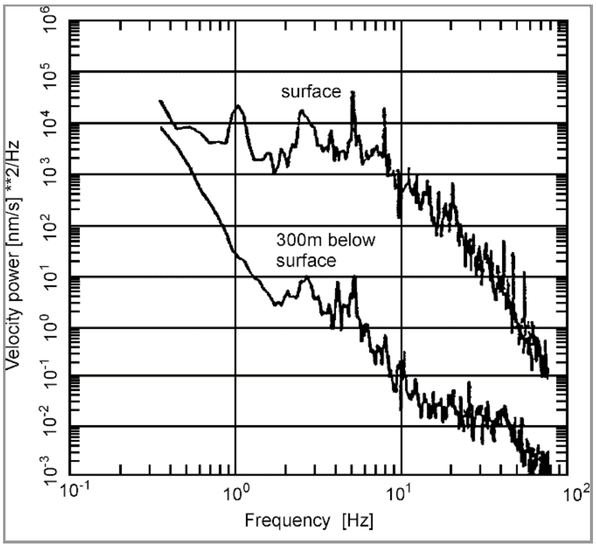

Fig. 2. 2 Velocity power density spectra as obtained for noise records at the surface (top) and at 300 m depth in a borehole (below) near Gorleben, Germany (Figure re-drawn from ***Bormann and Wielandt, 2013****)*

Another useful element for studying the nature of seismic noise is the ratio between Rayleigh and Love waves energy. Although several studies have been carried out over the last 30 years to determine this ratio, the results have not been unambiguous (Table 2.2). In all cases, the authors assumed that the noise is composed mainly by surface waves; the variability of the result is due to the methodology adopted in analysing the data.

Ohmachi et al. (1998) simulated the noise through the equations derived by **Harkrider (1964)** for a simple subsoil model (one layer above a half-space). The value of the obtained ratio between Rayleigh and Love waves ranges between 10% to 90%, with an average value equal to 30%, and is strongly influenced by the soil stress conditions.

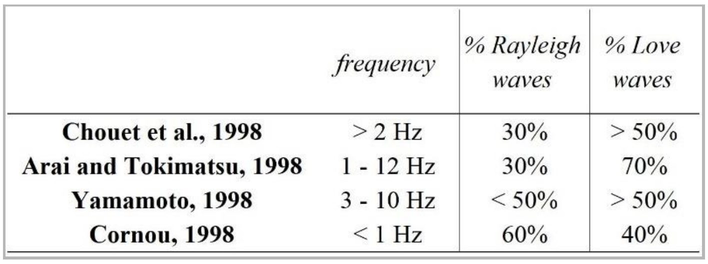

	frequency	*% Rayleigh waves*	*% Love waves*
Chouet et al., 1998	> 2 Hz	30%	> 50%
Arai and Tokimatsu, 1998	1 - 12 Hz	30%	70%
Yamamoto, 1998	3 - 10 Hz	< 50%	> 50%
Cornou, 1998	< 1 Hz	60%	40%

*Tab. 2. 2 Results of the proportion between Rayleigh waves and Love waves according to different authors (**Chouet et al., 1998**; **Arai and Tokimatsu, 1998**; **Yamamoto, 2000**; **Cornou, 2002**)*

Chouet et al. (1998) studied the tremors of the Stromboli volcano. The obtained results attribute a percentage of 30% to Rayleigh waves and 70% to Love waves; the ratio, however, refers to tremors induced by volcanic activity rather than to microtremors; therefore, it does not appear legitimate to assume that the tremors of the Stromboli volcano are a good approximation of microtremors.

Arai and Tokimatsu (1998) carried out noise analysis at four different locations in Japan. The results obtained with two different methods are in good agreement (Figure 2.4).

Yamamoto (2000) applied the method previously used by **Chouet et al. (1998)** to estimate the ratio between Rayleigh and Love wave energy. **Yamamoto (2000)** acquired seismograms at three different locations in the city of Morioka (Japan). Unlike **Chouet, et al., 1998**, **Yamamoto (2000)** determined the ratio of Rayleigh and Love waves as a function of frequency. The results obtained by **Yamamoto (2000)** are similar to those of **Arai and Tokimatsu (1998)**, so the authors concluded that approximately 30% of the noise at urban sites (noise frequency > 1 Hz) is composed of Rayleigh waves. Different results were obtained by **Cornou (2002)** using the high-resolution MUSIC analysis (**Schmidt, 1981**). The percentage of energy attributed by **Cornou (2002)** to Rayleigh waves is 60%; however, it should be noted that the frequency range studied is 0.2 - 1 Hz.

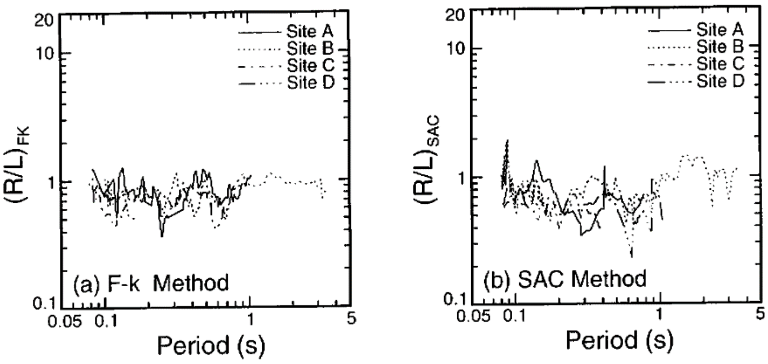

*Fig. 2. 3 Rayleigh - to -Love wave amplitude ratios in horizontal motions estimated from microtremor array data (Figure re-drawn from **Arai and Tokimatsu, 1998**)*

On the basis of the above, the scientific community's difficulties in establishing the precise nature of noise (body waves or surface waves?, Rayleigh waves or Love waves?) are evident, and it therefore appears complex to determine the relationship between the energy of the fundamental Rayleigh mode and the higher modes. Few works on this subject exist in the literature. **Tokimatsu (1997)** showed the possible existence of higher modes in Rayleigh waves. **Tokimatsu (1997)** calculated the noise in synthetic form by solving the equations of Rayleigh wave displacements for three stratified soil models then determining the corresponding dispersion curves (Figure 2.5). As can be seen from Figure 2.5, there is correspondence between the theoretical data from the fundamental mode (or mode 0) and those obtained in the simulation only in case 1, i.e., for a subsoil profile in which the S-wave velocity increases regularly with depth. In the cases 2-3, where the S-wave velocity profile varies irregularly, the higher modes are important for higher frequencies. Therefore, the mechanical and geological characteristics of the subsoil play a key role in exciting the upper modes of Rayleigh waves within the surface wave component of seismic noise.

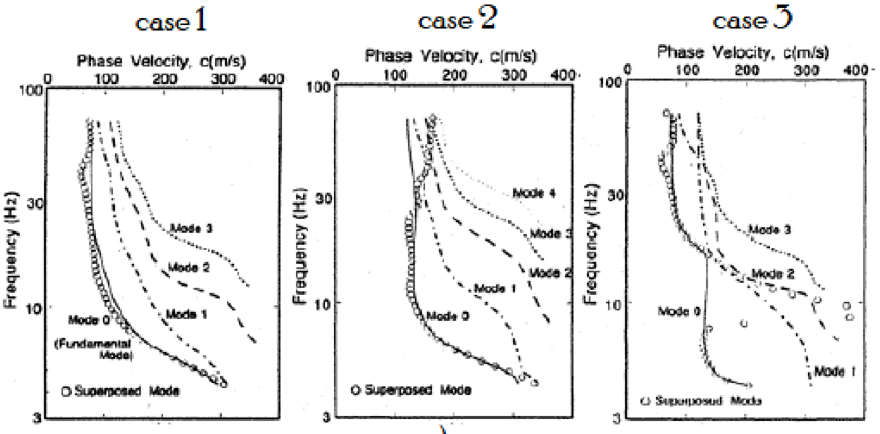

a)

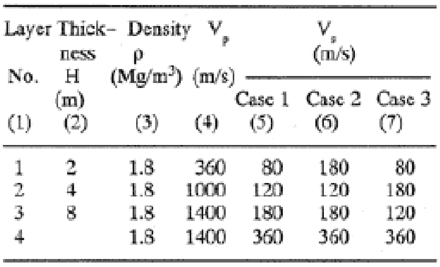

Layer No.	Thickness H (m)	Density ρ (Mg/m³)	V_p (m/s)	V_s (m/s)		
				Case 1	Case 2	Case 3
(1)	(2)	(3)	(4)	(5)	(6)	(7)
1	2	1.8	360	80	180	80
2	4	1.8	1000	120	120	180
3	8	1.8	1400	180	180	120
4		1.8	1400	360	360	360

b)

Fig. 2. 4 (a) Velocity dispersion curves calculated on the basis of (b) velocity profiles used by ***Tokimatsu, 1997****. The calculated dispersion curves (dotted line) are compared with the theoretical dispersion curves of the upper modes of Rayleigh waves (Figure re-drawn* ***from Tokimatsu, 1997****)*

Tokimatsu (1997), through a quantitative estimate of the ratio between the energy of the fundamental Rayleigh mode and the higher modes, concludes as follow:

- the existence of the higher modes of Rayleigh waves in seismic noise is possible;
- the subsoil profile, in particular the S-wave velocity profile with depth, plays an important role in the excitation of the higher modes.

2.1.2 Noise as a stationary process in time and space

Seismic noise varies both spatially and temporally. Figure 2.6 shows the results of a study by **Peterson (1993)**: it is observed that the spectra of noise acceleration from 75 locations scattered over the Earth's surface have similar but not identical trends.

A phenomenon is stationary over time if there are no systematic changes in mean value and variance. **Okada (2003)** showed that noise varies in intensity over time. Figure 2.7 shows noise recordings made in Sapporo (Japan) at three different times of the day, in the three spatial directions. It can be seen that the noise shows complex variations, but the degree of complexity does not vary throughout the entire three-minute recording. The large variation in signal amplitude over the entire day is evident.

Okada (2003) analysed the variation of microtremors at 10 different stations arranged as in Figure 2.8 near Obihiro (Japan) for one day. The overall shape of the spectra is essentially the same; they differ in frequencies greater than 1.5 Hz at different locations and times. The variation in time of the recordings is due to the temporal variation of the sources. The variation of the spectra at different stations, for frequencies greater than 1 Hz, is linked to the non-stationarity of the microtremors on this scale. Conversely, stationarity of the process can be observed for frequencies below 1 Hz. In conclusion, in light of the studies of the various authors mentioned, and as will be further clarified in the next section, the phenomenon can be considered stationary for time intervals of the order of a few hours. This is an essential prerequisite for representing the noise; since in this work the recordings of seismic noise signals are just over an hour in duration, it will be assumed, as a first approximation, that the process is stationary in time and space.

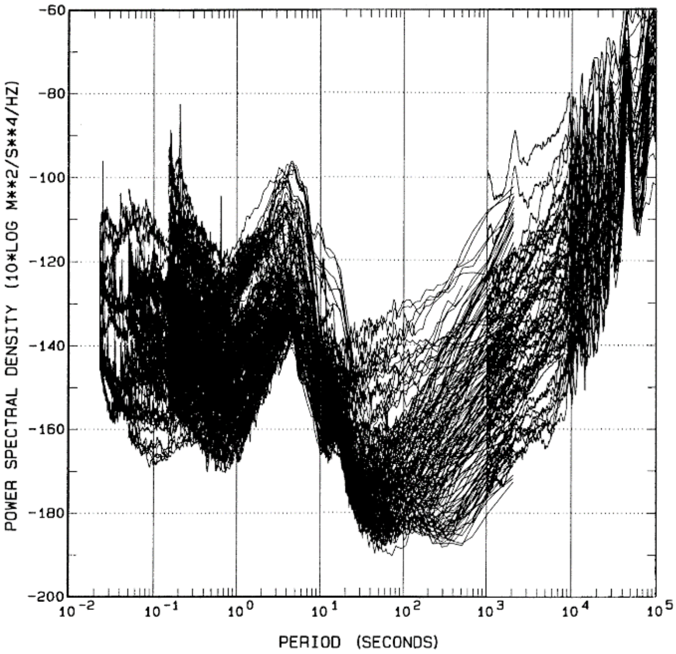

*Fig. 2. 5 An overlay of noise acceleration spectra of 75 locations around the Earth's surface (Figure re-drawn from **Peterson, 1993**)*

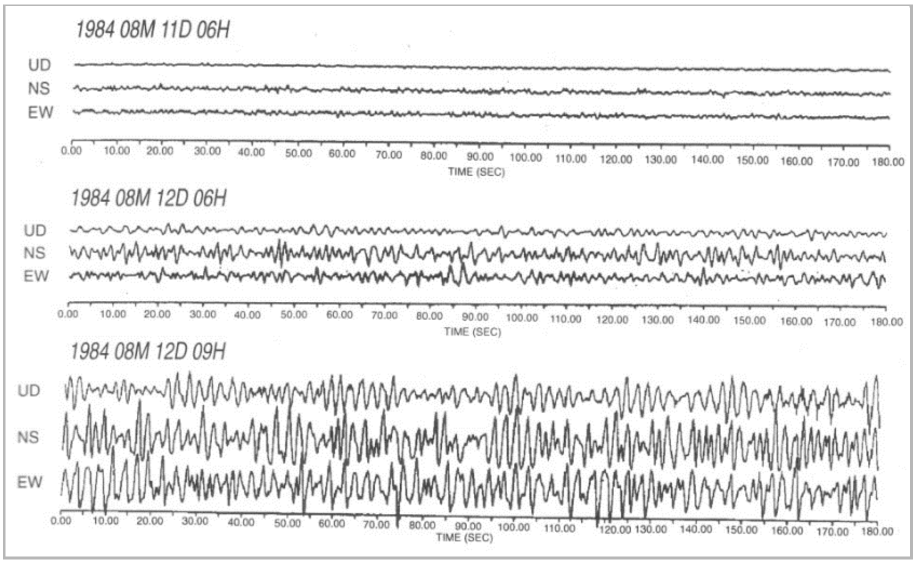

*Fig. 2. 6 Noise recordings made in Sapporo (Japan) at three different times of the day (Figure re-drawn from **Okada, 2003**)*

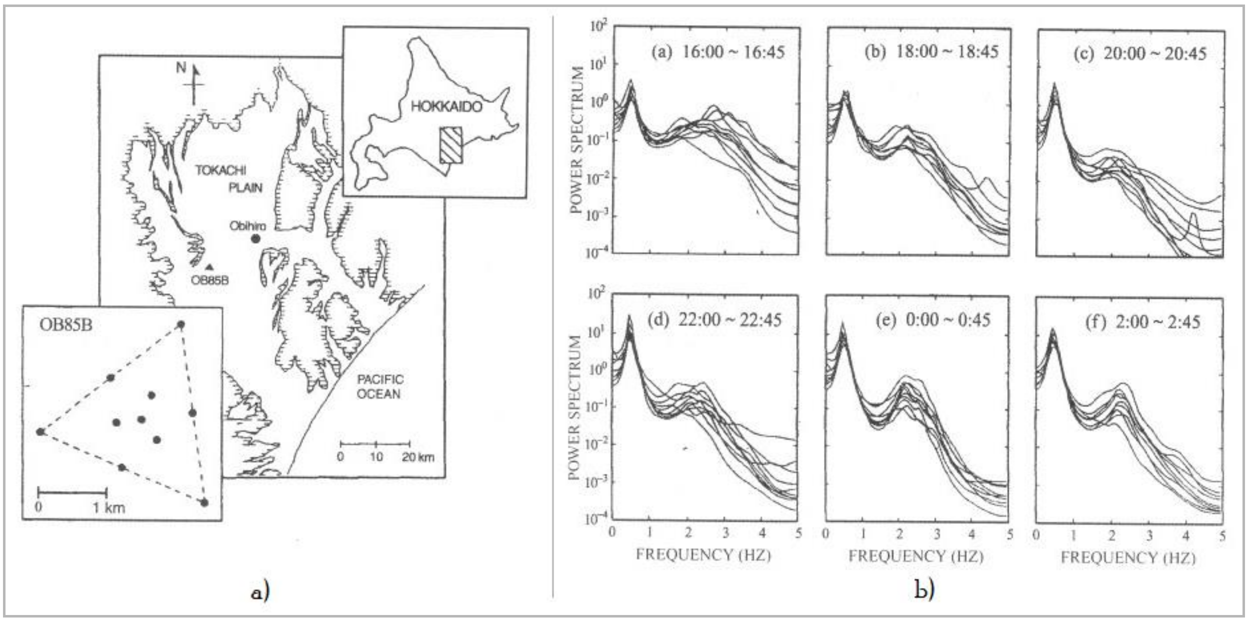

*Fig. 2. 7 Variability of microtremors at 10 different stations near Obihiro (Japan) during a day (Figure re-drawn from **Okada, 2003**)*

2.1.3 Microtremor spectrum

The waves contained in seismic noise are generated by sources of random intensity just as random is their distribution in both the space and time domains; moreover, they travel in mediums with extremely variable geological conditions. Consequently, the noise has a very complex form and cannot be described by simple mathematical equations; the amplitude of the noise cannot be predicted. Seismic noise is therefore stochastic, i.e. the amplitude of the signal is indeterminate and unrepeatable. Even though the statistical approach entails some difficulties, some authors (**Yanglom, 1962**; **Priestley, 1981**; **Sunahara, 1981**) believe that the use of statistical operators reduces the difficulty of the problem.

The amplitude of the noise can be viewed as a random variable and a probability density function associated with it. **Nogoshi and Igarashi (1970)** showed that the frequency distribution of the noise amplitude is asymptotic to a normal distribution as the sample size increases. **Sakaji (1998)** studied the stability of noise over time by determining the frequency distribution of the noise amplitude, considered as a random variable, and its correlation function (Figures 2.9 and 2.10).

In Figures 2.9 and 2.10, it is clearly demonstrated that the mean, variance, and autocorrelation function of the amplitude of the microtremors are constant for 10-minute sampling intervals and that the microtremors satisfy the properties of a stationary stochastic process. The stationarity of the signal was studied by **Parolai and Galiana - Merino (2006)** emphasised that signal stationarity can be achieved with one hour of recording. Furthermore, the frequency distribution of the amplitude of microtremors can deviate strongly from that of a normal distribution when noise due to a transient impulse (e.g., person walking, moving car) interferes with the data during acquisition. Therefore, microtremors can be analysed in terms of the theory of stochastic processes (**Yaglom, 1962**; **Priestley, 1981**; **Sunahara, 1981**) and their spectral representation can be determined.

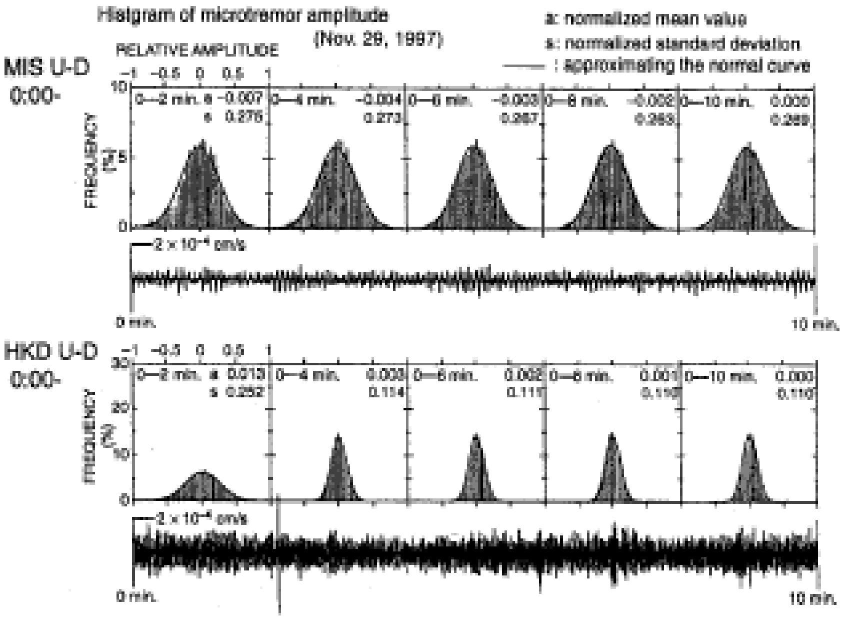

Fig. 2. 8 10-minute recordings of microtremors and histograms of their amplitudes. The curve is the probability density function determined by assuming that the histogram follows a Gaussian distribution (Figure re-drawn from ***Okada, 2003****)*

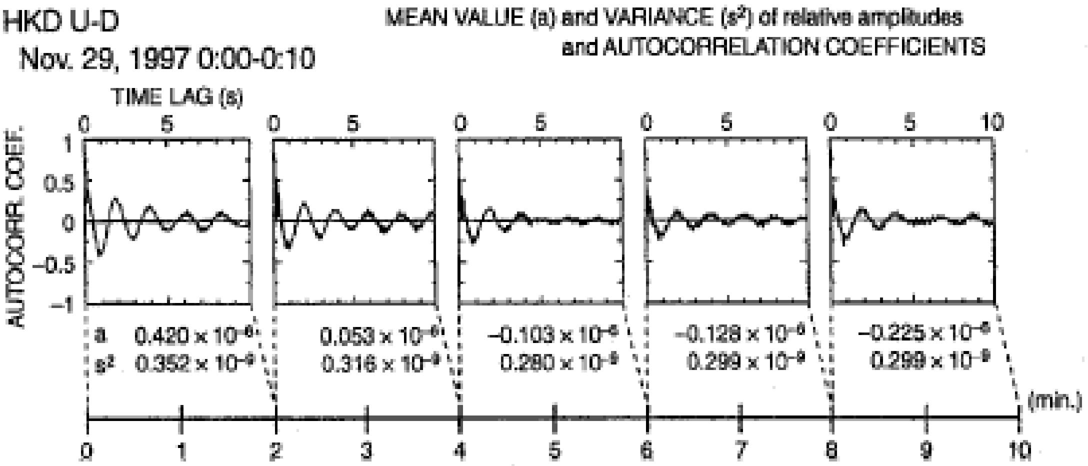

Fig. 2. 9 Autocorrelation coefficient of a microtremor recording (Figure re-drawn from ***Okada, 2003****)*

2.2 Empirical methods for site characterization

Various methods may be used for site effect evaluation (experimental-empirical, empirical, semi-empirical, theoretical, and hybrid methods) for a more in-depth discussion of which see **Pitilakis, 2004**. In this chapter, some methods belonging to the experimental - empirical category are discussed. The set of experimental methods for the assessment of site effects can generally be divided into two main sub-categories depending on or not they need a reference site, with respect to which the particular effects at other sites are estimated (see, e.g., **Parolai, 2012**).

The reference site method consists in comparing records at nearby sites, “where source and path effects can be believed to be identical” (**Bard, 1994**), through spectral ratios, taking the name Standard Spectral Ratio

(SSR). The assumptions of this technique are that the reference site, that is represented by a station located on outcropping bedrock, is free of any site effect, and the source information and the path effect are the same for this pair of records at two closely located sites; thus, the site response can be reliably estimated through the spectral ratios. This technique was proposed first by **Borcherdt (1970)** and is still widely used. **Andrews (1986)** generalised this technique extending it to large data sets recorded on local/regional networks, separating the contribution of the path, the source, and the site effects through the resolution of a large inverse problem, from which the name of the method, i.e., generalised inversion technique (GIT). For more details see **Parolai, 2012**.

Since also rock sites might have their own response, appropriate reference sites are not always available (**Steidl et al., 1996**). In addition, as discussed in **Chapter 1**, since rock sites often are located on hills, topographic effects need to be taken in account as well. For this reason, different methods that are not depending on reference sites have been developed. One of them is the Horizontal to Vertical Spectral Ratio (HVSR). The single-station method, developed since the early 1970s (**Nogoshi and Igarashi, 1970, 1971**), is now known as the Horizontal to Vertical Spectral Ratio method (HVSR or H/V ratio method). **Nakamura (1989)** developed this method further as a tool for the estimation of the site response of S waves, and for this reason the HVSR is also known as Nakamura's method. Originally, **Nakamura (1989)** proposed to use the spectral ratio between the horizontal and the vertical components of ambient noise recordings. Over the past 30 years, the simplicity and inexpensiveness of the H/V method have triggered its widespread use (**Delgado et al. 2000**; **Parolai et al., 2001**; **D'Amico et al., 2004, 2008**). **Dravinski et al. 1996** evaluated the reliability of HVNR spectra for different incident waves in deep basins demonstrating that Nakamura's Technique predicts well the fundamental resonant frequency of deep sedimentary basins; **Ogawa et al, 1998** indicated the peak horizontal ground velocity on surface with microtremors by the integration value of H/V, and proposed a method to estimate the regional distribution of the peak horizontal ground velocity in Kyoto city during 1995 Kobe earthquake; **Malagnini et al. 1996** used explosion, earthquake, and ambient noise recordings in order to evaluate site functions in a Pliocene sediment-filled valley using all spectral techniques; **Chávez-García et al. 1996** applied spectral techniques to evaluate not only 1-D effects but also topographic effects; **Satoh et al. 2001** gave a comprehensive analysis and comparison of the results obtained with various spectral techniques; many authors assessed site effect by computing a Fourier spectral ratio of the horizontal components over the vertical component of ambient noise measurements providing resonance frequency maps for large urban areas (**Parolai et al., 2001b** (Cologne, Germany), **Duval et al., 2001** (Caracas, Venezuela), **Picozzi et al., 2008** (Istanbul, Turkey), **Bonnefoy-Claudet et al., 2009**, **Pilz et al., 2009 and 2010** (Santiago de Chile, Chile), **Parolai et al., 2010b** (Bishkek, Kyrgyzstan), **Cadet et al, 2011** (Barcelona, Spain). Moreover, HVSR method have been used for the purpose of assessing the site effects of poorly consolidated covers, in seismic microzonation studies and following emergencies caused by seismic events (**Gallipoli et al., 2002, 2011**; **Paolucci et al., 2015**).

HVSR method was first applied to the S wave portion of earthquake recordings (EHV) by **Lermo and Chavez-Garcia (1994)** who found very good agreement between the spectral ratio with reference site and HVSR for three different cities in Mexico: Oaxaca, Oax., Acapulco, Gro., and Mexico City.

In the scientific community there is extended bibliography on comparative results on the applicability and reliability of SSR and HVSR, which represent the most common experimental methods for the estimation of site amplification due to local soil conditions.

Numerous authors compared site responses obtained with both methods, reference and non-reference site techniques (e.g., **Field and Jacob, 1995**; **Bonilla et al., 1997**; **Riepl et al., 1998**; **Triantafyllidis et al., 1999**; **Parolai et al., 2000; 2001a; 2004**; **Bindi et al, 2009**) showing that SSR and HVSR applied on the S-wave portion earthquake data usually provide site responses with similar shapes. According to **Parolai, 2012** both methods consistently estimate the fundamental resonance frequency of a site, although there is an underestimation of the amplification factor compared to SSR. **Raptakis et al. (1998, 2000)**, using a large and high quality earthquake data from EUROSEISTEST experimental site in Thessaloniki, proved that the significant differences between the amplitudes at the resonance frequency estimated by using SSR and HVSR methods are related to the significant amplification of the vertical component due to diffracted Rayleigh waves at the lateral discontinuities of the already mentioned (**Chapter 1**) valley near Thessaloniki in the epicentral area of the strong 1978 Ms = 6.4 earthquake.

2.2.1 Standard Spectral Ratio method (SSR)

Several authors (**Pitilakis, 2004**; **Parolai, 2012**) have confirmed that the Standard Spectral Ratio method, SSR, belonging to the reference site technique category, is the most popular and widely used method for seismic site characterisation. This method is defined as the direct spectral ratio of the same component of the same earthquake recorded at two nearby stations, a soil-site and a rock-site. The two horizontal components can be analysed separately or combined (Figure 2.11). "If the reference site is free of any site effect, these spectral ratios constitute a reliable estimate of site response" (**Bard, 1994**). This technique, introduced by **Borcherdt (1970)**, is the best known for determining the site function. Since the source information is the same for both recordings, when the two sites are close together, the path effect is also considered the same. Therefore, the ratio of the Fourier amplitude spectra only expresses the effect of the local ground conditions at the specific site.

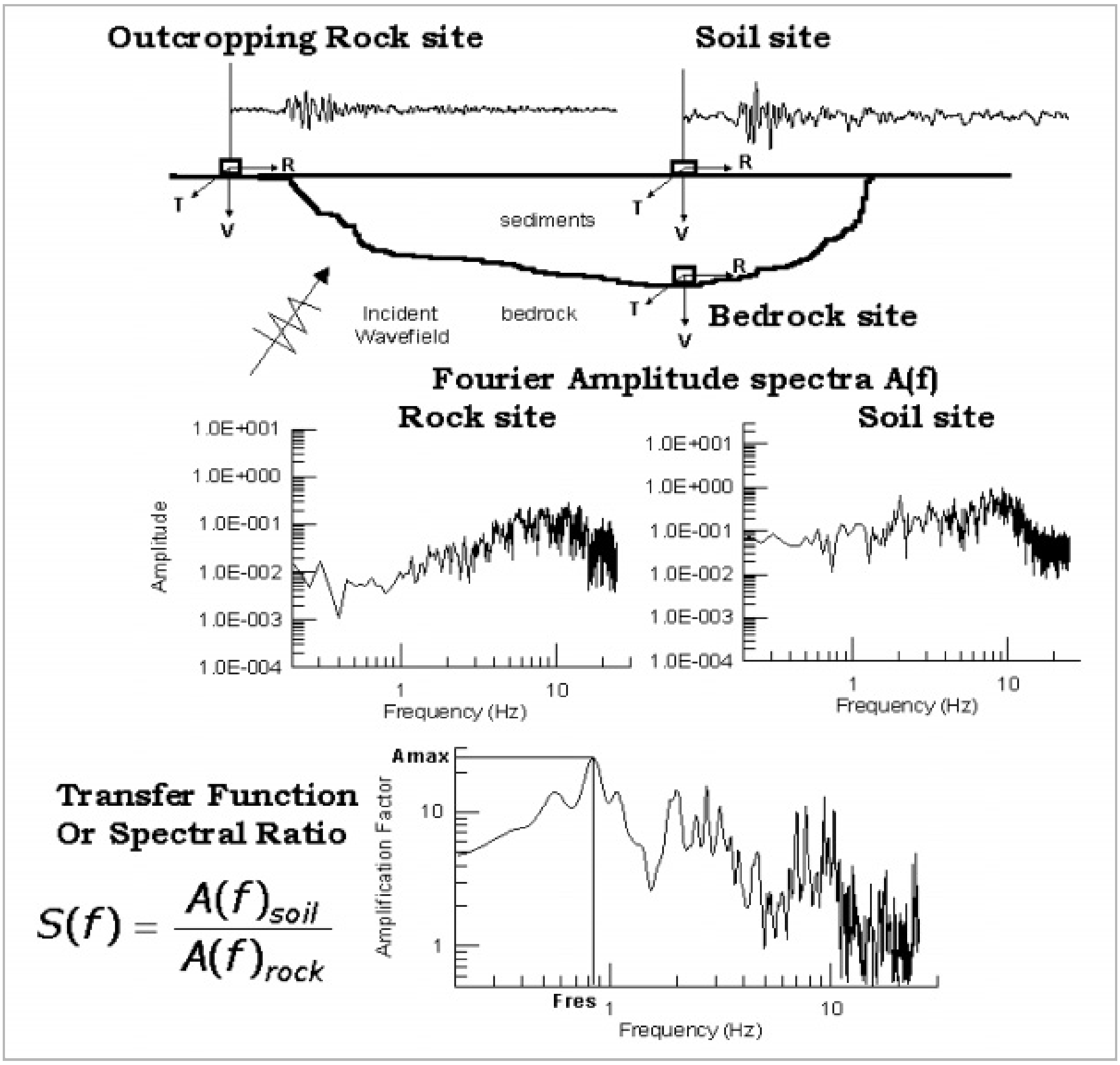

*Fig. 2. 11 General description of the Standard Spectral Ratio Technique (SSR) (Figure re-drawn from **Pitilakis, 2004**)*

Nevertheless, in theory this method is only applicable to cases where data are derived from dense local arrays with at least one station on outcropping rigid bedrock defined as the reference station. According to **Pitilakis, 2004,** for the application of this technique in the case of a surface reference station it is advisable to follow some basic conditions:

(i) at both soil site and reference site simultaneous recordings should be available;
(ii) no site effects, neither stratigraphic nor topographic must be present at the reference site;
(iii) with the aim to consider the effect of the propagating path of the seismic energy equivalent for the both the sites, the distance between the soil-site and the reference site should be smaller than the epicentral distance.

Since condition (iii) is often not possible or valid, **Steidl et al., 1996** urged that a careful examination of the reference site is mandatory for the correct estimation of amplification in sedimentary sites.

Borcherdt, 1970 indicated that between the source (input) i(t) and the recorded seismogram s(t), the major effects that can be visualised on a seismogram are related to the earth's crust [h_e(t)], the geology at recording site [h_g(t)] and the recording instruments [h_r(t)]. According Borcherdt, since each effect, to a first approximation, for most seismograms can be treated as a linear system, it is defined by a unit impulse response; therefore, considering the final seismogram s(t) as the convolution (∗) between the source and each effect yields:

$$s(t) = i(t) * h_e(t) * h_g(t) * h_r\,(t) \qquad 2.1$$

In terms of Fourier transforms the previous eq. Can be expressed as:

$$S(f) = I(f)H_e(f)H_g(f)H_r\,(f) \qquad 2.2$$

Indicating with S_s(f) and S_b(f) the Fourier transforms of two seismograms recorded on a sedimentary layer and at a nearby bedrock station from the same source respectively, the ratio between their absolute value reduces to:

$$\frac{S_S(f)}{S_b(f)} = \frac{H_{gS}(f)}{H_{gb}(f)} \qquad 2.3$$

provided similar recording instruments are used at each site and the travel path through the Earth's crust is basically the same for both sites (**Borcherdt, 1970**). Since the bedrock does not change the frequency characteristics of the signal as much as a thick soft layer, the ration in eq. (2.3) provides the seismic amplitude site response of the soft layer site.

Bard, 1999 stated that the basic principle of these technique may be described considering that the amplitude spectrum of the recorded ground motion $R_{ij}(f)$, for a network of I sites having recorded J events, can be written as:

$$R_{ij}(f) = E_{ij}(f).\,P_{ij}(f).\,S_i(f) \qquad 2.4$$

where $E_j(f)$ is the source function, $P_{ij}(f)$ is the source-to-site path and $S_i(f)$ is the local site effects contribution. According to **Bard, 1994**, writing the eq. (2.4) in logarithmic form yields to simple linear equation:

$$\ln R_{ij}(f) = \ln E_{ij}(f) + \ln P_{ij}(f) + \ln S_i(f) \qquad 2.5$$

The source function $E_j(f)$ and the path therm $P_{ij}(f)$ can be considered to be site independent (i.e. when the distance to the reference site is small compared to the source to-site distance) and the ratio of the amplitude spectra between target and reference sites gives the transfer function.

Following the formulations and the notations used by **Parolai, 2012**, the ratio between the spectral amplitude of two seismograms recorded on a sedimentary layer site (*j*) and at a nearby bedrock (reference *k*) station from the same source event (*i*) respectively with hypocentral distance (r), can be written in frequency (f) domain as:

$$\frac{U(f,r)}{U_{ik}(f,r)} = \frac{S_i(f)Z_j(f)A_{ij}(f,r)}{S_i(f)Z_k(f)A_{ik}(f,r)} \qquad 2.6$$

where, $U_{ij}(f,r)$ is the spectral amplitude of the ground motion observed at a recording site *j* for a event *i*, $S_i(f)$ is the source function, $Z_j(f)$ is the site response, $A_{ij}(f,r)$ is a function accounting for source-to-site path attenuation. So, in terms of Fourier Spectrum, the seismogram recorded at one station can be considered as the convolution of three terms: the source $S_i(f)$, the path $A_{ij}(f,r)$ and site response $Z_j(f)$. **Parolai, 2012** clearly indicated that “if the stations are nearby and the reference station is not affected by site effects”, then $Z_k(f)=1$ and $A_{ij}(f,r) \approx A_{ik}(f,r)$. Thus, the spectral ratio directly provides the seismic amplitude site response of the sedimentary layer site.

2.2.2 Horizontal-to-Vertical Noise Spectral Ratio (HVNSR)

Based on developments in engineering applications introduced by **Gutenberg (1958)** and **Kanai and Tanaka (1961)**, the single-station method using microtremors was first adopted by **Nogoshi and Igarashi (1970, 1971)**. This method is now known as the horizontal-to-vertical spectral ratio method (or H/V ratio method). It consists of determining the ratio between the horizontal and vertical components of spectral amplitudes. This method was further developed as a tool for the estimation of the site response of S waves by **Nakamura (1989)**, thus determining the resonance frequency of soft sedimentary covers resting on rigid bedrock, and for this reason the HVSR is also known as Nakamura's method. Initially, the proposal of **Nakamura (1989)** was to use the spectral ratio between the horizontal and the vertical components of ambient noise recordings. After the 1985 Guerrero-Michoacan earthquake the H/V method was widely used (**Bard, 1999**), because it allowed simple and low-cost measurements of the spectral ratio of seismic noise that were consistent with data observed during violent phenomena (e.g., earthquakes). In recent years, the method has been used to assess seismic impedance contrasts and evaluate possible site effects.

In the following, the various aspects of the H/V method will be discussed; in particular, the theoretical basis of the method, the procedure adopted for calculating the theoretical H/V ratio, the information that can be obtained by using this method and, in conclusion, the experimental procedure for reliably estimating the H/V curve from microtremors will be analysed.

2.2.2.1 Theoretical background of the spectral ratio method

Since the 1950s, some authors (**Kanai et al., 1954**; **Kanai et Tanaka, 1961**) have attempted to estimate site effects by analysing the absolute spectrum of microtremors. Two main assumptions of this approach are that (i) the horizontal component of microtremors, below the period of 1 s, is due to shear waves impinging vertically on the surface, and (ii) the spectrum of incident waves is white. Under these assumptions, the horizontal component reflects the transfer function from the subsoil to the site. However, there are two weaknesses: firstly, microtremors give information about the excitation function as well as the site-transfer function (**Udwadia and Trifunac, 1973**). Furthermore, as discussed in the previous chapter, microtremors contain a significant portion of surface waves (**Aki, 1957**; **Li et al., 1984**; **Horike, 1985**; **Yamanaka et al. 1994**). In an attempt to minimise source effects, **Nogoshi and Igarashi (1970)** proposed normalising the horizontal spectral amplitude with the vertical spectral amplitude. The method for estimating the H/V ratio consists of determining the two horizontal components of the motion, X_c and Y_c, then combining them to obtain a single horizontal component Hc and finally dividing this by the vertical component of the motion. The modulus of H_c can be obtained from the geometric mean of X_c and Y_c:

$$H_c(f) = \sqrt{X_c(f)Y_c(f)} \qquad 2.7$$

or by the quadratic mean:

$$H_c(f) = \sqrt{\frac{X_c^2(f) + Y_c^2(f)}{2}} \qquad 2.8$$

Since the authors showed a good match between the maxima of the H/V ratio measurements and the fundamental resonance frequency of S-waves, they introduced this method to assess subsurface structures and quickly estimate site effects. This method became popular after **Nakamura (1989)** revised it and provided a theoretical interpretation. The author, by means of some observations on the nature of noise and through semi-theoretical assumptions, established that the H/V curve is capable of correctly estimating the site transfer function for S-waves.

Since the 1990s, due to its simplicity and inexpensiveness, the H/V method has been widely used to assess the resonance frequency of poorly consolidated covers (**Delgado et al. 2000; Parolai et al., 2001; D'Amico et al., 2004, 2008; Gallipoli et al., 2002, 2011; Paolucci et al., 2015**). It should be pointed out that several researchers remain skeptical about the reliability of the method due to some theoretical and practical aspects that need further study and investigation. For these reasons, research in recent years has focused on understanding the physical processes behind the phenomenon (**Field and Jacob, 1993**; **Nakamura, 1996, 2000**; **Bard, 1999**; **Fah et al., 2001**; **Lunedei and Albarello, 2010; Albarello et al., 2011**). **Bard (1999)** produced a comprehensive review on the theoretical basis of the method and the weaknesses of the two opposing interpretations of the H/V method. The first was proposed by **Nakamura (1989)** and is based on the link with body waves, while surface wave effects are not considered; the second is based on the relationship between the H/V curve and the ellipticity curve of Rayleigh waves.

2.2.2.2 Nakamura's interpretation

Nakamura (1989)'s interpretation was initially based on three assumptions that some researchers (**Kudo, 1995**; **Bard, 1999**) considered neither appropriate nor realistic. Subsequently, **Nakamura (1996)** modified his theory by proposing other explanations. **Nakamura (1996)** separates the noise into body waves (b) and surface waves (s), expressing the vertical (S^{NV}) and horizontal (S^{NH}) components of the noise spectrum as:

$$\begin{cases} S^{NH} = S_b^H(f) + S_s^H(f) = H_t(f)B^H(f) + S_s^H(f) \\ S^{NV} = S_b^V(f) + S_s^V(f) = V_t(f)B^V(f) + S_s^V(f) \end{cases} \qquad 2.9$$

where the indices (*H*) and (*V*) indicate the horizontal and vertical components respectively, *Ht(f)* and *Vt(f)* represents the true transfer function (the transfer function or amplification function represents, as a function of frequency, the ratio between the shaking observed at the site of interest and that observed for the same event at a reference site located at the same distance from the source) for the horizontal and vertical components; B^H(f) [resp. B^V(f)] and S_s^H(f) [resp.S_s^V(f)] indicate the horizontal (resp. vertical) spectrum of the body and surface waves part of the noise referred to at the reference site (rock site). Using the relations given by (1.168), after some algebra, the ratio H/V between S^{NH} and S^{NV} can be written as:

$$A^{NHV}(f) = \frac{[H_t A_r^{NHV}(f) + \beta A_s]}{\beta + V_t} \qquad 2.10$$

where

- A_r^{NHV} is the noise H/V ratio at a rock site
- β is the portion of surface waves contained in the noise and it is measured on the vertical component, i.e. $\beta = S_s^V(f)/B^V(f)$
- A_s represents the horizontal to vertical ratio due to surface waves only $A_s(f) = S_s^H(f)/S_s^V(f)$

In this approach, since the next step consist, for the fundamental frequency f_0, in assuming that:

$$A^{NHV}(f_0) = H_t(f_0) \qquad 2.11$$

i.e., $A^{NHV}(f_0)$ is the transfer function $H_t(f_0)$ of site, it requires the following assumptions to be verified:
(i) the vertical component is not amplified at frequency f_0;
(ii) the *H/V* ratio is equal to 1 at f_0 on rock site;
(iii) β is much smaller than 1 at f_0;
(iv) $\beta A_s(f_0)$ is much smaller than $H_t(f_0)$.

The hypotheses (i) and (ii) may be accepted quite easily on the basis of experience (**Bard, 1999**), while the (iii) and (iv) assumptions have been the subject of much criticism since are more controversial. In particular, the (iii) is only valid if there is a strong impedance contrast such that S_s^V is zero around f_0, in which case the (iv) assumption could not be valid as $As(f_0)S_s^H(f_0)/S_s^V(f_0)$ takes on high values. However, we have $S_s^H(f_0)/S_s^V(f_0) = S_s^H(f_0)/B^V(f_0)$, which implies that the amplitude of the surface waves is much smaller than the vertical amplitude of body waves on rock, particularly when compared to the actual amplification of S-waves (**Bard, 1999**). Since there is no reason to assume that $S_s^H(f_0)/B^V(f_0)$ is small in relation to $H_t(f_0)$, $A^{NHV}(f_0)$ cannot be considered an approximation of $H_t(f_0)$. Finally, as the frequency varies, for the relationship $A^{NHV}(f) = H_t(f)$ assumptions (iii) and iv() cannot be considered correct on the basis of the ellipticity curves as shown in Figure 2.12 (**Bard, 1999**).

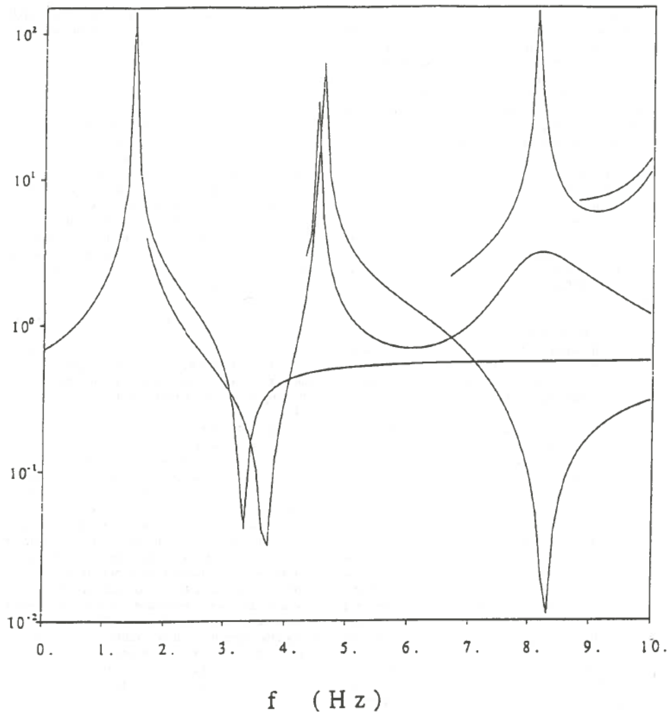

Fig. 2.12 Example of ellipticity curves of Rayleigh waves for a stratified half-space displaying the H/V ratio (log scale) vs frequency. The ellipticity curves are given as a function of frequency for the first 5 Rayleigh modes. The infinite peaks correspond to a vanishing of the vertical component, while the sharp troughs correspond to a vanishing of the horizontal component. (Figure re-drawn from ***Bard, 1999****)*

More recent studies (**Albarello and Lunedei, 2010**; **Lunedei and Albarello 2009, 2010**) have contributed to enriching knowledge about the nature of ambient noise using an interpretation of the HVSR curve based on a theoretical modelling of the noise field. **Albarello and Lunedei (2009)** have considered two of the various interpretative theses of the H/V curve derived from environmental noise measurements: the first is based on the assumption that HVSR curves are essentially conditioned by body waves vertically impinging on the free surface, the second considers that HVSR curves are determined by surface waves (Rayleigh and Love with the important contribution of higher modes). These interpretations are useful approximations of real physical processes and their reliability must be verified on a case-by-case basis. To analyse the problem, the authors developed a model in which the ambient noise is the complete wave field generated by a random distribution of independent point sources placed on the surface of a layered visco-elastic medium. **Albarello and Lunedei (2009)** showed that HVSR curves are adequately reproduced by surface waves even for frequencies larger than the resonance frequency. The authors also pointed out that interpretation by body waves more accurately describes the HVSR curve around the resonance frequency. Furthermore, **Lunedei et Albarello (2009, 2010)** showed that the HVSR curve depends on the extent of the source-free area around the receiver and that the most energetically significant contribution of body waves comes from local sources. This dependence of the HVSR curve on the distribution of sources implies that there may be significant variations in the HVSR curve due to the presence of human activities in the area where the ambient noise recordings are carried out. However, these variations only weakly modify the position of the maximum of the HVSR curve, which is a significant indicator (with a 10% uncertainty) of the resonance frequency of the investigated soil.

2.2.2.3 Experimental procedures for use of the HVNSR method

Mucciarelli and Gallipoli, 2001, in their critical review of previous years of the HVNSR technique, emphasised that there was no general agreement on a standard for data collection and processing, and that when it came to comparing the HVNSR technique with other methodologies or models, there was no single HVSR technique, but several variants of it. The proposed bibliographic study in this thesis confirms it. As underlined by the very recent comprehensive review by **Molnar et al., 2022,** which will be extensively quoted in this section, emerges that, among the seismic site characterization methods, the HVNSR technique has not yet obtained a unanimous consensus from the scientific community that allows the definition of standardised guidelines and commercial use.

The basic assumption of the method is that the vertical component is not amplified at frequency f_0, i.e., the resonance frequency of a soil deposit, in cases where the soil stratigraphy can be approximated to be flat and horizontal and is supposed to be free of any kind of influence (presence of buildings, tree, industrial facilities, etc.) related to the soil conditions at the recording site. From an experimental point of view, the application of the H/V method simply requires (i) recording microtremors in a site with a single seismometer with three orthogonal sensors and (ii) calculating, in terms of spectral ratio, the ratio of horizontal-to-vertical Fourier amplitude spectra (FAS). Figure 2.13 shows the general layout of the method which was applied in the context of this thesis to the recordings of ambient noise on a soil site in Matera (Southern Italy).

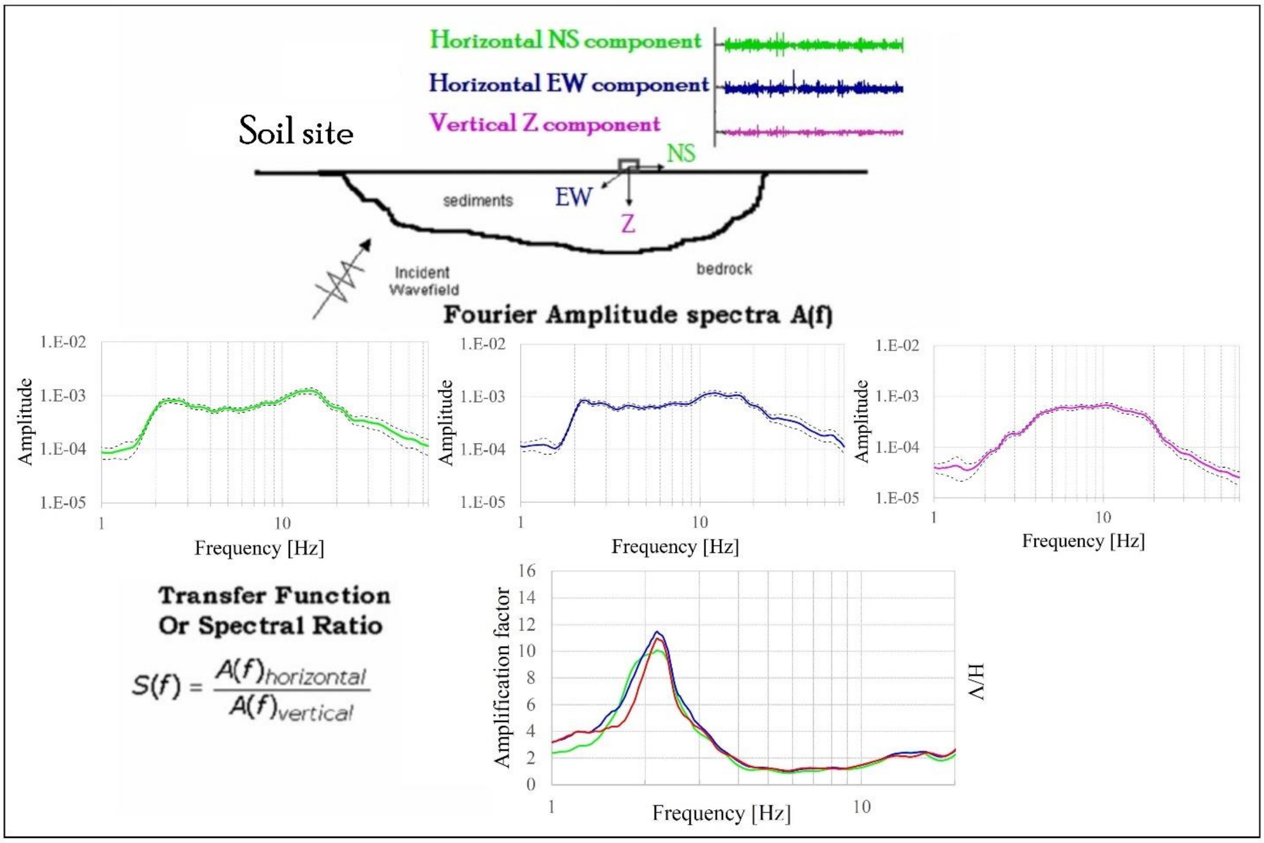

Fig. 2.13 General description of the Horizontal to Vertical Spectral Ratio (HVNSR) Technique applied to ambient noise.

There is no international standard for documenting the metadata associated with each microtremor record, but an example of a field metadata sheet has been generated in the HVNSR guidelines of **SESAME (2004)** and Canada (**Perret 2015**). An in-depth discussion has been reported in **Molnar et al., 2022**, and since this work was carried out by eminent authors, it has been extensively taken as a very useful reference.

As regards the equipment, the most suitable recording instrument is a three-component velocimeter with an internal noise of the acquisition system that, in the frequency band of interest, must be much lower than the recorded noise. Seismometers can be broadband (or low-frequency seismometers) or short-period (or higher natural frequency) models. The former are recommended for sites with deeper impedance contrasts, whereas the short-period for shallower impedance contrast sites are suitable. Nevertheless, according to some authors (**Castellaro and Mulargia 2009a**; **Chatelain and Guillier 2013**; **Molnar et al. 2020**) low-frequency peaks can be identified by short-period seismometers. However, **Strollo et al., 2008** suggest that 1-Hz short period electromagnetic sensors (SPESs) are preferred instead of 2- and 4.5-Hz SPESs when the frequency band of interest is only in the range 0.1 - 1 Hz. **Molnar et al. 2022** in their review show examples in which the average HVNSR obtained from simultaneous microtremor recordings with both high-sensitivity and broadband short-period seismometers, which are immediately adjacent, have almost identical H/V curves and peak frequency values. However, the authors point out that, at a site with low seismic noise, a very low f_0 (resonance frequency) (0.2-0.3 Hz) can be lost in the internal noise of a low-sensitivity short-period seismometer, regardless of the recording time duration. Other published comparisons between broadband and short-period seismometers can be found in **Castellaro and Mulargia (2009b)** and **Strollo et al. (2008)**.

Figure 2.14 shows a graph made by **Foti et al. (2018)** who illustrated different setups for the installation of seismometers that could mitigate climatic factors. The use of a coverage (e.g., a bucket) can help shading and keeping the seismometer cool, but on the other hand can lead to transmitting wind or rain droplet vibration into the ground due to its surface area; therefore, to avoid such kind of disturbances, the technician can wait for a less windy day or use of an umbrella with fewer contact points (**Molnar et al., 2022**). Some authors (**Castellaro and Mulargia 2009b**; **Piña-Flores et al. 2020**) have verified that measurements on hard road pavements and/or pedestrian pavements resting on softer soils create a velocity inversion in the subsoil that leads to a de-amplification, i.e., a reduction of the HVNSR curve below unity at frequencies above f_0, although it does not affect f_0 (**Chatelain et al. 2008**). A de-amplification of the HVNSR curve by recording on natural terrain is indicative of natural velocity inversions or low velocity zones (**Molnar et al., 2022**). Therefore, **Chatelain et al. 2008** suggested avoiding, or minimising, any other factors that degrade sensor-soil coupling or violate the requirement of free-field soil conditions.

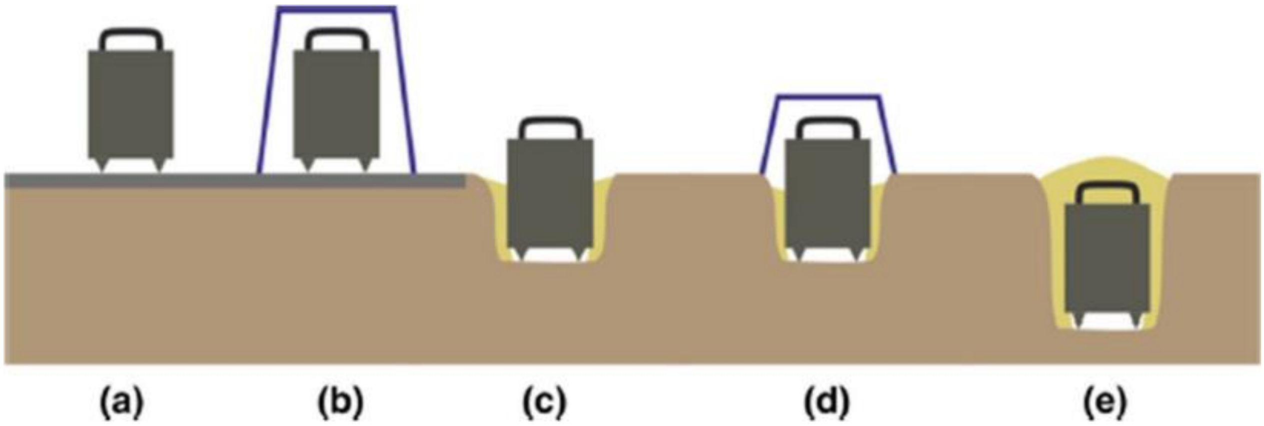

Fig. 2. 10 Different deployments for single station ambient noise measurement: (a) least desirable; (b) without infill and covered; (c) with infill; (d) partial infill and covered; (e) most desirable, but rare with infill (Figure re-drawn from ***Foti et al., 2018****)*

Sensor installation involves levelling the sensor on the surface of the measuring point, choosing a measuring point that guarantees ground-free-field conditions, and perfect coupling with the earth's surface. Therefore, vegetation must be removed and the instrument base or feet must be firmly embedded in the ground (Figure 2.16). The sensor must be protected from temperature fluctuations, wind, cable vibration problems or vibration from rain (**Mucciarelli, et al. 2005**; **Chatelain et al., 2008**). Another general criterion is to move the measurement point away, where possible, by a distance at least equal to the height of the nearest structure

(Figure 2.15), as the structure's resonance frequency may show up in the HVNSR curve (**Chatelain et al. 2008**; **Castellaro and Mulargia 2010**). **Molnar et al., 2022** provided a comprehensive table (adapted from **Koller et al., 2004**) of the acquisition parameters and their influence on the processed HVNSR.

Fig. 2.15 Different criterion for single station ambient noise measurement: (left) removing vegetation and firm embedding of the instrument's feet in the ground before measurement protecting it from wind; (centre) levelling of the sensor on the surface of the measuring point, especially in steep topographical conditions; (right) moving the measurement point away by a distance at least equal to the height of the nearest structure (trees and light poles in photo) to trying to follow the requirement of free-field soil condition

Mucciarelli (1998) and **Bard (1999)** reported on experimental procedures for recording noise and techniques for analysing the data. **Mucciarelli and Gallipoli (2001)**, **SESAME (2005)** and **Picozzi et al. (2005b)** proposed several statistical and experimental protocols for the H/V spectral ratio method. These techniques, although different, allow reliable H/V curves to be obtained and the fundamental frequency f_0 to be estimated. **Picozzi et al. (2005b)** analysed the statistical properties of the spectral H/V ratio in order to obtain optimal data processing strategies and to identify possible artefacts. Some authors have shown that in the presence of a nearby source that produces a high level of noise, the low-frequency branch of the HVNSR curve has a greater uncertainty (**Castellaro and Mulargia, 2009b**); on the other hand, **Lunedei and Albarello (2010)** confirmed that the presence of sources affects both sides of the HVNSR curve, i.e., at frequencies both lower and higher than f_0. **Mihaylov et al. 2016** considered it plausible that seismic waves from sources closer to the measurement site propagate only in the more superficial layers, thus obscuring the peaks due to the deeper structure.

In the general, considering the processing steps involved in the calculation of an HVNSR curve, it is important to take some significant parameters into account: window length, window selection, spectral smoothing, and horizontal mean spectrum. The window length should be at least 10 times the fundamental period (T0 = 1/f0) estimated by **SESAME (2004)**. **Picozzi et al. 2005** showed that a stable HVNSR is achieved with 20 or more-time windows, assuming that 15-20 windows are needed to achieve Gaussian statistics. **Molnar et al., 2022** used time windows of 30 to 60 seconds with a minimum of 20-50 windows to ensure statistical stability. The choice of window length is related to finding a compromise between spectral resolution and statistically significant results. It is therefore advisable to record a minimum of 15 minutes of microtremor data. Therefore, sites with very low resonance frequencies may require a total recording duration of one hour or more in order to have sufficient time windows for reliable processing. Non-stationary, or spurious, time windows, such as signal chunks with very high amplitudes at low frequencies (e.g., wind effects), or with low amplitudes (e.g., equipment problems), or with a wide frequency band of high amplitude noise (such as a saturated signal from a nearby noise source) can be removed through anti-triggering algorithms (**Mihaylov et al., 2016**; **Vallianatos and Hloupis, 2009**). However, some authors (e.g., **Mucciarelli and Gallipoli 2004**) suggest that transient noise windows should not be removed because with the information they contain, they can help to improve the agreement between HVNSR and EHVSR by introducing more body wave content (e.g., **Satoh et al. 2001**). **Parolai and Galiana-Merino 2006** argued that when a sufficiently high number of windows is used, the transients have little influence on the calculated average HVNSR. **Parolai et al., 2009** indicated that transient signals may amplify H/V ratio at low frequencies and are unable to degrade fundamental frequency estimates. The horizontal average spectrum can be defined by considering the arithmetic mean, geometric mean, vector mean, vector sum, quadratic mean or maximum horizontal value (**Albarello and Lunedei, 2013**). However, except for the maximum horizontal value procedure, bias is produced by all averaging procedures (**Albarello and Lunedei, 2013**); therefore, a monotonic and rapid reduction of bias can be achieved by increasing the number of time windows considered. **Molnar et al. (2022)** recommend the use of geometric averaging (**SESAME 2004; Cox et al., 2020**).

Konno and Ohmachi (1998) developed the most widely used frequency-sampling logarithmic smoothing procedure avoiding distortions in the peak amplitude independent of frequency with a filter coefficient b value of 40, where a low b value produces a very smooth curve and very uniform spectra, while a high b value produces more irregular spectra. For example, **Konno and Omachi (1998)** used b = 20 in their original work; however, the results of their paper clearly show that using a b value of less than 30 tends to distort HVSR peaks.

A key role is played by the selection of the minimum frequency peak (f0) of the HVNSR curve, which, although not among the important parameters involved in the HVNSR calculation, represents the output of the HVNSR calculation. f0 is interpreted as the fundamental frequency of the site and is associated with A0, which in turn is only used as a proxy for the strength of the impedance contrast and not as a direct measure of the amplification of the soil-rock site. Prior to interpretation, the practitioner must ensure that each peak frequency (f#) has a natural stratigraphic origin. One type of verification is to reprocess the HVNSR with reduced smoothing. In fact, if the peak is of anthropogenic origin, it should become sharper; this would not be the case for a peak of stratigraphic origin (**SESAME 2004**).

For example, Figure 2.17 shows the mean HV curves and spectral amplitudes in the three components (NS, EW, Z) of two measurements carried out at the same site a few days apart. The HV1 measurement is characterised by a pronounced anthropic peak at f = 1 Hz, which emerges by reducing smoothing, and which remains evident despite the application of a higher **Konno and Ohmachi (1998)** smoothing with b = 40 and width of the mobile window centred at each frequency (Hz) equal to 10% (Figure 2.16b1,b2). For better interpretation, the HV2 measurement was repeated a few days later and indeed the anthropic peak does not appear.

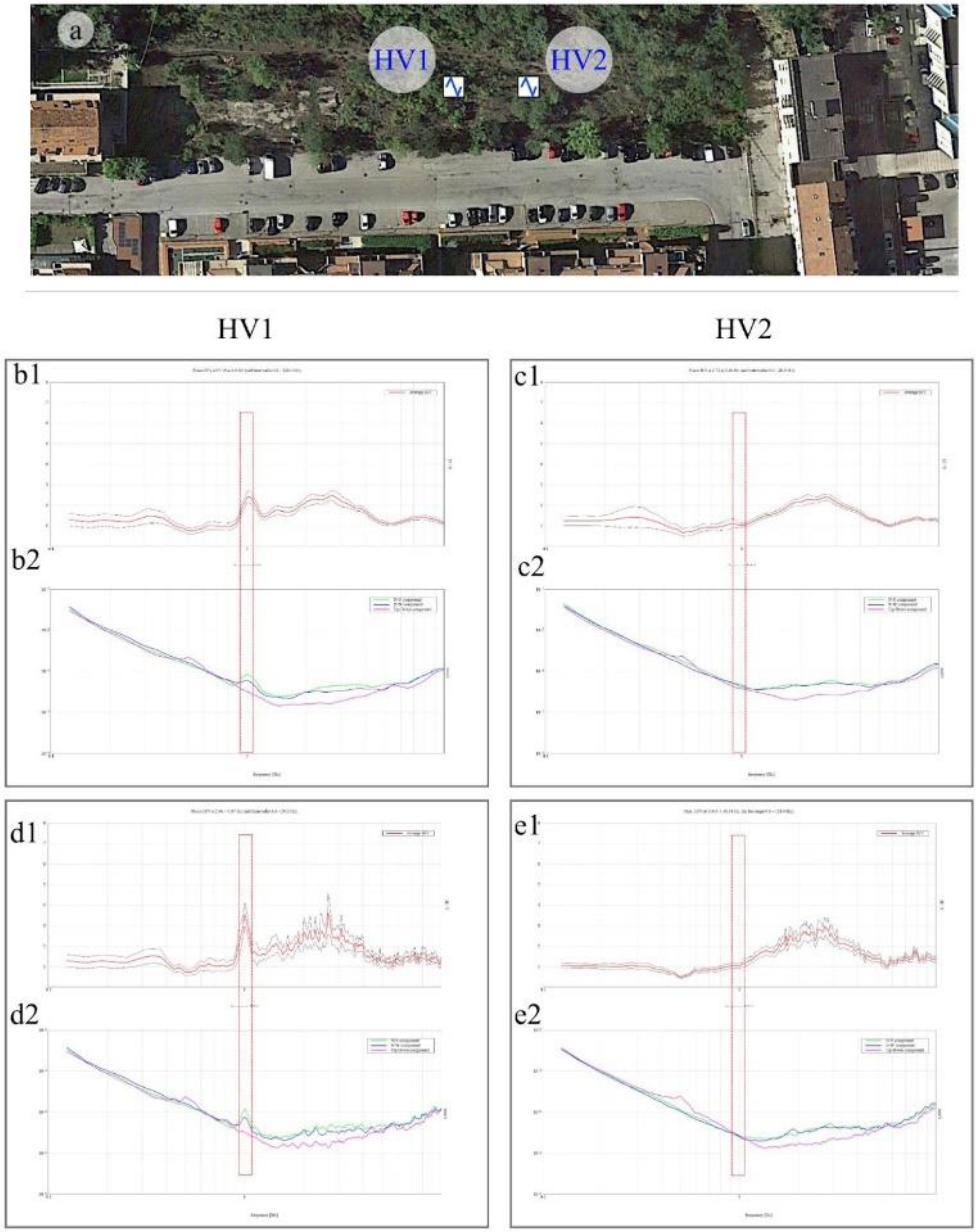

Fig. 2. 16 Confronto tra due HVNSR di rumore ambientale registrato due volte in due giorni diversi per migliorare l'interpretazione resa difficoltosa dalla presenza di un picco antropico. (a) HV1 and HV2 measurements from the top view; average HVNSR (b1,d1) and amplitude spectra (b2,d2) for HV1; average HVNSR (c1,e1) and amplitude spectra (c2,e2) for HV2 smoothed with pairs of filter coefficient b and smoothing percentage values of [b = 40; 1% for b1,b2,c1,c2] and [b = 40; 10% for d1,d2,e1,e2]. Red dotted rectangle indicates f = 1 Hz.

A more qualitative approach is to interpret the HVNSR curve together with the individual Fourier spectral curves of all three components. The horizontal spectra should show a local maximum if the dominant wave type is SH waves. The same characteristic indicates Love waves (**Molnar et al., 2022**). HVNSR peaks result from the amplified amplitudes of the horizontal components. If Rayleigh waves dominate the wave field, the vertical component of the spectrum is reduced to the resonance frequency and in this case, the spectral signature of the H/V peaks is found to be eye-shaped with the horizontal components higher than the vertical ones (**Castellaro and Mulargia 2009b**). These authors indicate that "this eye-shape is always the clear signature of a H/V peak with stratigraphic origin". Figure 2.17 shows the characteristic eye-shape of a peak caused by Rayleigh waves and of stratigraphic origin.

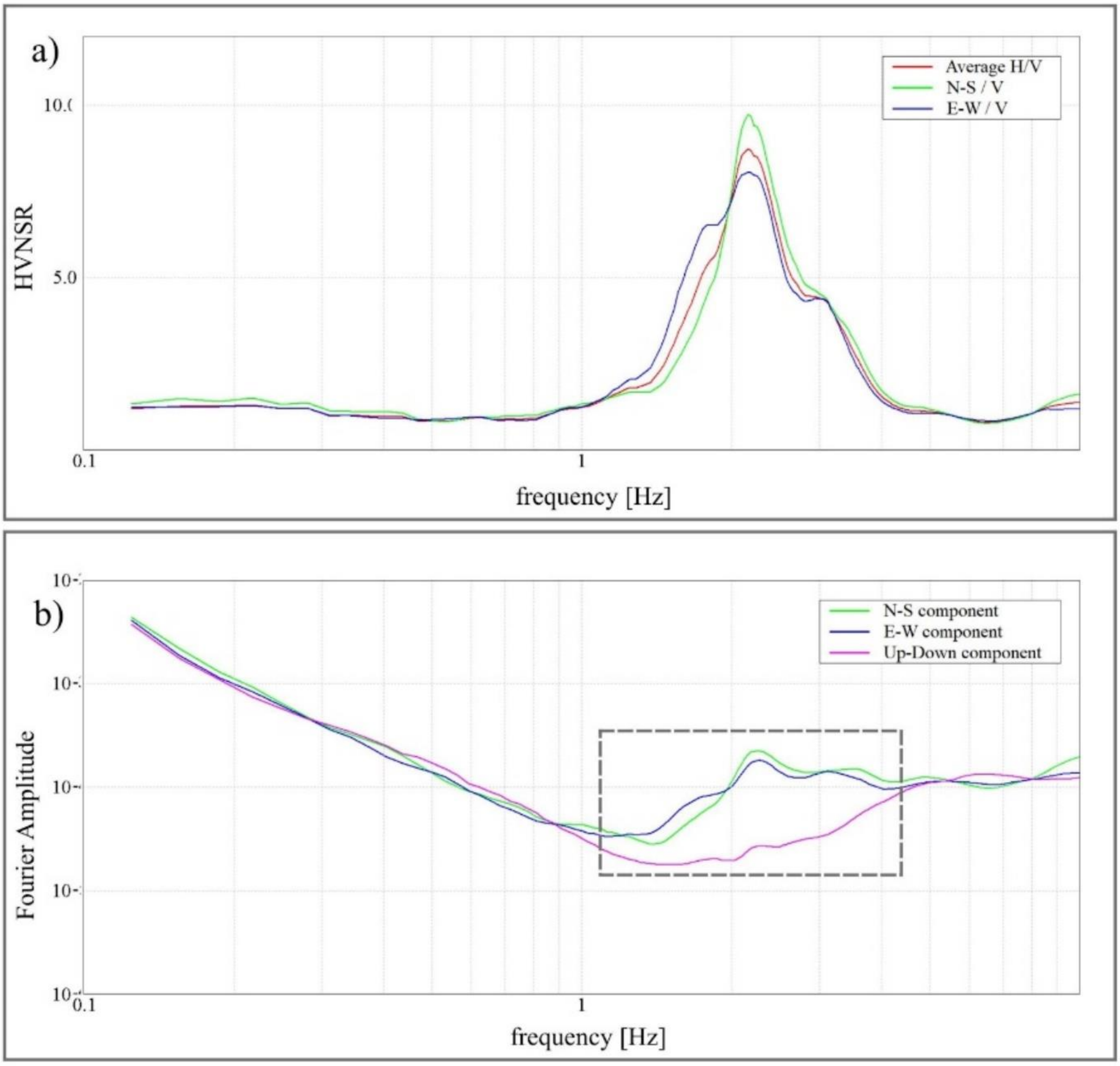

Fig. 2. 17(a) Average HVNSR (red line),North-SouthVNSR (green line), East-WestVNSR (blue line); (b) Corresponding individual time-averaged Fourier spectrum of each component with typical eye-shape (within dark gray box).

The case of signals produced by industrial facilities is different, as these types of signals can travel a great distance from the source and can influence microtremor data even at distances of several kilometres from the source, especially at low frequencies (wavelengths) (**Bokelmann and Baisch 1999**; **Cornou et al. 2004**).

The **SESAME guidelines (2004)** on HVNSR provide three criteria for the reliability of results of HVNSR curve identification (Figure 2.18).

Therefore, in addition to adjusting the processing parameters, the reliability of the HVNSR curve can be improved by following the criteria suggested by the **SESAME (2004)** guidelines. A more conservative scheme than the SESAME guidelines for classifying the reliability of results was proposed by **Albarello et al. (2011)**.

The authors defined a classification scheme consisting of three classes (A, B, C) to provide an immediate indication of the quality, trustworthy (A), suspicious (B), bad (C), of the individual measures and to avoid misinterpretations of the results. This scheme was used to determine, for example, 193 usable HVNSR curves from 223 Italian strong-motion stations (**Puglia et al. 2011**).

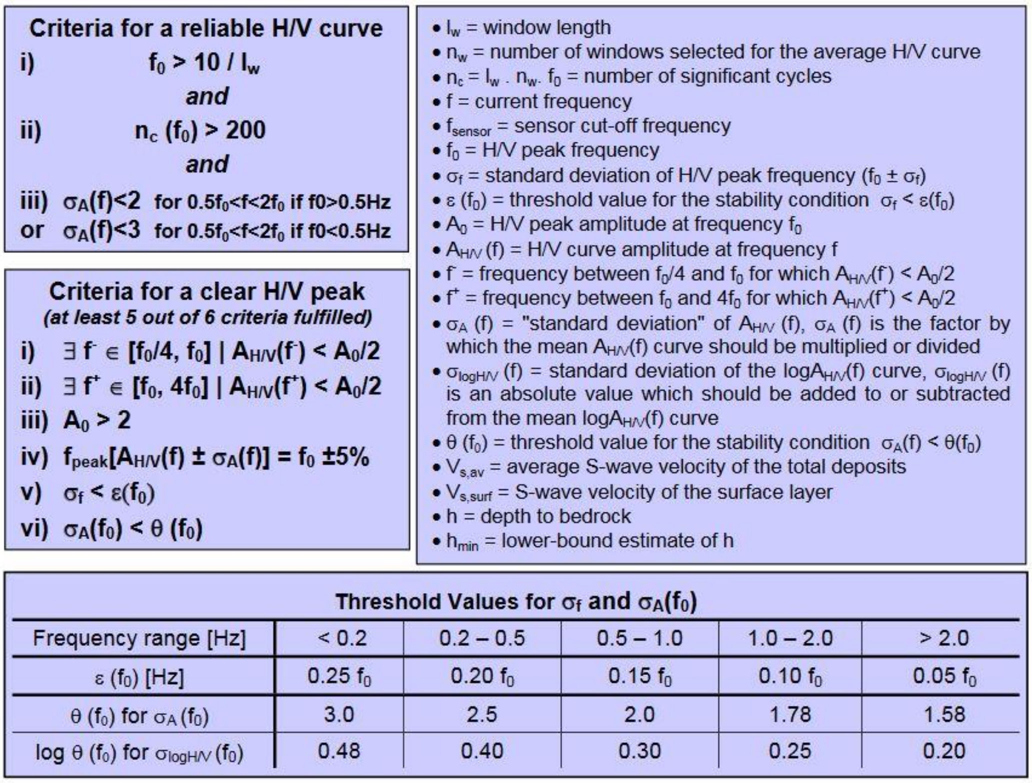

Criteria for a reliable H/V curve

i) $f_0 > 10 / l_w$

and

ii) $n_c(f_0) > 200$

and

iii) $\sigma_A(f)<2$ for $0.5f_0<f<2f_0$ if $f0>0.5Hz$

or $\sigma_A(f)<3$ for $0.5f_0<f<2f_0$ if $f0<0.5Hz$

Criteria for a clear H/V peak

(at least 5 out of 6 criteria fulfilled)

i) $\exists f^- \in [f_0/4, f_0] \mid A_{H/V}(f^-) < A_0/2$

ii) $\exists f^+ \in [f_0, 4f_0] \mid A_{H/V}(f^+) < A_0/2$

iii) $A_0 > 2$

iv) $f_{peak}[A_{H/V}(f) \pm \sigma_A(f)] = f_0 \pm 5\%$

v) $\sigma_f < \varepsilon(f_0)$

vi) $\sigma_A(f_0) < \theta(f_0)$

- l_w = window length
- n_w = number of windows selected for the average H/V curve
- $n_c = l_w \cdot n_w \cdot f_0$ = number of significant cycles
- f = current frequency
- f_{sensor} = sensor cut-off frequency
- f_0 = H/V peak frequency
- σ_f = standard deviation of H/V peak frequency ($f_0 \pm \sigma_f$)
- $\varepsilon(f_0)$ = threshold value for the stability condition $\sigma_f < \varepsilon(f_0)$
- A_0 = H/V peak amplitude at frequency f_0
- $A_{H/V}(f)$ = H/V curve amplitude at frequency f
- f^- = frequency between $f_0/4$ and f_0 for which $A_{H/V}(f^-) < A_0/2$
- f^+ = frequency between f_0 and $4f_0$ for which $A_{H/V}(f^+) < A_0/2$
- $\sigma_A(f)$ = "standard deviation" of $A_{H/V}(f)$, $\sigma_A(f)$ is the factor by which the mean $A_{H/V}(f)$ curve should be multiplied or divided
- $\sigma_{logH/V}(f)$ = standard deviation of the $\log A_{H/V}(f)$ curve, $\sigma_{logH/V}(f)$ is an absolute value which should be added to or subtracted from the mean $\log A_{H/V}(f)$ curve
- $\theta(f_0)$ = threshold value for the stability condition $\sigma_A(f) < \theta(f_0)$
- $V_{s,av}$ = average S-wave velocity of the total deposits
- $V_{s,surf}$ = S-wave velocity of the surface layer
- h = depth to bedrock
- h_{min} = lower-bound estimate of h

Threshold Values for σ_f and $\sigma_A(f_0)$

Frequency range [Hz]	< 0.2	0.2 – 0.5	0.5 – 1.0	1.0 – 2.0	> 2.0
$\varepsilon(f_0)$ [Hz]	$0.25 f_0$	$0.20 f_0$	$0.15 f_0$	$0.10 f_0$	$0.05 f_0$
$\theta(f_0)$ for $\sigma_A(f_0)$	3.0	2.5	2.0	1.78	1.58
$\log \theta(f_0)$ for $\sigma_{logH/V}(f_0)$	0.48	0.40	0.30	0.25	0.20

*Fig. 2. 18 Three criteria for a reliable H/V curve and six criteria for a clear H/V peak are presented in the **SESAME (2004)** guidelines.*

Regarding 1D and 2D/3D stratigraphic conditions, the evaluation of effects related to them is crucial to avoid stratigraphic misinterpretations. **Molnar et al., 2022** do not recommend selecting f0 from plateau curves since there is no standardised procedure to select f0 for broad peaks. In general, irregularly shaped peaks and large differences between orthogonal HVNSRs are indicative of lateral heterogeneity. In fact, when the conditions for lateral homogeneity are not fulfilled by the subsurface geology, the information on the geometry and mechanical properties of the subsurface contained in the spectra of the individual components can lead to misinterpretation if the two components are combined (**Sgattoni and Castellaro 2020**). **Molnar et al., 2022** provided a concise demonstration of the variability of HVNSRs for 1D and 2D/3D site conditions. The authors showed two different sets of HVNSRs obtained at two sites characterised by different topographic conditions 1D (flat) and 2D/3D (sloping) respectively. In the first case, the f0 is consistent between all tested locations (~1.5 Hz), indicating homogeneous 1D site conditions; whereas in the second case, the authors showed the greatest variability between HVNSRs obtained in the same way, presenting broader peaks (more narrow resonance frequencies), thus indicating 2D/3D effects. **Molnar et al., 2022** through a cluster analysis determined up to eight subsets of variable HVNSRs, confirming a highly variable spatial dependence of HVNSRs across the study site. Therefore, they deemed further analysis of the directional HVNSRs necessary to decipher 2D/3D effects.

With regard to studies performed at a larger scale, such as regional microzonation studies (e.g., **Roca and Oliveira 2001**; **Moscatelli et al. 2020**), or urban-scale studies (**Gallipoli et al., 2019**), measurements should first be obtained with a wider spacing and then reduced to a larger scale where rapid variations in f0 are observed. The interpretation of the spatial variability of f0 can serve as a proxy for the geological variability of the site (**Gallipoli et al., 2019**).

2.2.2.4 Analysis, procedure, and instrumentation for the application of the HVNSR method in this thesis work

Mucciarelli, 1998 and **Bard, 1999** suggested guidelines to facilitate the correct analysis of microtremor recordings. Later, the **SESAME project** proposed an analysis protocol. The different approaches are, however, aimed at achieving the same goal: having stable HVSR curves capable of providing reliable estimates of the resonance frequency. The results of each analysis presented in this thesis were obtained using the GRILLA software, which accompanies the TROMINO digital tromograph (see below). The analysis procedure adopted will be briefly explained in the following:

- for the frequency range of engineering interest (usually 0.1-10 Hz) the length of the windows extracted from the recordings varies from 20 to 60 seconds; this allows a good compromise between the frequency resolution of the H/V curves and a recording duration that is not excessive;
- seismic noise recordings require preliminary analysis [elimination of linear trends (detrends) and tapering] to ensure the validity of the stationarity assumption before using the Fast Fourier Transform (FFT) to calculate spectral amplitudes (**Cooley and Tukey, 1965**);
- the horizontal spectral amplitudes of the microtremors are combined with the estimates of H/V values both using geometric average of the horizontal components over the vertical one

  $$\frac{H}{V}(f) = \frac{\sqrt{A_{NS}(f)A_{EW}(f)}}{A_Z(f)} \qquad 2.12$$

  or the RMS (Root Mean Square) average of the horizontal components over the vertical one

  $$\frac{H}{V}(f) = \frac{\frac{\sqrt{[A_{NS}^2(f)A_{EW}^2(f)]}}{2}}{A_Z(f)} \qquad 2.13$$

  where A_{NS} and A_{EW} are the smoothed spectra, in terms of amplitude, of the horizontal (North-South and East-West) components and A_z is the smoothed spectrum of the vertical component;
- the number of required windows, and thus the duration of the recording, must be long enough to ensure statistical stability of the signal (12 and 14 minutes of recording have been selected in this thesis work for measurements on soil and buildings respectively). The large number of samplings performed with this technique allows estimating a 95% confidence interval on the mean amplitude H/V (Figure 2.19), a value that is representative of the experimental uncertainty on f_0.

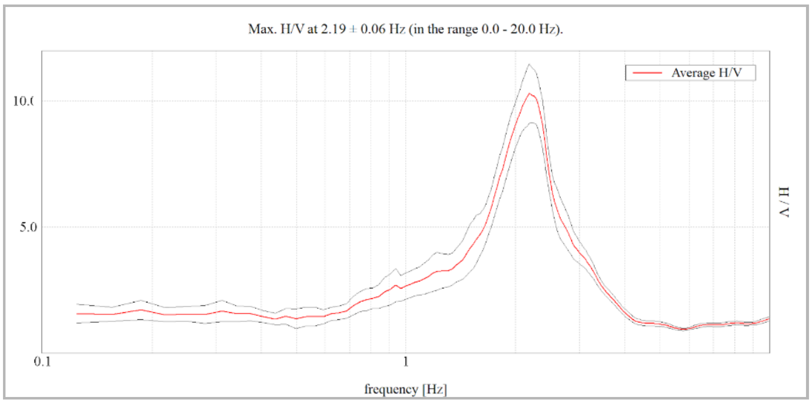

Fig. 2. 19 Example of the experimental mean H/V curve (red line) and 95% confidence interval from the mean value (black lines).

- the smoothing of the spectrum of each component is a fundamental operation for the analysis (**Konno and Ohmachi, 1998**). It allows the stabilisation of the H/V curves avoiding the presence of spurious peaks due to seismic, instrumental, and numerical noise as can be seen in Figure 2.20. Two smoothing percentage values, which is the width of the mobile window centred at each frequency (Hz) used to smooth, have been selected. The larger the percentage of smoothing is, smoother are the spectra. The **Konno and Omachi** window exponent b has been specified equal to 40. The larger b is, less smoothed are the spectra;

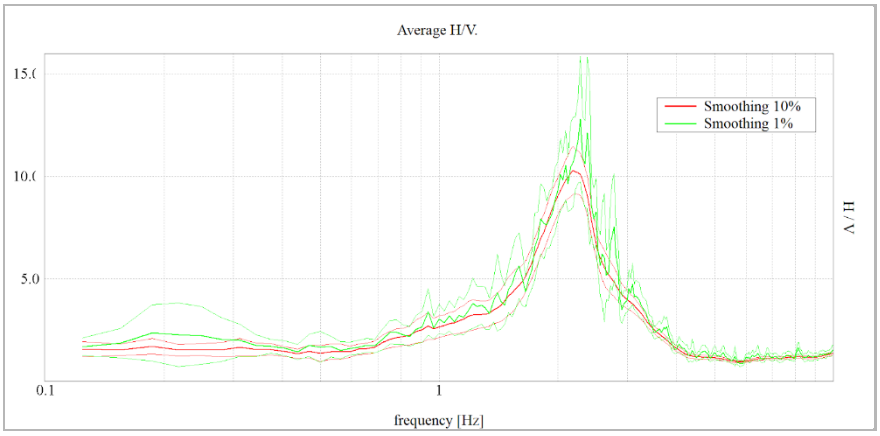

Fig. 2. 20 experimental H/V curve after smoothing with a triangular window of amplitude 10% of the mean value (red line) and 1% (green line). Clearer palettes show the 95% confidence intervals.

- It was noted in the previous chapter that the assumption of stationarity in time is fundamental to all methods of analysing microtremors, so strong transient phenomena near the sensors can lead to incorrect estimates of the H/V ratio. Since the stability of the frequency of the H/V maximum is fundamental to a correct estimation of both f0 and therefore the thickness of the sedimentary cover, using a maximum due to a transient signal source can lead to an incorrect estimate of the geological structure of the area analysed. In order to identify and exclude possible H/V peaks that are not representative of geological structure, the stationarity of the spectral ratio of the recording is analysed (Figure 2.21a);
- Furthermore, through a directional analysis of the H/V curves, it is possible to highlight the presence of intense sources during data acquisition. To perform this analysis, the horizontal components of the motion are rotated in a range of 0°/180° and combined to calculate the H/V ratio at regular intervals (Figure 2.21b).

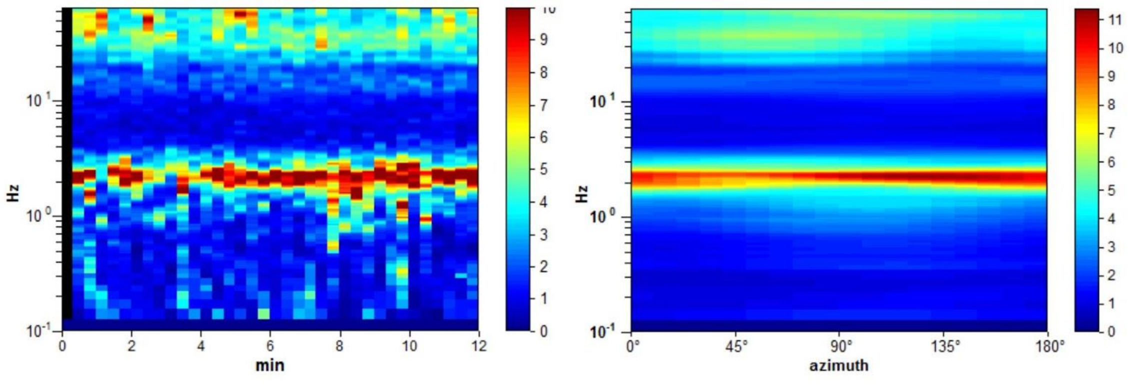

a) b)

Fig. 2.21 (a) Contour plot of the calculated H/V curves for each window. The colour palette scale on the right indicates the H/V amplitude; (b) contour plot of the H/V curves obtained from the rotation and combination of the horizontal components of motion. The colour palette scale on the right indicates the amplitude H/V

The microtremor recordings used and processed with HVNSR method in this thesis were carried out with the TROMINO digital tromograph (technical specifications at www.tromino.it), an instrument specially designed for this purpose. It is a highly portable instrument, without external cables, compact (dimensions: 10x7x14 cm, weight: 1 kg), consisting of three orthogonal electrodynamic sensors (velocimeters), powered by two 1.5 V batteries, and equipped with an internal GPS antenna (Figure 2.22). The extreme portability of this instrument allows measurements to be taken in all types of terrain and slopes, in sites that are unreachable with heavy, vehicle-mounted instruments. One operator is sufficient to make all the recordings and the speed of installation and recording (a few minutes for installation, and the dime-duration for complete signal acquisition) allows a large number of measurements to be made in a short time and at a very low cost.

Fig. 2.22 TROMINO digital tomograph used in recording.

2.3 Seismic data analysis techniques for structural characterization

The response of structures and civil engineering infrastructure under dynamic conditions is often evaluated with numerical models. The high complexity of numerical models does not guarantee the structural characterisation and fully realistic description of the structure's behaviour. Therefore, experimental techniques are spreading with great success. The latter approaches allow to derive the primary modal parameters of structures and infrastructures with expeditive methods, non-invasive, and low-cost sensors carrying out static tests. These methods consist of determining the structure’s main modal parameters in a linear and non-linear domain by using both earthquake and ambient noise data (wind, microtremors, microseisms and other types of local noise) allowing the modal characteristics of the structure to be obtained with simple, lightweight, and non-invasive equipment. The same tests can be conducted on damaged buildings, making it possible to estimate the possible variations in structural characteristics as a result of the damage. Using different methods of analysis has the double advantage of (1) evaluating the behaviour of a structure/infrastructure at different scales and (2) improve/facilitate the interpretation of the obtained results.

There are many applications of HVNSR technique on seismic noise recorded in civil engineering structures in the literature, such as: buildings, aimed at characterising the main modal characteristics of the structure, and the fundamental frequencies of oscillation related to the fundamental vibration modes. For example, an alternative way to estimate the fundamental frequency of a building was introduced by **Mucciarelli et al. (2001)**. The proposed methodology is essentially based on microtremor measurements conducted at each floor of a building and processed according to **Nakamura's (2000)** technique, according to which the response function at a floor can be obtained by carrying out the ratio between the Fourier spectra of the horizontal and vertical components at the same point under the assumption that the vertical component does not change during propagation inside the building. Nakamura himself introduced this technique in order to assess the amplification factor between the ground and the various floors of a building. With this method, since white noise is used as initial input, the influence of the source can be excluded.

Gallipoli et al., 2004, made a series of ambient noise measurements on buildings and civil structures to evaluate the reliability of fundamental frequency determinations by means of observations of horizontal-to-vertical spectral ratios of microtremors. **Navarro et al., 2007** studied the dynamic behaviour of RC building structures in Adra town (south-eastern Spain) by using microtremor measurements. **Oliveira** and **Navarro, 2009** estimated the fundamental periods of vibration of circa 200 RC buildings in Portugal from in-situ experimental HVNSR technique; **Gallipoli et al., 2009** estimated the fundamental frequencies of over 60 existing buildings in Italy analysing ambient vibration measurements by means of HVNSR; **Gosar et al., 2012** determined the fundamental frequencies of about 60 masonry buildings in five Slovenian towns by microtremor excitation; **Ditommaso et al., 2013** estimated through HVNSR technique the frequencies of 68 buildings with different characteristics, such as age, height and damage level after the 2009 L’Aquila earthquake using ambient noise recordings by means of a portable three-directional tromometer; **Stanko et al, 2017** applied the HVNSR method for determination of dynamic building parameters, namely fundamental frequencies from ambient noise measurements inside the buildings in Varaždin city (North Croatia).

Imposa et al., 2018 investigated the modal properties of a historic monastery located in downtown Catania (Southern Italy) computing the spectral ratios between the ambient vibrations Fourier spectrum of horizontal components recorded on the various building floors and the same components as sampled in the free field. The authors, among other conclusions, emphasised that the comparison between the eigenfrequencies of the buildings and the resonance frequencies of the foundation soil pointed out the existence of potential soil-structure resonance during a seismic event. The authors evaluated that the latter effect can explain the moderate damage observed in the San Nicolò l’Arena church and in the eastern cloister as a consequence of the M5.7 earthquake that struck southeastern Sicily in 1990.

Gallipoli et al., 2023 performed ambient seismic noise measurements elaborated by using the HVNSR method on hundreds of buildings in Italy classified by building type, age of construction, etc., publishing a database of all the data collected and producing T-H period-height relationship for both different building types and different lithologies of foundation soils.

Another technique belonging to the category of experimental methods to characterise the modal parameters of a civil engineering structure (probably giving better results than the HVNSR technique), is the reference site method, the Standard Spectral Ratio, SSR.

For example, **Parolai et al., 2005** calculated H/V ratio and the spectral ratio between corresponding components of the ambient seismic noise recorded simultaneously inside the buildings of the Holweide Hospital in the City of Cologne (Germany) and at a reference station (RSM). The authors highlighted that while HVNSR method could be simpler and faster because of less equipment involved, the SSR method has the advantage of producing more stable results and deleting automatically the influence of the soft soil, which might influence/dirty some eigenfrequencies of the structure. **Gallipoli et al., 2010** estimated the fundamental frequencies of about 250 existing buildings in Europe analysing ambient vibration measurements applying different spectral techniques including SSR and HVNSR.

The scientific community's commitment to study site effects that could be triggered by seismic events in order to safeguard the built heritage of the urban environment through geophysical techniques aimed at studying soil-structure resonance effects, as emerges from previous literature, has a long history. In recent years, there has been a growing awareness of the need to monitor the health of structures not only during emergencies, but also, and especially, in peacetime, of other types of structure that play a strategic role in civil society, namely civil engineering infrastructure like bridges. Geophysical techniques can be applied to characterise the static and dynamic behaviour of critical infrastructures like bridges that can be considered the backbone of the road network. Unfortunately, history teaches us that the loss of load-bearing capacity of strategic infrastructures as bridges can cause catastrophic events. The strategies to avoid any potential accident are prevention and monitoring, in this context of which, structural health monitoring plays a key role. In this thesis work I made experimental investigations on two bridges by analysing seismic ambient noise applying two techniques: an operational modal analysis and a seismic interferometric technique, namely the Frequency Domain Decomposition method (FDD) and ambient noise deconvolution interferometry (ANDI) respectively. **Bindi et al. (2015)** and **Petrovic et al. (2015)** applied them to an 8-story RC hospital in Thessaloniki (Greece) and on eight buildings of different construction types in the cities of Bishkek (Kyrgyzstan) and Dushanbe (Tajikistan), respectively; **Garcia-Macias et al. (2019)** and **Lacanna et al. (2019)**, tested them for the dynamic identification of heritage structures; **Todorovska et al. (2020)** implemented a system in a 48-story skyscraper located in Kunming, China. The potentiality of ANDI for SHM of other structural bridge typologies has been explored by e.g. **Salvermoser et al. (2015)**, **Jian et al. (2020)**, **Garcia-Macias and Ubertini (2021)**. **Salvermoser et al. (2015)** carried out structural monitoring of a highway bridge using ambient noise recordings of road traffic. **Jian et al. (2020)** studied the response of the Bay Bridge in California using multichannel deconvolution of both earthquake and ambient noise recordings. **Garcia-Macias and Ubertini (2021)** combined ANDI and OMA techniques for the dynamic characterization of the Chiaravalle Viaduct (Marche Region). Therefore, the joint application of ambient noise deconvolution interferometry and frequency domain decomposition to civil infrastructures like bridges is not completely new but will probably gain more and more importance in the future.

The objective of this part of the thesis work is to advance the body of knowledge of the joint application of HVNSR, SSR, Ambient noise deconvolution Interferometry ANDI (see Section 2.5.4) and Frequency Domain Decomposition, FDD (see section 2.5.3) by deepening the experimental investigations and searching for an effective way that returns the modal parameters of the infrastructures in terms of eigenfrequencies and mode shapes, moving from the global scale to the local scale in an effective way in terms of propagation velocities of the material of which the infrastructures under study are made, combining vibrational approaches and waveforms. In this regards, four seismic methods were used in this thesis work for the static and dynamic characterization of structures and some infrastructures: the horizontal to vertical noise spectral ratio (HVNSR), the standard spectral ratio (SSR) on earthquake data, an operational modal analysis (OMA) on seismic noise, that is the Frequency Domain Decomposition technique (FDD), and a seismic interferometric method by means of the ambient noise deconvolution interferometry (ANDI) method.

2.3.1 HVNSR method: microtremor recording, analysis and interpretation

In order to estimate the main modal characteristics of a building and/or infrastructure (fundamental vibration frequencies, equivalent damping and mode shapes), earthquake-induced vibrations and ambient noise can be used as input signals. Although the earthquake signal makes it possible to discern the characteristics of the structure in various displacement ranges in greater detail, the time duration of the acquisitions are longer and more costly. In contrast, ambient noise has the advantage of being an ever-present source in nature, generated by human and natural activities, is ubiquitous and composed of waves in a frequency range of 0.05 Hz-100 Hz (**Gutenberg, 1958**). This signal can be measured both on the building and its foundation soil by installing one or more seismometers rapidly and non-invasively. The configuration of the sensor installation on the building depends on the desired degree of precision in the estimation of the primary modal parameters (**Gallipoli et al., 2010**; **Castellaro, 2016**): (i) a single measurement on the top floor of the building could be sufficient to estimate the fundamental frequencies and equivalent damping, while (ii) to achieve a discrete knowledge of the eigenmodes of vibration it is sufficient to record ambient noise simultaneously on the lowest floor or in the free field, at an intermediate floor, and on the highest floor. The best solution to estimate complete mode shapes is to make synchronous acquisitions of ambient noise at each floor and in the free field using a reference station (see section 2.3.2). In addition, simultaneous measurements near the centre of masses and in the corner of the top floor are necessary to assess possible rocking modes. Considering the complexity of a building, being made up of structural and non-structural elements, in order to correctly estimate the main modal properties, it is necessary to position the sensors near the beam-pillar nodes in reinforced concrete buildings and at the load-bearing walls for masonry buildings. Figure 2.23 shows two examples of application of HVNSR method to the single station ambient noise measurements acquired in two buildings in reinforced concrete building and masonry respectively. In the reinforced concrete building the sensor was located near a beam column, oriented along the direction of maximum length of building (Figure 2.23 a2). For the masonry building the sensor was located on the edge of the roof in line with the load-bearing wall (Figure 2.23 b2). When applying the HVNSR technique to noise recordings within a civil engineering structure, in order to estimate the eigenmode frequencies, it is better to study the spectral amplitudes of the horizontal and vertical components by searching for the frequencies at which the energy rates are highest, i.e., the spectral amplitudes have peaks. For example, the NH/V curve and the FAS in N-S direction (Figure 2.23 a3, a4) exhibit a peak at the same frequency value 4.2 Hz for the RC building. While the 1st mode of vibration of the masonry building is visible only on the FAS curve at 2.6 Hz in E-W horizontal direction (Figure 2.23 b4).

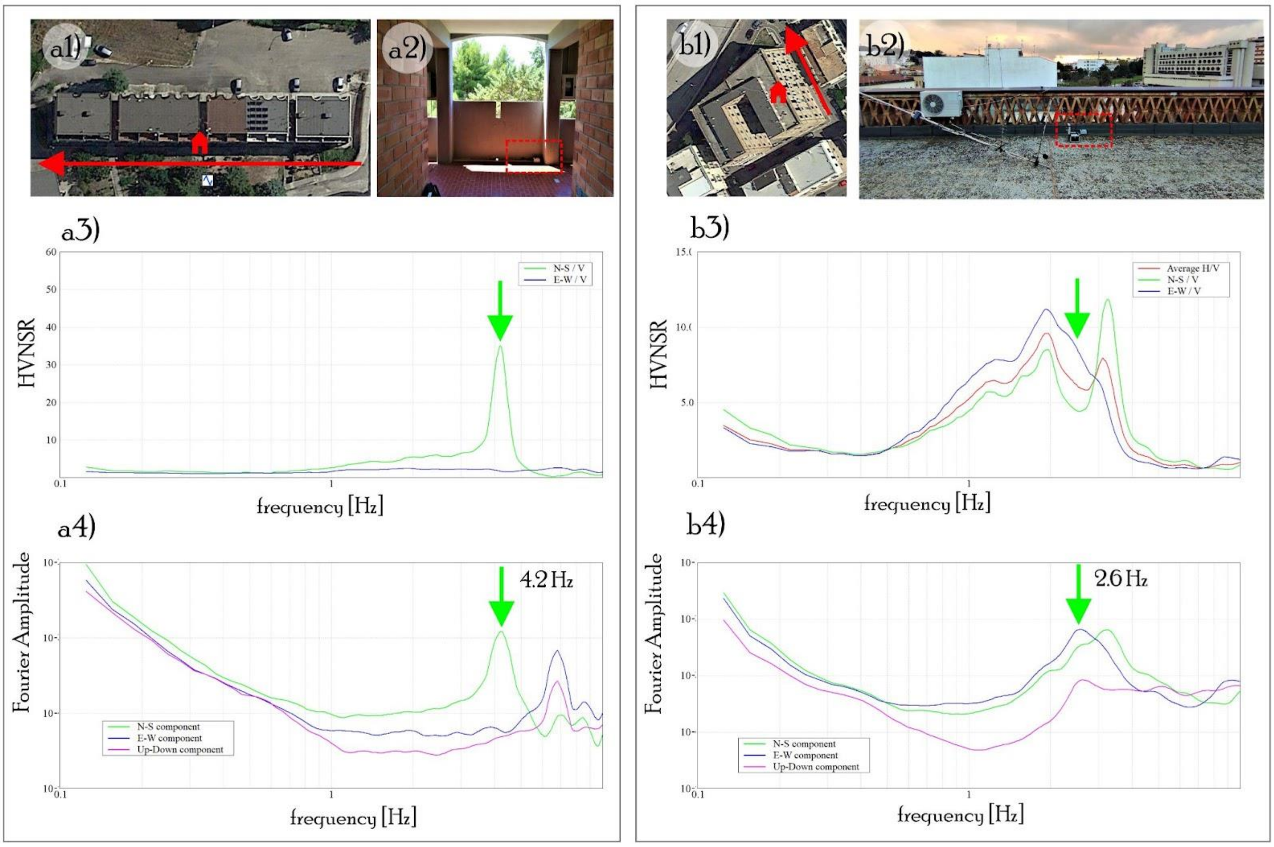

Fig. 2.23 Examples of single station ambient noise measurements elaborated with HVNSR method for a RC building (a1,2,3,4) and a masonry building (b1,2,3,4); (a1,b1) plan of buildings and location of sensor (red arrow indicate the direction/orientation of the sensor); photo of the sensor location inside the building (a2) and on the roof (b2); HV ratio (a3,b3); Fourier amplitude spectra (a4,b4); green arrow indicate the eigenfrequencies of the 1st mode for both the buildings (a4,b4); for the RC building the NH/V curve and the FAS in N-S direction (a3, a4) exhibit a peak at the same frequency value 4.2 Hz; the 1st vibration mode of the masonry building is visible only on the FAS curve at 2.6 Hz in E-W horizontal direction (b4), while at the same frequency no peak is visible on the VH curves (b3).

2.3.2 SSR method: microtremor recording, analysis and interpretation

The theoretical aspects of the SSR method have already been outlined in the previous section (2.4). SSR and HVSR are appropriate techniques to estimate the main vibrational mode of buildings higher than 10 metres (**Gallipoli et al., 2010**). However, it is worth emphasising that building small or very stiff is better to be characterised avoiding HVNSR. In figure 2.24 is shown an example of seismic noise used for rapid characterisation of buildings applying SSR method of E. Duni Classical High School structure (**Tragni et al., 2019)**. From the results of the SSR analysis, the authors evaluated for each floor of the building two main modes of vibration, one in the transverse direction (east - west component) at 2.7 Hz and the other in the longitudinal direction (north - south component) at 4.2 Hz (Figure 2.24b, e). The authors indicated an asymmetry in the behaviour between the two extremes of the building: the right side, being more rigid due to the presence of the trapezoidal structure of the entrance staircase, essentially vibrates in the horizontal plane (Figure 2.24b), the left side also presents a rocking component at 2.7 Hz; this frequency is indeed evident not only on the transverse component but also on the vertical one (Fig. 2.24b). The authors indicate that this behaviour is even more evident in the results obtained along the horizontal array, i.e. in the most rigid part of the building (point A in Figure 2.24a) the fundamental frequency is 4.2 Hz and the motion occurs predominantly in the longitudinal direction; as one moves towards the most flexible part (point D in Figure 2.24a) the authors evaluated that the fundamental frequency not only decreases, but also assumes a transverse and vertical component, thus inducing a rocking motion at 2.7 Hz (Figure 2.24d). Moreover, **Tragni et al. (2019**) also estimated the mode shapes, which show a regularity of the inter-storey course of the stiffer part of the building with a prevalence of motion in the longitudinal direction, while the mode shapes of the more flexible part show an irregularity in both directions due to the different dimensions of the top floor (Figure 2.24c). The possibility of obtaining such information on the largest number of buildings, both public and private, as well as on infrastructure, would make it possible to characterise the urban heritage and to assess possible dangerous interactions between it and the urban subsuoil that could increase damage during seismic events.

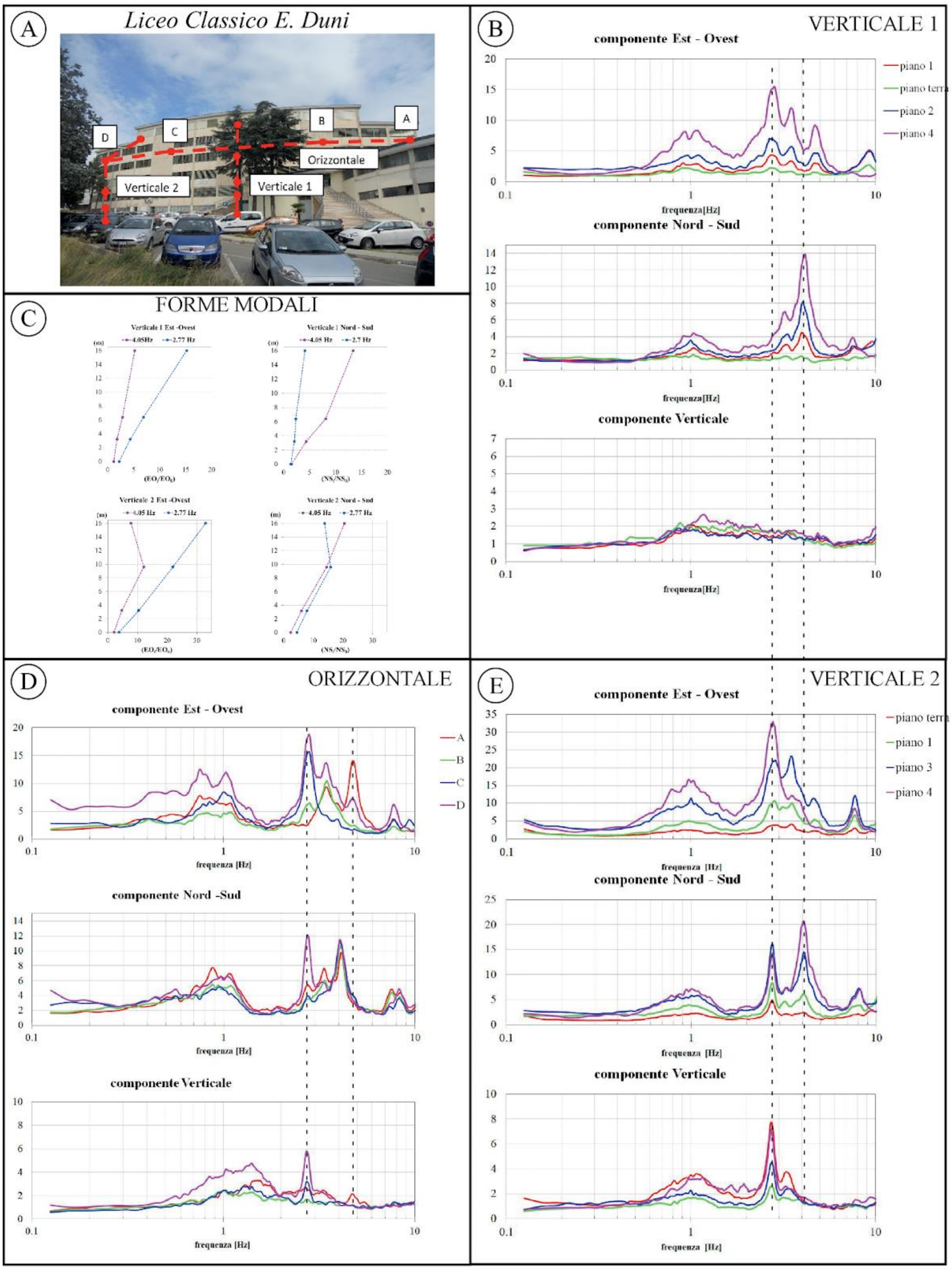

*Fig. 2. 24 a) Indication of the measurement points; SSR functions, obtained in the two main directions of the building, longitudinal and transversal, on each floor of the Liceo Classico "E. Duni" building in the two vertical array configurations (B-vertical 1; E-vertical 2) and in the horizontal one (D); C) mode shapes obtained on vertical 1 and vertical 2 (**Tragni et al., 2019**)*

2.3.3 Frequency Domain Decomposition (FDD)

The FDD method is an Operational Modal Analysis (OMA) approach in the frequency domain and enables evaluating the eigenfrequencies and mode shapes. **Brincker et al. (2001)** state that, when the loading is white noise, the structure is slightly damped, and the mode shapes of closely spaced modes are geometrically orthogonal. Taking the singular value decomposition (SVD) of the spectral matrix, the spectral matrix is decomposed into a set of auto spectral density functions, each corresponding to a single degree of freedom (SDOF) system. When the assumptions of the method are not satisfied, the decomposition into SDOF systems is approximate, but still the results are much more accurate than the results of the classical approach (**Ibrahim and Milkulcik, 1976**; **Vold et al., 1982**; **Juang and Pappa, 1985**; **Van Overschee and De Moor, 1996**). **Bricker et al. (2001)** state that:

$$G_{yy}(j\omega) \; = \bar{H}(j\omega)\, G_{xx}(j\omega) H(j\omega)^T \qquad 2.\,14$$

express the relationship between the unknown inputs x(t) and the measured responses y(t), where $G_{xx}(j\omega)$ is the (*r x r*) power spectral density (PSD) matrix of the input with r being the number of inputs, $G_{yy}(j\omega)$ is the (m x m) PSD matrix of the output with m being the number of the responses, which results from the pre and post-multiplication of the PSD matrix of the input $G_{xx}(j\omega)$ with the (*m x r*) frequency response function (FRF) matrix of the system *H(jω),* where the overbar and superscript T denote the complex conjugate matrix and transposed matrix, respectively. xx and yy are related to the already mentioned unknown inputs x(t) and measured responses y(t), respectively.

Following **Bendat and Piersol (2010)**, the frequency response function *H(jω)* for a constant-parameter linear system is given by the Fourier transform of the unit impulse response function *h(τ)* that describes the system:

$$H(j\omega) \; = \int_{-\infty}^{\infty} h(\tau) e^{-j\omega\tau} d\tau \qquad 2.\,15$$

Equation (2.15) can be written in polar notation as:

$$H(f) \; = |H(f)| e^{-j\phi(f)} \qquad 2.\,16$$

Where $|H(f)|$ is the gain factor of the system and *Φ(f)* is the phase factor of the system. Since the properties of *H(f)* are independent of the nature of data flowing through a structural system its estimation can be done using deterministic data, transient data, or stationary random data in case of linear systems.

Brincker et al. (2001) suggest that the FRF can be written in partial fraction (i.e. pole-residual) form:

$$H(j\omega) \; = \sum_{k=1}^{n} \frac{R_k}{j\omega - \lambda_k} + \frac{\bar{R}_k}{j\omega - \bar{\lambda}_k} \qquad 2.\,17$$

where n is the number of modes, λ_k is the pole and R_k is the residue:

$$R_k \; = \phi_k {\gamma_k}^T \qquad 2.\,18$$

where ϕ_k and γ_k are the mode shape vector and the modal participation vector, respectively.

The power spectral density matrix of an input represented by white noise is constant $G_{xx}(j\omega)$ = C.

Substituting $G_{xx}(j\omega)$ = C and Eq. (2.17) in (2.14) yields:

$$G_{yy}(j\omega) \ = \sum_{k=1}^{n} \sum_{s=1}^{n} \left[\frac{R_k}{j\omega-\lambda_k} + \frac{\bar{R}_k}{j\omega-\bar{\lambda}_k}\right] \times C \left[\frac{R_s}{j\omega-\lambda_s} + \frac{\bar{R}_s}{j\omega-\bar{\lambda}_s}\right]^H \qquad 2.\ 19$$

where superscript H denotes a complex conjugate and transpose.

Brincker et al. (2001) state that in the case of light damping residue matrix of the output, the PSD becomes proportional to the mode shape vector and, assuming an independent white noise input, one would get the results (in terms of PSD matrix of the output) directly from equation (2.14).

The first step in the Frequency Domain Decomposition method is to estimate the PSD matrix. Each element of the PSD matrix is obtained as a cross-correlation of pairs of Fourier spectra of non-overlapping moving windows of velocity signal recordings for each component (NS, EW, Z). The total numer n of cross-correlations will depend on the number of sensors (e.g., in the case of five sensors, there will be 15 components and thus n = 120 combinations), for each moving window. Then, **Brincker et al. (2001)** propose to decompose the output power spectral density matrix $\hat{G}_{yy}(j\omega)$ known at discrete frequencies ω = i by applying the singular value decomposition (SVD) method to the matrix. The SVD method, as **Brunton and Kutz (2019)** explain very well, is one of the most important matrix factorizations of the computational era, and is a unique matrix decomposition that exists for any complex-valued matrix **X** ∈ $\mathbb{C}^{n\times m}$:

$$\boldsymbol{X} = \boldsymbol{U\Sigma V}^{*} \qquad 2.\ 20$$

where **U** ∈ $\mathbb{C}^{n\times n}$ and **V** ∈ $\mathbb{C}^{m\times m}$ are unitary matrices ($UU^T = U^TU = I_{nxn}$; $VV^T = V^TV = I_{mxm}$) with orthonormal columns, and **Σ** ∈ $\mathbb{R}^{n\times m}$ is a matrix with real, non-negative entries on the diagonal and zeros off the diagonal. The symbol $*$ denotes the complex conjugate transpose. The columns of **U** are called left singular vectors of **X** and the columns of **V** are right singular vectors. The diagonal elements of **Σ** ∈ $\mathbb{R}^{n\times m}$ are called singular values and they are ordered from largest to smallest. The rank of **X** is equal to the number of non-zero singular values. Therefore, applying SVD to the output power spectral density matrix $\hat{G}_{yy}(j\omega)$ yields:

$$\hat{G}_{yy}(j\omega_i) \ = U_i S_i U_i^H \qquad 2.\ 21$$

where the unitary matrix $U_i = [u_{i1}, u_{i2}, \dots, u_{im}]$ hold the singular vectors u_{ij}, and the diagonal matrix S_i hold the scalar singular values s_{ij}. The FDD method identifies the natural frequencies from the peaks in the singular value plots of the diagonal matrix s_i, and the mode shapes from the corresponding singular vectors u_{ij} of the unitary matrix U_i.

Bricker et al. (2001) warn that if a harmonic is present, this corresponds to a local amplification of the auto spectral density function of all the SDOF systems, therefore they indicate that all, or nearly all, of the singular values in the spectral plot will show a peak at the frequency where the harmonic is present. Thus, if one observes that at a certain frequency most of the other singular have a peak at that same frequency, and not only the first singular value has a peak, then this is strong indication that the peak does not represent a structural response but a harmonic (**Brincker et al., 2001**). **Brincker et al. (2001)** invite the readers to see an example of the application of this feature of the FDD technique in **Brincker et al. (2000)**. Moreover, they highlight that “if a structural mode is close to the harmonic, the harmonic does not destroy the mode shape estimate”.

2.3.4 Ambient Noise Deconvolution Interferometry approach (ANDI)

In the frequency domain, the deconvolution of a signal $u(t)$, recorded at a generic location, by the signal $u_{ref}(t)$ recorded at a reference location (considered as a virtual source) assuming the two signals are generated by the same source, is defined as follows (e.g., **Snieder and Safak 2006**):

$$D(\omega) = \frac{u(\omega)}{u_{ref}(\omega)} \qquad 2.22$$

where $u(\omega)$ and $u_{ref}(\omega)$ are the Fourier transforms of the motions recorded at the generic and reference sites, respectively, and $\omega = 2\pi f$ is the angular frequency, f is the eigenfrequency. In the case of a building installation, the reference sensor is installed at the top or bottom, while in the case of a bridge (i) all the sensors must be installed on the same structure, i.e. the deck (for both a bridge and a multi- span viaduct) and (ii) the reference sensor is located on the deck at the support. Since this problem is ill-conditioned, the regularized Tikhonov deconvolution (**Tikhonov and Arsenin 1977**; **Bertero and Boccacci, 1998**):

$$D(\omega) = \frac{u(\omega)u^{*}_{ref}(\omega)}{\left|u_{ref}(\omega)\right|^{2} + \varepsilon} \qquad 2.23$$

is applied. (2.23) corresponds to the transfer function between $u(\omega)$ and $u_{ref}(\omega)$, where ε is a regularisation parameter that controls the degree of filtering applied to stabilise the deconvolution and to avoid numerical instability (**Snieder and Safak, 2006**); $u^{*}_{ref}(\omega)$ is the complex conjugate of the Fourier transform of the recorded signal at the reference position. Among different possible regularisation schemes (e.g., **Bertero and Boccacci, 1998**; **Bindi et al., 2010**), the so-called water-level regularisation (e.g., **Wiggins and Clayton, 1976**) where ε is defined as a percentage of the average spectral power can be applied:

$$\varepsilon = \frac{\sum_{i=1}^{nfft}\left|u_{ref}(\omega)\right|^{2}{}_{i}}{nfft}\alpha \qquad 2.24$$

where $\left|u_{ref}(\omega)\right|^{2}{}_{\mathrm{i}}$ is the power spectral amplitude of the i-th sample of the reference signal, *nfft* is the number of samples, and α is the water level whose value equal to 10^{-3} is a good compromise between stability and resolution of problem analysed in this thesis work. Therefore, assuming a linear time-invariant system, deconvolution interferometry can be applied on both ambient noise and earthquake data to determine impulse response function in the time domain of a signal propagating between two distinct sensor positions by applying the IFFT to the deconvolved wavefield *D(ω)* in frequency domain (2.23) (see **Chapter 4**).

Chapter 3: Soil-structure interaction in the city of Matera

3.1 Introduction

Historical and recent earthquakes (e.g., 1886 Charleston earthquake, 1906 San Francisco earthquake, 1964 Niigata and Alaska earthquake, 1980 Irpinia earthquake; Sumatra 2004, L'Aquila 2009, Chile in 2010, Haiti 2010, Tohoku, Japan, in 2011, Central Italy 2016-2017, Afghanistan 2022 among others) teaches us that when earthquakes strike urban areas it can cause negative effects on vulnerable elements. On the other hand, it is estimated that the current acceleration of the global urbanisation phenomenon will result in about 66% of the world's population living in cities by 2050. According to a United Nations report, in Europe, about 80% of the population lives in urban areas (**United Nations, 2014**). Italy consists, on average, of medium-sized cities (50,000–200,000 inhabitants) and its historical centres are building heritage highly exposed to catastrophic (e.g., earthquakes, landslides, volcanic eruptions, etc.) and extreme climatic events. In Italy from 2008 the 'Guidelines for Seismic Microzonation' (**GSM; MS working group, 2015**) are applied to mitigate seismic risk. It is a tool for urban planning that plays an important role in the selection of new settlement areas, in the definition of eligible actions and their priorities, and in the choice of methods to implement seismic risk mitigation actions in urban areas. Moreover, technical procedures for soil characterization have been defined (**Commissione Tecnica MS3907, 2014**), applied and tested for example during the Abruzzo and Emilia earthquakes (**Gallipoli et al., 2011**; **Mucciarelli et al., 2011**; **Paolucci et al., 2015**) and subsequently improved (**Commissione Tecnica MS3907, 2015a, 2015b, 2015c**). However, the guidelines for seismic microzonation in Italy focus mainly on geological-technical problems like seismotectonic, lithostratigraphy, and instabilities (landslides, rockfalls, liquefaction, etc.), completely neglecting the presence of buildings. **Kanamori et al. (1991)** observed the effects of high-rise buildings in Los Angeles, excited by atmospheric shock waves generated by the space shuttle Columbia on its return, showing that a seismic P wave was excited by the motion of high-rise buildings and that the proximity of the natural period of the high-rise buildings to that of the Los Angeles basin enabled efficient energy transfer from shock wave, through the building, to seismic wave. **Gueguen et al. (2000)** conducted experimental studies on a five-story reinforced-concrete building model located in the EuroSeisTest site at Volvi (Greece) highlighting that since the building vibrations generate waves to the foundation soil, their presence in densely urbanised areas may cause non-negligible modifications to the ground motions compared to free-field conditions. **Gallipoli et al. (2006)** confirmed that buildings may act as seismic sources; during a large displacement-release test on a two-story reinforced concrete building located in Bagnoli (Naples, Italy), the authors measured near the building a noticeable ground motion represented by an acceleration exceeding 5% g. **Laurenzano et al. (2010)** studied the dynamic soil-structure interaction of two adjacent buildings on a local soft slope deposit affected by the 2002 Molise earthquake (Italy) using spectral element method. **Bindi et al. (2015)**, and **Petrovic and Parolai (2016)** carried out experiments on real buildings using noise and earthquake data recordings confirming the relevance of buildings as possible excitation sources. **Petrovic et al. (2018)** estimated the output energy released from buildings as secondary sources to the soil, and the wavefield radiated back was estimated to be significant for three case studies (e.g., for the Bishkek case, at 145 m depth, 10% of the estimated real input energy is expected to be emitted back from the building; for Istanbul, at 50 m depth the value is also 10–15% of the estimated real input energy, while for Mexico City at 45 m depth it is 25–65% of the estimated real input energy). When the seismic interaction involves an entire city with the shallow soil layers during seismic events, the term site-city interaction (SCI) is used (e.g., **Gueguen et al., 2002**; **Semblat et al., 2004**; **Kham et al., 2006**; **Varone et al., 2020**). The latter authors studied the multiple interactions between a building network and the site and highlighted that the SCI effect causes variations in ground motions, amplification levels and kinetic energy near buildings. **Piro et al. (2020)** evaluated SSI for historical masonry buildings and different kinds of foundation soil from a numerical point of view. Moreover, it is known that whenever the main vibration frequency of the building is very close to the resonance frequency of the foundation soil, the soil – building resonance phenomenon is activated, which can cause an increase in shaking and thus damage to the structure during an earthquake (**Gallipoli et al., 2019**). The soil-structure resonance phenomenon can result in increased damage to the building during earthquakes (**Bard et al., 1996**; **Tsogka and Wirgin, 2003**; **Mucciarelli et al., 2004, 2011**).

Another important aspect of land safety in urban areas is the implementation of smart technologies for intervention management. To improve knowledge of risks and strengthen prevention, widespread dissemination of scientific data and results is needed through the active involvement of public administrations (service-oriented approach). One of the most widely used tools for open data dissemination is WebGIS through which can achieve multiple purposes and different contexts (such as tourism, archeology, agriculture, environment, etc.). **Shi et al. (2010)** linked the genetic classification of China's soils with soil taxonomy through an ad hoc developed WebGIS system. **Manna et al. (2020)** demonstrated how to support the planning and management of olive groves and provide operational assistance to stakeholders through a geospatial decision support system. The literature demonstrates that WebGIS technologies are also widely used for natural risk assessment and communication (**Muller et al., 2006**; **Frigerio et al. 2010, 2014**; **Fago et al., 2014**). For example, WebGIS tools have been used for geo-hydrological risk analysis and risk management related to floods or landslides (**Aye et al., 2016a,b**; **Huang et al., 2015**; **Salvati et al., 2009**), slope stability analysis (**Thiebes et al., 2013**) or online mapping of unstable rock slopes (**Oppikofer et al., 2015**). In the field of seismic risk, where the presented thesis work is located, WebGIS and geodatabase technologies have already been used in some applications: **Pessina et al. (2009)** developed interactive tools for seismic hazard scenario definition and risk analysis ; **Bozzoni et al. (2014)** assessed seismic damage in the seaport of Gioia Tauro using a complex WebGIS architecture; **Francini et al. (2018)** developed a methodology for selecting the optimal routes in case of a seismic event through a WebGIS platform; **Rovithis et al. (2018)** published databases for sharing accelerograms of earthquakes in urban areas of Kalochori, (Greece); **Scibek et al. (2020)** used a web-based GIS to reveal data on the permeability of fault zones and surrounding protolithic rocks at sites around the world. Some authors have implemented and published software systems for storing and visualising subsoil data that can be used for seismic microzonation (**Di Felice et al., 2013**). Nevertheless, no databases or WebGIS tools for soil-structure interaction in urban areas have been published yet.

Here, two studies are presented that address soil-structure interaction in the city of Matera: (i) development of a systemic approach at the urban scale to characterise the main physical properties of the urban subsurface and the overlying built environment, based on the application of non-invasive, rapid and low-cost geophysical technologies, digital archiving and dissemination of all available geological, geotechnical, geophysical, and engineering data and results, obtained in this part of the thesis work, through a WebGIS-based for open data sharing and dissemination approach; (ii) comparison between an experimental and an analytical approach for estimation of interactions of masonry buildings with their foundation soils at the neighbourhood scale.

3.2 Evaluation of the soil-building resonance effect of the city of Matera (Italy)

The test site of this part of the thesis has been the city of Matera, located in the Basilicata region (southern Italy). Matera is located on the eastern edge of the Bradano Trough, a wide depression set in the Mesozoic bedrock (Altamura limestone) during the middle Pliocene, which represents the foreland ramp of the Southern Apennines (**Beneduce et al., 2004**) and is characterised by a system of horsts and grabens (**Tropeano et al., 1994**). First, available data on soil were collected: a total of 300 geological, geotechnical, and geophysical surveys of the last 20 years, and a detailed geological map (1:4000) that was georeferenced and digitised into vector shapefiles (points and polygons) in GIS and reproduced in Figure 3.1. Because the stratigraphic sequence (section ABC; Figure 3.1B) in most of the urban area consists of stiff and hard Altamura limestone from bottom to top, fractured and weathered Gravina calcarenite, sub-Apennine clays of variable thickness (about 40–50 m), and somewhere a shallow thin sand layer, it can cause a high impedance contrast for most of the city. Therefore, Matera is a site of particular interest in terms of local seismic response. Moreover, the primary geomechanical properties are affected by the presence of inhomogeneities caused by the granulometry and the different degree of diagenesis. In a previous study, **Gallipoli and Lupo (2012)** reported the average value of shear wave velocity estimated by downhole tests for each soil type (≅ 1052 m/s for Altamura limestone, ≅ 914 m/s for Gravina calcarenite, ≅ 367 m/s for sub-Apennine clay and ≅ 250 m/s for sands).

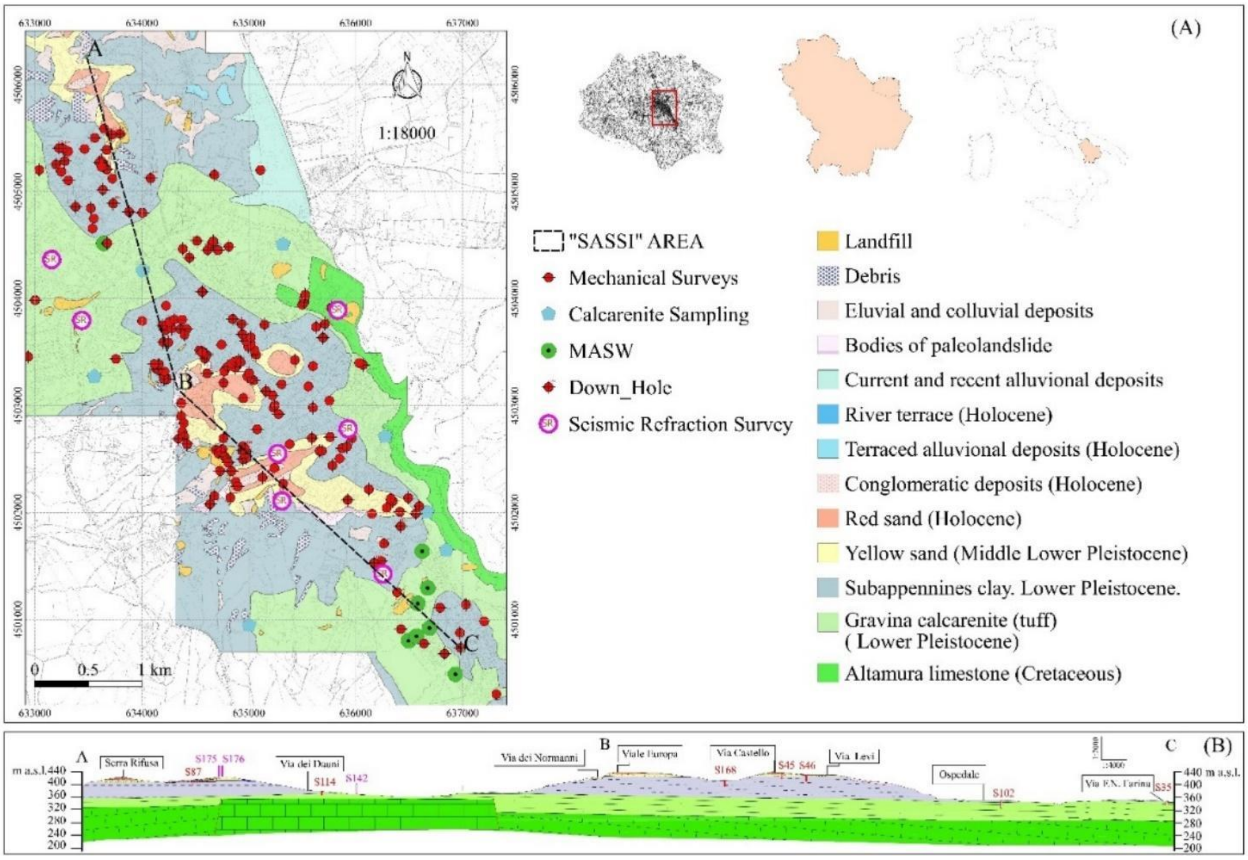

*Fig. 3.1 Location of available geophysical and geo-mechanical surveys superimposed on the detailed geological map of the city of Matera. (B) Stratigraphic sequence of the section ABC (modified from **Lupo and Gallipoli, 2012**).*

3.2.1 The built environment

After having collected the available geological-geotechnical and geophysical data on the urban shallow soils, open spatial data on buildings were searched. Matera has two important databases for the built environment: the Basilicata Region Geotopographic Database (RSDI - Regional Spatial Data Infrastructure of the Basilicata Region, 2015, http://rsdi.regione.basilicata.it/) which contains information on the height and use of buildings, and the Open-Data (OD) Matera (http://dati.comune.matera.it/) which reveals information on age and building typology. Two shapefiles from RSDI (original names: 'edifici_is' and 'unità volumetrica'), one from OD Matera (original name: rnc_4326.shp), and two from ISTAT (Italian National Institute of Statistics) databases (original names: 'R17_11_WGS840 and 'R17_indicatori_2011_sezioni') were downloaded. Since much of the data in this part of the thesis was processed with spatial analysis software and, in particular, with vector or polygonal geometries in shapefile format, it is worth noting that the General Population and Housing Census (Italian National Institute of Statistics, ISTAT, 2018) reports a number of 6061 buildings for Matera, while the regional geo-topographic database reports a number of polygonal geometries equal to 25,497. This difference is due to the fact that in most cases buildings consist of a series of geometries that identify structures such as balconies, turrets, emergency staircases, towers, and other components of the buildings.

For this reason, I carried out the following three operations: i) first, resolving the geometries belonging to the same buildings into one; ii) assigning the height of the highest element of the building to the new resolved geometry; (iii) merging all the information related to the building typology (Figure 3.2A; masonry, reinforced concrete moment-resisting frame buildings, etc.), the year of construction (Figure 3.2B), the use and state of preservation (Figure 3.2C), and the number of floors (Figure 3.2D). Therefore, the analysis discussed in this part of the thesis concerns 4049 geometries (out of 6061) for which the geology of the building foundation soil is known. Figure 3.2 shows that the most recently built areas are located in the northeast and southeast of the city. Most of the 4049 studied buildings have "residential" use (3401) and 4–5 floors (1158) and are mostly made of reinforced concrete (RC) moment-resisting frame (2249) with very good state of conservation (1029); masonry buildings are predominant in the historical centre, where the older buildings are also found. Since the "Sassi" area, a troglodyte settlement with houses, churches, monasteries, and hermitages, was built into and completely merged with the natural caves of the calcareous formations (which as a whole is named Murgia), it was excluded from the analysis.

The aggregation of ISTAT data by neighborhoods allows for considerations and assessments at the territorial level., i.e., the historic neighborhoods (Piccianello, Historical Centre, Cappuccini-Agna) are mainly masonry dwellings, while the newer neighborhoods are predominantly reinforced concrete moment-resisting frame buildings with a better state of preservation (Figure 3.3).

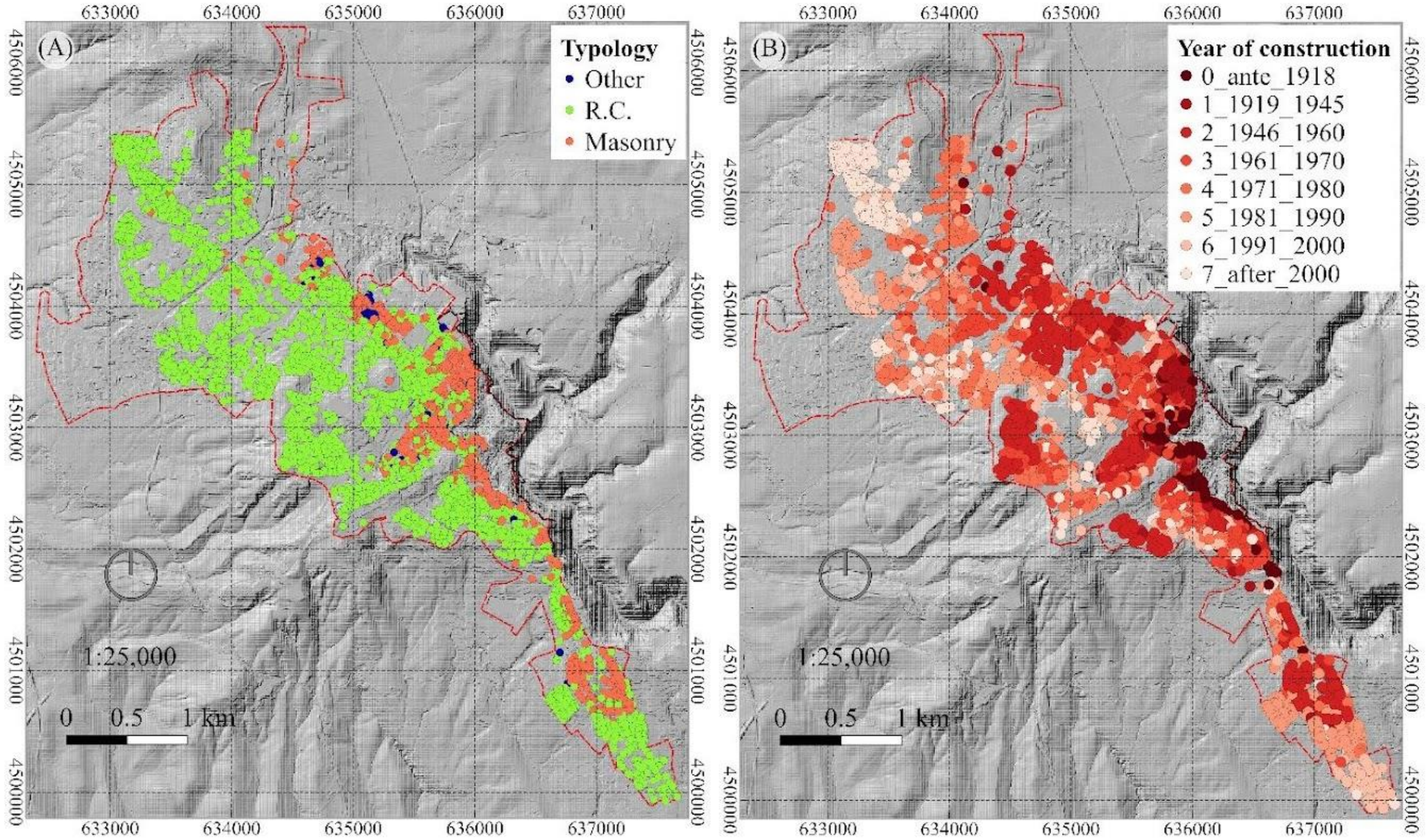

Fig. 3.2 Spatial distributions of buildings in the city of Matera classified according to (A) building typology; (B) year of construction; (C) state of conservation; (D) number of floors. The black dashed line encloses the "SASSI" area (not included in this study).

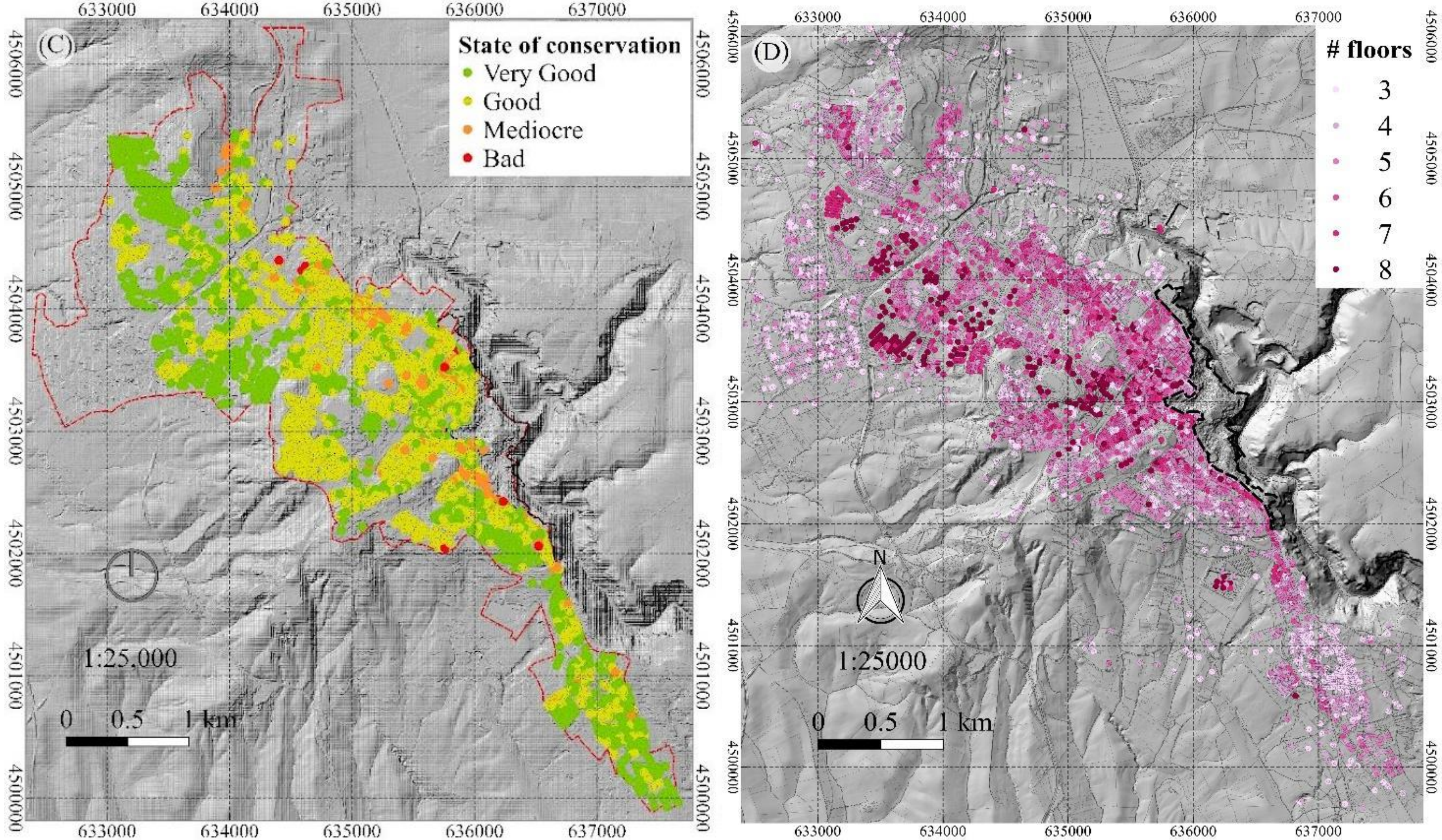

Fig. 3.2 (continued)

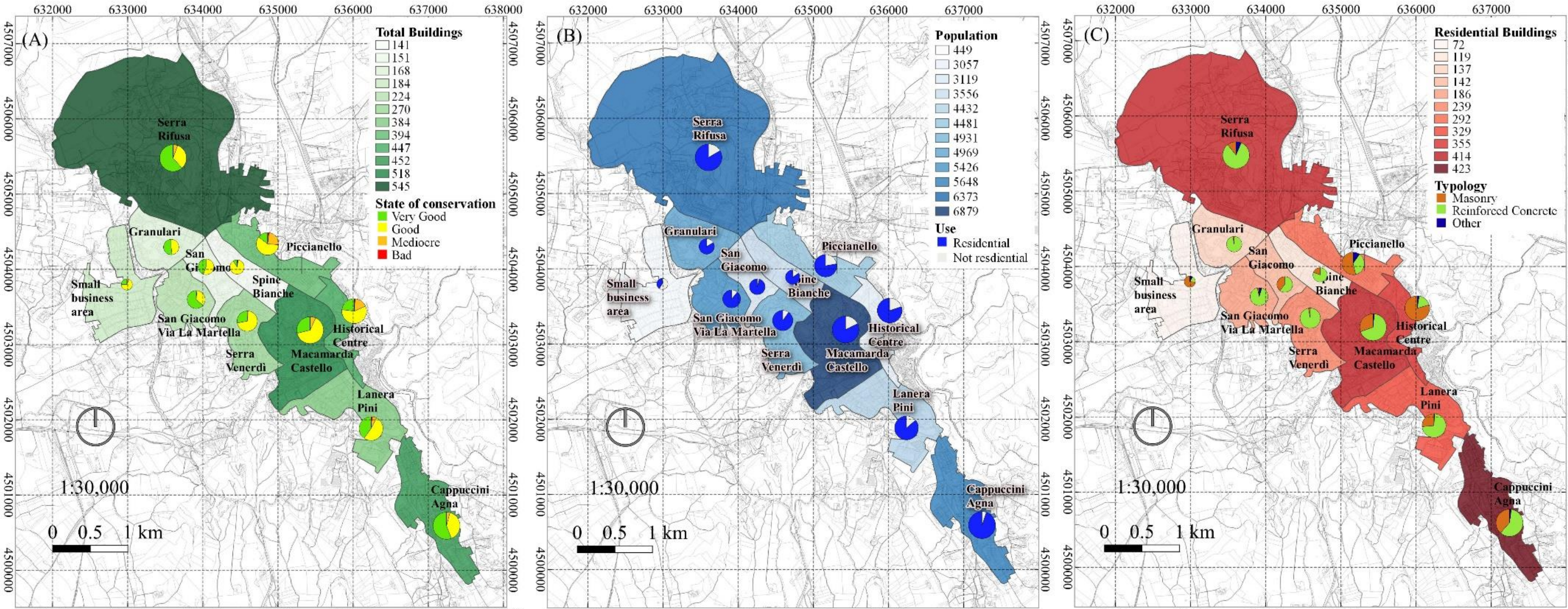

Fig. 3.3 Figure 2. Spatial distribution of ISTAT census variables aggregated by neighbourhood and classified according to (A) number of total buildings; (B) population; (C) number of residential buildings, including a pie chart of (A) building state of conservation, (B) building use, (C) built typology.

3.2.2 Single-station seismic ambient noise measurements on soils and buildings

230 single-station seismic ambient noise measurements elaborated by means of HVNSR method were carried out (186 made by myself as part of this thesis work) divided as follows: 134 (10 existing) on the soils and 96 (34 existing) on the buildings (Fig. 3.4). As explained in Chapter 2, the use of a single station to record ambient noise is non-invasive, easy to perform, and therefore allows as many measurements as possible to be made over an extended area and on a large number of buildings. The measurements were analysed using the Horizontal-to-Vertical Noise Spectral Ratio (HVNSR) technique, which is among others site characterization methods one of the most predominantly conducted for estimating the fundamental frequencies of soils and buildings (**Chávez-García and Cárdenas, 2002**; **Gallipoli et al., 2004**; **Gallipoli et al., 2010**; **Mucciarelli et al., 2011**; **Pan et al., 2014**; **Castellaro, 2016**; **Salameh et al., 2016, Molnar et al., 2022**).

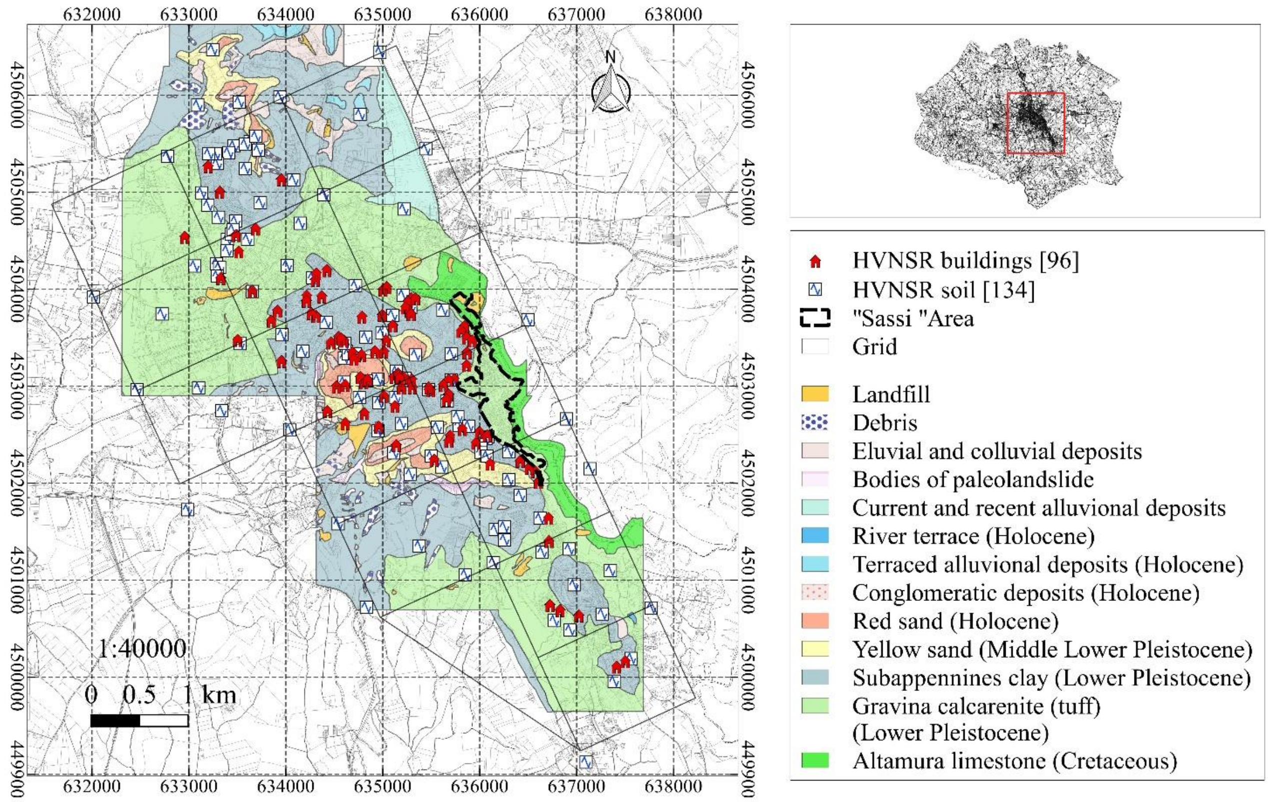

Fig. 3.4 Locations of single station seismic ambient noise measurements performed on the soil and buildings overlaid with the detailed geological map.

Aiming to sample all shallow soils characterised by different lithology, thickness, stratigraphy and geotechnical characteristics, I performed measurements in three ways: (i) most of the soil measurements are made in a regular grid with an average sampling step of 1.7 km, (ii) many others are made at irregular intervals near previous geological and geotechnical surveys to validate the HVNSR functions, (iii) the remaining measurements were made in the youngest parts of the city and where strategic buildings (schools, hospitals, barracks, industries, etc., Figure 3.4). Since the soil seismic response, both in weak and in strong motion, is always a complex composition of wave fields from different sources. On the other hand, the presence of buildings modifies the ground motion of the cities. For this reason, trying to isolate the effect of the soil from that of the buildings would have been a too hard and a likely unsuccessful task. Therefore, although not always possible, aiming to avoid locations where the influence of buildings, industrial facilities, and traffic on urban soil was reduced as much as possible, particular attention was posed to the selection of the measurement site.

Following the indications reported in Chapter 2, I carried out measurements on soil with a duration of 14 minutes, a sampling frequency of 128 Hz, and at a distance at least equal to the height of the nearest buildings or trees. To verify that the soil frequency characteristics are well determined under urban conditions, I compared the obtained amplification functions with those obtained under 'real free-field' conditions for each lithology. For example, the comparison between HVNSR functions obtained on sub-Apennine clay under different urban conditions shows that the HVNSR_90 measurements (Lat, Lon: 4506000,634000; Figure 3.5) should be considered a ‘real free-field’ and the associated HVNSR function exhibits the same behaviour at others carried out in the urban area. A representative sample of buildings for the measurement in terms of building typology, year of construction, and height was selected (Fig. 3.4). As described in Caption 2, a 12-minute long recording (sampling rate of 128 Hz) was carried out for each building by placing the sensor on the top floor near the column-beam junction for the reinforced concrete building, close to the load-bearing wall for the masonry ones, and always (excepted for square shape plan buildings) aligned with the main (or more rigid) building axes (**Gallipoli et al., 2010**; **Castellaro, 2016**).

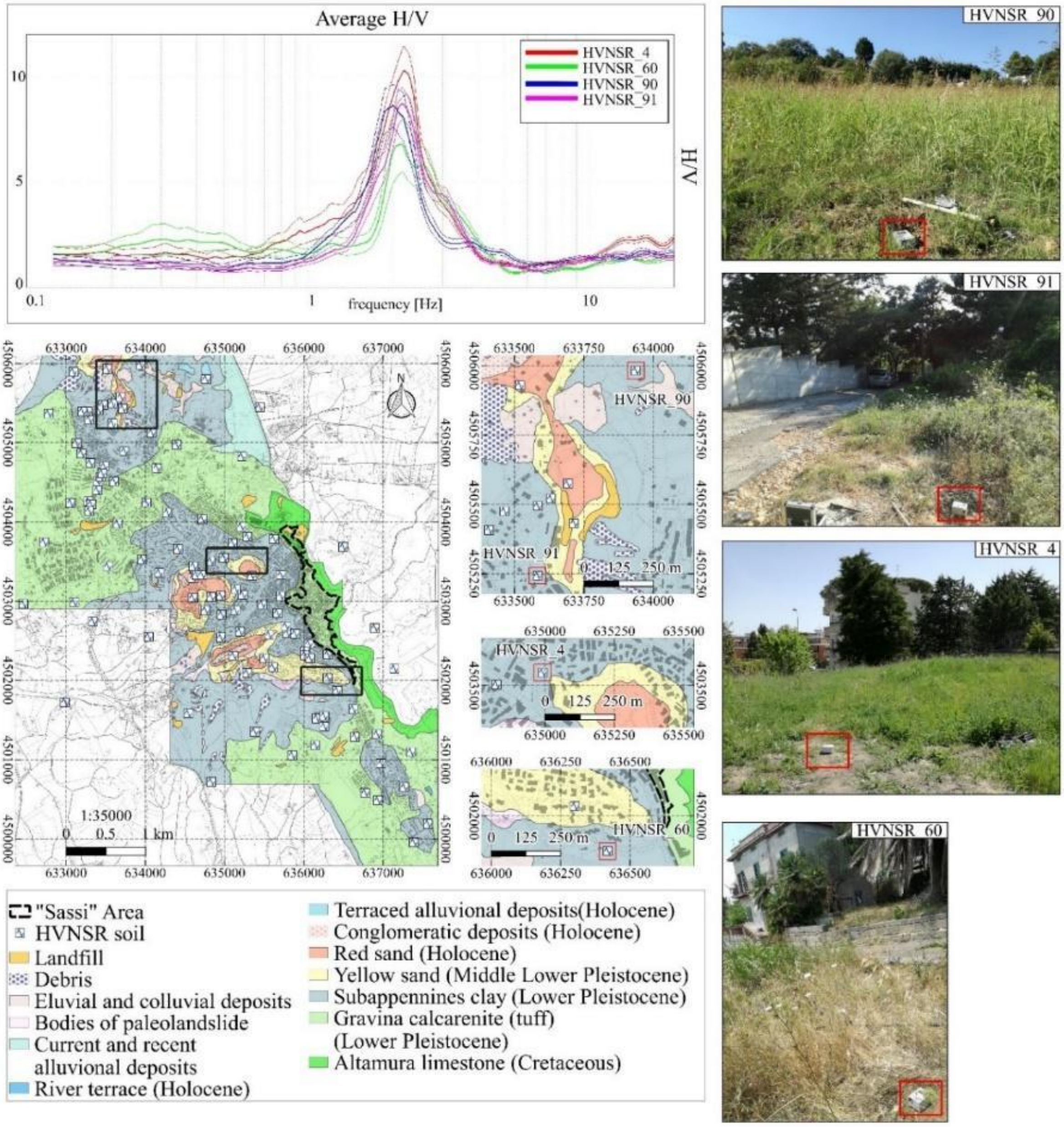

Fig. 3.5 Comparison between HVNSRs obtained on sub-Apennine clay with different urban conditions. The HVNSR_90 measurement has been performed on 'real free-field'.

3.2.3 Main frequencies of urban soils

With the exception of four sites with flat amplification functions, the HVNSR method was applied to 120 ambient noise measurements to estimate the main fundamental frequency (f0_s) and relative amplitude (A0_s) at each point. These new measurements were integrated with 10 existing HVNSR curves evaluated for urban soils, increasing the area of the city of Matera covered by surveys from 18 to 1758 ha, with an average density of 3.7 surveys/km^2. In total, the density of all surveys in the urban area is about 11.25 surveys/km^2. The estimated fundamental resonance peak f0_s is mainly in the ranges between 1 and 6 Hz (Figure 3.6A), with the median value of 3 Hz. The fundamental frequency below which 75% of the values are concentrated is 3.6 Hz; only in ten cases the frequencies resulted to be higher than 6 Hz. The estimated fundamental resonance frequency f0_s is lower for the sites located on sub-Apennine clays (about 2.7 Hz), than for sites on outcropping calcarenite (about 3.3 Hz, seeFigure 3.6B). The HVNSRs on calcarenite have amplifications that spans a wide range of frequencies with lower amplitude values (Figure 3.7) due to a low impedance contrast between calcarenite and underlying Altamura limestone (Vs ~914 vs 1052) and are flatter than those on sub-Apennine clay sites. The latter represent the vast majority of the estimated HVNSRs and exhibit distinct resonance peaks (Vs ~367 vs 914 m/s) due to the strong impedance contrast between clays and the underlying Gravina calcarenite.

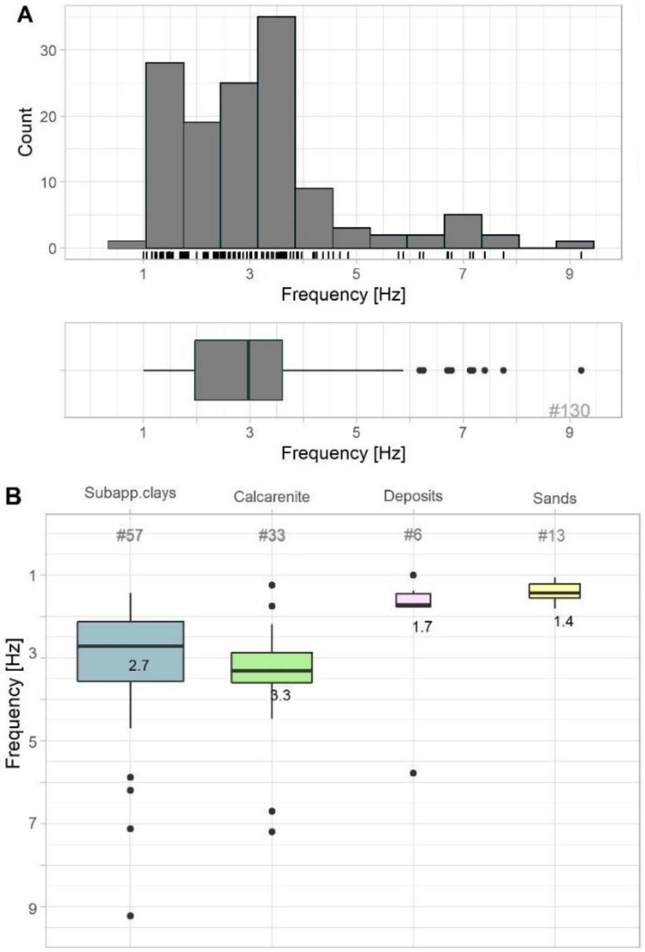

Fig. 3.6 Empirical distribution of the HVNSR fundamental resonance frequencies estimated on soils: (A) whole dataset and (B) split by outcropping soils. Black ticks (in A) and dots (in B) represent single measurements. Boxplot width (in B) is proportional to the square-root of the number of measurements for each group (reported in grey).
The upper and lower hinges of the box correspond to the first and third quartiles (the 25th and 75th percentiles); the central line in the box is the median (50th percentile); whiskers extend for 1.5 times the interquartile ranges. For 21 measurements the geology is not known

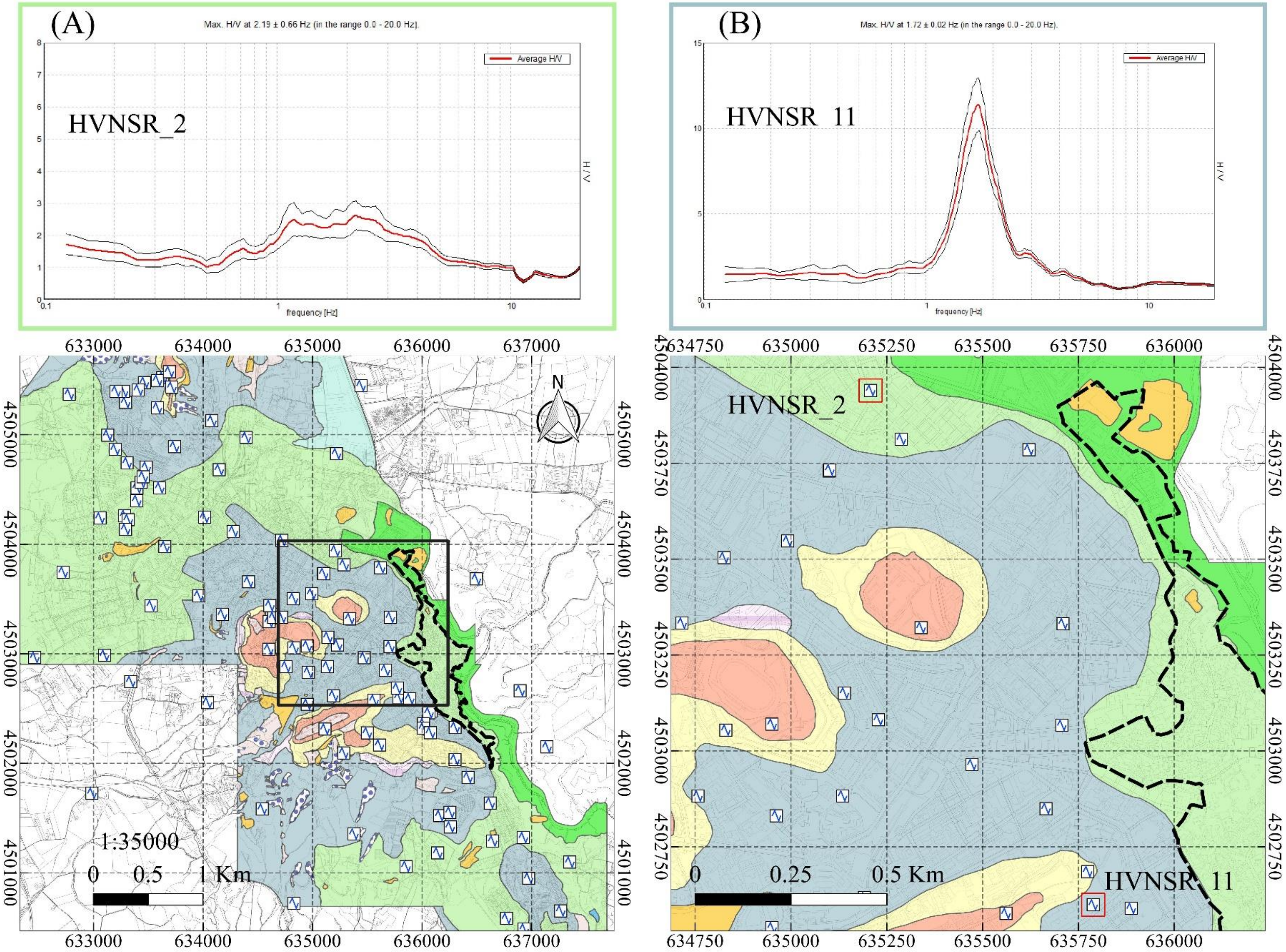

Fig. 3.7 Two HVNSR functions estimated on Gravina calcarenite (A) and sub-Apennine clays (B). The estimated HVNSR exhibits clear resonance peaks on sub-Apennine clay site while calcarenite HVNSR looks flatter.

3.2.4 Soil iso-frequency and iso-amplitude maps

To determine the soil-structure resonance levels for the built-up area of the entire urban area of Matera, it was necessary to move from a sparse and discrete type of measurement distribution to a continuous type in the spatial domain. To this end, I created iso-frequency and iso-amplitude maps for the urban soil (**Cadet et al., 2011**; **Brax et al., 2018**; **Pinzón et al., 2019**) using a deterministic interpolator, the Inverse Distance Weight (IDW). The weighted sum of the measured target variable of the n points around the unsampled location, whose value is unknown for both the main resonance frequency and amplitude, is given by:

$$\hat{Z}(s_0) = \frac{\sum_{i=1}^{n} w(s_i) Z(s_i)}{\sum_{i=1}^{n} w(s_i)} \qquad 3.1$$

where $\hat{Z}$ indicates the estimated value at a given point s_0 and Z are the values of the known values at the s_i locations. For each measurement, the weights $w(s_i)$ $(= \frac{1}{D})$ must sum to 1 based on the inverse Euclidean distance D $(= d(s_i, s_0)^p$)to the unsampled point (s_0), and the measured value is used when s_0 coincides with a sampled point. As distance increases, the effect on the estimates of a given unsampled point decreases. The weights can be adjusted by tuning the power exponent *p*, which in most cases and in this study has the value 2 (**Bivand et al., 2013**). The accuracy of values predicted by using the deterministic interpolation method at unsampled locations cannot be considered unaffected by some uncertainty factors; for example, (i) the power parameter assigned to distances (here set to 2) affects the weighting of nearby observations, (ii) the assumption of smooth variation in space may be true within the same geology, but it is not necessarily true along transitions between different lithologies. For this reason, I am aware that a power exponent optimization procedure guided by an error measurement, or the use of more sophisticated geostatistical interpolators, may in the future provide a more accurate procedure that allows for more refined modelling of spatial variability, taking into account not only spatial anisotropy but also information conveyed by covariates (e.g., geology).

Figure 3.8 shows the iso-frequency and iso-amplitude maps resulting from the application of the IDW deterministic interpolator. As expected, in the area of the city centre (long. 634000 - 636000; lat. 4503500 - 4501500), the soils with higher amplification values are present at lower frequencies, which is due to the thick layers of sub-Apennine clays overlying the Gravina calcarenite, as indicated by the geology; while, the soils whose fundamental peaks have higher frequencies and lower amplifications characterise the N-NW and SE areas of the city, where the Gravina calcarenite outcrop and the soft layers are thinner, probably because the impedance contrast between the Gravina calcarenite (tuff) and the limestone is not strong as as that between the clays and the underlying calcarenite. Some validation has been done on soft soils and the measured values are very close to the interpolated ones.

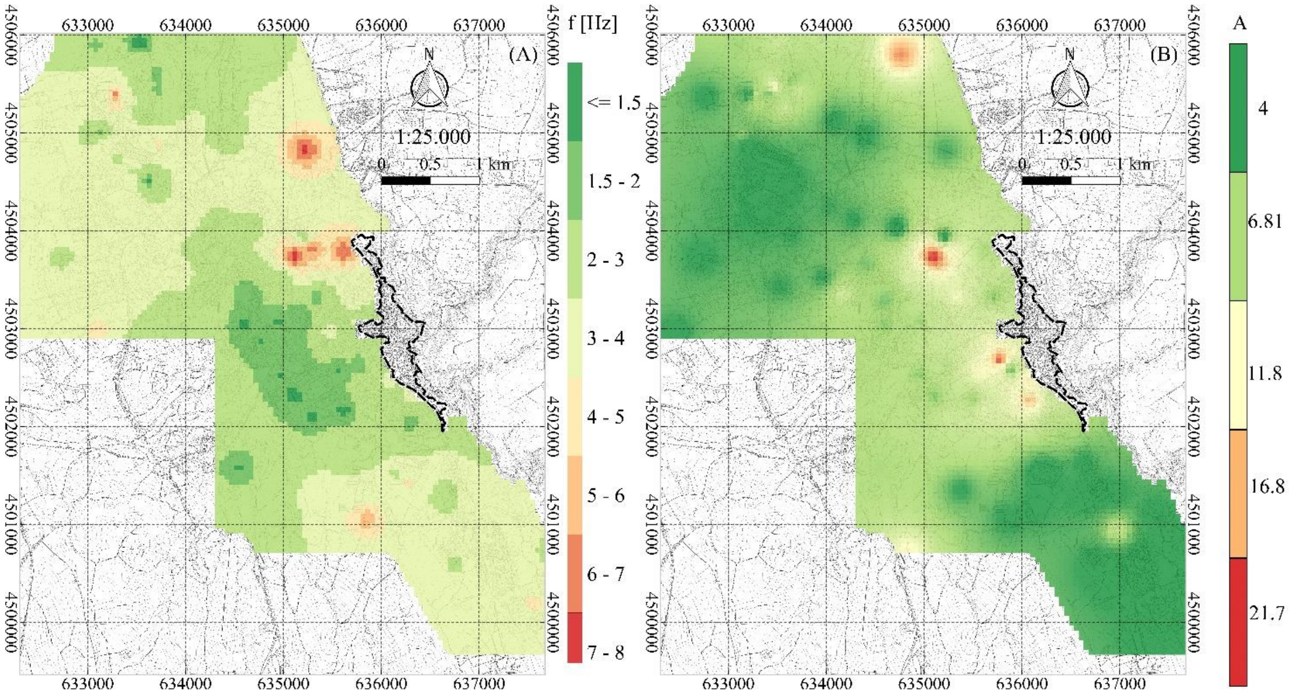

Fig. 3.8 (A) Iso-frequency and (B) iso-amplitude maps obtained with IDW interpolation from the 117 HVNSR curves overlaid with the topographic map of Matera. Map cell size 50 × 50 m^2.

3.2.5 Fundamental vibrational frequencies of buildings

By integrating the 34 existing with the 62 new HVNSR functions estimated for buildings, the percentage of the studied buildings increased from 0.8% (#6) to 2.5% (#18) for masonry buildings (out of 732) and from 1.5% (#28) to 4.2% (#78) for reinforced concrete buildings (out of 1872). The percentage was calculated with respect to the total number of buildings located in the studied area (#2648). For reinforced concrete buildings, the pie chart in Figure 3.9B shows for each macro-area the percentage ratio between the measured buildings with respect to the total number of buildings for the considered macro-area, while the percentage ratio between the number of reinforced concrete buildings for a selected macro-area and the total number related to the urban area as a whole is plotted in Figure 3.9C. From the two pie charts just described it emerges that there is good agreement between the two proportions (measurements vs number of buildings per macro area; number of macro-area buildings vs number of buildings in the study area). Due to logistical issues (impossibility of access, etc.), the same does not apply for masonry buildings (Figure 3.9D, E).

For each ‘macro-area’, most of the buildings are located on layers of SubApennines clays or Gravina calcarenite, except for the buildings in the ‘Granulari’ districts or ‘Small business area’, which are almost completely built on Gravina calcarenite (Figure 3.10).

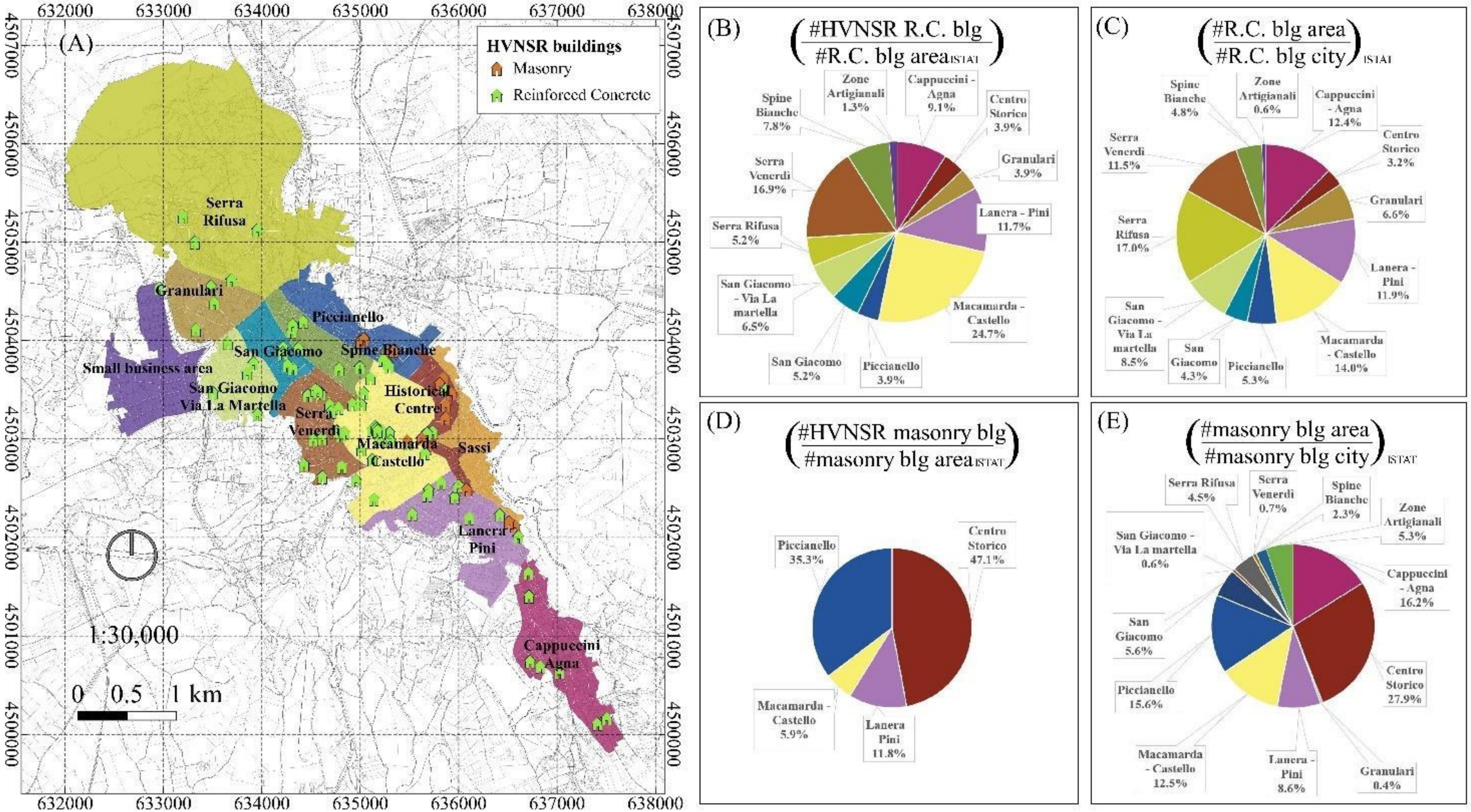

*Fig. 3.9. (A) Map of neighbourhoods and studied building locations; pie charts showing proportion (in percent) of studied and total number of buildings in the analysed macro-area for (B) reinforced concrete and (D) masonry; proportion (in percent) of number of buildings for each area relative to total number of buildings in the studied urban area for (C) reinforced concrete and (E) masonry, according to census variables (ISTAT) (**Tragni et al. 2021**)*

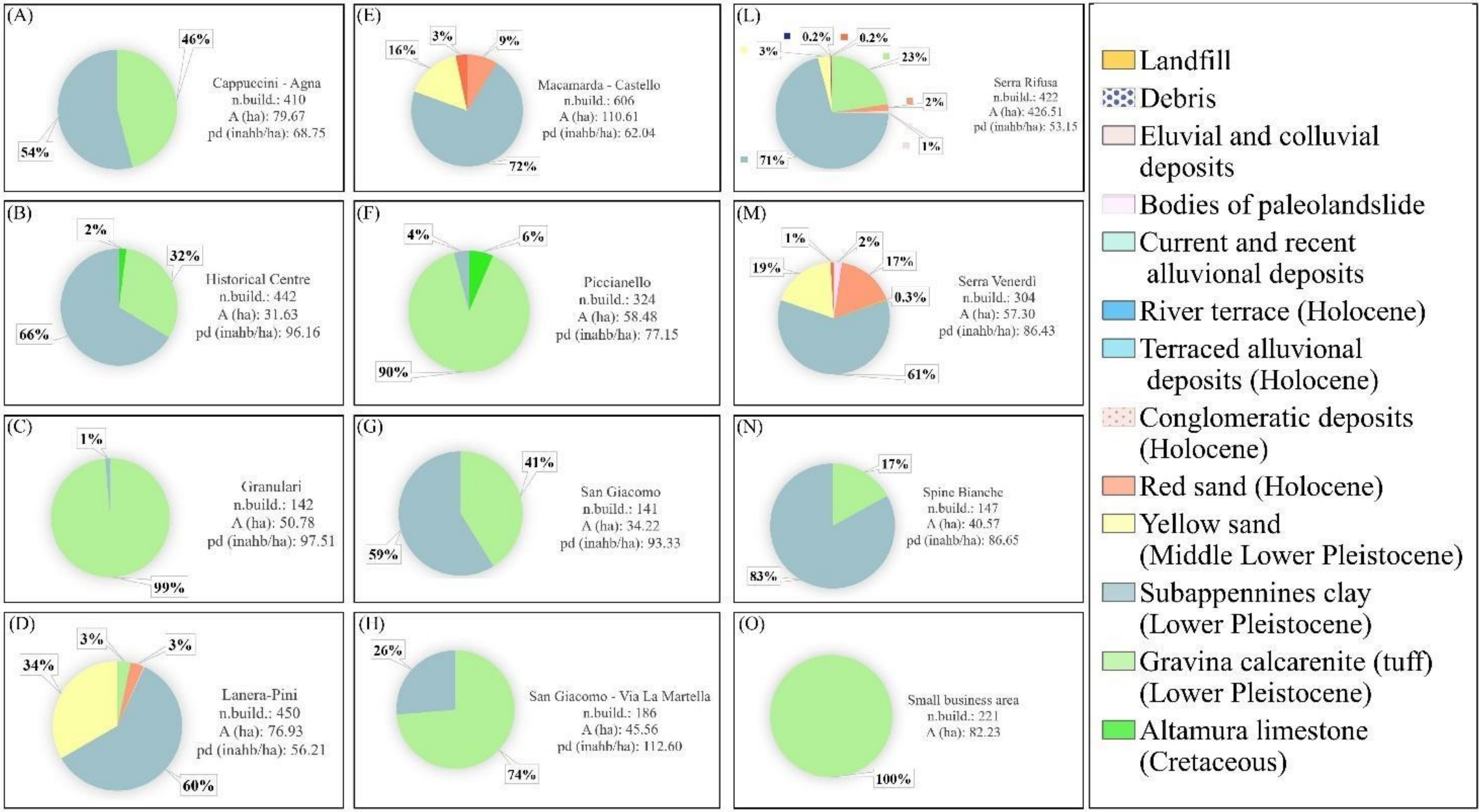

*Fig. 3.10 (A–O) Pie charts showing proportions (in percent) of major foundation soil geology for each macro-area. Every diagram reports the name of the macro-area, the number of buildings (n.build.), the extension of the area in hectares (A(ha)), and the population density expressed as inhab/ha (pd) (**Tragni et al., 2021**)*

The height of the 96 measured buildings ranges from about 7 to 30 m and their first vibrational frequency f0_b ranges from 1.4 to 8.3 Hz (Figure 3.11). The distribution of the first vibrational frequency did not deviate much from a normal distribution around the median value of 3.9 Hz. Almost all values are below 7 Hz; the higher values correspond to the two lower reinforced concrete buildings (heights of 7.3 and 7.9 m).

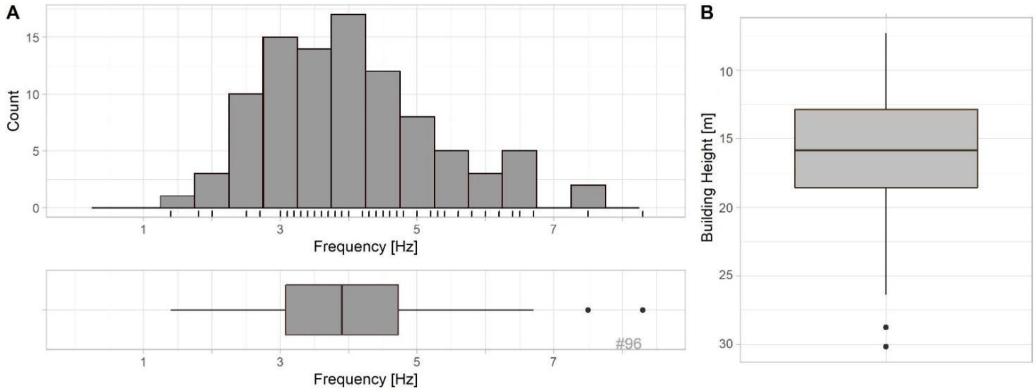

Fig. 3.11 (A) Iso-frequency and (B) iso-amplitude maps obtained with IDW interpolation from the 117 HVNSR curves superimposed to the topographic map of Matera. Map cell size 50 × 50 m2.

On average, the first vibrational frequencies of reinforced concrete buildings are significantly lower and more variable than those of masonry buildings, with median values of about 3.8 Hz and 4.5 Hz, respectively (Figure 3.12A). Regardless of building type, the average values of the first vibrational frequency decrease as the number of floors increases (Figure 3.12B), although this is an expected relationship, it can be taken as a sign of good data quality. Moreover, the first vibrational frequencies show, on average, a weak decreasing trend as a function of year of construction (Figure 3.12C), which is probably due to the seismic design techniques imposed by the normative, which have been increasingly adapted to new knowledge over the years. Finally, it is noted that buildings located on stiffer lithotypes (calcarenite) have, on average, higher frequencies (about 4.9 Hz) than buildings located on sub-Apennine clays (about 3.8 Hz) and on sands (about 3.0 Hz) (Figure 3.12D).

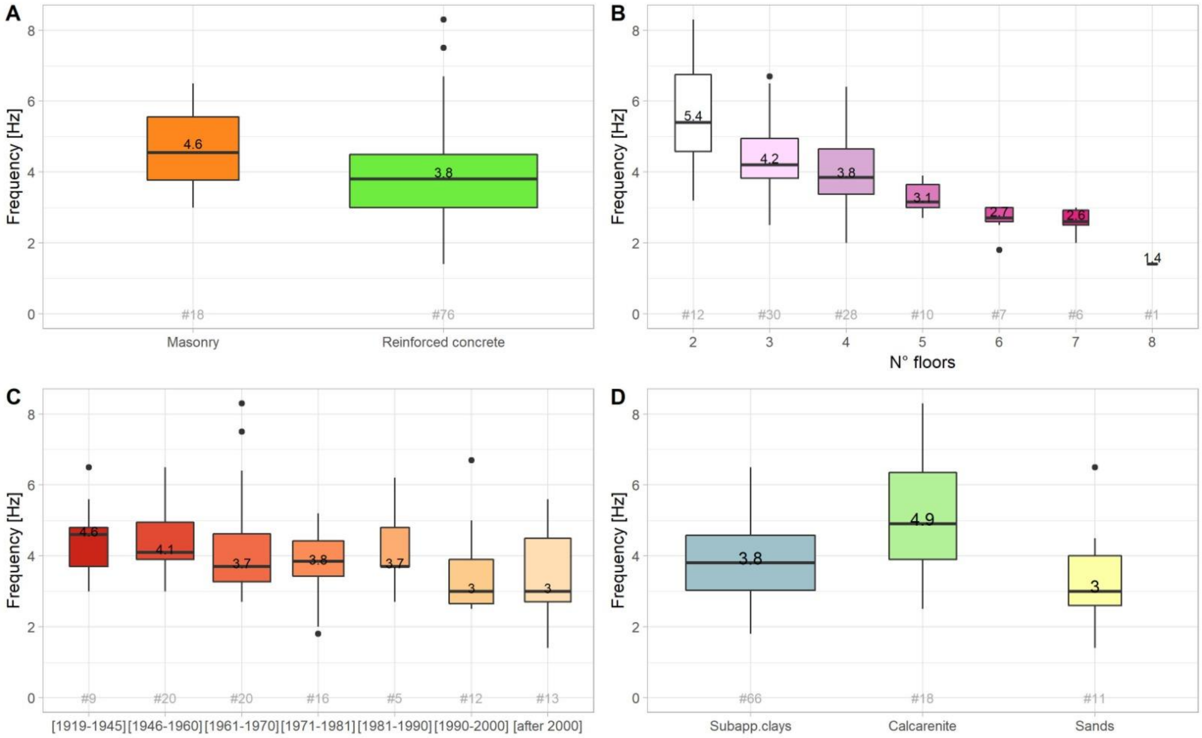

Fig. 3.12 Empirical distributions of the first HVNSR vibrational frequency of the 96 buildings as a function of (A) construction material, (B) number of floors, (C) year of construction and (D) soil foundation lithology. Other symbols as in Fig. 3.6

3.2.6 Map of the first vibrational frequencies of 4049 buildings

To estimate the first vibrational frequencies for all buildings, I used a simple linear model with zero intercept of the form *T = a*H*, where *T* is the first vibrational period *T(s)*, *H* is the corresponding height for the measured buildings, and a is the angular coefficient equal to *0.0167*, estimated by means of an ordinary least squares approach (Figure 3.13A).

The experimental relationship is presented in the period *vs* height domain rather than in the frequency *vs* height domain so that it can be compared with relationships estimated by other authors around the world. The angular coefficient is consistent with those estimated by **Navarro et al. (2007)** for 39 Spanish buildings; **Guler et al. (2008)** for 6 Turkish buildings; **Gallipoli et al. (2010)** for 244 European buildings; **Michel et al. (2010)** for 60 French buildings; **Chiauzzi et al. (2012)** for 12 Canadian buildings; **Pan et al. (2014)** for 116 Singaporean buildings; **Al-Nimry et al. (2014)** for 29 Jordanian buildings; **Salameh et al. (2016)** for 330 Lebanon buildings (Figure 3.13B). The experimental T–H relationship give significantly lower period values than those of the EC8, reaching differences of about 100% (Figure 3.13B), as also discussed by **Gallipoli et al (2023)**. The proposed formulation in the EC8 derives from the work of **Goel and Chopra (1997)** and it is based on measured periods of RC MRF (Reinforced Concrete Moment Resisting Frame) buildings from their motions recorded during several earthquakes in California. However, **Goel and Chopra (1997)** advise that "since these recommendations are developed based on data from buildings in California, they should be applied with discretion to buildings in less seismic regions of the US or other parts of the world where buildings design practice is significantly different than in California."

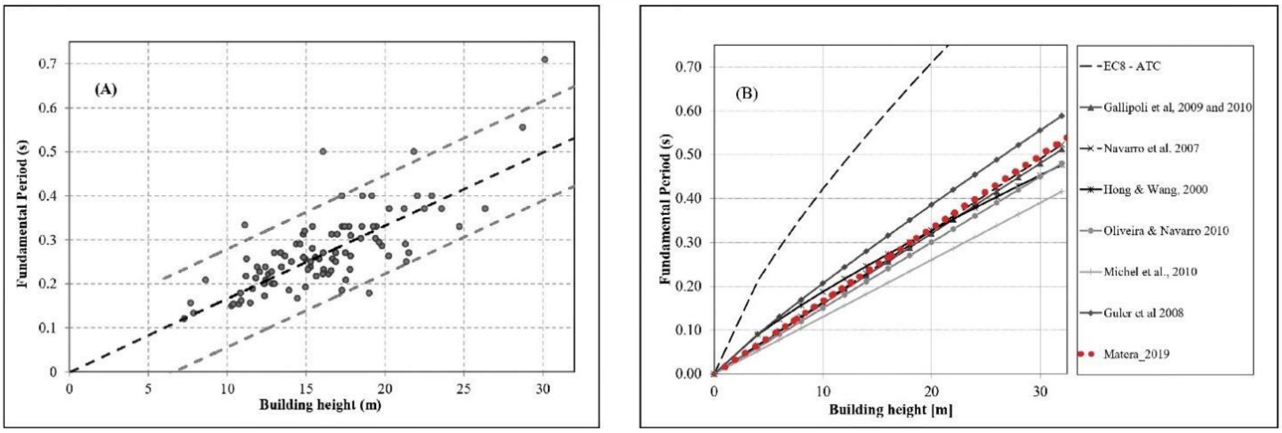

Fig. 3.13 Experimental relationship between building period and height for (A) the 96 sampled buildings and (B) our relationship in comparison with other published studies. (A) The dashed black line represents the predicted values (T = 0.0167H), the grey dashed lines represent the prediction interval of the regression.

The empirical relationship T = 0.0167H to estimate the frequencies f0_b of the first mode for the 4049 buildings for which the height is available and that fall within the height range of the studied buildings (7–30 m), obtaining the map of the first vibrational building frequencies have been used (Figure 3.14). The building frequencies were approximately between 2 and 8.5 Hz with higher frequencies for buildings in the northwestern (industrial area) and southeastern parts of the city (lower heights) and lower frequencies (greater heights) for buildings in the city centre.

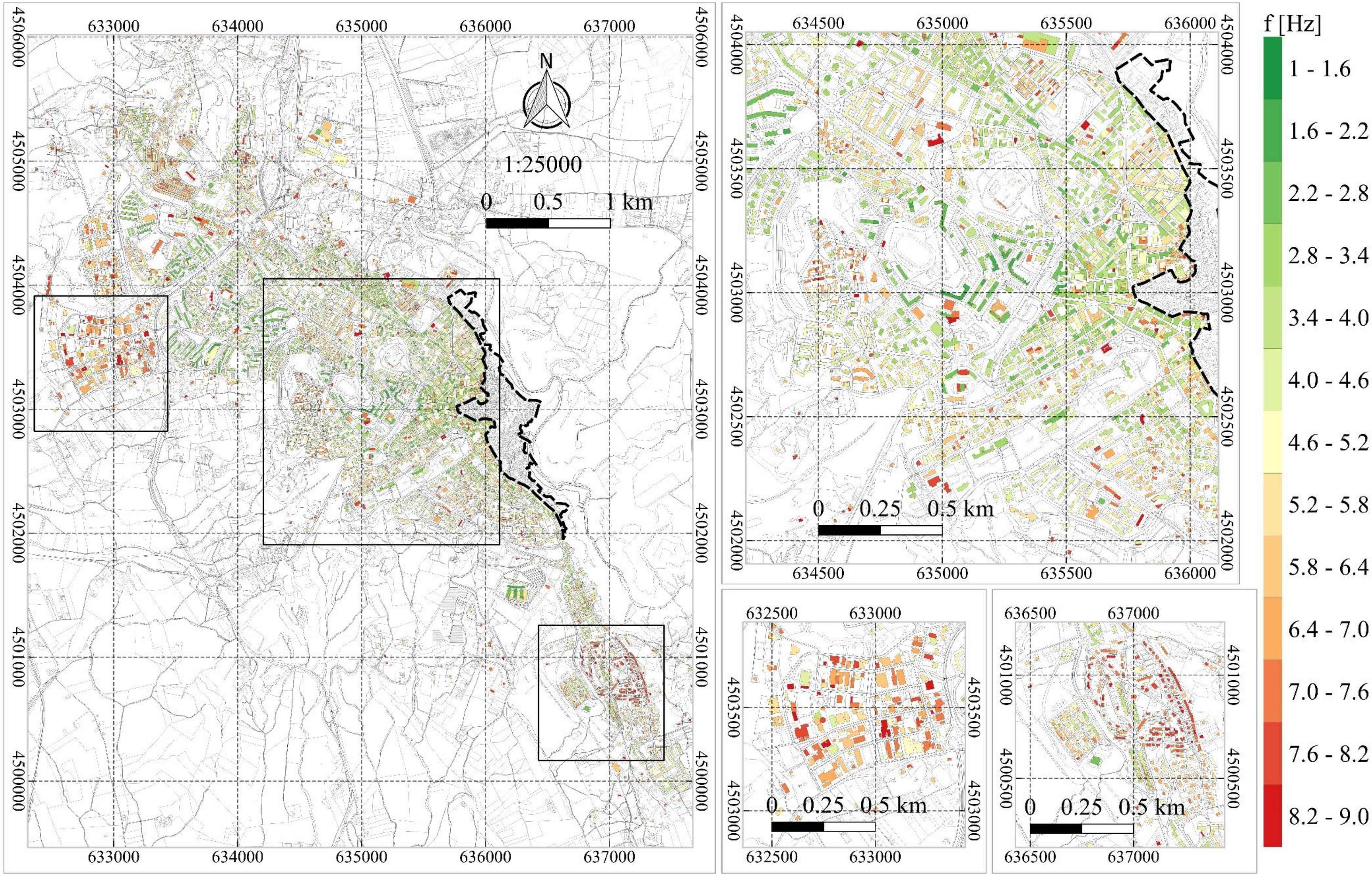

Fig. 3.14 (A) The estimated first HVNSR vibration frequency for the 4049 buildings; (B) Enlarged view of the city centre and (C) the northwest and southeast areas.

3.2.7 Soil – building resonance map

Some important insights for the evaluation of the soil-building resonance already become clear when comparing the univariate distributions of the fundamental frequencies of the 96 buildings and corresponding foundation soil. The values of the two distributions overlap to a large extent, i.e., the first vibrational frequencies of the entire building stock are approximately in the same range as those of the soils (Figure 3.15). This already suggests that most of the buildings could have first vibrational frequencies quite close to those of the foundation soils.

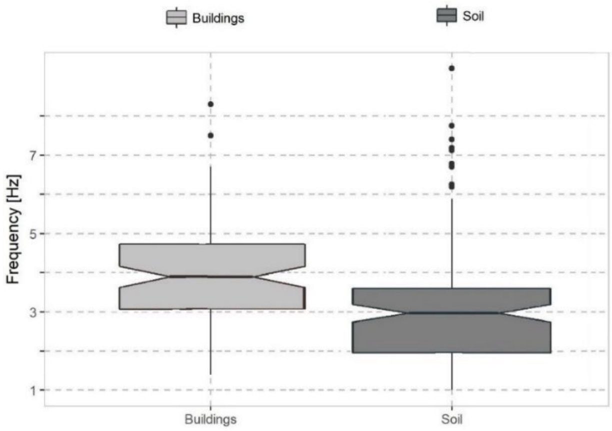

Fig. 3.15 Empirical distributions of the HVNSR fundamental frequency for soils and buildings. Other symbols as in Fig. 3.6 (after ***Gallipoli et al., 2019****)*

Fig. 3.16 shows the HVNSR functions estimated for a reinforced concrete building with 6 floors and the corresponding foundation soil (SubApennine clays) and shows that their main frequencies are very close.

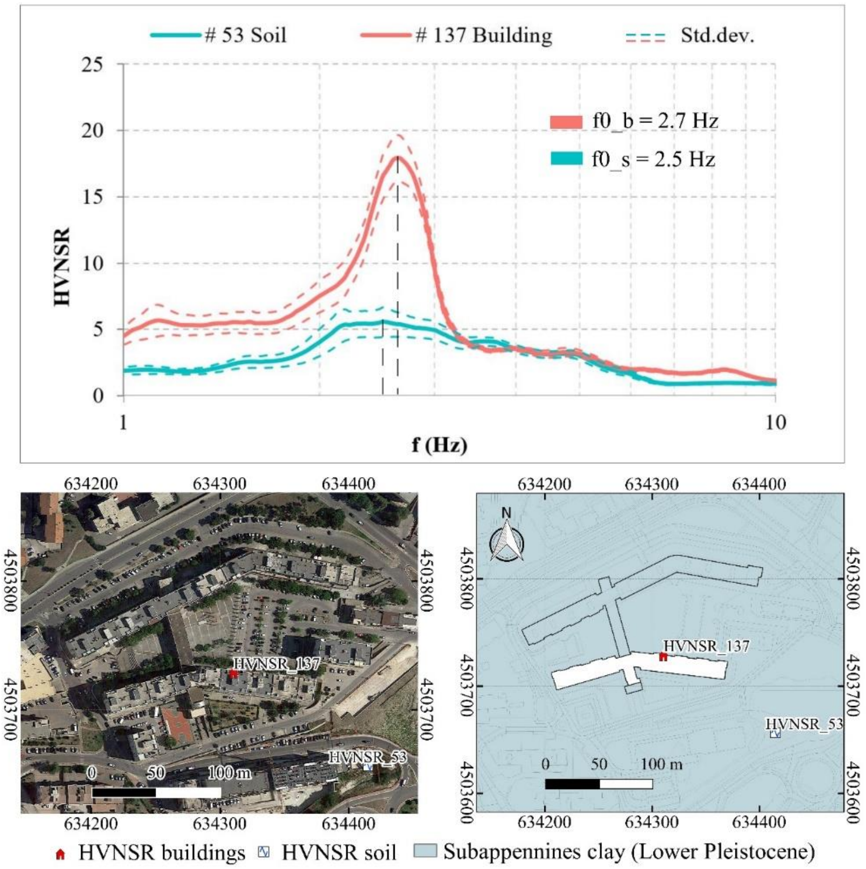

Fig. 3.16 (Top panel) HVNSR functions estimated for a 6-floor reinforced concrete building and the corresponding foundation soil; (bottom panels) details on location of building on orthophoto image and geological map.

To evaluate the soil-building resonance in the spatial domain, it was necessary to compare the iso-frequency distribution maps of the soil and the building. Before doing this, the first question to be addressed was how close f0_b and f0_s must be to each other for a "perfect" resonance to occur. For this purpose, a frequency band was first defined for each HVNSR function whose amplitude is above a threshold equal to 2. This value (red dashed line in Figure 3.17) represents the threshold above which amplification is assumed to occur (**Gallipoli et al., 2019**). Therefore, for each HVNSR function of the soil, the intersection points between the HVNSR curve and the selected amplitude threshold are two frequencies (hereafter called f1_s and f2_s, where f1_s < f2_s) which were interpolated to obtain a frequency range for each grid pixel of in a map.

The relationships between f1_s, f2_s and f0_s are expressed by f0_1 (= f0_s – f1_s), f2-0 (=f2_s – f0_s), and Δf=(f2_s – f1_s). The sum of the minimum values of f0_1 and f2_0 for each HVNSR measurement corresponds to the narrowest sought frequency interval that can be approximated by:

$$\Delta f_{min} \cong 2 \min_{1\leq i\leq 134} \left\{ \begin{matrix} \min(f_{0\_s} - f_{1\_s})_i \\ \min(f_{2\_s} - f_{0\_s})_i \end{matrix} \right. \cong \min_{1\leq i\leq 134} (f_{2\_s} - f_{1\_s})_i \qquad 1.183$$

where *i* represents the total number of HNVSR functions. The minimum value for which it has been found an amplification (greater than 2) was Δf ≈ 0.4 Hz (i.e., f0_s ± 0.2, that corresponds to coordinate pairs (f0_1 = 0.193 Hz; f2_0 = 0.228 Hz) with respect to HVNSR_44 and shown with a green circle in Figure 3.17). For conservative reasons, resonance was assumed to occur whenever f0_b is in the range f0_s ± 0.3 Hz (Δf ≈ 0.6 Hz is the value that accounts for less than 96% of the total values and is represented by the red diamond in Figure 3.17). The remaining 4% are the points beyond the black dotted lines in Figure 3.17.

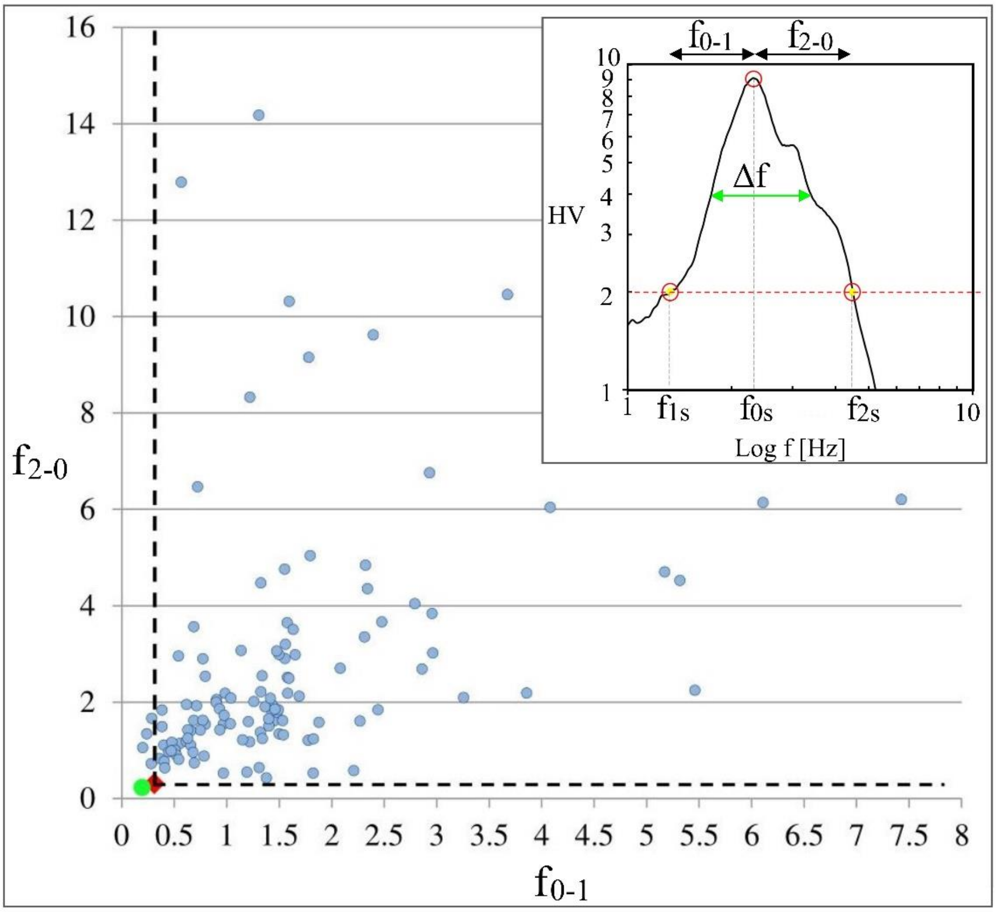

Fig. 3.17 Distribution of semi-range frequencies for 134 HVNSR (green circle the smallest range; red diamond the range selected in this thesis work; blue circle the 132 remaining measurement); (top right) example HVNSR curve estimated on sub-Apennine clays: the yellow points identify f1_s, f0_s and f2_s, respectively.

When considering buildings, f1_b and f2_b (with f1_b < f2_b) can be estimated as the reciprocal of the prediction ranges estimated in the experimental period-height relationship in Figure 3.13a. Note that the prediction equations are linear in the period-height domain, but become curvilinear in the frequency-height domain; therefore, they are closer together for taller buildings and farther apart for less tall buildings.

To understand where the ‘perfect’ soil-building resonance effect occurs, one can add to each 4043-building polygon (6 buildings lie outside the interpolated soil map) the interpolated value of the relative foundation soil frequency of the underlying pixel and check the condition f0_s-0.31≤f0b≤ f0s+0.31. Because the spatial area of the soil was discretized by using a grid of pixels (50 x 50 m), many buildings overlapped with more than one pixel of the soil iso-frequency map. Therefore, the frequency of foundation soil for each building was estimated using the weighted average of the f0_s values of all intersected pixels. Weights were assigned based on the intersection area between the building (polygon vector) and each pixel (normalized to give sum 1), i.e., the soil iso-frequency map in raster format. It is found that 313 (≅ 7.7% of the total) buildings are characterised by the first vibrational frequency that essentially matches that of the foundation soil (Figure 3.18). These buildings, which exhibit perfect resonance conditions with the soil, are mainly located in the centre of the urban area and are founded on sub-Apennine clay soils.

Each HVNSR curve have a shape characterised by the fundamental peak and a band of frequencies, or ranges of soil resonance frequencies, for which the amplitude is higher than the considered threshold (*HV* = 2). Therefore, a more detailed investigation may be represented by the quantification of the percentage intersections between the ranges of soil resonance frequencies and of building vibration frequencies that may be considered as a qualitative estimation of the soil-building resonance levels. All possible overlaps between the amplified soil frequency range [f2_s - f1_s] and that of the building [f2_b - f1_b] are grouped in three major cases (Table 2): CASE 1) ranges that are completely disjoint, meaning that no resonance is triggered; CASE 2) ranges that are partially overlapping in a limited frequency range, and, CASE 3) when one range is completely contained in the other, the resonance effect is complete.

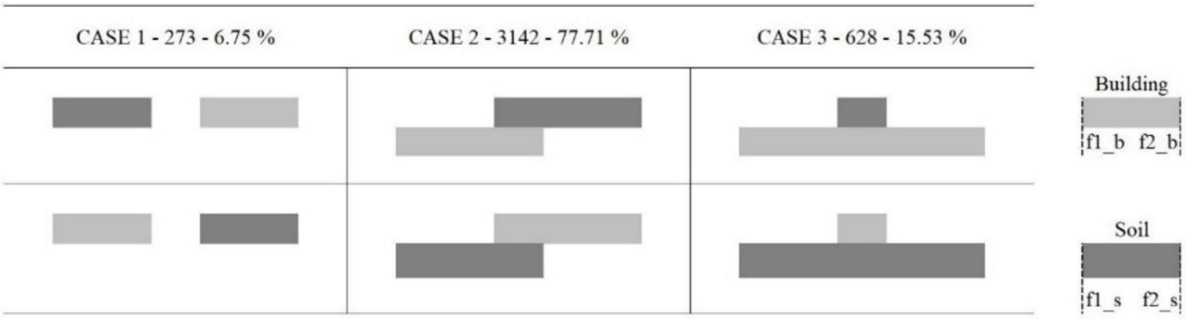

Table 3.1 Cases in which the frequencies of the building (in light grey) overlap (or not) with those of the soil (in dark grey).

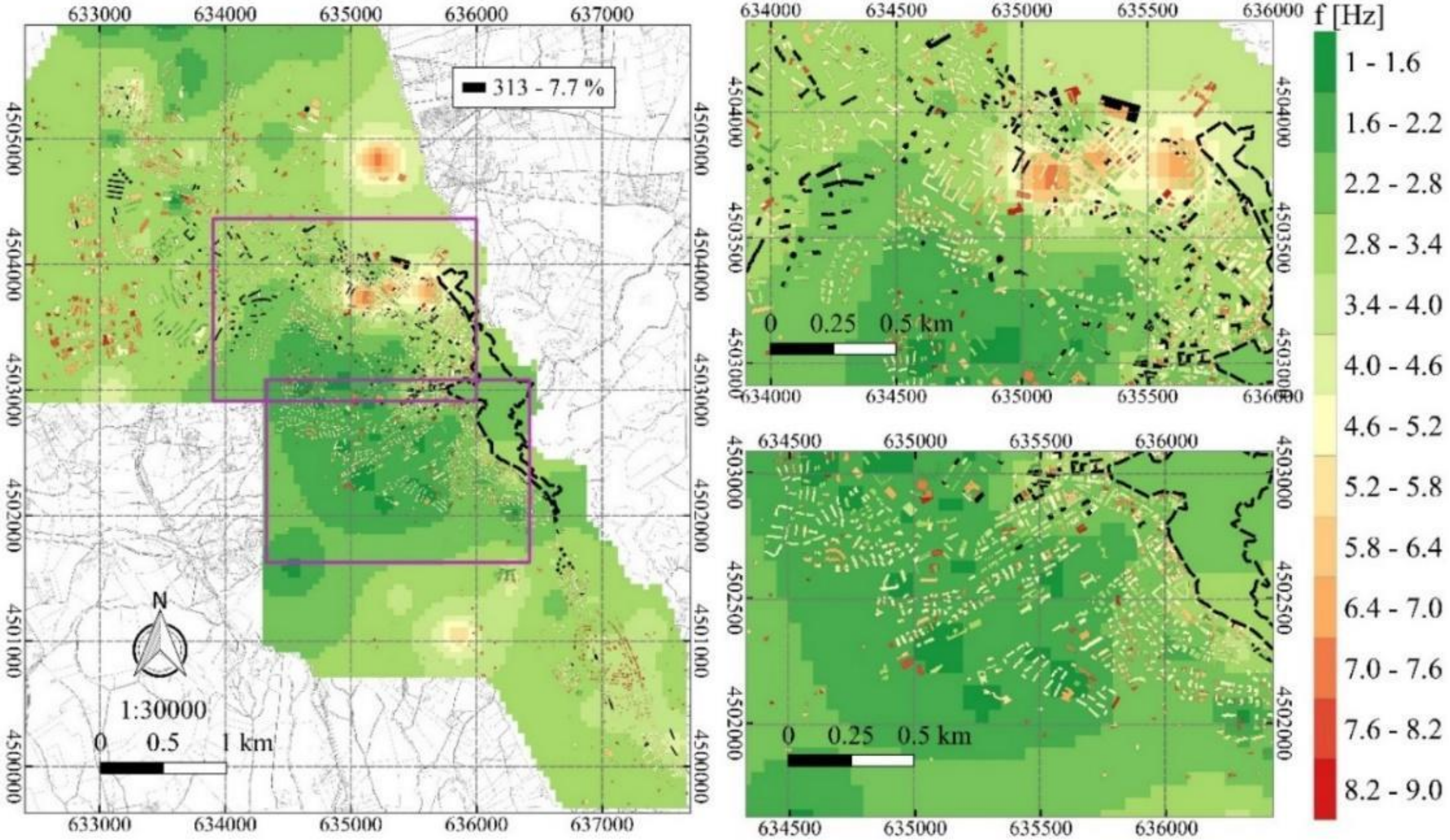

Fig. 3.18 Soil-Building Resonance Map for (left) the entire city of Matera and (rigth) for two enlarged views. The first vibrational frequencies of the buildings (f0_b) and the soil (f0_s) are classified using the same frequency range and colour palette. The buildings with a complete resonance effect with the soil are shown in black.

Therefore, based on the estimated resonance levels, I classified each building and created a spatial map (Figure 3.19) using a traffic light colour system coded by a colour scale from green (low probability of resonance occurring) to red (high probability of resonance occurring). Analysis of the map reveals the following: There is a complete overlap between [f2_b - f1_b] and [f2_s - f1_s] for 628 buildings (15.5%, case 3 in Figure 3.19B). The colour used for this class was red because a heavy resonance level was assigned for these buildings which are located on subApennine clays and on Gravina calcarenite;

- About 5.3% of the buildings (216) are characterised by a large overlap between [f2_b - f1_b] and [f2_s - f1_s]. Most of these buildings are coloured dark orange to indicate a high resonance level;
- The limited overlap between [f2_b - f1_b] and [f2_s - f1_s] concerns 2547 buildings (63%). For these buildings, the colours light orange and light yellow to indicate the average resonance level;
- 652 buildings (16.1%), where there is no overlap or only a very narrow range between soil and building frequencies, are characterised by a low resonance level. These buildings are shown in dark and light green colours.

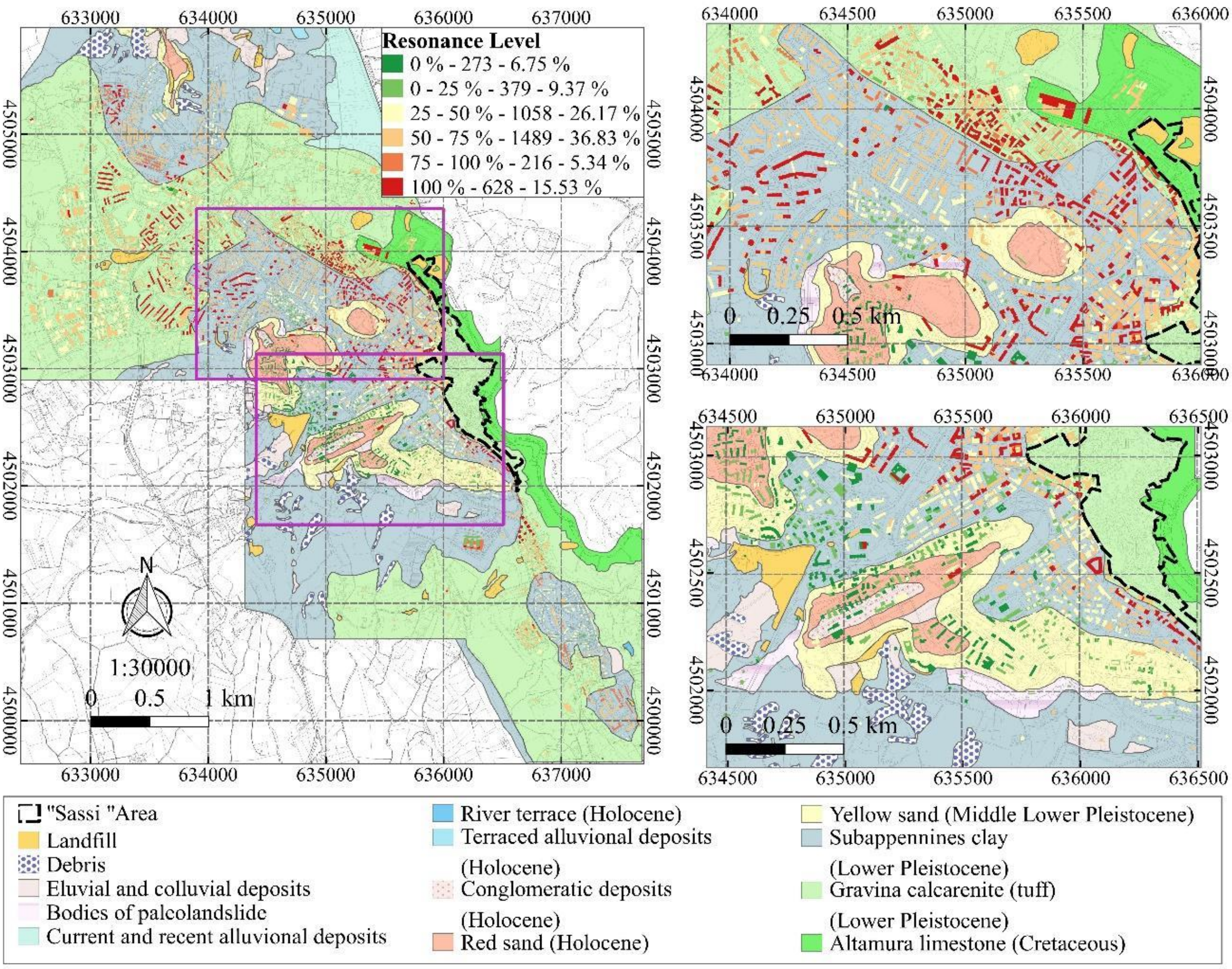

Fig. 3.19 Map of Soil-Building Resonance levels for (left) the entire city of Matera and (right) for two enlarged views, superposed to the detailed geological map.

In addition, this approach allows for further assessments to support mitigation strategies, both on an urban and suburban scale, by combining the geophysical and engineering data contained in the layers; for example, by matching data on the preservation status of buildings with the probability of occurrence of soil-building resonances, one could estimate the number of buildings for which seismic retrofitting is recommended (Figure 3.20).

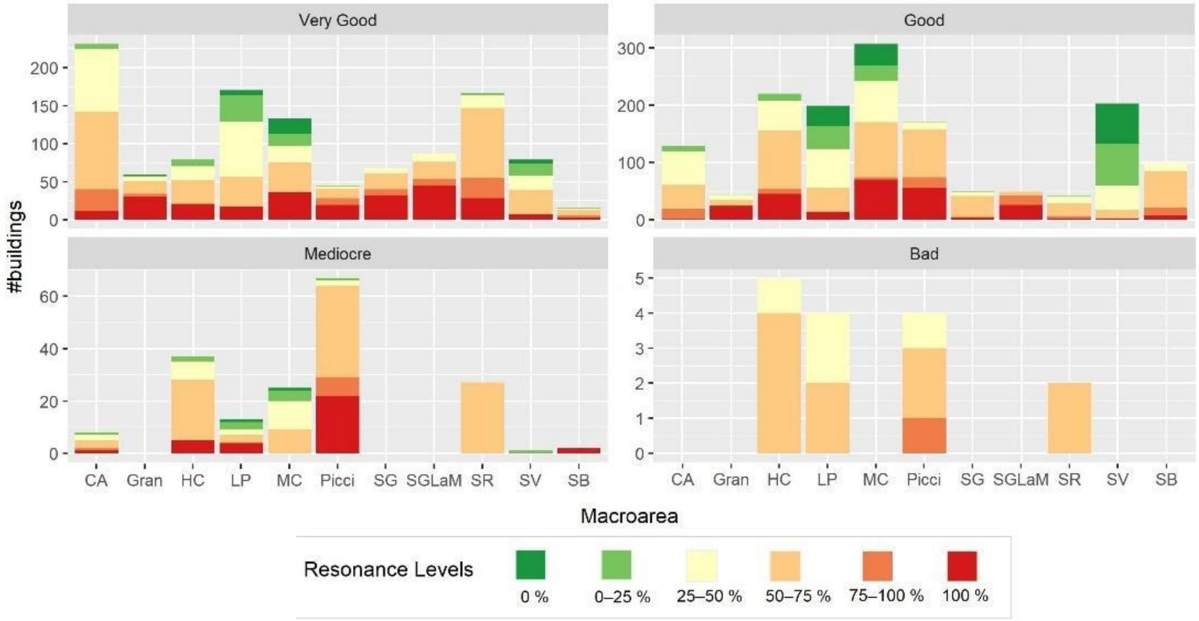

Fig. 3.20 Bar charts showing the number of buildings for each macro-area, highlighting the probability levels of occurrence of resonance and the state of preservation of the buildings (very good, good, mediocre, bad). CA: Cappuccini-Agna; Gran: Granulari; HC: Historic Centre; LP: Lanera-Pini; MC: Macamarda-Castello; Picci: Piccianello; SG: San Giacomo; SGLaM: San Giacomo-Via La Martella; SR: Serra Rifusa; SV: Serra Venerdì; SB: Spine Bianche.

3.2.8 Sharing Soil and Building Geophysical Data for Seismic Characterization of Matera Using CLARA WebGIS

All 'products' obtained from the measurements and subsequent data processing and analysis have been reorganised into a Spatial Data Infrastructure (SDI) using open-source technologies with the dual function of a geodatabase and disseminating WebGIS. The aim of this effort is to visualise and download through web services, un compliance with the Open Geospatial Consortium (OGC) standards: (i) 488 geological, geotechnical, and geophysical data; (ii) the spatial distribution of the main resonance frequency for urban soils; (iii) the main vibrational frequencies for the 4043 buildings; (iv) the spatial distribution of soil–building resonance levels for the urban area of Matera, which represents the innovative core. This is the first time, that the urban environment has been seismically characterised as a unique entity (urban subsoil and overlying buildings), and all data are fully available via CLARA WebGIS which is accessible at https://smartcities-matera-clara.imaa.cnr.it/.

Two types of data sources populate the CLARA WebGIS:

- (i) open data: the Regional Spatial Data Infrastructure of the Basilicata Region (RSDI) [http://rsdi.regione.basilicata.it/] which contains information on the height and use of buildings, the Open-Data (OD) Matera (http://dati.comune.matera.it/) which share information on age and building typology, and (iii) Italian National Institute of Statistics (ISTAT) databases [https://www.istat.it/it/archivio/104317];
- (ii) all experimentally collected geophysical data on shallow soils and buildings. All data are organised into 25 layers with specific vector geometries (Table 4); the queries to the database do not need to use SQL language, allowing the graphical formulation with the hand cursor icon.

CLARA	Vector Geometry	#	Download
OD Age of construction	point	2648	-
OD Typology	point	2648	-
OD State of conservation	point	2648	-
RSDI Height max	point	4522	-
RSDI edifici is	polygon	11,802	-
RSDI unità volumetrica (volumetric unit)	polygon	25,497	-
ISTAT Sassi area	polygon	1	-
ISTAT Census variables	polygon	318	-
Calcarenite Sampling Station	point	8	*
Down hole	point	18	*
HVNSR soil	point	117 (10)	**(*)[1]
HVNSR buildings	point	96 (34)	**(*)
MASW	point	8	*
Mechanical Surveys	point	234	*
Seismic Refraction Surveys	point	7	*
Surface features	point	2	-
Geomorphology	polygon	301	-
Geology	polygon	13	-
MOPS	polygon	52	-
Building resonance level	polygon	4043	-
Building frequency	polygon	4043	-
Soil isofrequency map	polygon	7652	-
Soil isoamplitude map	polygon	7652	-
DSM m (Orthometric Heigths)	raster	-	-
DSM blg Height	raster	-	-

Table 4 Characteristics of all existing objects in the CLARA WebGIS.

[1] ** and ** indicate existing and new geological/geophysical data, respectively, that can be downloaded.*

The large amount of available data for the Matera area has been studied, collected, digitised, and organised. In this part of the thesis work, I addressed the archiving and harmonisation of 319 georeferenced geological, geotechnical, geophysical, and seismic surveys (downholes, mechanical surveys, calcarenite sampling stations, MASW, HVNSR, seismic refraction surveys) in a geodatabase (Figure 3.20). About the 11% of which consists of seismic surveys on buildings (Table 4). In addition to the geological map, the geomorphological and MOPS (homogeneous microzones from a seismic response perspective) maps of urban areas derived from microzonation studies were also digitised and georeferenced. Through the WebGIS user interface, the user can access, visualise, query and download the data by clicking on the geometries.

Information can be viewed at all levels; after clicking on the geometry, the factsheets of all visible geometries located under the selected point (Figure 3.21) can be viewed in the nested mode. Clicking on the hyperlink in the last row of each attribute table allows downloading the data. Please note that ~87% of the survey certificates can be downloaded for geological-technical surveys, while ~12.5% of the data are related to the results collected from previous studies.

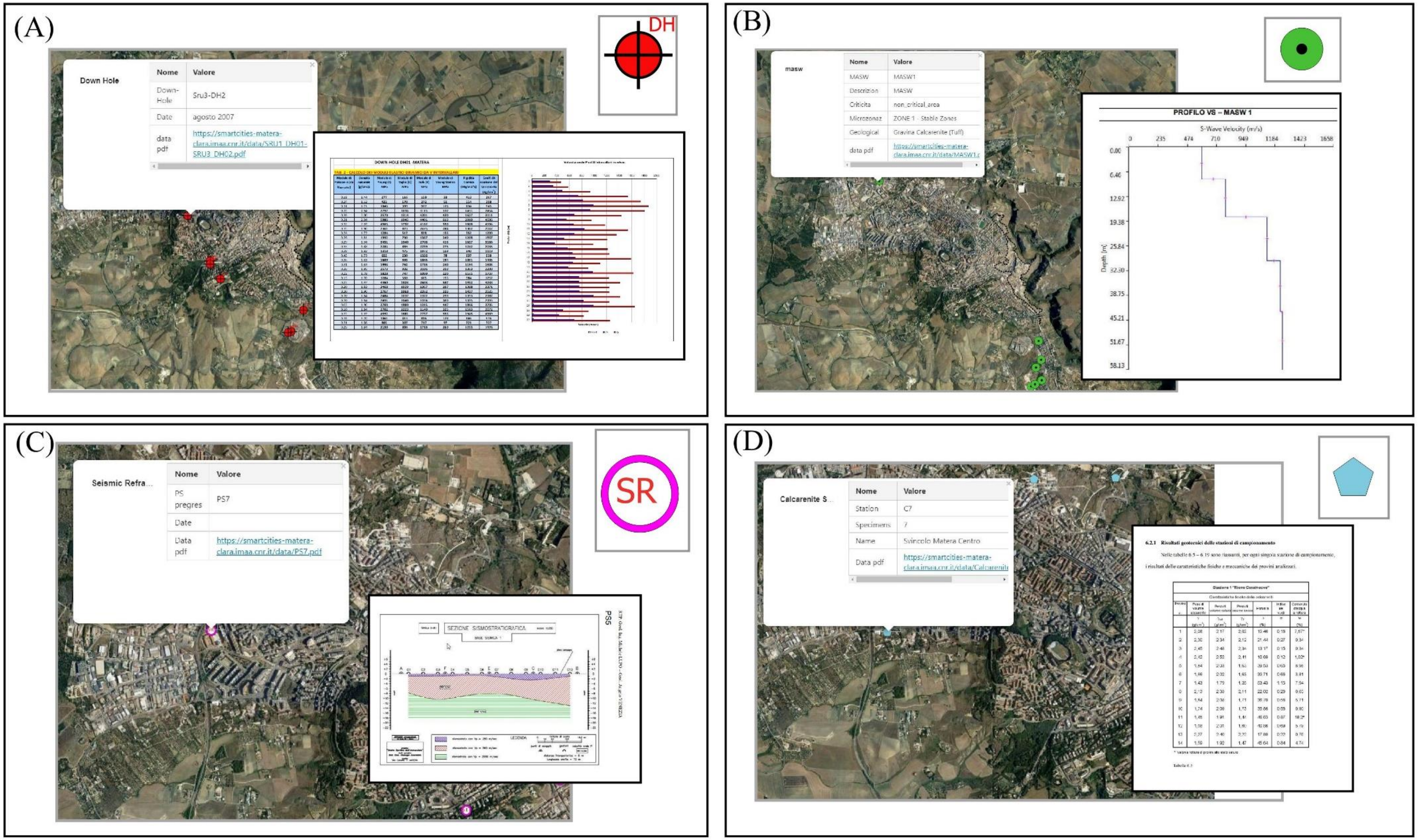

Down Hole

Nome	Valore
Down-Hole	Sru3-DH2
Date	agosto 2007
data pdf	https://smartcities-matera-clara.imaa.cnr.it/data/SRU1_DH01-SRU3_DH02.pdf

masw

Nome	Valore
MASW	MASW1
Descrizion	MASW
Criticita	non_critical_area
Microzonaz	ZONE 1 - Stable Zones
Geological	Gravina Calcarenite (Tuff)
data pdf	https://smartcities-matera-clara.imaa.cnr.it/data/MASW1.p

Seismic Refra...

Nome	Valore
PS pregres	PS7
Date	
Data pdf	https://smartcities-matera-clara.imaa.cnr.it/data/PS7.pdf

Calcarenite S...

Nome	Valore
Station	C7
Specimens	7
Name	Svincolo Matera Centro
Data pdf	https://smartcities-matera-clara.imaa.cnr.it/data/Calcarenit

Fig. 3.21 Examples of factsheets displayed by clicking on the appropriate geometries (polygon in subplot F) or symbols (upper right corner of each subplot A–E), and examples of downloadable files of existing geological/geotechnical/geophysical surveys for (A) downhole; (B) seismic refraction survey; (C) mechanical survey; (D) MASW; (E) calcarenite sampling station; (F) geological map.

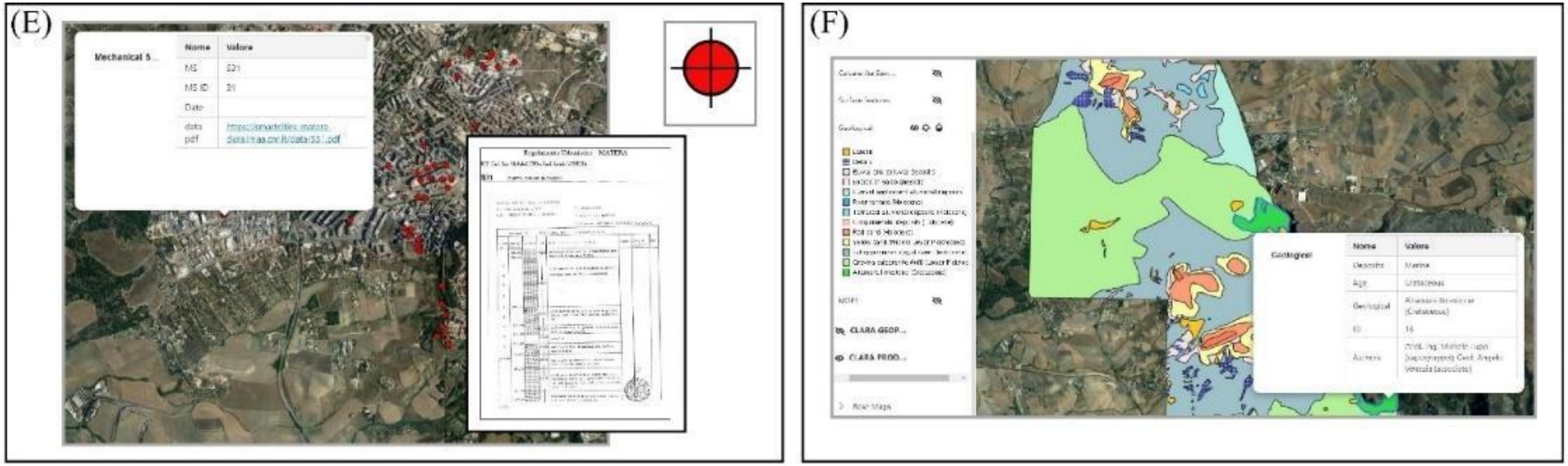

Nome	Valore
MS	S31
MS ID	31
Date	
data pdf	[illegible]

Nome	Valore
Deposits	Marine
Age	Cretaceous
Geological	[illegible]
ID	14
Authors	[illegible]

Fig. 3.21 (continued)

Clicking on the HVNSR point of interest with the hand icon cursor, displays a factsheet with all the information related to that point (Figure 3.22). The thirteen fields shown in the factsheet have been given self-explanatory names: the coordinates or measurement locations in UTM WGS84 33N, EPSG 32633 in 'X' and 'Y' are given; the HVNSR amplitude threshold, that is the value beyond which amplification is considered to occur is indicated by the 'A_Thresold' field; according to the method explained earlier, in 'F0 soil' and 'A0 soil' the value of the soil fundamental resonance frequency (Hz) and the relative amplitude, respectively; 'F1 soil' (<'F0 soil') and 'F2 soil' (>'F0 soil') are the two frequencies (Hz) where the HVNSR curve intersects the 'A_Thresold' value; the hyperlinks to the downloadable HVNSR file in text and curve bmp format are included in the 'Data_asc' and 'Data_bmp' fields; the neighbourhoods whose names are not translatable, except for the 'Historic Center' ('Centro Storico') and the 'Small Business Area' ('Zona Artigianale') (**Piano Strutturale Comunale, 2017**), are indicated in the 'Macro Area' field.

The 96 building HVNSRs in the same point-vector layer, labelled 'HVNSR buildings', were merged. By clicking on a point, the attribute table with fifteen fields with self-explanatory names is available (Figure 3.23): the coordinates (lon, lat) in UTM WGS84 33N, EPSG 32633 are reported in 'X' and 'Y' fields respectively; the building typology (R.C. or masonry) is indicated in 'Type' ; 'F0 blg Hz' refers to the main vibrational frequency of the building, determined by the HVNSR technique; the specific use for which a building was designed and constructed (i.e., residential, commercial, public, etc.) is 'Use'; by clicking on the hyperlink in the 'Data asc zip' and 'Data bmp' fields, the user can download the HVNSR file in text format and the HVNSR curve in bmp format, respectively.

3.2.8.1 CLARA WebGIS results: Soil Iso-frequency, Soil Iso-Amplitude, Building Frequency Distribution, and Soil-Building Resonance Maps

The soil iso-frequency and iso-amplitude maps obtained by interpolation of soil resonance frequency values ('F0 soil Hz') and relative amplitude values ('A0 soil') were uploaded to the WebGIS. By clicking on any cell of the 'Soil iso-frequency' (or 'Soil iso-amplitude') map layer (Figure 1. 70A, B), a factsheet can be displayed in multilevel form containing the interpolated 'F0 soil Hz' or amplitude 'A0 soil' value. Clicking on one of the geometries of 'Building frequency', both the estimated main vibrational frequency of the building 'F0 blg Hz' and the interpolated frequency of its foundation soil 'F0 soil Hz' are displayed in the same factsheet (Figure 3.24C).

The attribute table of this last layer consists of thirteen fields (Figure 1. 70C.2), most of which are taken from the layers shown above. The new field 'Class f b' indicates the class of the frequency range ('F0 b range Hz') to which the building belongs, indicated in the penultimate row of the factsheet.

The core product of this part of my thesis work, the soil – building resonance level map, was also uploaded to WebGIS as well. When the user clicks on any of the 4043 polygons in the 'Soil – building resonance levels' layer, an attribute table with fourteen fields is displayed (Figure 3.25 B). Most of the entries in the factsheet were taken from other layers, except for a field called 'resonance level', which contains the concatenation of three pieces of information: the class of resonance occurrence probability to which the building belongs, the total number of buildings in that class, and the percentage with respect to the analysed building stock (4043).

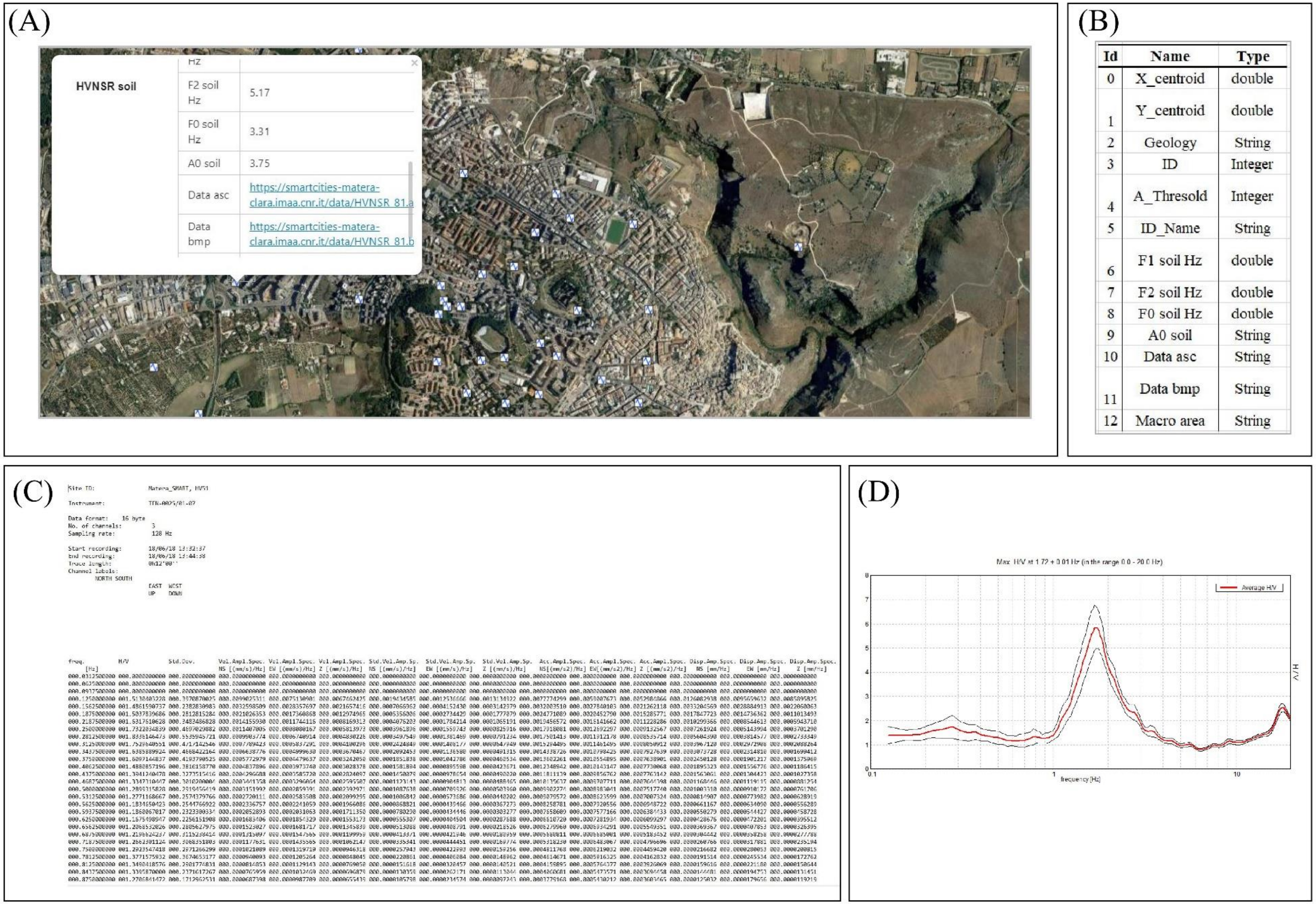

HVNSR soil

Hz	
F2 soil Hz	5.17
F0 soil Hz	3.31
A0 soil	3.75
Data asc	https://smartcities-matera-clara.imaa.cnr.it/data/HVNSR_81.a
Data bmp	https://smartcities-matera-clara.imaa.cnr.it/data/HVNSR_81.b

Id	Name	Type
0	X_centroid	double
1	Y_centroid	double
2	Geology	String
3	ID	Integer
4	A_Thresold	Integer
5	ID_Name	String
6	F1 soil Hz	double
7	F2 soil Hz	double
8	F0 soil Hz	double
9	A0 soil	String
10	Data asc	String
11	Data bmp	String
12	Macro area	String

```
Site ID:                Matera_SMART, HV51

Instrument:             TRN-0025/01-07

Data format:    16 byte
No. of channels:         3
Sampling rate:           128 Hz

Start recording:        18/06/18 13:32:37
End recording:          18/06/18 13:44:38
Trace length:           0h12'00''
Channel labels:
        NORTH SOUTH
                        EAST  WEST
                        UP    DOWN

freq.       H/V         Std.Dev.    Vel.Ampl.Spec. Vel.Ampl.Spec. Vel.Ampl.Spec. Std.Vel.Amp.Sp. Std.Vel.Amp.Sp. Std.Vel.Amp.Sp. Acc.Ampl.Spec. Acc.Ampl.Spec. Acc.Ampl.Spec. Disp.Amp.Spec. Disp.Amp.Spec. Disp.Amp.Spec.
   [Hz]                             NS [(mm/s)/Hz] EW [(mm/s)/Hz] Z [(mm/s)/Hz]  NS [(mm/s)/Hz]  EW [(mm/s)/Hz]  Z [(mm/s)/Hz]   NS[(mm/s2)/Hz] EW[(mm/s2)/Hz] Z [(mm/s2)/Hz] NS [mm/Hz]     EW [mm/Hz]     Z [mm/Hz]
```

Fig. 3.22 (A) Pop-up window showing the factsheet of a sample measurement (HVNSR_51) on soil; (B) types of attributes; screenshots of the downloadable (C) HVNSR text file and (D) HVNSR curve bmp file.

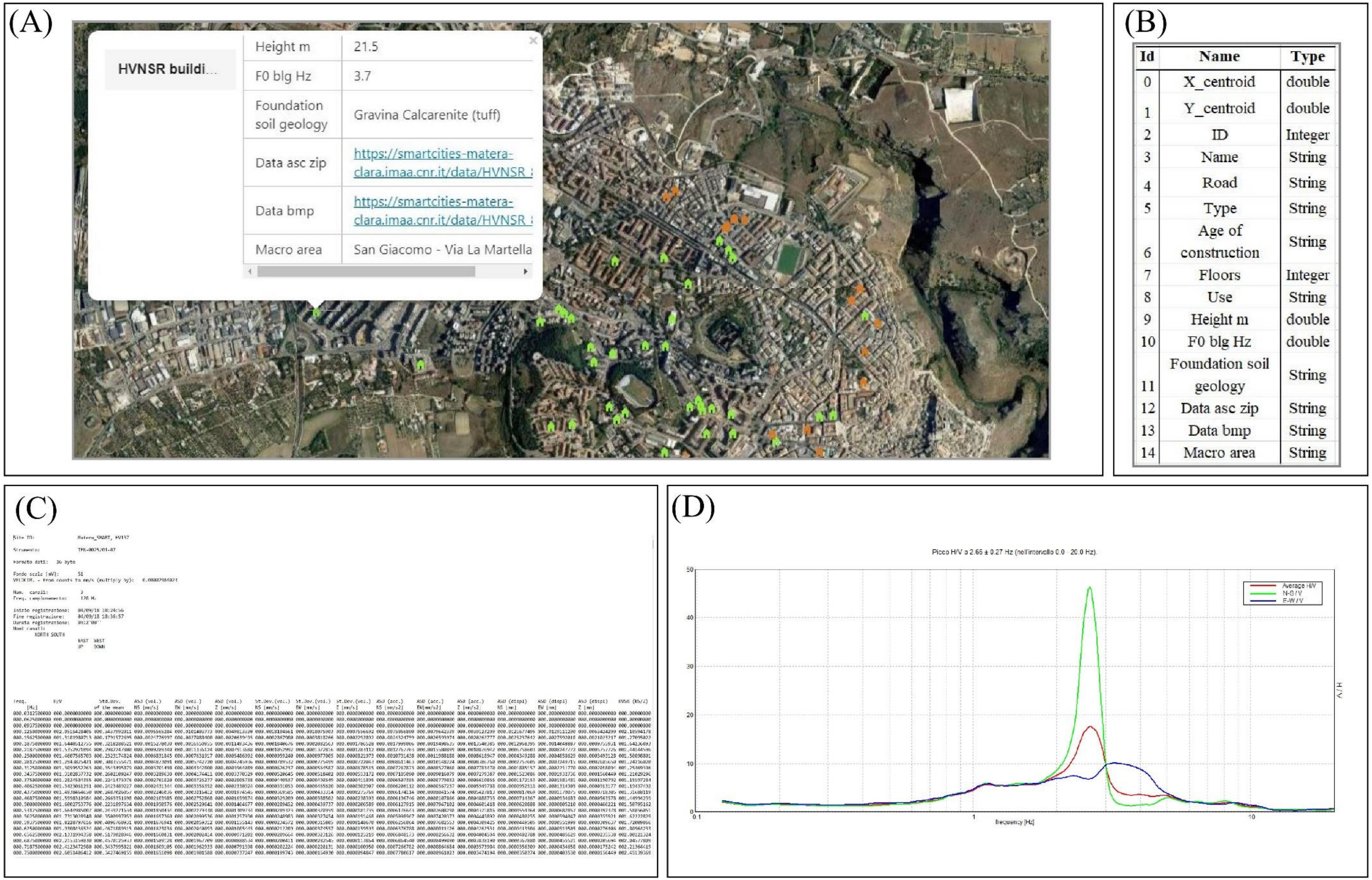

HVNSR buildi...	
Height m	21.5
F0 blg Hz	3.7
Foundation soil geology	Gravina Calcarenite (tuff)
Data asc zip	https://smartcities-matera-clara.imaa.cnr.it/data/HVNSR
Data bmp	https://smartcities-matera-clara.imaa.cnr.it/data/HVNSR
Macro area	San Giacomo - Via La Martella

Id	Name	Type
0	X_centroid	double
1	Y_centroid	double
2	ID	Integer
3	Name	String
4	Road	String
5	Type	String
6	Age of construction	String
7	Floors	Integer
8	Use	String
9	Height m	double
10	F0 blg Hz	double
11	Foundation soil geology	String
12	Data asc zip	String
13	Data bmp	String
14	Macro area	String

```
Site ID:                Matera_SMART, HV137

Strumento:              TEN-0025/01-07

Formato dati:   36 byte

Fondo scala [mV]:       51
VELOCIM. - from counts to mm/s (multiply by):   0.00002984023

Num.  canali:            3
Freq. campionamento:     128 Hz

Inizio registrazione:   04/09/18 18:24:56
Fine registrazione:     04/09/18 18:36:57
Durata registrazione:   0h12'00''
Nomi canali:
        NORTH SOUTH
                        EAST  WEST
                        UP    DOWN
```

Fig. 3.23 (A) Pop-up window showing the factsheet of a sample measurement (HVNSR_69) on an R.C. building; (B) attribute types; screenshots of the downloadable (C) HVNSR text file and (D) HVNSR curve bmp file.

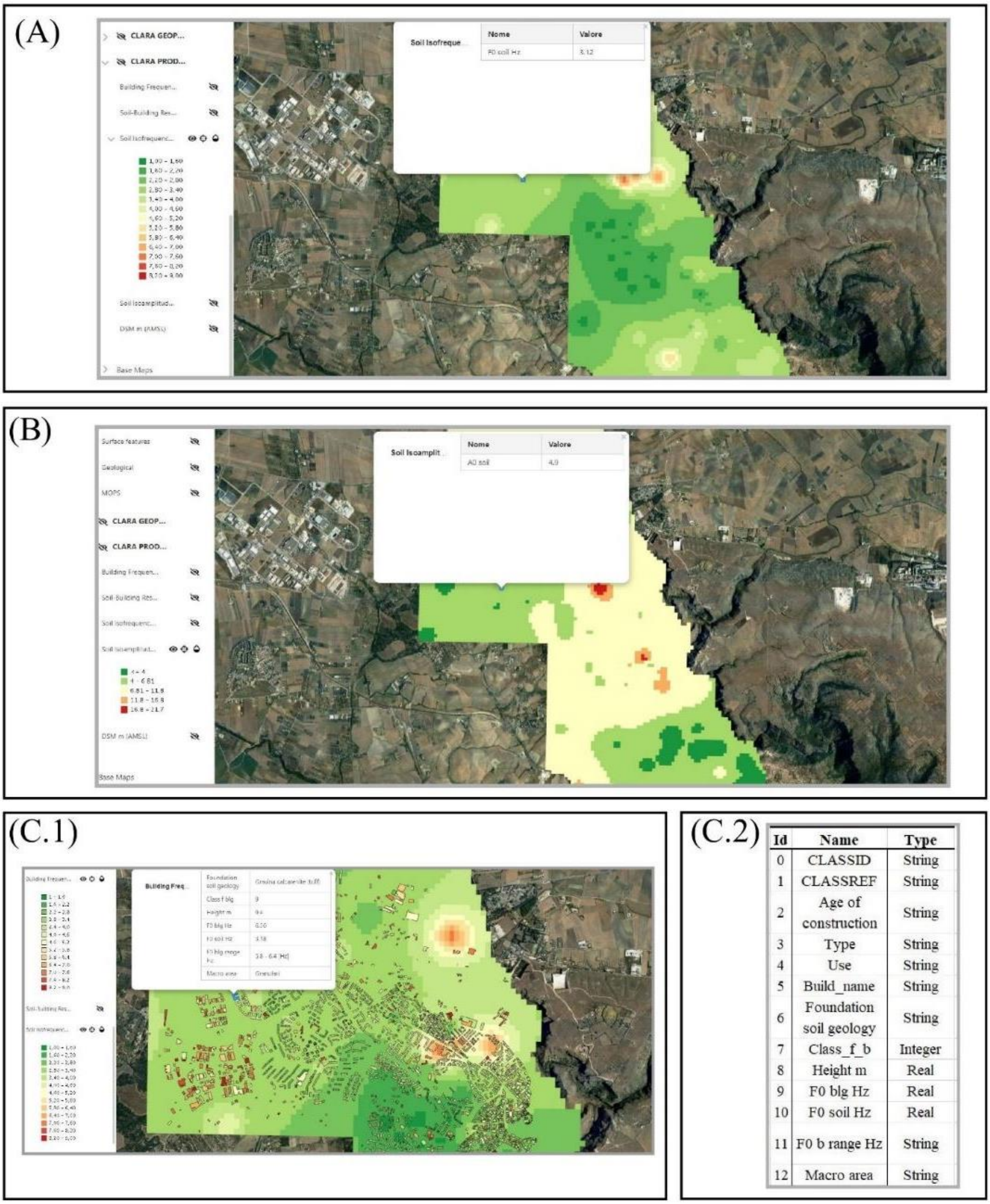

Soil Isofreque...

Nome	Valore
F0 soil Hz	3.12

Soil Isoamplit...

Nome	Valore
A0 soil	4.0

Building Freq...

Foundation soil geology	Gravina calcarenite tuff
Class f blg	9
Height m	9.4
F0 blg Hz	6.00
F0 soil Hz	3.18
F0 blg range Hz	3.8 - 6.4 [Hz]
Macro area	Granulari

Id	Name	Type
0	CLASSID	String
1	CLASSREF	String
2	Age of construction	String
3	Type	String
4	Use	String
5	Build_name	String
6	Foundation soil geology	String
7	Class_f_b	Integer
8	Height m	Real
9	F0 blg Hz	Real
10	F0 soil Hz	Real
11	F0 b range Hz	String
12	Macro area	String

Fig. 3.24 Screenshot of map view and pop-up window showing (A) soil iso-frequency map; (B) soil iso-amplitude (C.1) building frequency distribution overlying soil iso-frequency map. The building frequency layer has an attribute table composed of thirteen fields (C.2)

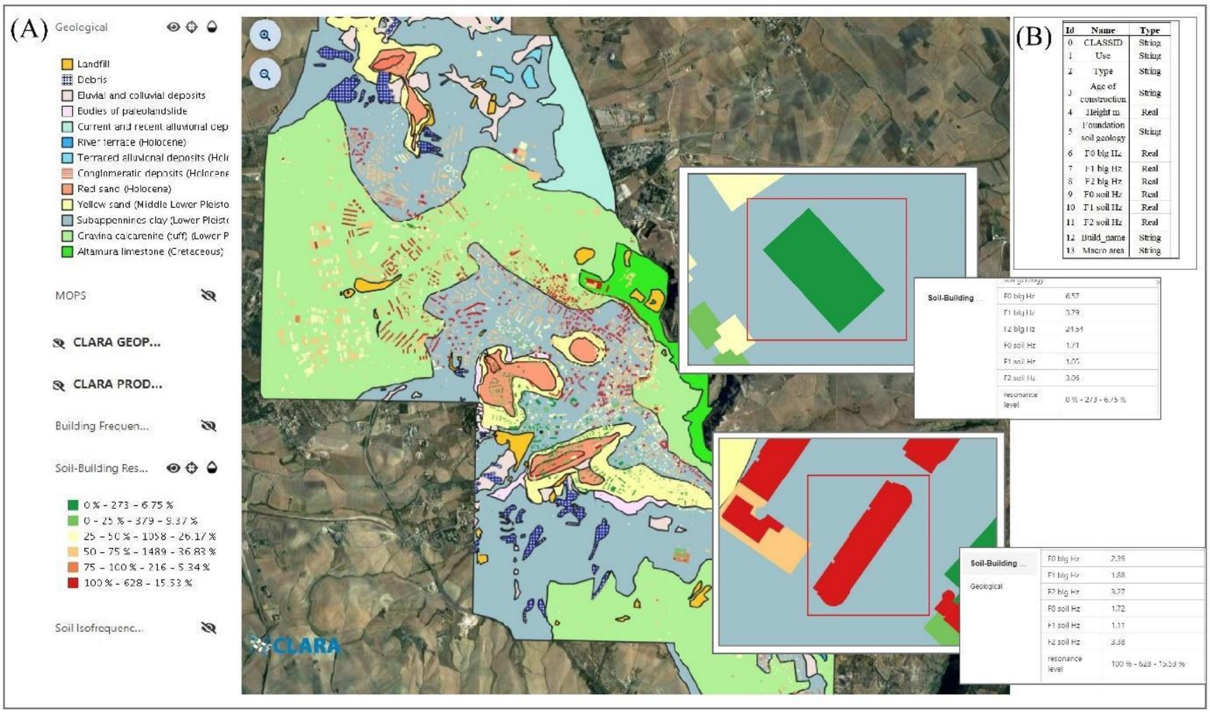

Soil-Building

F0 blg Hz	6.57
F1 blg Hz	3.79
F2 blg Hz	21.54
F0 soil Hz	1.71
F1 soil Hz	1.05
F2 soil Hz	3.06
resonance level	0 % - 273 - 6.75 %

Soil-Building ...

Geological

F0 blg Hz	2.39
F1 blg Hz	1.88
F2 blg Hz	3.27
F0 soil Hz	1.72
F1 soil Hz	1.11
F2 soil Hz	3.38
resonance level	100 % - 628 - 15.53 %

Id	Name	Type
0	CLASSID	String
1	Use	String
2	Type	String
3	Age of construction	String
4	Height m	Real
5	Foundation soil geology	String
6	F0 blg Hz	Real
7	F1 blg Hz	Real
8	F2 blg Hz	Real
9	F0 soil Hz	Real
10	F1 soil Hz	Real
11	F2 soil Hz	Real
12	Build_name	String
13	Macro area	String

Fig. 3.25 (A) Screenshot of the soil–building resonance levels overlaying the geological map in the Matera urban area. The insets show two examples: a red-coloured building with ‘F1 blg Hz’ and ‘F2 blg Hz’ values within the interpolated soil frequency range (100% probability of resonance occurrence), and a green-coloured building with 0% probability of resonance occurrence, together with the associated pop-up windows; (B) attribute table of soil-building resonance level layer.

3.2.9 Discussion

In this section a potentially useful approach for the identification of the areas and buildings of the city for which the resonance effect can induce an increase in damage during an earthquake is proposed. The seismic characteristics of shallow soils and the soil - buildings interaction evaluation effects at different sites could be thus studied adopting the approach proposed here.

The intersection between soil and building frequency ranges above a certain amplitude threshold, corresponding to the estimated resonance levels, should not be considered as ‘magic’ deterministic numbers, but must be specifically examined on a case-by-case basis. The proposed methodology inevitably involves some uncertainties: i) the uncertainty of the measurements; ii) the uncertainty of the resonance frequency and amplitude, i.e. of the HVNSR analysis of the measurements; iii) the technique used for the spatial interpolation of the resonance frequencies (fo, f1_* and f2_*); iv) the statistical inference on the T vs H relationship; vi) the frequency ranges chosen and vi) the geological mapping together with its digitization in the GIS. Regarding the latter, it should be noted, for example, that 249 buildings are located near the geological boundaries, resulting in an uncertain assignment of the buildings to the geological classes.

However, thanks to the knowledge of the spatial distribution of the site effects in terms of amplification effect, the primary characteristics of buildings, and of soil-building resonance levels estimations, a three-part objective have been achieved: (i) through CLARA's WebGIS every citizen is aware of the characteristics of buildings and foundation soils, so this knowledge makes each individual citizen more resilient to the effects of a seismic event; (ii) preventing the potential losses in economic and social terms; (iii) reducing recovering phase time to facilitate the return of the urban system to equilibrium pre-existing conditions.

Sharing the basic principle according to which the use of the areas potentially exposed to seismic amplification and to the related secondary effects (road obstruction, interruption of services, slowdown of rescue services, etc.) should be more carefully regulated, then the mapping of the soil-building resonance level estimation becomes crucial for the implementation of mitigation and prevention strategies (urban planning laws, land-use planning, planning for intervention in emergencies and to manage post-earthquake crises). For years, the need of creating for each building a certificate containing all available information have been discussing in the technical and scientific communities. CLARA WebGIS contains both basic information on each building (height, age of construction, typology, use, etc.) and geological/geotechnical data of the relative foundation soil, namely the estimates of the fundamental frequency of all urban soils and the vibrational frequency in the linear elastic domain for 4043 buildings within the urban area. Such information constitutes invaluable knowledge for freelance engineers, as it is key for numerical models of seismic retrofitting. CLARA WebGIS allows further evaluations in support of mitigation strategies, both on an urban and suburban scale, thanks to the availability of open data such as geophysical and engineering data contained in the layers.

3.3 Analytical vs experimental soil-structure interaction effects assessment at neighborhood scale

The soil-structure interaction effects on the dynamic response of masonry buildings in the linear domain can be evaluated through simplified analytical approaches based on the traditional model of compliant-base oscillator (**Veletsos and Meek, 1974**; **Maravas et al., 2014**). However, these approaches are strictly valid under extremely simplified assumptions of homogeneous subsoil and regular foundation, while in the cases of stratified subsoil and/or irregular foundation geometry the application is problematic. For these reasons, **Piro et al. (2020)** proposed a procedure, summarised in the flowchart in Fig. 3.26, based on 'equivalent parameters' extending the traditional analytical formulation and allowing the simplified analytical formulae to be applied in cases of more complex and realistic layered soil and irregular geometry of the foundation.

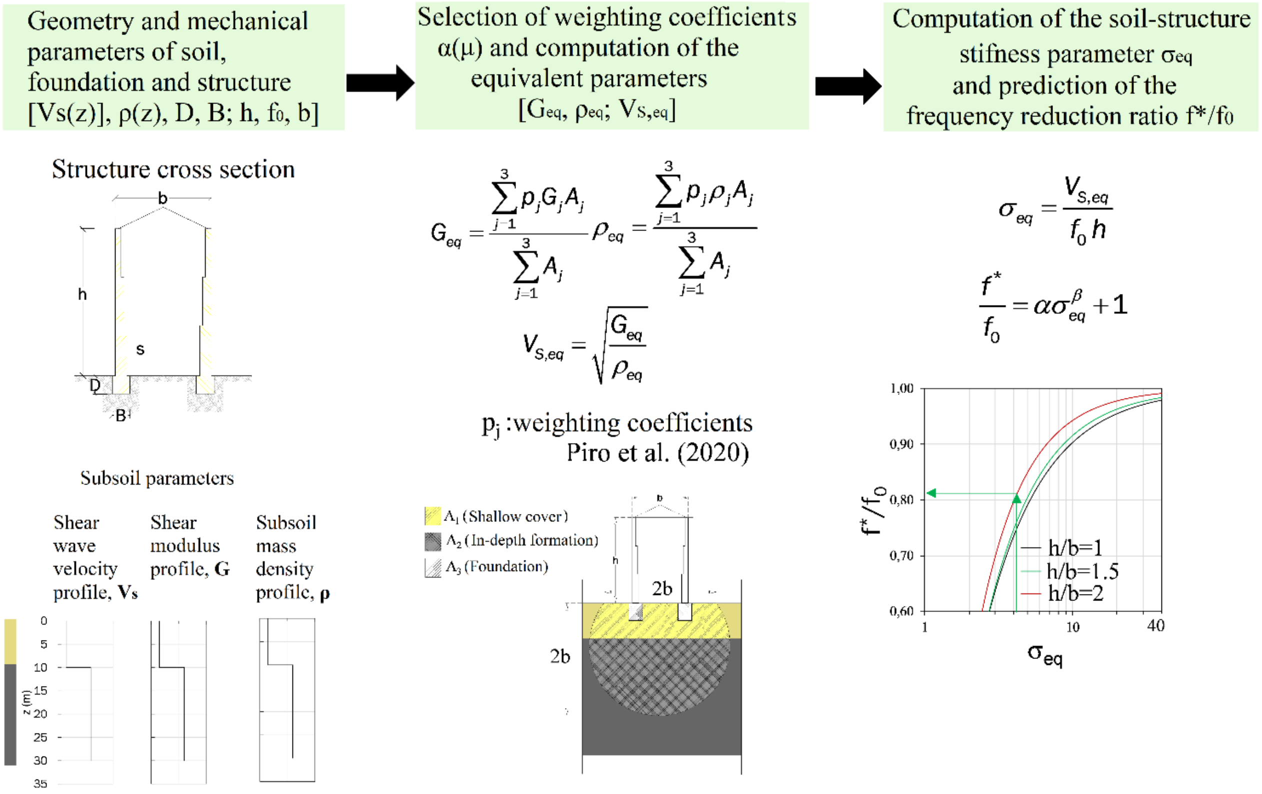

Fig. 3.26 Flow chart of the adopted methodology in the study of Piro et al., 2020 proposed for the estimation of the frequency reduction ratio f/f0.*

The procedure proposes to compare the analytical results obtained from traditional approaches and those of linear dynamic analyses on complete subsoil-foundation-structure (SFS) models, assuming alternative configurations of the foundation system (embedded floating foundation or underground storey), a variable number of floors (two, three or four) and different subsoil profiles (homogeneous or layered models). Figure 3.26 shows that the adoption of the approach of **Piro et al. (2020)** for estimating the frequency of existing masonry buildings; it requires the following data:

- the embedment D and width B of the foundation system;
- the height h, width b, and fixed-base frequency f_0 of the structure;
- the shear wave velocity profile V_S of the soil, and the mechanical properties (shear stiffness modulus, G, and density, ρ) of the materials resting within the significant volume affected by the kinematic motion in the foundation, which is assumed to extend 2b at the surface and in depth (indicated by the areas A_j in Fig.3.26).

In order to consider the influence of the foundation embedment and the layered subsoil, weight coefficients, p_j, were derived to calculate the equivalent values, in the significant volume, of both the shear stiffness modulus, G_{eq}, and the density ρ_{eq}. With these values, the 'equivalent shear wave velocity', V_{Seq}, and the 'equivalent subsoil-structure relative stiffness', σ_{eq}, are derived. Finally, knowing the slenderness ratio, h/b, of the case study, the frequency variation f^*/f_0 (where f* is the frequency of the subsoil-foundation-structure system) is estimated as a function of σ_{eq} through the expression shown in Fig. 3.26, where α and β are coefficients provided by **Piro et al. (2020)** as a function of h/b.

3.3.1 Application of the approach to the case study of Matera buildings

The procedure described above was validated with reference to the study (section 3.2) conducted in the city of Matera (Figure 3.26). For this section of the study, were selected seven buildings for which all soil and structural data necessary for the analytical model were available. This validation phase was conducted in collaboration with Prof. Silvestri of the University of Naples Federico II in the framework of DPC-ReLUIS 2019-2021 project.

The main geological formations (Fig. 3.26a) outcropping in the north-west and south-east areas of the urban centre, as well as in the 'Sassi' area, are Altamura limestone (AL) and Gravina calcarenite (GC). The latter lies beneath a deposit of Sub-Apennine clay (SC) with thicknesses varying from a few metres, in the area near the Sassi, to 40-50 m in the innermost area. The subsoil has been extensively investigated through numerous geognostic investigations, down-hole tests and refraction seismic tests (**Gallipoli & Lupo, 2012**), showing how the thickness of the clays increases from 7 m to 40 m, moving from east to west, i.e., as the distance from the calcarenite outcrop increases (Sassi area). The shear wave velocities of the different materials (Table 3.4) were obtained from both down-hole and refraction seismic tests, performed in the vicinity of the selected buildings, while for the density of each material, reference was made to typical values for soft clays (SC), soft rocks (GC) and hard rocks (AL). The properties reported in Italian Technical Code (abbreviated here as **NTC'18**; cf. **MIT 2018**) were assigned to the masonry, for tuff masonry with irregular texture, as it represents the typical masonry type in the historic centre near the "Sassi" area.

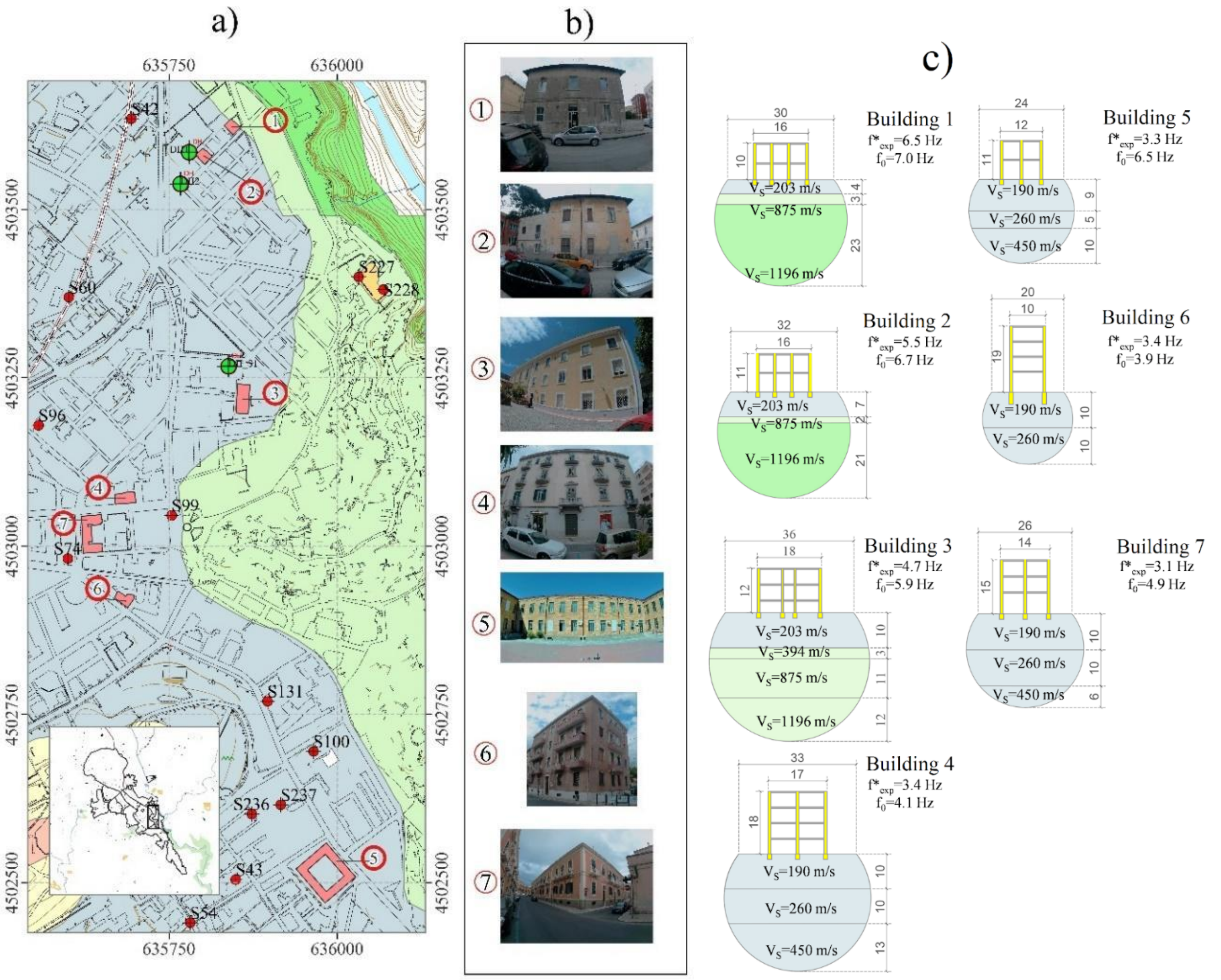

Fig. 3.26 (a) Geological map with the location of subsoil surveys (red dot geognostic investigations; green dot: down-hole) and selected buildings of the study (red circle); (b) photos of the examined buildings; (c) soil-foundation-structure, SFS reference schemes for the application of the simplified method

	sub-Appenine clay (SC)	Gravin a Calcarenite (GC)	Altamura limestone (AL)	Tuff masonry
V_S(m/s)	190 - 450	394 - 1195	945	-
ρ (kg/m^3)	1750	1950	2750	1600
G_0 (MPa)	63 - 254	303 - 3934	2456	450

Table 3.4 Mechanical properties of different materials

In Table 3.5 the height (h) and the dimension at the base of the buildings (length b_L; width b_T) are reported. These values were taken from the created database, while the thickness (s) of the masonry, the enlargement on each side of the load-bearing walls at the foundation level, and the foundation embedment (D) was obtained from relationships, empirical data and correlations used in the practice of art for the design of masonry buildings (**Augenti & Parisi, 2019**). These relationships correlate the number of storeys to the thickness of the masonry. A thickness s = 0.70 m was assumed for two-storey buildings, for three-storey buildings s = 0.81 m, for four-storey buildings s = 0.93 m and for five-storey buildings s = 1.03 m. The width of the foundation was estimated by adding 0.15 m to each side of the elevation walls, while the depth of the laying surface was set at 1.5 m for two- and three-storey buildings and 2.00 for four- and five-storey buildings. The fixed-base period ($T_0 = 1/f_0$) was estimated from the obtained correlation with height ($T_0 = 0.0137h$) from spectral ratios measured on masonry buildings in the urban centre of Matera founded on calcarenite (Figure 3.27).

ID	Number of storeys	*s(m)*	*D (m)*	*h (m)*	$b_T(m)$	$b_L(m)$
1	2	0.70	1.50	10	16	19
2	2	0.70	1.50	11	16	19
3	3	0.81	1.50	12	18	43
4	4	0.93	2.00	18	17	31
5	2	0.70	1.50	11	12	67
6	5	1.03	2.00	19	10	25
7	3	0.81	1.50	15	14	55

Table 3.5 Geometrical features of the case studies buildings of the case study.

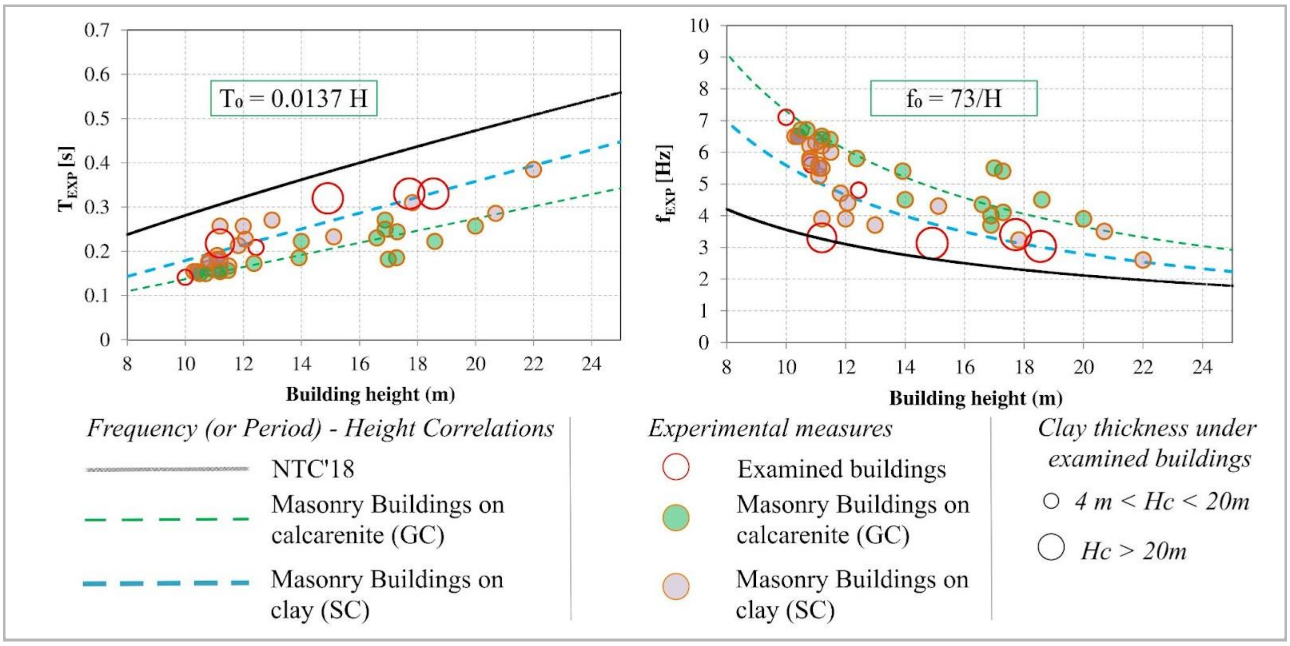

3.27 Empirical correlations between experimental measured period (or frequency) and height of masonry buildings from case studies [founded on calcarenite (green dashed line) or clayey soil (blue light dashed line)] and comparison with their code-based analytical counterpart (black dotted line). For the T_0 (resp. f_0) vs H relationship related to masonry buildings on calcarenite, the empirical relationships in the plots are reported. Red circle: examined buildings founded on sub-Apennine clay.

Fig. 3.26c shows the cross-sections of the seven analysed SFS systems, considering the stratigraphy obtained from the closest geognostic investigations. The main characteristics of each building are also shown: height, h, base, b_T, fixed base frequency, f_0 and experimental frequency, f^*_{EXP}, measured along the building cross-section. With reference to buildings 1, 2 and 5, it can be observed, how, with the same number of floors, the fundamental frequency decreases as the thickness of the clays increases, highlighting the influence of this aspect on the interaction of the ground structure (Figure 3.28).

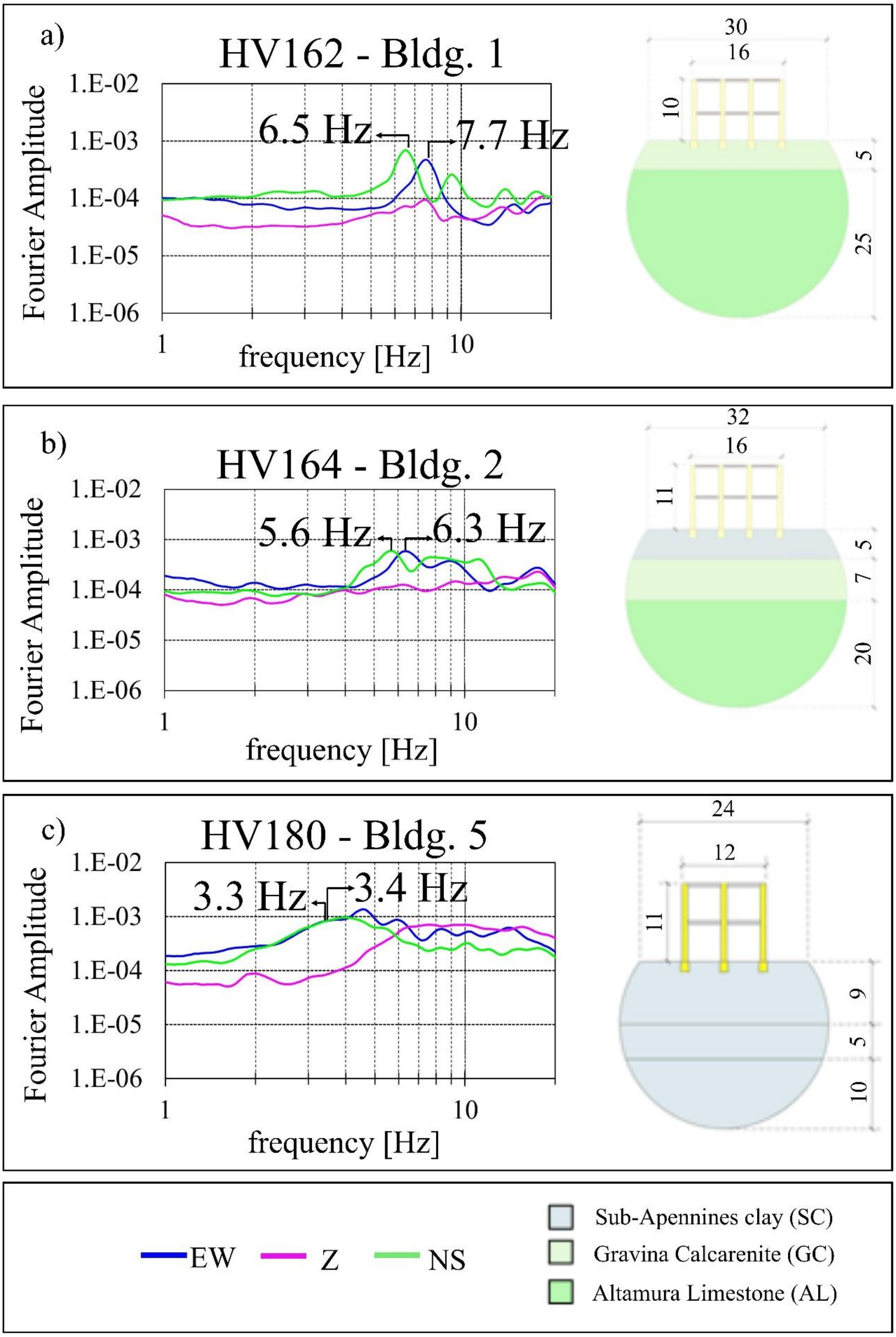

Fig. 3.28 Fourier amplitude spectra of the recorded seismic ambient noise elaborated with the non - reference method HVNSR and soil-foundation-structure, SFS reference schemes for the masonry buildings a) 1, b) 2, and c) 5selected for this part of the study. (blue line - East-West horizontal component; green line: North-South horizontal component; fuchsia line: vertical component). Next to the building number, the measurement identifier is reported for the information collected in the study to be checked at this link (https://smartcities-matera-clara.imaa.cnr.it/)

Once all the parameters of the SFS system were defined, the weight coefficients, p_j, were assigned by comparing the seismic impedance ratios, μ, between the shallow cover and the foundation soil that characterise the significant volume below the analysed buildings with those used in the parametric study by **Piro et al. (2020)** for different stratigraphy-types. The latter were obtained by combining the subsoil categories B, C and D according to **NTC'18**, in order to obtain D-B, D-C and C-B sequences. Following the procedure described in Fig. 3.25, the equivalent parameters G_{eq}, ρ_{eq} and $V_{S,eq}$ were thus calculated, and finally the corresponding value of f^*/f_0.

Figure 3.29 shows the comparisons between the experimental periods, T^*_{EXP}, and those obtained by applying the simplified method, T^*. The latter were calculated using both the method based on the equivalent parameters (empty symbols) of **Piro et al. (2020)** and the traditional approach (full symbols) based on the formulation of **Veletsos & Meek (1974)**, i.e. in the calculation of (equation in Figure 3.25) the shear wave velocity of the soil layer at the bedding plane was used as the shear wave velocity. It is observed that the periods obtained from the traditional formulation are always greater than the experimental values in almost all cases. On the contrary, the period values obtained with the method proposed by **Piro et al. (2020)** are very close to the experimental ones, highlighting how the procedure is promising for expeditive estimations or in any case for identifying situations in which the effects of soil-structure interaction must be taken into account.

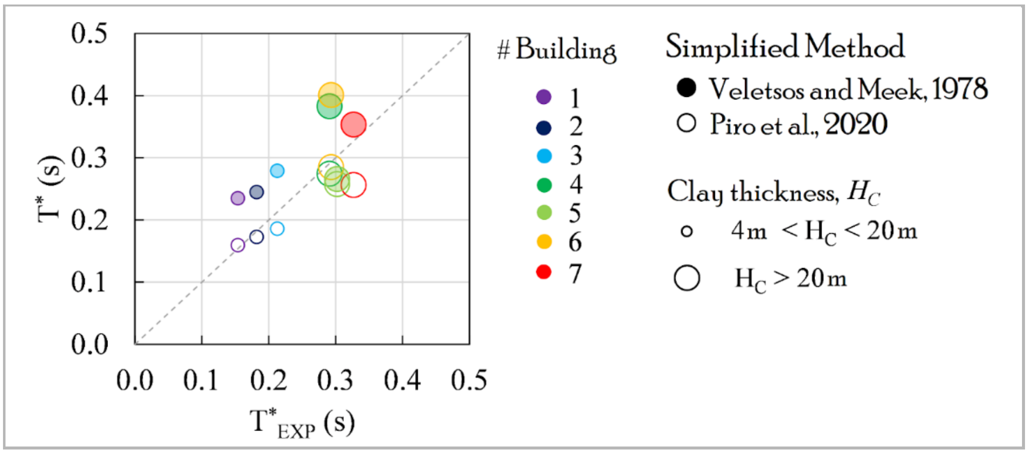

Fig. 3.29 Comparison between experimental and analytical periods; the analytical periods are calculated using both the ***Veletsos and Meek, 1978****, and the* ***Piro et al., 2020*** *approach.*

Chapter 4: An integrated geophysical approach for the structural characterization and the soil interaction assessment of a road infrastructure: the Gravina Bridge case study

In this part of the thesis, a geophysical approach composed of several geophysical techniques is applied to a road infrastructure, the Gravina Bridge in southern Italy. For this purpose, different experimental data acquisition (sections 4.3) and analysis techniques (sections 4.2.1 and 4.4) were used to characterise the foundation soil (resistivity values, fundamental frequency, and seismo-stratigraphic model) and estimate the primary modal parameters of the infrastructure (eigenfrequencies, mode shapes, equivalent viscous damping ratio, ambient noise wave propagation velocities).

Introduction

Bridges are critical infrastructures that form the backbone of the road network in all regions of the world and play a strategic role directly linked to the economic development of a nation. However, in Italy, a continuous deterioration of the road network is observed, as the load-bearing capacity of most bridges is decreasing due to ageing. There are many examples of recent infrastructure collapses both in Italy and worldwide (Harbin Yangmingtan Bridge, China, 2012; North America footbridge, Miami Florida, 2018; Morandi Bridge, Genoa, 2018; Albiano Magra Viaduct collapse, Tuscany, 2020). Structural Health Monitoring (SHM) plays a key role in averting these catastrophic events by managing the critical infrastructures service-life and by taking advantage of technological development and sensor innovation through the collection and validation of accessible operational data. Understanding the extent of degradation over time and its impact on the remaining service-life and capacity of strategic civil engineering structures is essential for owners/managing companies/operators to make well-informed decisions about how to optimise the repairs. Traditional bridge maintenance policies are primarily based on visual inspections of a built structure, focusing mainly on the typical failure points. These practices are unlikely to detect damage at an early stage, they are very expensive and labour intensive and, most importantly, they rely on subjective data, as the accuracy and reliability of inspections often depend on a combination of factors (**Moore et al., 2001**). Nowadays, the professional community is trying to move to a measurement-based, objective approach. For example, the new Italian "Guidelines for the Classification and Risk Management, Safety Assessment and Monitoring of Existing Bridges" (**Bridges Guidelines, MIT 2020**) take a multi-level approach (census, visual inspections, analysis of relevant risks, and classification on a territorial level). The code recommends a risk-based strategy with instrumental monitoring measures and occasional dynamic testing to determine dynamic properties. Over the years, SHM has evolved into a measurement-based objective approach using a combination of non-destructive testing for retrieving changes in main structural characteristics over time (**Ponzo et al., 2010**; **Ditommaso et al., 2012, 2015**; **Ditommaso and Ponzo, 2015**; **Iacovino et al., 2018**; **Gallipoli et al., 2020**). This new concept of SHM systems allows scheduled maintenance without excessive costs for estimating the operational performance of buildings and bridges to minimise infrastructure downtime. **Orcesi and Frangopol (2011)** highlighted that the spatial and temporal update of numerical prediction models can be facilitated by a field calibration model using SHM data. In fact, ''there is no better way for a bridge engineer to understand the shortcomings of the mathematical models used for design or evaluation of bridges than to investigate the behaviour through field testing'' (**Bakht and Jaeger, 1990**). **Karbhari and Lee (2010)** defined SHM as ''the use of in-situ, non-destructive sensing and analysis of structural characteristics, including the structural response, for the purpose of estimating the severity of damage/deterioration and evaluating the consequences thereof on the structure in terms of response, capacity, and service-life''. Automated seismic and operational monitoring of several bridges around the world is ongoing (**Magalhães et al., 2012**; **Cross et**

al., 2013; **Gentile and Saisi**; **2015**, **Sun et al., 2017**; **Çelebi et al., 2019**). The evaluation of possible differences in modal parameters before and after seismic events due to earthquake-induced damage (**Snieder et al., 2007**; **Picozzi et al., 2010, 2011**; **Ponzo et al., 2010**; **Iacovino et al., 2018**; **Gallipoli et al., 2020**; **Ditommaso et al., 2021**) or before and after retrofit (**Çelebi and Liu, 1998**) has always been of interest to the technical and scientific communities. The estimation of modal parameters (eigenfrequencies, mode shapes, and viscous damping) using earthquake spectral analysis techniques (**Kanai and Yoshizawa, 1961**) is widely used. However, these methods are often very expensive and therefore not applicable to most operations because heavy equipment is required to apply controlled and measurable excitation. Therefore, techniques using ambient noise and weak motion for structural characterization are gaining popularity (**Parolai et al., 2005**; **Gallipoli et al., 2009, 2010, 2020**; **Picozzi et al., 2010**; **Stabile et al., 2013**; **Serlenga et al., 2021**). Moreover, the capabilities and advantages of the Operational Modal Analysis (OMA) are currently gaining attention in the civil engineering community. The experimental estimation of the modal parameters of a structure by recording only the natural and freely available excitation generated by environmental sources and operational loads (wind, traffic, microtremors, etc.) is the modal testing procedure-based approach of OMA. The limitations of experimental modal analysis (EMA) are overcome with OMA, while several advantages are offered: (i) lower cost compared to experimental laboratory testing; (ii) simulation of boundary conditions and artificial excitation in a laboratory environment are not required; (iii) it is possible to obtain the dynamic characteristics of the entire system and not only a part of it; (iv) no interference with the normal use of the road network and flexibility in the installation of instruments during the test, which are therefore fast and low-cost; (v) identification of closely spaced modes of a complex structure thanks to the multi-input multi-output analysis method. The main assumption of OMA is that ambient noise provides an input over a wide frequency range covering all frequencies of engineering interest (**Overschee and Moor, 1996**; **Peeters and Ventura, 2003**; **Bindi et al., 2015**). Operation Modal Analysis algorithms can be divided into two types, depending on whether they operate in the frequency domain (Basic Frequency Domain (BFD), Frequency Domain Decomposition (FDD), etc.) or in the time domain (Random Decrement Technique (RDT), Stochastic Subspace Identification (SSI), etc.). Several studies have shown that approaches in the time or frequency domain may be suitable for identifying modal parameters of a variety of structures by OMA (**Brincker et al., 2005**). It is worth noting that in the context of OMA identification methods, the external force is not recorded, thus requiring the application of concepts from stochastic mechanics (**Barone et al., 2008**). The most important and commonly used OMA procedures are the Peak Picking combined with the Half Power (PP+HP) (**Bendat and Piersol, 2011**) and the Frequency Domain Decomposition (FDD) (**Brincker et al., 2001**). Frequency Domain Decomposition (FDD) technique has several advantages: Detection of natural mode shapes, even closely spaced ones, with high accuracy, even for complex structures; reliability of measurements and results of dynamic identification user friendly. Moreover, the FDD method uses only the spatial information related to the locations of the sensors (**Rainieri and Fabbrocino, 2014**). In the literature, there are numerous authors who applied OMA methods (especially the FDD method) to both bridges and buildings: e.g. **Magalhaes et al. (2010)** applied different OMA methods PP, NExT/ERA, SSI-COV, p-LSCF for the structural identification of the Humber Bridge, a single-span road suspension bridge (North Lincolnshire, England); **Benedettini and Gentile (2011)** extracted the modal parameters of the Vittorio Sora Bridge (Quinzano D'oglio, Brescia, Lombardy, Italy) from ambient vibration data using two different output-only techniques, the Enhanced Frequency Domain Decomposition (EFDD) in the frequency domain and the data-driven Stochastic Subspace Identification (SSI) in time domain; good results in terms of natural frequencies and mode shape estimates were obtained by applying FDD to data from the long span "Infante D. Henrique" bridge (Porto, Portugal) monitoring system in the study of **Magalhaes et al. (2011)**; the results of the experimental modal analysis of the Paderno iron arch bridge (1889 - Lombardy, Italy) were presented by **Gentile and Saisi (2011)**; **Foti et al. (2012)** used several OMA analysis techniques in both the frequency and time domains (for example FDD, CFDD, EFDD, SSI) for the dynamic identification of the Postiguet footbridge in Alicante (southeastern Spain); **Bedon et al. (2016)** estimated the natural frequencies, damping ratios and mode shape components by applying the EFFD method to ambient vibrations recorded on the Pietratagliata cable-stayed Bridge (Udine, Italy); **Roselli et al. (2017)** applied the frequency-domain decomposition (FDD), the enhanced frequency-domain decomposition (EFDD), and the stochastic subspace identification (SSI) to consider the seasonal effects on the dynamic behaviour of the ‘‘Ponte delle Torri’’ bridge (Spoleto, Perugia, Umbria Region, Italy), a large ten-arcade historic masonry bridge; **Benedetti et al. (2021)** applied FDD method for the modal identification of the Multi-Span Baghetto Bridge, a steel–concrete composite bridge (Lecco, Lombardy). There are several studies in the literature on the application of OMA methods for the identification of modal properties of bowstring arch bridges, built with the same structural typology of the Gravina Bridge that this part of the thesis work focuses on; for example, **Turker and Bayraktar (2014)** evaluated the dynamic characteristics of the Ali Çetinkaya Bridge (Samsun, Turkey) using the Enhanced Frequency Domain Decomposition (EFDD) and Stochastic Subspace Identification (SSI) techniques; **Zordan et al. (2014)** performed an OMA analysis for the identification of the modal parameters of the Canonica Bridge (Canonica D’Adda, Lombardy) from output-only time-histories using the Frequency Domain Decomposition (FDD) method implemented in the ARTeMIS software; **Ferrari et al. (2015, 2016, 2019)** applied the PP, FDD, and SSI methods for the modal identification of the Brivio Bridge (Lombardy, Italy); **Whelan et al. (2018)** carried out an output-only system identification of the modal parameters of the Marquette–Joliet Bridge (Marquette, Iowa, USA) using the stochastic subspace state-space system identification algorithm; **Meixedo et al. (2021)** carried out the identification of the modal properties of the Sado Bridge (Lisbon, Portugal) by applying the Enhanced Frequency Domain Decomposition method (EFDD); **Zonno and Gentile (2021)** studied the dynamic behaviour of the Brivio Bridge (Lombardy, Italy), a historic RC arch bridge, applying the Frequency Domain Decomposition (FDD) technique; **Borlenghi et al. (2022)** monitored the Brivio reinforced concrete arch bridge using an Operational Modal Analysis, the FDD method. OMA techniques have also been applied to standard structures such as buildings. The seismic response and dynamic characteristics of an 8-story hospital RC-building in northern Greece have been studied by **Bindi et al. (2015)** and **Karapetrou et al. (2015)** by applying nonparametric identification methods on ambient vibration data; the FDD method was used to monitor a building in Central Asia by performing the modal analysis by **Petrovic et al. (2015)**; operational modal analysis was applied for structural identification in historic masonry structures in Italy by **Macias and Ubertini (2019)**.

Recently, also the seismic interferometry (e.g., **Snieder and Safak 2006**) has been gaining attention; it represents a scientific discipline that can be applied, in the context of structural health monitoring, on both earthquake data and ambient noise recordings by using common data processing techniques, such as cross-correlation, cross-coherence, or deconvolution interferometry (e.g., **Snieder et al., 2009**). The deconvolution interferometry can be used to identify the dynamic structural characteristics in terms of wave propagation properties (e.g., **Todorovska and Trifunac, 2008**; **Petrovic et al., 2018**) and their variations (e.g., **Garcia-Macias and Ubertini, 2021**). Damage detection in buildings is one of the purposes for which deconvolution interferometry has been mainly used so far (e.g., **Todorovska and Trifunac, 2008**; **Pianese et al., 2018**). The joint application of ambient noise deconvolution interferometry (ANDI) and OMA methods such as FDD has been used in several studies. **Brincker et al. (2000)** first introduced the FDD technique for the modal identification of output-only systems, i.e. when the estimation of modal parameters is conducted without knowing the input exciting the system; **Petrovic et al. (2015)** studied the dynamic behaviour of a recently constructed building; **García-Macías and Ubertini (2019)** applied operational modal analysis for structural identification in historic masonry structures in Italy; **Lacanna et al. (2019)** applied the integrated approach to cultural heritage. The modal parameters of a 48-story skyscraper in Kunming (China) were estimated by implementing a system based on ANDI for SHM purposes (**Todorovska et al., 2020**). Structural typologies other than buildings and the changes in their structural characteristics caused by ageing and damage can also be monitored by exploiting the considerable potential of OMA SHM systems consisting of ANDI and standard OMA-based systems. Nonetheless, a few studies have been conducted on the dynamic behaviour of bridges combining the waveform and vibrational approaches. Seismic ambient noise measurements of road traffic were performed for structural monitoring of a highway bridge (**Salvermoser et al., 2015**). The response of the San

Francisco Bay Bridge (California) was evaluated by applying multichannel deconvolution to both earthquake and ambient seismic noise recordings (**Jian et al., 2020**). The joint application of ANDI and FDD techniques for the structural assessment of the Chiaravalle Viaduct (Marche region) was conducted by **Garcia-Macias and Ubertini (2021)**.

4.1 The Gravina Bridge

The ‘‘Gravina’’ is a bow-string bridge in Matera (southern Italy) on the state road 655 “Bradanica”, connecting Foggia, the highway A16 Napoli-Canosa di Puglia (Candela exit) and Matera. The bridge crosses the graven bed of the Gravina stream (Figure 4.1) and was completed in summer 2015 (**Matildi et al., 2015**). The geomorphology of the area is characterised by a canyon about 20 m deep, with steep sides and normally low water flow. The Gravina’s hydraulic risk periods are approximately every six months, because the stream fills with several metres of turbulent water during large hydraulic floods Therefore, foundations inside the graven were avoided and the construction of shallow foundations with abutment walls on outcropping Gravina calcarenite was preferred (Figure 4.2b). The area where the bridge is built is also of historical and archeological relevance because of the presence of caves and cavities where there were already remote anthropic settlements (‘‘Sassi’’ area in the centre of Matera). Although this area is 12 km away from the ‘‘Sassi’’ (described in Chapter 3), the topographical, historical, and anthropological environment is the same; therefore, the construction design of the bridge is characterised by details of valuable shape, suitable for the area and is characterised by effective simplicity on the one hand, while aiming for maximum durability on the other (**Matildi et al., 2015**). The Gravina Bridge consists of nine circular hollow sections connecting a pair of leant tubular arches ϕ 1.70 m. The infrastructure is 144 m long, measured at the base of the arches, with a deck that has a total width of 18.80 m and a steel – concrete composite section connected to the arch by 19 pairs of 6 m long suspension cables as inter-axis. Each pair of suspension cables has fully locked coils, with a fixed end on the arch side and an adjustable end on the deck. The shape of the arch has been optimised to minimise the bending stresses. The exterior isostatic structure has a restraint system achieved with two different design types composed of eight elastomeric isolators: four under the arch bases (type 1) and four under the main girders (type 2) (Figure 4.3).

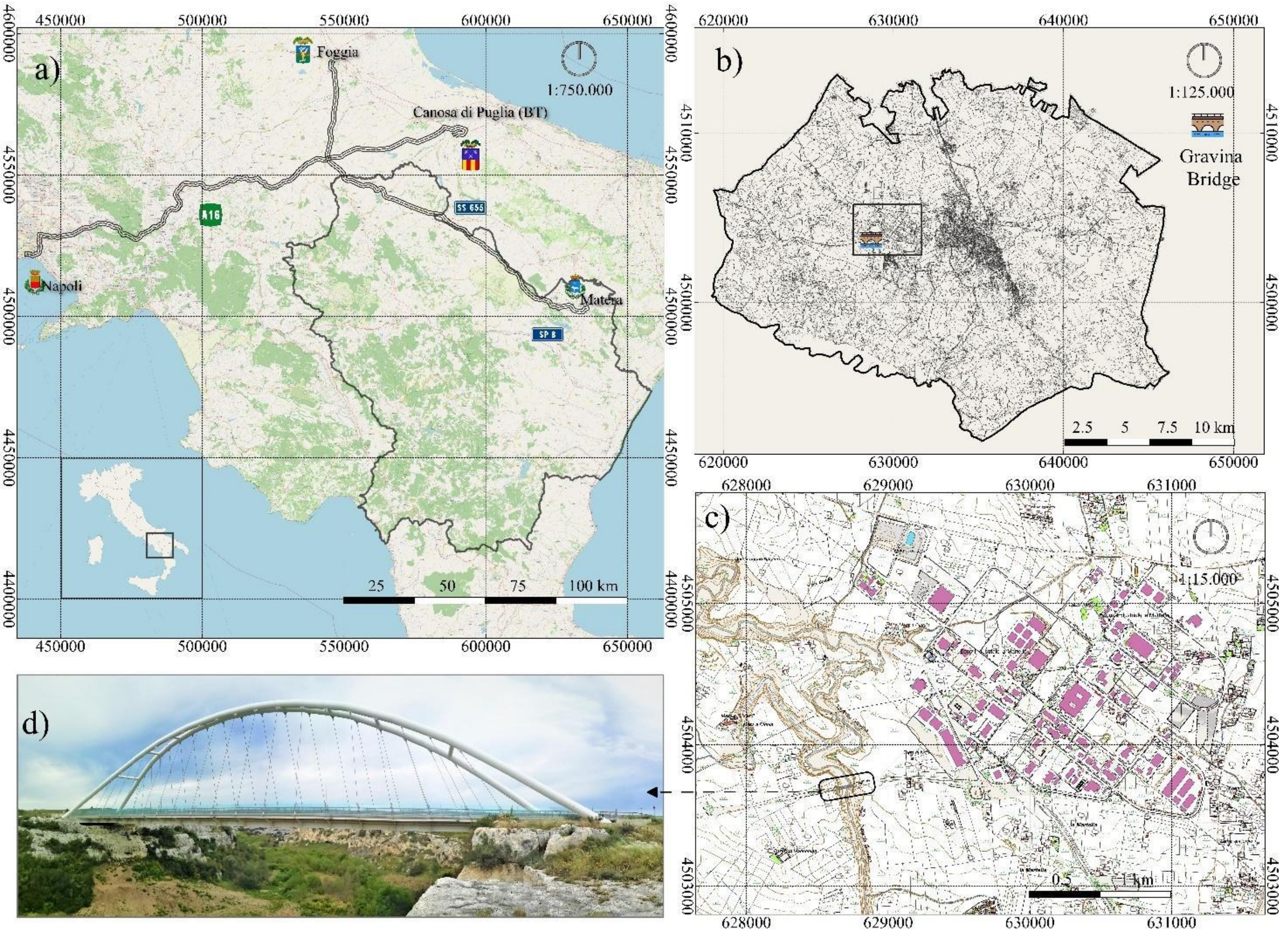

Fig. 4.1 (a) Plan of the state road 655 "Bradanica", at km 136 + 675, connecting Foggia, A16 highway Napoli-Canosa di Puglia (Candela exit) and Matera, with the territory of the Basilicata Region outlined by the thin black line; (b) cartographic map of the location of the bridge in the western area of the city of Matera; (c) the location of the bridge in the industrial area of Matera; (d) Photo of the Gravina Bridge.

4.2 Characterization of the foundation soil

The area where the Gravina Bridge is located, in the western part of Matera, is characterised by the outcropping lithological units of the Bradanica Trough. Although this area is 12 km away from the city centre, the foundation soil of the bridge is the same of the urban area (as described in Chapter 3) and is composed, from bottom to top, of Cretaceous (or Altamura) Limestones Fm, the Gravina Calcarenite Fm (upper Pliocene - lower Pleistocene), and SubApennine Clay Fm (Pleistocene), as shown in Figure 4.2b (**Tropeano and Sabato, 2000**; **Beneduce et al., 2004**). Because geological and stratigraphical information is available from direct geognostic investigations carried out in 2001 in the area before the construction of the bridge, the geological setting is confirmed. A 40-m deep borehole drilled on the east side of the bridge towards Matera, allows to obtain a stratigraphy that reports in sequence: 18 m of yellow bioclastic calcarenite with some fracture layers (Gravina Calcarenite Fm), followed by brown-grey limestones with intercalations of reddish sand levels (Altamura Limestone Fm). A geognostic investigation carried out on the western side of the bridge towards Candela shows a sequence of strata consisting of1 m of silty clays and coarse brown sands from top to bottom (Sub-Apennine Clay Fm), 16 m of material attributable to the Gravina Calcarenite Fm, and 23 m (from 17 m to the bottom of the borehole at 40 m depth) of limestones belonging to the Altamura Limestones Fm.

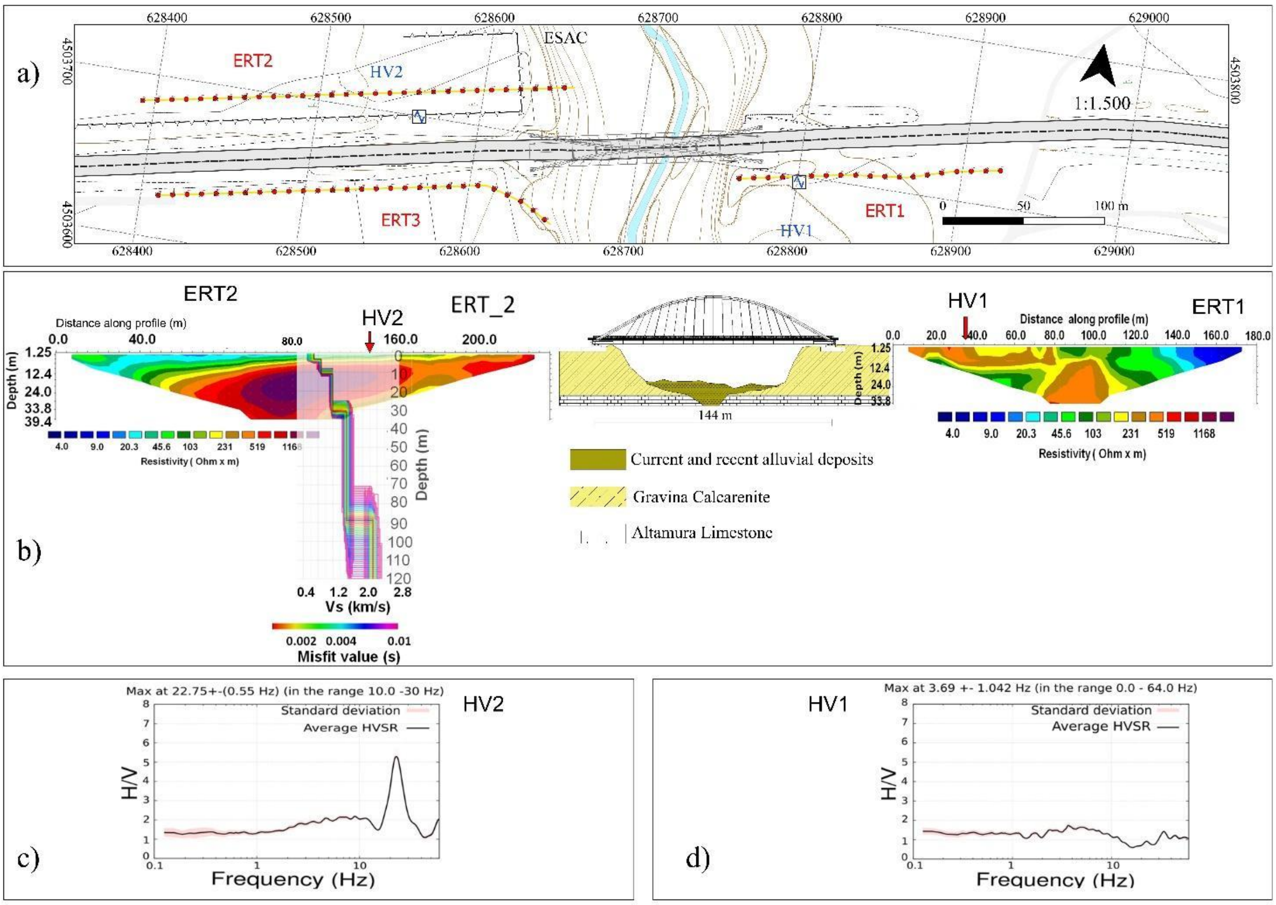

Fig. 4.2 (a) Location of measurements carried out for soil characterization, (b) from left to right: ERT2 (geo-Electrical Resistivity Tomographies) together with the 1D shear-wave velocity model estimated using ESAC, geological sketch of the foundation soils of the Gravina Bridge, and ERT1; (c) HV2; (d) HV1 (HV - Horizontal-to-Vertical Noise Spectral Ratio, HVNSR).

4.2.1 Geophysical methods

Two-dimensional (2D) characterisation of the foundation soil of the Gravina Bridge was performed on both sides of the structure using three different geophysical methods (Figure 4.2a): three high-resolution geoelectrical resistivity tomographies (ERT), an enhanced spatial autocorrelation (ESAC) with seismic arrays and two single-station seismic ambient noise measurements elaborated by horizontal-to-vertical noise spectral ratio (HVNSR). In particular, ERT1 and HV1 were conducted on the Matera side; ERT2, ERT3, HV2 and the ESAC were performed on the Candela side. The more complex stratigraphic sequence resulting from drilling on the west side was the reason for the greater number of geophysical surveys carried out.

geo-Electrical Resistivity Tomographies

Syscal Pro Switch 48 (IRIS Instruments) georesistivimeter connected to two multielectrode cables has been used to acquire apparent electrical resistivity values, using Wenner array, setting a constant spacing of 5 m between the adjacent electrodes (Figure 4.2a). 2D images of the distribution of resistivity values in the subsoil down to 35 m depth represent the core of the inversion results. Following the geological setting of the area the resistivity distribution has been interpreted (see section 4.3.1.4). Details on the experiment and analysis procedures can be found in **Serlenga et al. (2021)**.

Horizontal-to-Vertical Noise Spectral Ratio

Two single-station seismic ambient noise measurements, namely HV1 and HV2 (Figure 4.2a; 14–20 min duration) were carried out using a 24-bit digital velocimeter (Moho-Tromino) with a sampling rate of 128 Hz. For each site, both the horizontal and vertical components of the recorded data were processed in the same way: the waveforms were divided into non overlapping 20-s moving windows; for each signal window, the mean and the trend were removed; tapering and zero padding was carried out for each window; discrete Fourier transform was calculated to obtain the spectral amplitudes; smoothing by means of triangular windows with a width of 5% of the central frequency on the retrieved spectra was applied. Finally, the Euclidean average of the N–S and E–W horizontal spectral components in a single horizontal spectrum (H) was calculated. For each of the 20-s long windows, the HVNSR was computed (**Nakamura, 1989**; **Mucciarelli, 1998**; **Gallipoli et al., 2004**). Finally, the average HVNSR of all 20-s windows and its standard deviation ±σ were obtained.

Extended Spatial Auto Correlation

For the experimental set-up of the extended spatial auto correlation (ESAC) a bi-dimensional C-shaped seismic array of 24 geophones (4.5Hz frequency) with variable inter-distance and length of 50–240 m was deployed (Figure 4.2a). A Geometrics-Geode recording instrument (a 24-bit data logger with 144-dB dynamic range and a sampling rate of 125 Hz) for a duration of 30–40 min has been used. The ESAC method (**Ohori et al., 2002**; **Okada, 2003**; **Parolai and Galiana-Merino, 2006**) was used to process acquired data with the aim to highlight the coherent phase between all recordings. The correlation analysis between the signals recorded by different sensors at different frequencies, i.e., the coherence function allowed obtaining the information about the subsoil characteristics. The obtained Rayleigh wave dispersion curve made it possible to estimate the S-waves velocity profile. Details on the experiment and analysis procedures can be found in **Serlenga et al. (2021)**.

4.2.2 Joint interpretation of geophysical results

On the Matera side, according to the tomographic section in Figure 2c, the ERT1 is characterised by high resistivity values (ρ>200Ωm) in the southwestern area, just where the bridge foundations are located, and by lower resistivity values associated with conductive material (ρ<50Ωm) in the northeastern area, i.e. toward the city of Matera. The conductive feature can be associated with the clayey-silty deposits of the Sub-Apennine Clay Fm, while the resistive feature can be associated with the Gravina Calcarenite Fm (Figure 2b). Since HV1 has a flat amplification curve, it confirms that there are no seismic impedance contrasts between the Altamura Limestone and the overlying Gravina Calcarenite Fm (Figure 4.2d). On the Candela side, the ERT2 is characterised in the upper western part of the section profile by shallow conductive material (ρ<50Ωm) that can be associated with clayey-silty deposits, while the underlying resistive material (ρ>200Ωm) can be associated with the Gravina Calcarenite (Figure 4.2b). The HV2 shows a well-defined amplitude peak of more than 5 at a frequency of about 23 Hz, which is due to the seismic impedance contrast between very shallow soft soils (clayey) and the underlying calcarenite (Figure 4.2c). The seismo-stratigraphic model provided by the ESAC analysis is composed by five layers (Figure 4.2b); (i) the first layer about, with a thickness of about 3.0 m and a shear wave velocity of Vs ≅ 690 m/s, can be associated with a very consistent and compact blue-grey clay layer; (ii) the thickness of the second layer is ≅ 8.0 m, its Vs ≅ 880 m/s, and it can be associated with very thickened soils that refer to the altered part of the calcarenite; (iii) the third layer, from 11 to 31 m, is characterised by extremely thickened soils with a Vs ≅ 1200 m/s referable to the compact and slightly altered calcarenitic layers; (iv) the fourth layer, between 31 m and 90 m, has a Vs ≅ 1570 m/s referable to weakly fractured limestones. Finally, the layer at depths greater than 90 m is characterised by f Vs ≅ 2280 m/s that can be associated with very compact limestone (Cretaceous Limestones Fm). The ERT, HVNSR, and ESAC analyses made it possible to obtain results in good agreement with each other and with the geological knowledge.

4.3 Structural Health Monitoring: data acquisition

In order to characterise the primary modal parameters (eigenfrequencies, mode shapes and associated equivalent viscous damping factors, and wave propagation velocities) of the Gravina Bridge, four accelerometric and twelve velocimetric stations (capable to acquire high quality seismic signals in ambient vibration conditions) were deployed. Permanent real-time earthquake monitoring and on-demand monitoring through ambient vibration tests (AVT) have been performed (Figure 4.3). All equipment was deployed on the road infrastructure and surrounding soil as described in the following sections. Three different types of seismic data were collected with these two types of monitoring: (i) earthquakes recordings and seismic noise in (ii) AVT-OC and (iii) AVT-SV. The geophysical data were acquired in different time periods:

- June 2019 - end of March 2020 for acquisition of earthquake real-time recordings;
- 12 July 2019, 29 October 2019, and 22 January 2020 for the AVTs;
- during the second on-demand test (2019/10/29) the microwave radar interferometry was performed to collect electromagnetic data (Figure 4.3c).

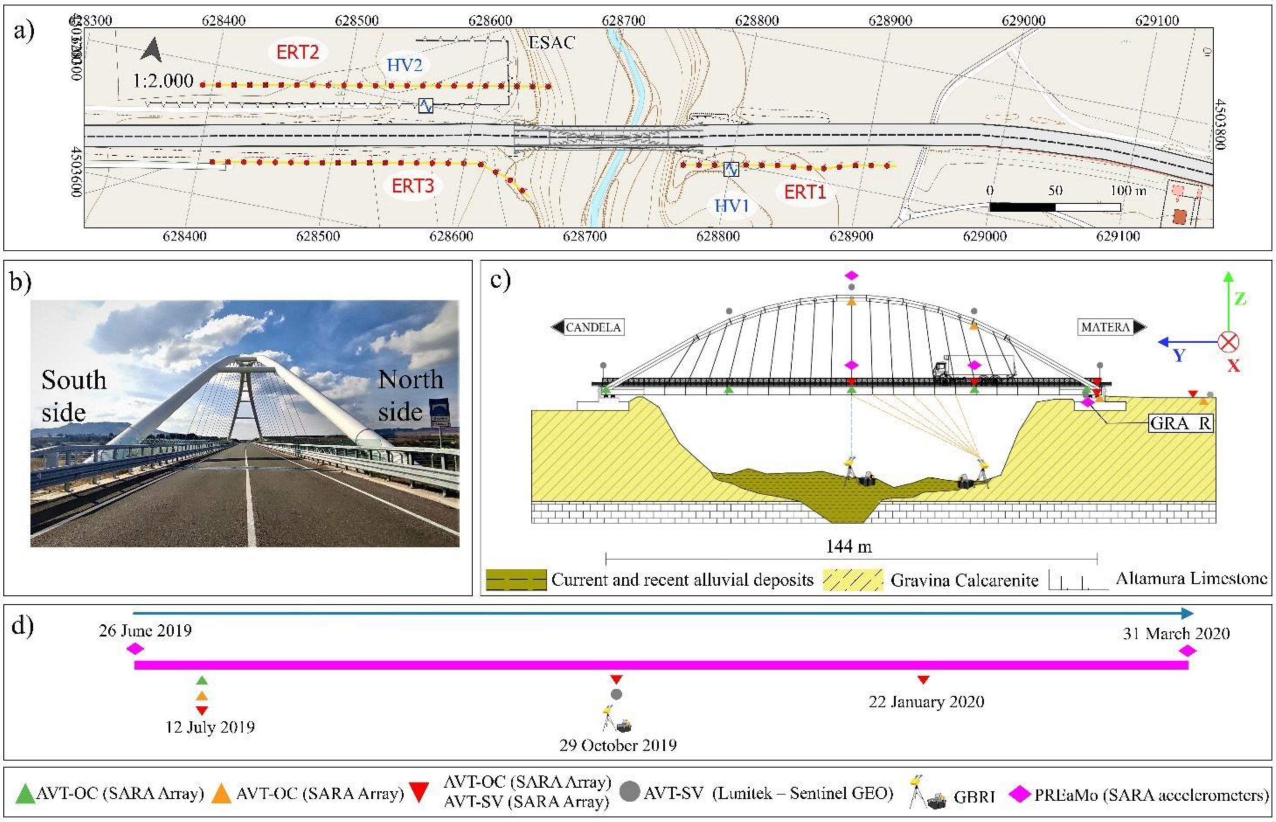

Fig. 4.3 a) Top view of the bridge; (b) Picture of the Gravina Bridge to emphasise Soth side and North side; (c) Elevation and experimental setup of the instrumentation deployed for the structural characterization; (d) Time evolution of the geophysical tests carried out in this study.

Table 4.1 summarises the applied analysis techniques and different signals used. The theoretical background of these techniques has been reported in **Chapter 2**.

Permanent real-time earthquake monitoring and on-demand ambient vibration tests (**Green, 1995**; **Salawu and Williams, 1995**; **Farrar et al., 1997**) were conducted. In this study, two types of ambient vibration tests, AVT, (Table 4.1), ambient vibration test in operational condition (AVT-OC) and ambient vibration test in special conditions, i.e., with special vehicles (AVT-SV), were performed to gain further insight into the actual modal properties and to increase the robustness of the estimates, regardless of the source selected. Earthquake monitoring was performed with four accelerometers, while the ambient vibration test were carried out by deploying 12 seismometers with different geometrical arrangements both in operational conditions (AVT-OC) and using special vehicles (AVT-SV) on the bridge and a single station seismometer on soil.

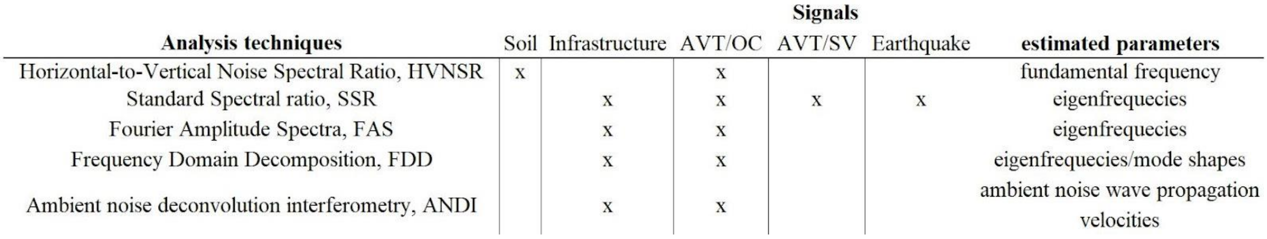

	Signals					
Analysis techniques	Soil	Infrastructure	AVT/OC	AVT/SV	Earthquake	**estimated parameters**
Horizontal-to-Vertical Noise Spectral Ratio, HVNSR	x		x			fundamental frequency
Standard Spectral ratio, SSR		x	x	x	x	eigenfrequecies
Fourier Amplitude Spectra, FAS		x	x			eigenfrequecies
Frequency Domain Decomposition, FDD		x	x			eigenfrequecies/mode shapes
Ambient noise deconvolution interferometry, ANDI		x	x			ambient noise wave propagation velocities

Table 4.1 Geophysical analysis techniques used in this thesis work for the characterisation of the infrastructure and the related foundation soil. The fourth, fifth and sixth columns indicate the type of signal for which each analysis technique has been adopted. The last column indicates which parameters have been estimated. AVT/OC: ambient vibration test in operational condition; AVT/SV; ambient vibration test with special vehicles.

4.3.1 Permanent real-time earthquake monitoring

Local and regional earthquake data collection began in summer 2019 with the installation of four triaxial permanent accelerometers (SARA Electronic Instruments SL06-SA10 with 1 g full scale and 200 Hz sampling frequency) in a stand-alone configuration: three were installed on 26 June 2019, and the fourth one on 12 July 2019. The sensors were placed so that the X-component of the sensors was oriented parallel to the transverse direction of the bridge, the Y-component was oriented parallel to the longitudinal axis and the Z-component was oriented parallel to the upward vertical direction (Figure 4.3c — magenta diamonds). The instruments acquired in real-time and in continuous mode until 31 March 2020 (Figure 4.3d). Two sensors were placed along the deck, one on the abutment wall, and one inside the arch of the bridge. The selected locations were the quarter and the midpoint of the deck (L/4 and L/2, respectively, where L represents the longitudinal extent of the infrastructure), above the support on the abutment wall (Matera side) and at the top of the arch. All sensors were located on the south side of the infrastructure (Figure 4.3b,c). The names of the accelerometric stations are as follows: GRA14 (at L/4), GRA12 (at L/2), GRA_R (on the abutment wall) and GRARC (at the top of the arch). The GRARC station inside the arch of the bridge (Figure 4.4a) proved to be the noisiest station with a very low signal-to-noise ratio (SNR, hereafter), so its data could not be used in this study. The accelerometric station GRA_R, located above the abutment wall, was used as the reference (R) for the SSR analysis; specifically, this sensor was installed near the elastomeric isolator under the southern main longitudinal beam (Figure 4.4c).

During the period from June to October 2019, a total of 19 earthquakes were recorded: characterised by an epicentral distance of 5 km to 950 km and a local magnitude range Ml = 1–5. The earthquakes in the immediate vicinity of the Gravina Bridge occurred in the last days of June and the first ten days of July 2019 with local magnitude between 1 and 2.4 Ml (Figure 4.5 a). The acceleration stations on the deck at L/4 and L/2 (GRA14 and GRA12) and at the reference point (GRA_R) recorded 11 earthquakes simultaneously. The time histories recorded simultaneously at L/4, at L/2 of the deck, and at the reference point, show that the maximum acceleration of the 2.4-Ml earthquake that occurred about 5 km from the bridge and has the maximum value of about 1.1 x 10^{-2}g (Figure 4.5b), and occurred at the reference point.

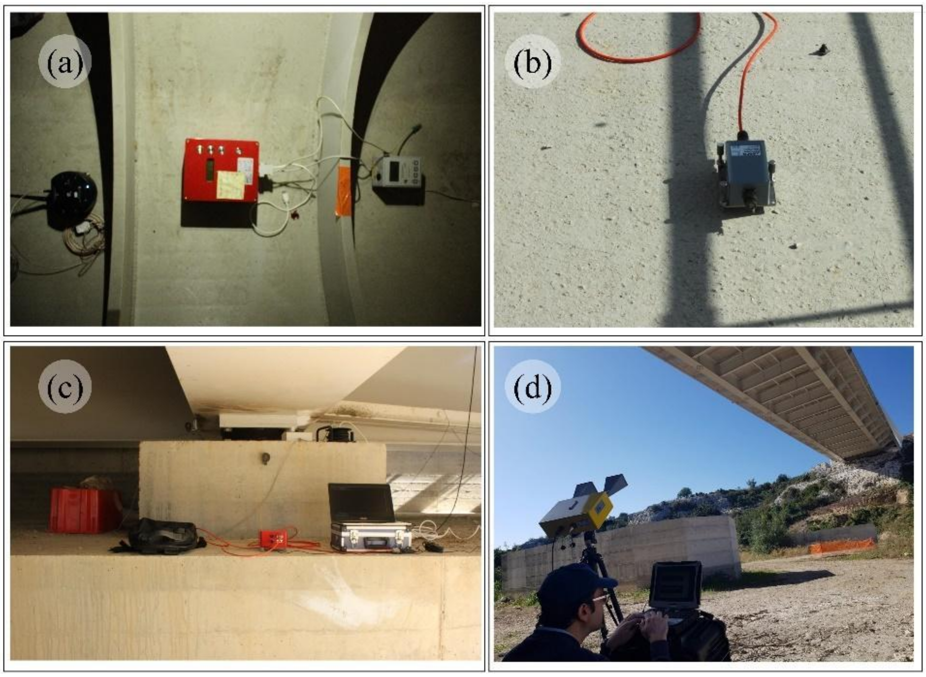

Fig. 4.4 Some pictures of the geophysical instrumentations adopted in this study and installed in different points of the structure. (a) accelerometer inside the tubular arch; (b) velocimeters placed on the deck; (c) instrumentation close to the seismic isolator, with the GRA_R accelerometer which is located inside the red box; and () GBRI under the bridge

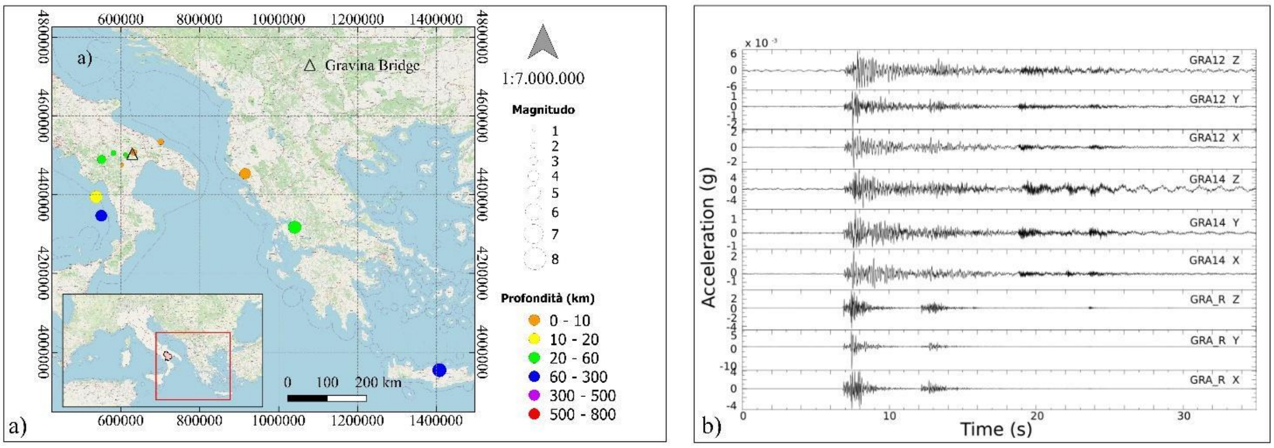

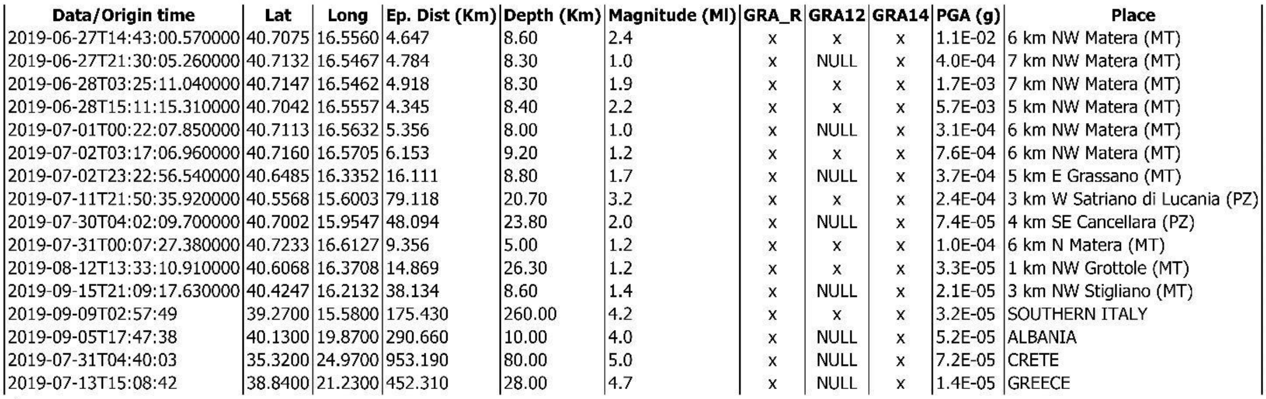

Data/Origin time	Lat	Long	Ep. Dist (Km)	Depth (Km)	Magnitude (Ml)	GRA_R	GRA12	GRA14	PGA (g)	Place
2019-06-27T14:43:00.570000	40.7075	16.5560	4.647	8.60	2.4	x	x	x	1.1E-02	6 km NW Matera (MT)
2019-06-27T21:30:05.260000	40.7132	16.5467	4.784	8.30	1.0	x	NULL	x	4.0E-04	7 km NW Matera (MT)
2019-06-28T03:25:11.040000	40.7147	16.5462	4.918	8.30	1.9	x	x	x	1.7E-03	7 km NW Matera (MT)
2019-06-28T15:11:15.310000	40.7042	16.5557	4.345	8.40	2.2	x	x	x	5.7E-03	5 km NW Matera (MT)
2019-07-01T00:22:07.850000	40.7113	16.5632	5.356	8.00	1.0	x	NULL	x	3.1E-04	6 km NW Matera (MT)
2019-07-02T03:17:06.960000	40.7160	16.5705	6.153	9.20	1.2	x	x	x	7.6E-04	6 km NW Matera (MT)
2019-07-02T23:22:56.540000	40.6485	16.3352	16.111	8.80	1.7	x	NULL	x	3.7E-04	5 km E Grassano (MT)
2019-07-11T21:50:35.920000	40.5568	15.6003	79.118	20.70	3.2	x	x	x	2.4E-04	3 km W Satriano di Lucania (PZ)
2019-07-30T04:02:09.700000	40.7002	15.9547	48.094	23.80	2.0	x	NULL	x	7.4E-05	4 km SE Cancellara (PZ)
2019-07-31T00:07:27.380000	40.7233	16.6127	9.356	5.00	1.2	x	x	x	1.0E-04	6 km N Matera (MT)
2019-08-12T13:33:10.910000	40.6068	16.3708	14.869	26.30	1.2	x	x	x	3.3E-05	1 km NW Grottole (MT)
2019-09-15T21:09:17.630000	40.4247	16.2132	38.134	8.60	1.4	x	NULL	x	2.1E-05	3 km NW Stigliano (MT)
2019-09-09T02:57:49	39.2700	15.5800	175.430	260.00	4.2	x	x	x	3.2E-05	SOUTHERN ITALY
2019-09-05T17:47:38	40.1300	19.8700	290.660	10.00	4.0	x	NULL	x	5.2E-05	ALBANIA
2019-07-31T04:40:03	35.3200	24.9700	953.190	80.00	5.0	x	NULL	x	7.2E-05	CRETE
2019-07-13T15:08:42	38.8400	21.2300	452.310	28.00	4.7	x	NULL	x	1.4E-05	GREECE

c)

Fig. 4.5 (a) Selection of earthquakes used for data analyses. The dots represent the epicentral positions, while the black triangle indicates the Gravina Bridge. The upper left panel shows all the 19 earthquakes. The black rectangle shows a panoramic view of the area zoomed in the main panel. The selected base map is Open Street Map; (b) Seismic traces of the 2.4-Ml earthquake that occurred about 5 km from the bridge. From top to bottom, recordings of the vertical, longitudinal, and transverse component from GRA12, GRA14, and GRA_R accelerometers, respectively, are shown; (c) List of recorded events during the period from 26 June 2019 to 25 October 2019.

4.3.2 Ambient Vibration Test (AVT): On demand measurements

On demand measurements included both seismic and electromagnetic signals. These tests consisted of two different types of on-demand AVT:

1. Dynamic tests under operational conditions (AVT-OC) (**Gentile C and Saisi, 2011**; **Kudu et al., 2014**) aiming at recording ≅ 30 min of ambient vibrations caused by natural forces (wind, earth tremble, etc.) or normal traffic, were performed. To evaluate potential eigenfrequency variations due to weather-related temperature fluctuations of the materials, the on-demand measurements were carried out during summer, fall, and winter seasons (12 July 2019, 29 October 2019, and 22 January 2020, respectively; Figure 4.3d);
2. On 29 October 2019, according to the availability provided by the National Autonomous Roads Corporation (ANAS) managing the Gravina Bridge, dynamic tests were carried out with special vehicles (AVT-SVs) using a 40-ton truck as a source of vibration, moving at a constant velocity of 50 km/h and passing over a wooden plank placed at different points of the bridge to record signals. Three different tests were conducted with special vehicles and three locations were selected where the wooden plank was placed: in the two-quarters of the bridge deck (L/4 and L3/4) and in the middle of the roadway (L/2) (Figure 4.3c). Because the acquisitions required a half an hour interruption of traffic, support from ANAS was needed to make it possible.

Two different seismic arrays composed of five and seven 4.5 Hz velocimeter arranged in four different geometrical configurations (Figure 4.3c) were deployed to record seismic signals. Both the first (five SARA-Electronic Instruments SR04DA) and the second array (Lunitek—Sentinel GEO) were used for AVT-OC and AVT-SV. Data were acquired at two different sampling rates: 200 Hz for the SARA sensors, and 250 Hz for the Lunitek sensors. Table 4.2 summarises the four different configurations described here in detail:

Configuration (1a): Three velocimeters were placed on the deck (at the support-0L, at L/4, and at L/2), one velocimeter was located near the seismic isolator, and one velocimeter was positioned on the soil and served as reference station. This configuration acquired seismic noise during both AVT-OC and AVT-SV (red triangles in Figure 4.3 c).

Configuration (2a): All five sensors were placed along the deck of the bridge at the following positions: 0L, L/4, L/2, L3/4, and L. The seismic signals during AVT-OC were acquired without the use of a reference station installed on the soil (green triangles in Figure 4.3c).

Configuration (3a): The SARA seismic array was composed of four sensors; three of which were deployed entirely inside the arch at L/2 and L/4, and above the isolator under the arch basis to study the structural behaviour of the arch during AVT-OC. The fourth velocimeter was positioned on soil and served as a reference station (orange triangles in Figure 4.3c).

Configuration (4a): A Lunitek array of seven sensors (grey filled circles in Figure 4.3c) was used to investigate the structural behaviour of the tubular arch during AVT-SV; five sensors were placed inside the arch along its entire extent at the ends, at the quarters (L/4 and L3/4) and in the middle, i.e. at the top of the structure (L/2). The two remaining velocimeters were located directly under the base of the arch and on the soil which served as a reference station.

Configuration	Equipment	Isolator	0L	L/4	L/2	L3/4	L	Soil	AVT	Dates
1a	Sara	X	X-**D**	X-**D**	X-**D**			X	OC + SV	12 July 2019, 29 October 2019, and 22 January 2020
2a	Sara		X-**D**	X-**D**	X-**D**	X-**D**	X-**D**		OC	12 July 2019
3a	Sara	X		X-**A**	X-**A**			X	OC	12 July 2019
4a	Lunitek		X-**A**	X-**A**	X-**A**	X-**D**	X-**A**	X	SV	29 October 2019

Table 4.2 The letter D stands for DECK, the letter A stands for ARCH. The second column indicates which equipment was used in each configuration. The second to last column indicates the type of ambient vibration test (AVT) for which each configuration has been adopted.

For all arrays, the reference station was placed on soil on the Matera side, where no amplification was observed, i.e., on the calcarenite soil (Figure 4.2). For both arrays, the components of the sensors were oriented in the same manner as the accelerometric stations, i.e., the X component of the sensors was oriented parallel to the transverse direction of the bridge, the Y component parallel to the longitudinal direction and Z pointing upwards. The time histories recorded simultaneously by the Lunitek and SARA seismic arrays during the dynamic test with special vehicles on 29 October 2019 are shown in Figure 4.6. For each component, the figure shows the traces recorded by the sensors placed at the following points of the structure: 0L on the deck, L/4 (deck and arch), and L/2 (deck and arch).

The IBIS-S (Image By Interferometric Survey of Structures) system from the Italian company IDS S.p.A was used to acquire electromagnetic data. By using a scenario sampling rate of 60 Hz, the selected configuration allowed the measurement of targets up to a radial distance of 70 m. The sensors were placed following two different configurations:

Configuration (1b): Longitudinal positioning of the IBIS-S system with respect to the bridge. This setup allowed it to illuminate several points of the bridge, from the quarter to the midpoint (Figure 3a). Configuration (2b): The IBIS-S system was positioned directly below the L/2 deck; the measurement was conducted by pointing the antennas at 90° to the horizontal plane of the bridge (Figure 4.3c).

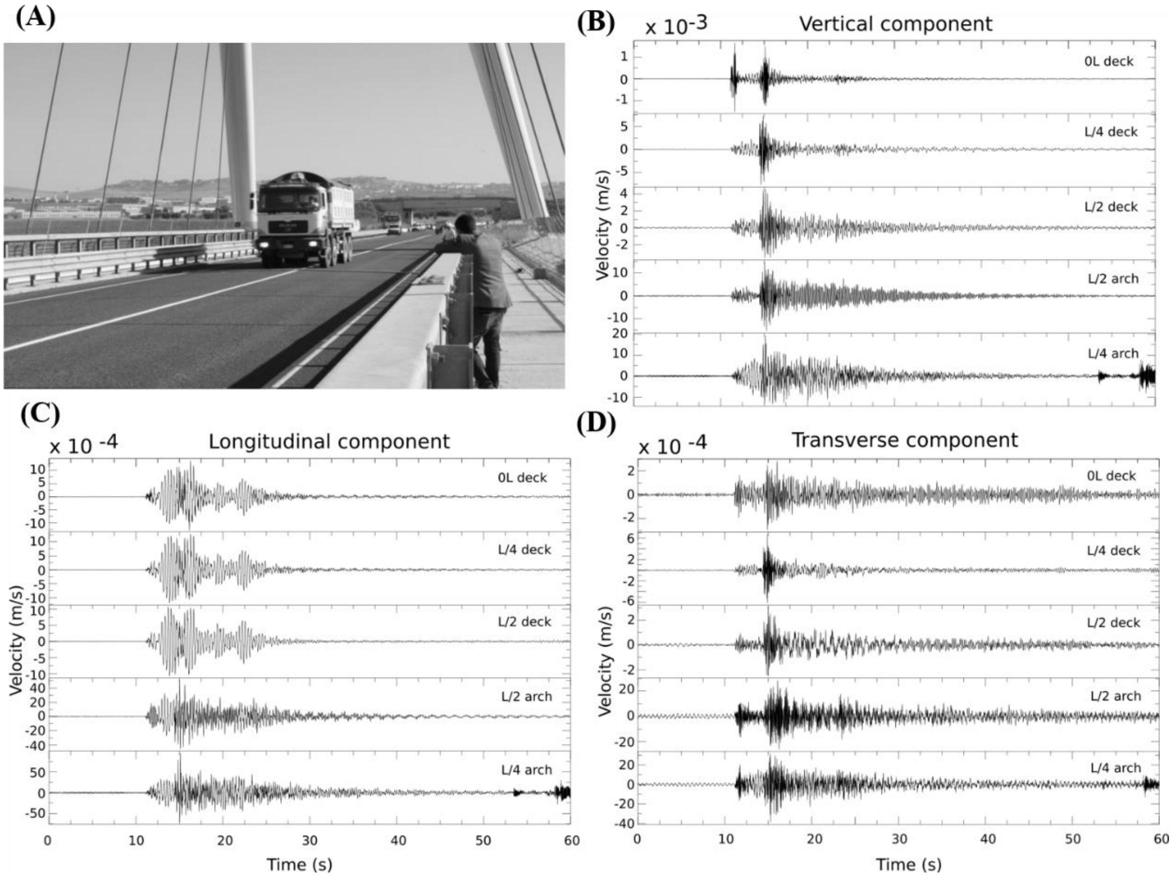

Fig. 4.6 Ambient vibration recordings in special condition during dynamic test at five different points of the bridge during AVT-SV on 29 October 2019. The positions of each sensor are indicated in the upper right of each plot. (a) Photo of the moment when the truck passes over the wooden plank positioned at L/4 on the roadway. Time histories of the vertical (b), longitudinal (c), and transverse components (d).

4.4 Data analysis and results

Estimation of the eigenfrequencies

The modal properties of the bridge were characterised at five different points by applying standard spectral analysis, i.e., Fast Fourier Transform (FFT), the Standard Spectral Ratio (SSR) technique, an Operational Modal Analyis (OMA) technique, i.e., the Frequency Domain Decomposition (FDD) method, and a seismic interferometric method, the Ambient Noise Deconvolution Interferometry (ANDI). Using and comparing the results of different methods had two advantages (i) evaluating the behaviour of the structure at different scales (global and local) and (ii) validating and simplifying the interpretation the results by comparing the results obtained from different techniques.

4.4.1 Spectral analysis – Fast Fourier Transform

An assessment of the distribution of the energy content of the ambient noise recorded during the two measurement campaigns of 2019 July 12th (configuration 2a, deck) and 2019 October 29th (configuration 4a, arch), was performed by spectral analysis of the data (Figure 4.7). The spectral analysis was performed on non-overlapping moving windows, to which standard processing operations (de-trend, tapering, band-pass filter) were applied. Since for the analysis for each moving window a sample number nfft of 16384 was chosen, the signals recorded in configuration 2a (deck) with a sampling rate of 200 Hz and in the configuration 4a (arch) with a sampling rate of 250 Hz were divided into 63 (80-s long time; spectral resolution of about 0.0122 Hz=1/16384*0.005s) and 57 (65-s long time; spectral resolution of about 0.015 Hz = 1/16384*0.004s) windows respectively. The input data were first detrended; then, to reduce the distortion due to the finite length of the signal, a 5% cosine taper function was applied to each window; finally band-pass from 0.1 – 5 Hz was applied. The results of all signal windows were stacked calculating the mean of the results of all moving windows.

In total, six vibration frequencies were identified for both deck and arch.

Six frequencies were determined on the deck, corresponding to six modes: three vertical flexural and three probably vertical torsional modes. Three predominantly vertical modes were identified at 0.75 Hz, at 1.35 Hz, and at 1.98 Hz (Figure 4.7a). In each of these modes of oscillation, however, also the longitudinal component is involved, although the spectral amplitudes in this direction are an order of magnitude smaller than those in the vertical direction (Figure 4.7a). Three other deck modes at 0.98 Hz, 1.5 Hz, and 2.1 Hz are likely torsional modes, because although the peaks are visible only in the transverse components (Figure 4.7a), the energy contribution in vertical direction is significantly larger and the spectral amplitudes of the Z components are an order of magnitude larger (Figure 4.8).

As for the arch, the first six vibrational modes were identified at the same frequencies (0.79 Hz, 1.02 Hz, 1.39 Hz, 1.58 Hz, 2.00 Hz, and 2.1 Hz) as those of the deck. However, except for the sixth mode of vibration at 2.1 Hz, which is purely transverse, all components are involved for the other five modes (Figure 4.7b).

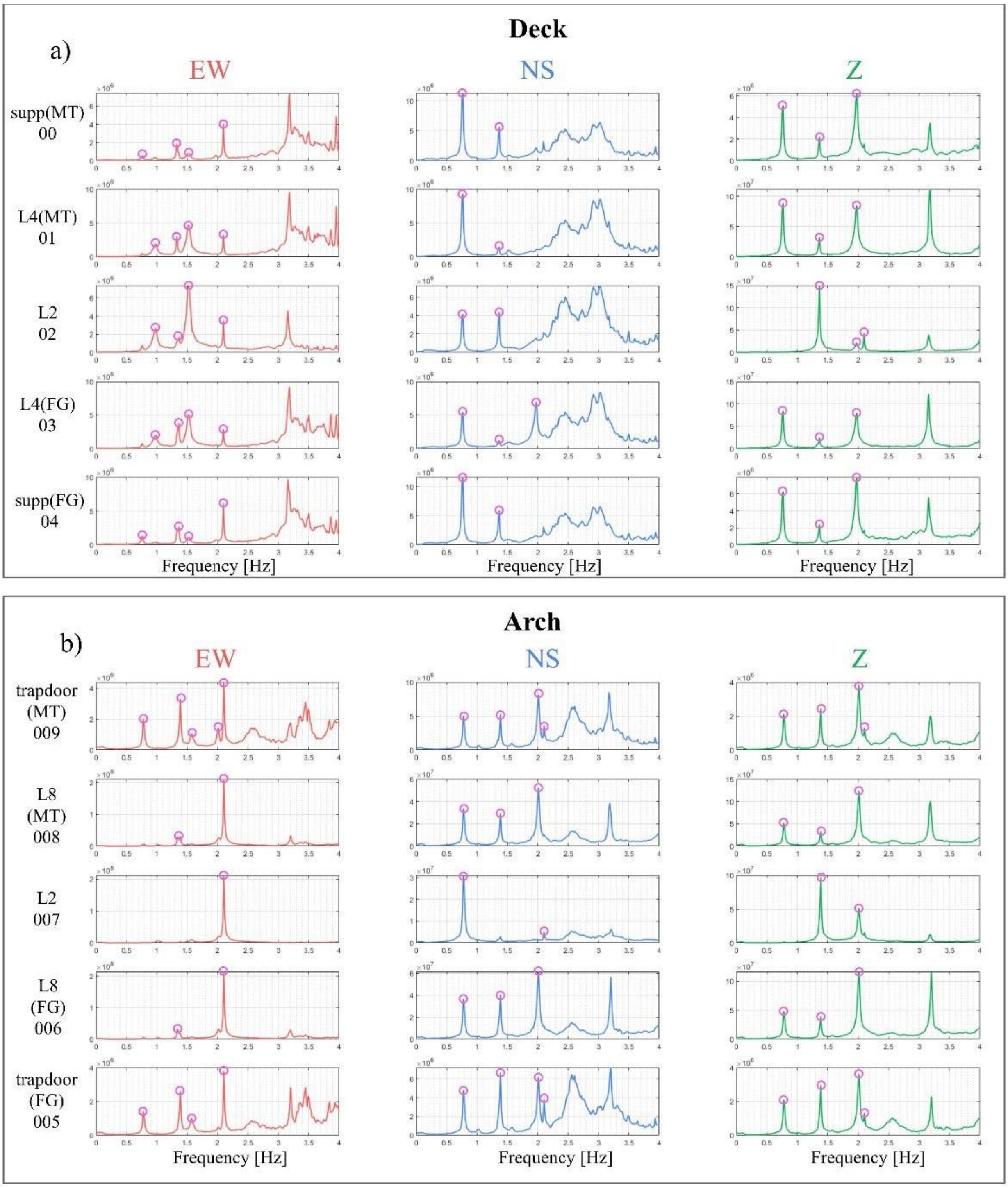

Fig. 4.7 FFT of the signals recorded during the ambient vibration tests with the Configuration 2a on the deck (a) and the Configuration 4a inside the arch (b). red: transverse component (EW); blue: longitudinal component (NS); green: vertical component (Z). fuchsia circle: eigenfrequency peaks.

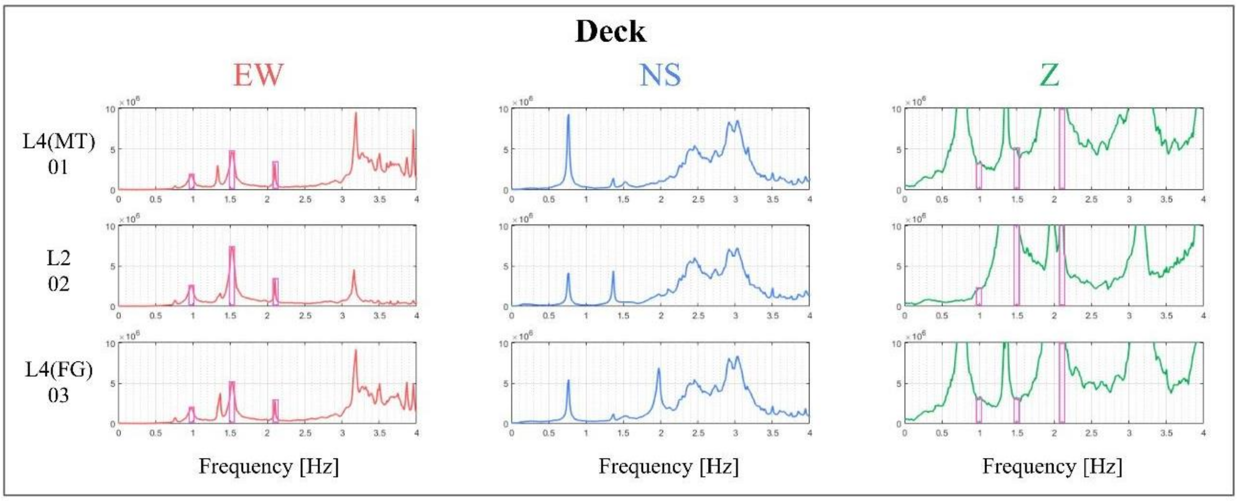

Fig. 4.8 FFT of the signals recorded with the SARA array during ambient vibration tests with Configuration 2a on the deck (sensors at the quarters [01 and 03] and middle of the deck [02]). The Y-axis of each plot is normalised to the maximum value of the transverse amplitude spectra in the range of the bandpass filter 0.1 - 5 Hz. red: transverse component (EW); blue: longitudinal component (NS); green: vertical component (Z). fuchsia rectangles: vibration frequency peaks and amplitude spectra in transverse and vertical direction at 0.98 Hz, 1.5 Hz, and 2.1 Hz.

4.4.2 Standard Spectral Ratio (SSR)

The modal properties of the Gravina Bridge were retrieved by applying the Standard Spectral Ratio (SSR) method (**Borcherdt, 1970**; **Parolai et al., 2005**; **Gallipoli et al., 2009**) at five different points: three on the deck (0L, L/4, and L/2) and two on the arch (L/4 and L/2). For each point, recordings of ambient vibration under both operational (AVT-OC) and special conditions (AVT-SV) due to the use of heavy vehicles were used as input of the SSR method. Since accelerometric data were only available at points L/4 and L/2, the analysis of earthquake recordings was performed using the SSR method at these points. First, a common pre-processing of the signal (de-mean, de-trend, tapering, and smoothing) was carried out in the same way for all different data types. The only difference was the choice of the time window selection. The analysis of the time series of local earthquakes was applied only to windows containing the entire earthquake recording, while for the analysed regional earthquake only the S-wave phase was selected. The spectral resolution of the earthquake SSR was 0.025 Hz. The ambient vibrations recorded on July 12, 2019, under operating conditions for 30 minutes were divided into 150-s long time windows (spectral resolution of about 0.007 Hz), with an overlap of 80% (**Bonnefoy - Claudet et al., 2006**). Therefore, the average SSRs and the σ standard deviations were calculated for the total number of 60 time windows. For the ambient vibrations generated during the dynamic tests with special vehicles, a spectral analysis was performed on a single 80-s long time window of the signal centred on the recorded data of the dynamic experiment, obtaining a frequency resolution of 0.0125 Hz. Subsequently, only one SSR was obtained for each component, and no average and standard deviations were computed. In the following, the results of SSR analyses obtained in each studied point are described. The sensor installed on the rigid soil was chosen as the reference sensor for ambient noise reconrdings, under both operational and special conditions, and the sensor under the main girder was chosen as the reference sensor in the case of earthquake data. For clarity, for each plot where SSRs obtained from two different types of ambient vibrations data are overlapped, the SSR functions were normalised with respect to the maximum value obtained from the three components and the two different types of data analysed.

4.4.2.1 0L-support Matera side

Figure 4.9 shows the semi-log plot of SSR curves resulting from the analyses of AVT-OC and AVT-SC for this point of the bridge in configuration 1a (see Table 2). The curves were normalised with respect to the longitudinal component of AVT-SV (dashed line). The 1st mode is at about 0.76 Hz in the vertical and longitudinal components (Figure 4.9) and the 3rd mode (about 1.35 Hz) is observed in the longitudinal component. The intrinsic uncertainty associated with the spectral resolution, which is about 0.007 and 0.0125 Hz for the AVT-OC and AVT-SV SSRs, respectively, affects the estimates of frequency peaks. Moreover, the SSRs obtained from the analyses of the two different types of AVT data are in very good agreement. As expected, the curves related to the AVT-SV are characterised by higher amplitudes than those obtained from recordings in operational conditions.

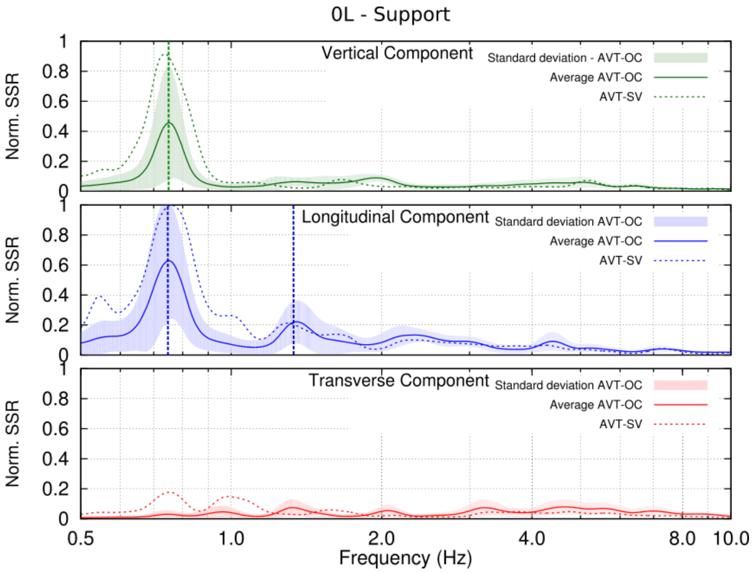

Fig. 4.9 Standard spectral ratios computed at point 0L, on the deck of the bridge, using both AVT-OC and AVT-SV data. From top to bottom, the results related to vertical, longitudinal, and transverse SSR components are shown. The vertical dashed lines highlight the main frequency peaks retrieved by means of SSR analyses.

4.4.2.2 L/4 arch Matera side

Figure 4.10 shows the obtained SSR functions of the ambient noise recorded in AVTC-OC and AVT-SV in configurations 3a and 4a, respectively (Table 4.2), at the quarter of the arch are depicted. These curves have a very similar shape to those observed at 0L. Specifically, the main vibrational mode is at 0.76 Hz in the vertical and longitudinal components, and a second significant peak is observed at about 1.35 Hz in the vertical, longitudinal, and transverse components (3rd mode of vibration). It is worth highlight that comparing these results with those obtained at the support (0L), the highest amplitude of the 1st mode is on the vertical component instead of the longitudinal one. The SSR functions estimated at this bridge point in the transverse direction have peak amplitude lower than the ones observed on the vertical and longitudinal components. There is a very good agreement between the results obtained in the vertical and longitudinal directions by SSRs on AVT-OC and AVT-SV, especially at frequencies below 2.0 Hz. In particular, the estimated peak values differ from each other up to 0.02 Hz.

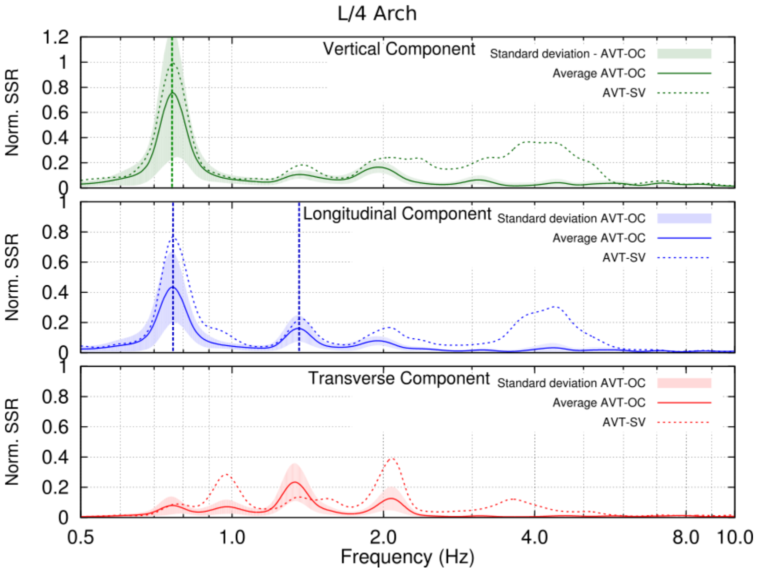

Fig. 4.10 Standard spectral ratios computed at point L/4, on the arch of the bridge, using both AVT-OC and AVT-SV data. From top to bottom, the results related to vertical, longitudinal, and transverse SSR components are shown. The vertical dashed lines highlight the main frequency peaks retrieved by means of SSR analyses.

4.4.2.3 L/4 deck Matera side

Due to the availability of 19 earthquake recordings of the installed accelerometer it was also possible to perform analyses of the earthquake data at the quarter of the deck. Figure 4.11 shows that the estimates are very similar to those already shown for SSR of the ambient noise recording at the arch's L/4 point, namely:

- the eigenfrequencies related to the 1st mode is f ≅ 0.76 Hz, both on the vertical and longitudinal component;
- the amplitude value of the peak of the first mode is higher in the vertical direction than in the longitudinal direction;
- very good agreement between the results obtained by analysing different data sets.

Moreover, it was possible to observe the eigenfrequencies related to the 2nd and 4th modes at about f = 0.97 and f = 1.50 Hz, respectively, in the transverse direction, although a discrepancy of up to 0.06 Hz were observed between the peaks obtained from the data of AVT-OC and AVT-SV (acquired in configuration 1a, Table 4.2; Figure 4.11b). The earthquake SSRs provided frequency information consistent with that obtained from analysis of seismic ambient noise. The large standard deviation observed in the earthquake data is likely related to a large variability in the energy content, location, and magnitude of the selected earthquakes (Figure 4.11a).

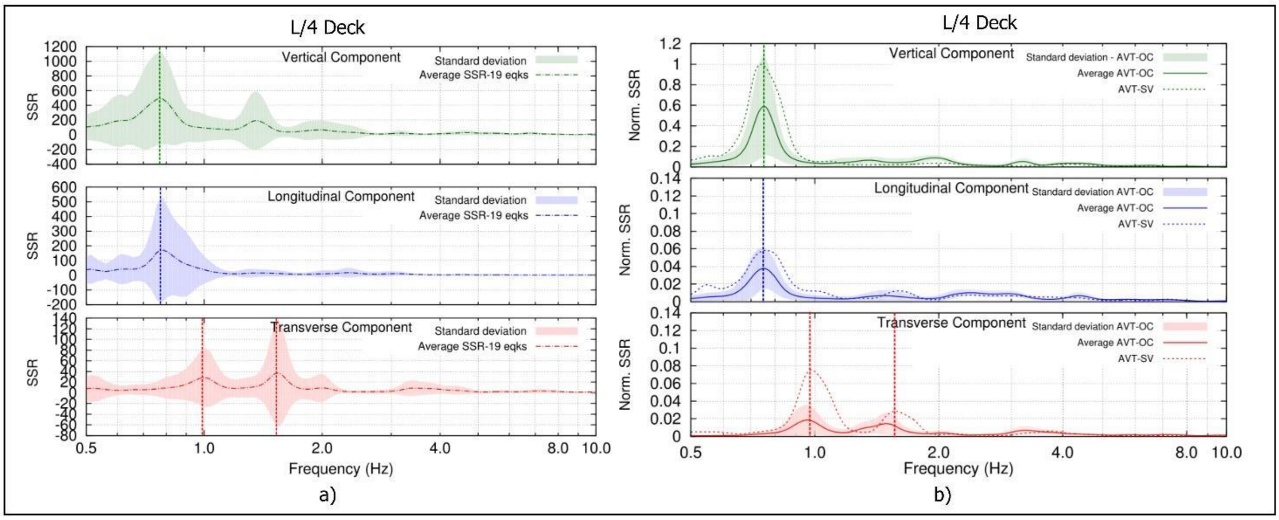

Fig. 4.11 Standard spectral ratios computed at point L/4, on the deck of the bridge. (a) Results retrieved from the analysis of earthquake data. (b) Results retrieved using both AVT-OC and AVT-SV data. From top to bottom, the results related to vertical, longitudinal, and transverse SSR components are shown. The vertical dashed lines highlight the main frequency peaks retrieved by means of SSR analyses. For each type of signal the st.dev and the average have been calculated on the values of the spectral ratios.

4.4.2.4 L/2 arch South side

Since the accelerometric station installed at this point of the bridge was exposed to very high noise level, no earthquake data could be adopted for the SSR analysis. Attempts were made to filter the data in different frequency ranges to emphasise possible seismic event recordings, but no meaningful results were achieved. Therefore, only the seismic noise recorded during the tests (configurations 3a and 4a, Table 4.2) was analysed. At this point of the bridge, all eigenfrequencies can be seen (Figure 4.12): the 1st mode at 0.76 Hz in the longitudinal direction, the 2nd mode at 0.97 Hz in the transverse component, the 3rd at 1.35 Hz in the vertical SSR function, the 4th at 1.50 in the transverse direction, the 5th at about 1.98 Hz, which includes both the vertical and longitudinal components, and the 6th mode at f = 2.10 Hz, which is a pure transverse bending mode. Good agreement was found between the SSR functions obtained by analysing two types of ambient noise data, AVT-OC and AVT-SV. The estimated frequency peak values have a maximum difference of 0.04 Hz for the transverse component.

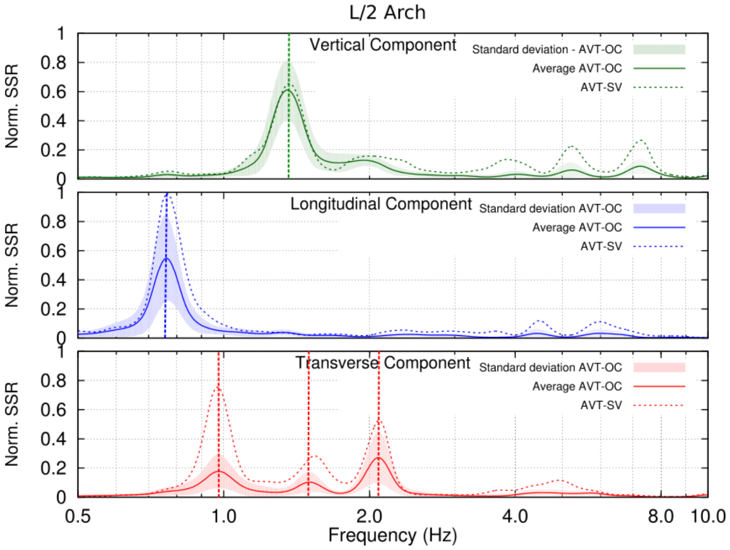

Fig. 4.12 Standard spectral ratios computed at point L/2, on the arch of the bridge using both AVT-OC and AVT-SV data. From top to bottom, the results related to vertical, longitudinal, and transverse SSR components are shown. The vertical dashed lines highlight the main frequency peaks retrieved by means of SSR analyses.

4.4.2.5 L/2 deck South side

The same eigenfrequencies determined for point L/2 point on the arch, were also estimated also for the L2 deck point by analysing both the ambient vibrations data acquired in configuration 1a (Table 4.2) and the earthquake recordings (Figure 4.13): the 1st mode at about 0.76 Hz in the longitudinal direction, the 2nd mode at 0.97 Hz in the transverse SSR function, the 3rd eigenfrequency at 1.35 Hz mainly vertical with a significant contribution in the longitudinal direction, and the 4th mode at 1.5 Hz in the transverse component. Very good agreement in the determination of the eigenfrequencies by SSR analyses between the data from 11 earthquakes (Figure 4.13a) and ambient noise (Figure 4.13b) was observed. The maximum differences in the estimated frequency peak values are 0.02 Hz.

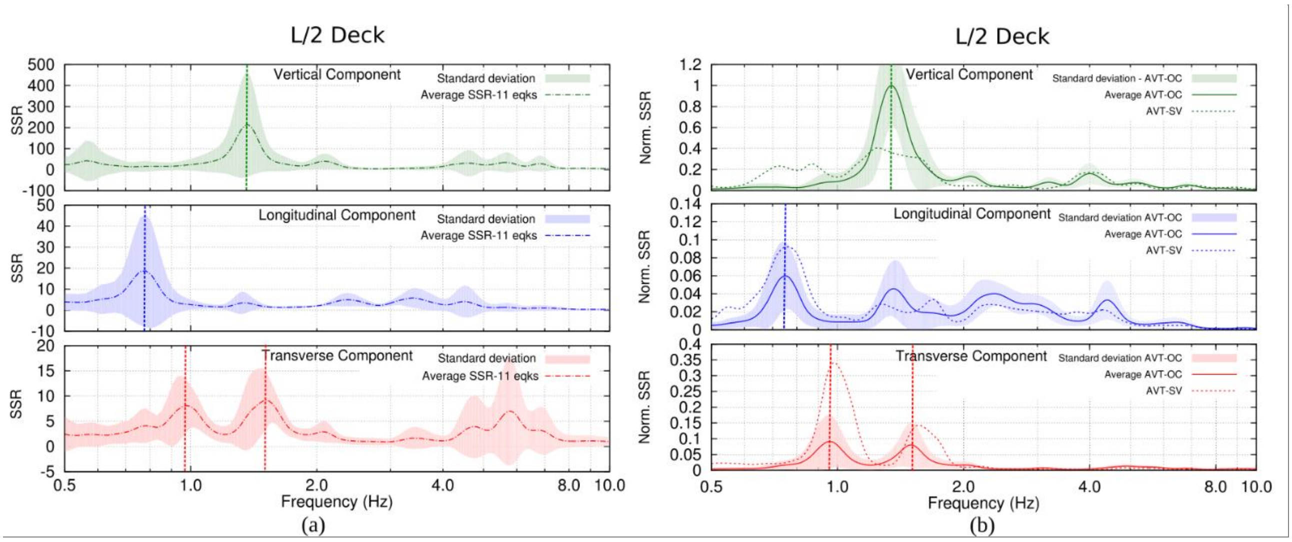

(a) (b)

Fig. 4.13 Standard spectral ratios computed at point L/2, on the deck of the bridge. (a) Results retrieved from the analysis of 11 earthquake data. (b) Results retrieved using both AVT-OC and AVT-SV data. From top to bottom, the results related to vertical, longitudinal, and transverse SSR components are shown. The vertical dashed lines highlight the main frequency peaks retrieved by means of SSR analyses.

4.4.3 Ground-based Microwave Radar interferometry (MRI)

MRI has the great potential to check the complete state of a structure at once and can be considered as a powerful remote sensing tool from an engineering point of view, i.e., for vibration measurement of structures/infrastructures such as bridges and and historical buildings (**Pieraccini et al., 2008**; **Atzeni et al., 2010**; **Gentile, 2010**; **Roädelsperger et al., 2010**; **Stabile et al., 2012, 2013**).

With the aim of determining the displacement time history along the sensor-target line of sight (LOS), between the sensor and the target, ground-based MRI was performed on October 29, 2019, based on a radar system with two antennas transmitting electromagnetic signals in Ku or X band and receiving echoes from the target with an IBIS S device. The higher measurement accuracy (sensitivity of 0.01– 0.02 mm), comparable to standard accelerometers, simultaneous measurement of the different points of large structures, and the possibility of usein in all weather conditions (i.e., rain, smoke, fog, and dusty environment) are the main advantages of this technique. A disadvantage is that it is very difficult to perform continuous monitoring of the entire structure. In the following, the results of the analysis of the data acquired in configuration 1b are described. Since six points, in configuration 1a, (represented by the transverse beams connecting the main girders) have the highest SNR peaks along the distance profile, they were Sselected as the six targets corresponding to the six partitions from L/4 (target 1 in Figure 4.14a, b) to L/2 (target 6 in Figure 4.14a, b).

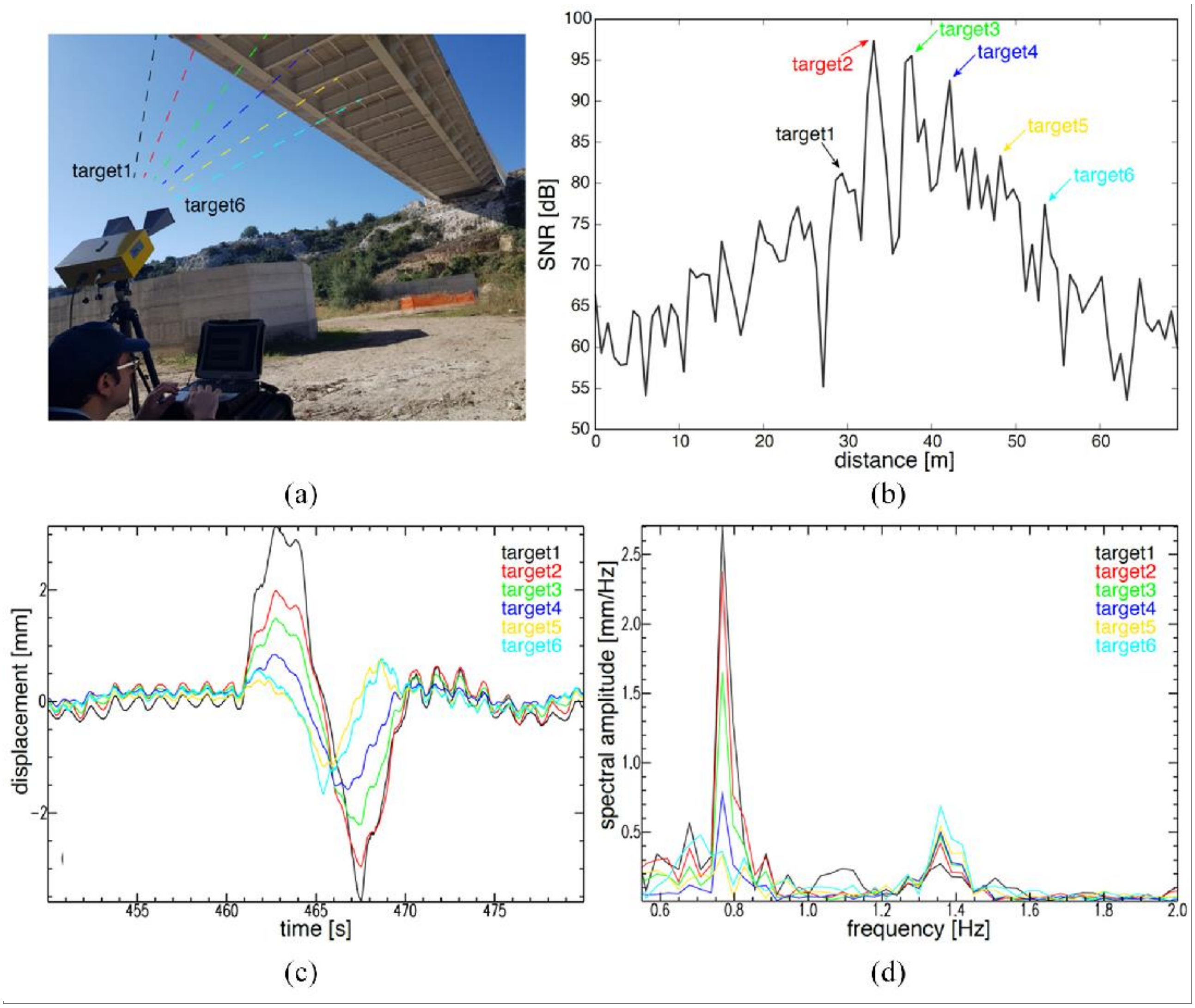

(a) (b)

(c) (d)

Fig. 4.14 (a) Installation of the IBIS-S sensor under the Gravina Bridge with the indication of the six partitions from L/4 (target 1) to L/2 (target 6), selected as targets. (b) Selection of the six targets along the distance profile. Each target is marked with a different color. (c) Radial displacement time histories of the six targets. (d) Amplitude spectra of the six targets.

Following **Stabile et al. (2013)** and THE references therein, radar signals backscattered from the selected targets were processed. Since this remote sensing is inherently incapable of revealing the displacements outside the LOS, only the first vertical eigenfrequencies related to the 1st and 3rd mainly vertical modes at f = 0.75 and f = 1.35 Hz, respectively, were highlighted using this method. The maximum displacement spectral amplitude of the eigenfrequency at f = 0.75 Hz is at L/4 (target 1, black curve in Figure 4.12d) and gradually decreases toward L/2 (target 6, light cyan curve in Figure 4.14d). Moreover, the eigenfrequency at f = 1.35 Hz has the maximum value of displacement spectral amplitude at L/2 (target 6, light cyan curve in Figure 4.12d) which decreases toward L/4 (target 1, black curve in Figure 4.12d). This behaviour is in good agreement with observations made with OMA (SSI and FDD) and SSR. Details on the experiment and analysis procedures can be found in **Serlenga et al. (2021)**.

4.4.4 Operational Modal Analysis (OMA)

OMA is also referred to as ambient modal identification and has been established as a modal testing method to experimentally estimate the modal properties of a structure by recording only the ambient vibration noise and operational loads (**Rainieri and Fabbrocino, 2014**). Both Subspace Stochastic Identification (SSI - The theoretical scientific treatment of this method is beyond the scope of this thesis), as well as Frequency Domain Decomposition (FDD – Theoretical background in Chapter 2) were applied to the ambient vibrations recorded on 12 July 2019 under operating conditions (configuration 2a in Table 2), and yielded the first six eigenfrequencies (for both deck and arch), as shown in Figure 4.15. As described in the theoretical part of (**Chapter 2**), the FDD method identifies the natural frequencies based on the peaks in the singular value plots of the diagonal matrix obtained by decomposing the power spectral density (PSD) matrix using the singular value decomposition (SVD) method.

Because a linear array was used in two different configurations to cover both the deck and the arch on the south side of the infrastructure only, it is not possible to construct 3D mode shapes that comprehensively and definitively represent both flexural and torsional modes. However, based on previous results of the application of OMA techniques by other authors, in both time and frequency domains for the same structural typology (e.g., **Turker and Bayrakatar, 2014**; **Zordan et al., 2014**; **Ferrari et al., 2015, 2016, 2019**; **Garcia Macias et al., 2015**; **Whelan et al., 2018**; **Meixedo et al., 2021**; **Zonno and Gentile, 2021**; **Borlenghi et al., 2022**) it is possible to hypothesise which are the torsional and which are the bending modes.

Eigenfrequencies estimations

Six vibration modes were identified in the frequency range of 0–5 Hz for the deck. The observed vibration modes can be roughly divided into the following categories: vertical bending modes of the deck and vertical torsional modes of the deck, which also contain a transverse component. Table 4.3 compares the corresponding eigenfrequencies obtained by the two different identification methods (SSI and FDD). The absolute value of the percentage discrepancy D_f (%) between the frequencies obtained by FDD and SSI does not exceed 4.78% with respect to the FDD estimates (D_F(%)= (f_{SSI} -f_{FDD})/f_{FDD}).

First, the 1st and 3rd vertical mode shapes of the bridge were reconstructed using the spectral amplitudes and associated phases obtained from the Fast Fourier Transform (FFT) of the seismic noise recorded under operational conditions. For this purpose, the signals of the vertical components in configuration 2a (Table 4.2) were used.

Deck mode	*Direction of motion*	f_{SSI} (Hz)	f_{FDD} (Hz)	D_F (%)
1st	*Vertical Bending*	0.76	0.757	0.42
2nd	*Torsional Vertical/Transverse*	0.97	0.964	0.58
3rd	*Vertical Bending*	1.35	1.355	0.37
4th	*Torsional Vertical/Transverse*	1.5	1.501	0.097
5th	*Vertical Bending*	2	1.965	1.76
6th	*Torsional Vertical/Transverse*	2.2	2.100	4.78

Table 4.3 Experimentally identified modal frequencies using FDD and SSI methods, mode shapes of the bridge deck and frequency discrepancy between f_{SSI} and f_{FDD}.

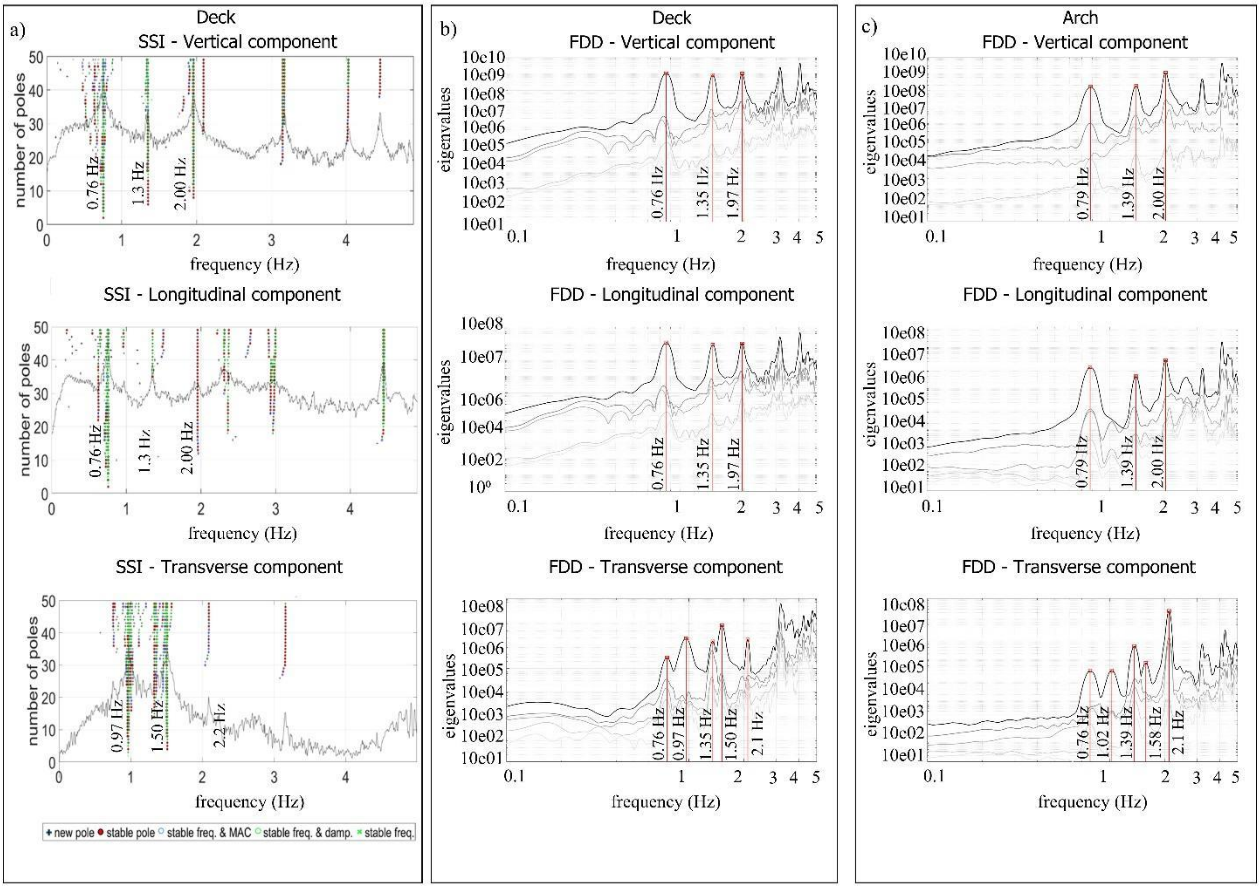

Fig. 4.15 OMA results for the vertical, longitudinal, and transverse components, by analysing AVT-OC data collected on the deck on 12 July 2019 using (a) SSI and (b) FDD, and (c) by analysing AVT-OC data recorded inside the arch on 29 October 2019 and evaluated by using FDD.

4.4.5 Frequency variations

4.4.5.1 Non-stationary inter-event

The S-transform analysis (**Stockwell et al., 1996**), a time-frequency analysis was applied on both earthquake and ambient vibration recordings generated by dynamic tests under special conditions, with the aim of evaluating the non-stationary structural behaviour. A scalable sliding Gaussian window was used to process the signal; in this way, the robustness of results provided by the short-time Fourier transform was improved. Subsequently, the continuous wavelet transform tool was used to provide frequency-dependent resolution that preserves a direct relationship to the Fourier spectrum. In this way, an indication of the possible damage evolution can be observed by studying time-frequency variations (**Mucciarelli et al., 2011**; **Ditommaso et al., 2012, 2015**; **Ditommaso and Ponzo, 2015**; **Iacovino et al., 2018**; **Gallipoli et al, 2016**, **2020**). Therefore, the vertical recordings of the 2.4-Ml earthquake and seismic noise acquired during the dynamic test under special conditions (configuration 1a in Table 4.2) at L/4 and L/2 with accelerometers and velocimeters were evaluated using time–frequency analysis. Applying the S-transform to the earthquake recordings leads to the results in Figure 4.16a, b: Since the studied seismic event produced only weak motion, no variations are detected at the 1st eigenfrequency at 0.76 Hz on L/4 deck and at the 3rd eigenfrequency at 1.35 Hz on the L/2 deck. Since the maximum motion amplitudes induced by the passage of a 40-tons truck moving at a constant velocity of 50 km/h over a wooden plank were not high enough to cause a non-stationary behaviour of the Gravina Bridge, analogous results were obtained using the ambient vibrations special conditions (Figure 4.17a, b). Details of the experiment and analysis procedures can be found in **Serlenga et al. (2021)**.

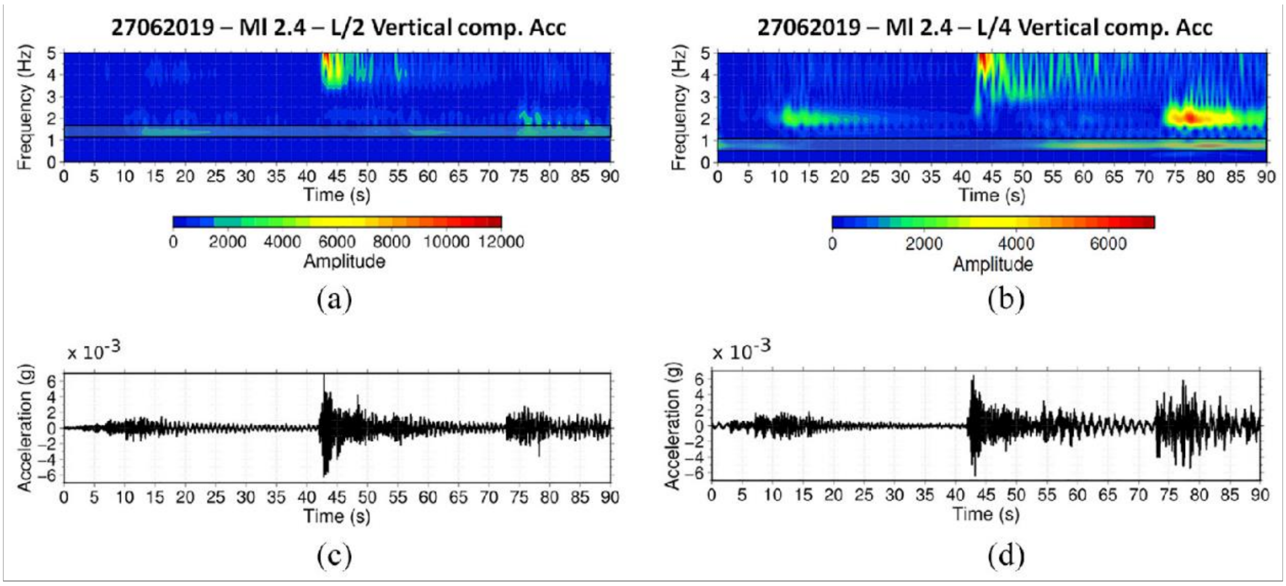

Fig. 4.16 (a) S-transform computed on 90 s of seismic signal recorded by L/2 accelerometer, (b) S-transform computed on 90 s of seismic signal recorded by L/4 accelerometer, (c) seismic signal recorded at L/2 and analysed by means of S-transform technique, centred on the recording of the 2.4-Ml earthquake (PGA 1.1 31022 g, cf. Table 1), and (d) seismic signal recorded at L/4 and analysed by means of S-transform technique, centred on the recording of the 2.4-Ml earthquake (PGA 1.1 31022 g, cf. Fig. 4.5).

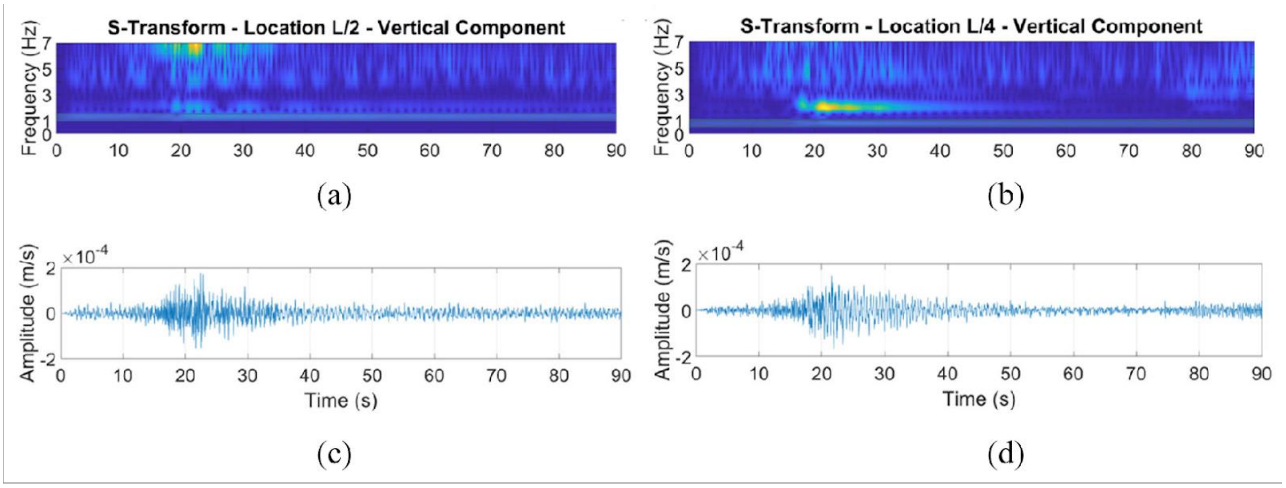

Fig. 4.17 (a) S-transform computed on 90 s of AVT-SV data recorded by velocimeter at L/2, (b) S-transform computed on 90 s of AVT-SV data recorded by velocimeter at L/4, (c) seismic signal recorded at L/2 and analysed by means of S-transform technique, and (d) seismic signal recorded at L/4 and analysed by means of S-transform technique.

4.4.4.2 Variations with the temperature

The fundamental frequencies estimated from processing signals recorded at two different times of the year, i.e., measurements in summer and in autumn, show small differences (less than 5%). The results of the two tests performed under different temperature conditions (35° in July and 10-12° in October), suggest that natural frequencies tend to increase with decreasing temperature (Table 4.4). However, only two tests were conducted, so no further information on the effects of the environment on the natural frequencies can be obtained.

Deck Mode	***Direction of mode***	***f_{FDD}*(Hz)** July 12th (≈35°)	***f_{FDD}*(Hz)** October 29th (≈10-12°)	**$\Delta_f(T°)$(%)**
1st	*Vertical Bending*	0.757	0.793	4.62
2nd	*Torsional Vertical/Transverse*	0.964	1.022	5.67
3rd	*Vertical Bending*	1.355	1.389	2.42
4th	*Torsional Vertical/Transverse*	1.501	1.572	4.47
5th	*Vertical Bending*	1.965	2.014	2.42
6th	*Torsional Vertical/Transverse*	2.100	2.106	0.29

Table 4.4 Experimentally identified modal frequencies, mode shapes of the bridge deck and frequency discrepancy between f_{FDD} in summer and autumn.

4.4.6 Esstimation of equivalent viscous damping factor: logarithmic decrement method (LDM)

The evaluation of the experimental equivalent viscous damping factor (z) from a signal recorded on a vibrating structure using the logarithmic decrement method (LDM, **Clough and Penzien, 2003**) has been performed. The LDM technique is usually applied only to free vibrations motion. However, in this study the equivalent viscous damping factor under stationary conditions for the six estimated eigenfrequencies was evaluated by applying this method to the impulse response function (**Snieder and Safak, 2006**) of seismic ambient noise recorded in operational conditions (configuration 2a in Table 4.2). A viscous damping factor of about 2% to 3% was estimated for the six eigenfrequencies. Figure 4.18b shows the value of 2.2% as the viscous damping factor obtained by the analysis of the eigenfrequency of 0.76 Hz at point L3/4. Since the station at L3/4 is characterised by consistent energy of both 1st and 2nd vertical modes of the bridge (high value of SNR), it was selected. Details of the experiment and analysis procedures can be found in **Serlenga et al. (2021)**.

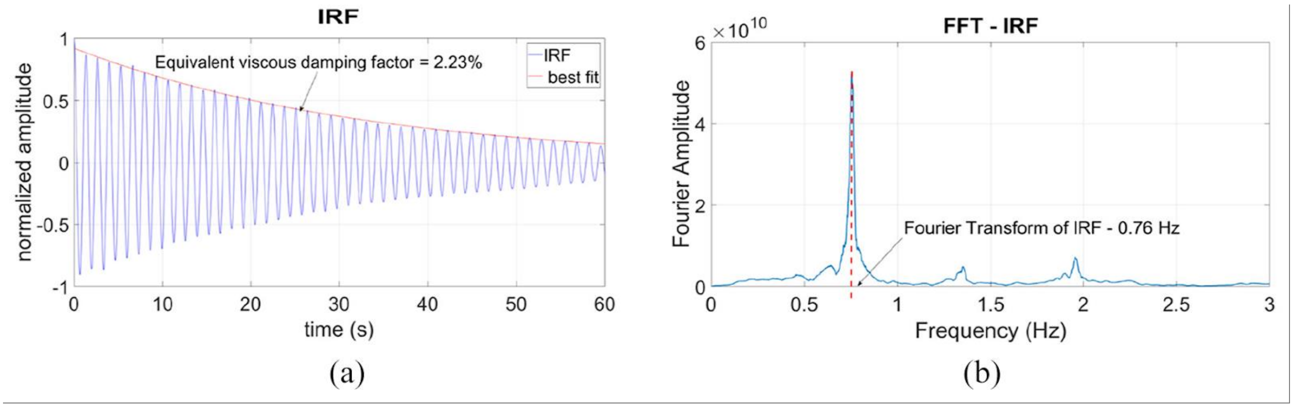

(a) (b)

Fig. 4.18 (a) Application of the LDM to the IRF evaluated from AVT-OC signal recorded at L3/4 and (b) Fourier transform of the same IRF showing the peak at 0.76 Hz (vertical red dashed line), representing the 1st mode of vibration.

4.4.7 Mode shapes

The mode shapes of the Gravina Bridge were evaluated using the Frequency Domain Decomposition method. The decomposition of the power spectral density (PSD) matrix using the Singular Value Decomposition (SVD) allows us to obtain six mode shapes. Figures 4.19 and 4.20 show the derived mode shapes of all eigenfrequencies for the deck and the arch, respectively, obtained by plotting on the y-axis for each mode the displacement values of the mode shape vector normalised by the component with the largest modulus, and on the x-axis the position of the sensors (green: vertical - Z, red: transverse - X, blue: longitudinal - Y).

4.4.7.1 Deck Mode shapes

The 1st mode of the deck at 0.76 Hz is a bending mode with a major contribution in the vertical direction (as confirmed by the numerical model) and a minor one in the longitudinal direction. The 2nd mode of the deck at about 1 Hz is probably a vertical torsional mode. Although the singular value plots of both SSI and FDD show a peak in the transverse direction only (Figure 4.19), it appears from the FFT of the signals recorded from all the sensors deployed on the deck that at this frequency (~1 Hz) the greater energy content is concentrated in the vertical direction (Figure 4.8). The 3rd mode of the deck at $f = 1.35$ Hz is a vertical bending mode with a contribution also in the longitudinal and transverse directions. The 4th mode of the deck at $f = 1.50$ Hz is likely a vertical torsional mode with a contribution from the transverse component. The 5th mode at $f \approx 2$ Hz of the deck is mainly a vertical bending, but also has a slight contribution in the longitudinal direction. The 6th eigenfrequency $f = 2.1$ Hz of the deck refers to a vertical torsional mode, which also contains a non-negligible contribution in the longitudinal and transverse directions.

Following the presentation of the results, it should be noted that the vertical bending mode shapes of the deck always remain the same for ambient noise with and without traffic. In contrast, the vertical torsional mode shapes change slightly depending on the content of the recorded ambient noise signal. If the noise contains traffic, the transverse component is emphasised, while for noise recorded without through traffic on the infrastructure, the torsional mode shapes are characterised by a clear predominance of the vertical component.

4.4.7.2 Arch Mode shapes

This part of the bridge has a more complex behaviour than the deck. With the exception of the 1st mode ($f = 0.79$ Hz), which has a similar shape to the 1st mode of the deck in the vertical direction and also provides a contribution in the longitudinal direction (Figure 4.21), from the 2nd to the 5th mode of the arch, all components are involved with comparable contributions. The 6th mode at the eigenfrequency $f = 2.1$ Hz is a pure transverse mode for the arch. Very good agreement was obtained between the spectral analysis (FFT) of the signals recorded inside the arch (Figure 4.7b) and the mode shapes resulting from the extrapolation of the corresponding singular vectors of the unitary matrix derived from the application of the singular value decomposition to the input power spectral density matrix (Figure 4.15).

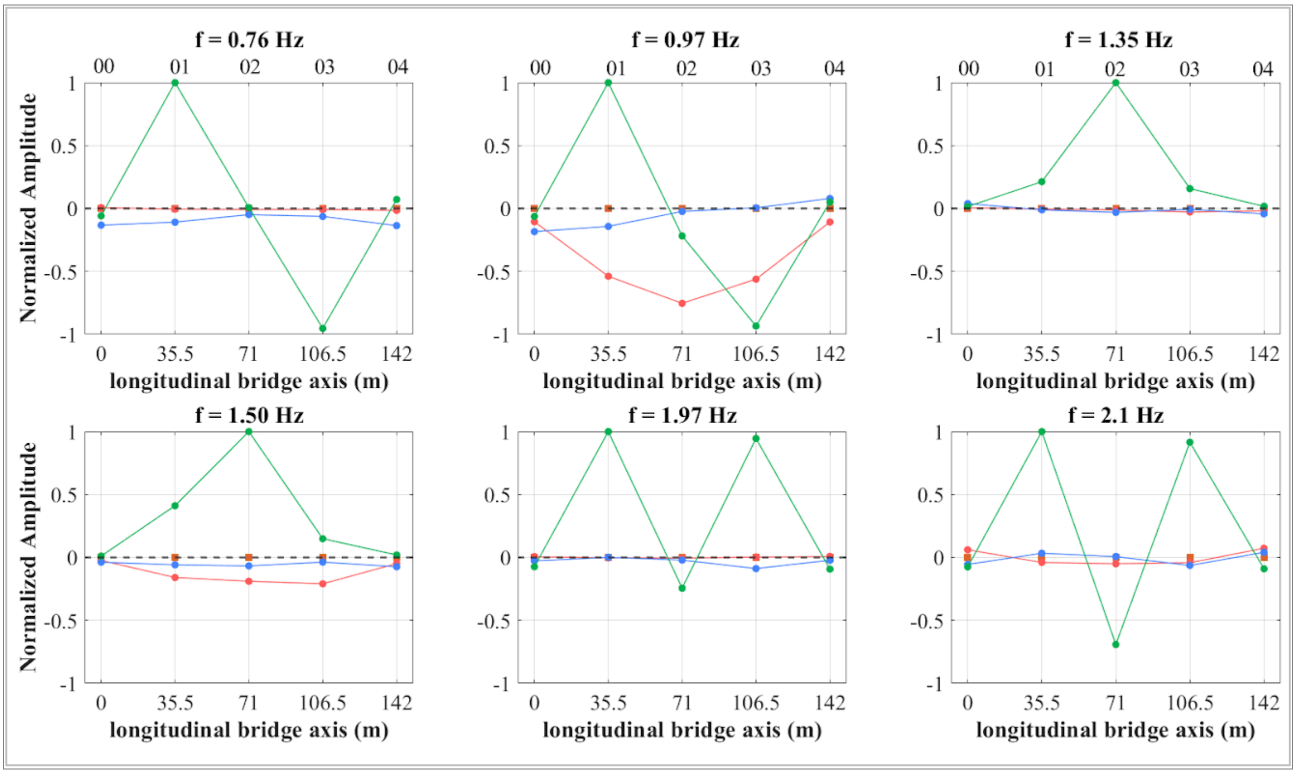

Fig. 4.19 Mode shapes corresponding to the six eigenfrequencies of the deck. Red, blue and green lines refer to the X (transverse), Y (longitudinal) and Z (vertical) directions, respectively; y-axis: for each mode the displacement values of the mode shape vector normalised by the component with the largest modulus.

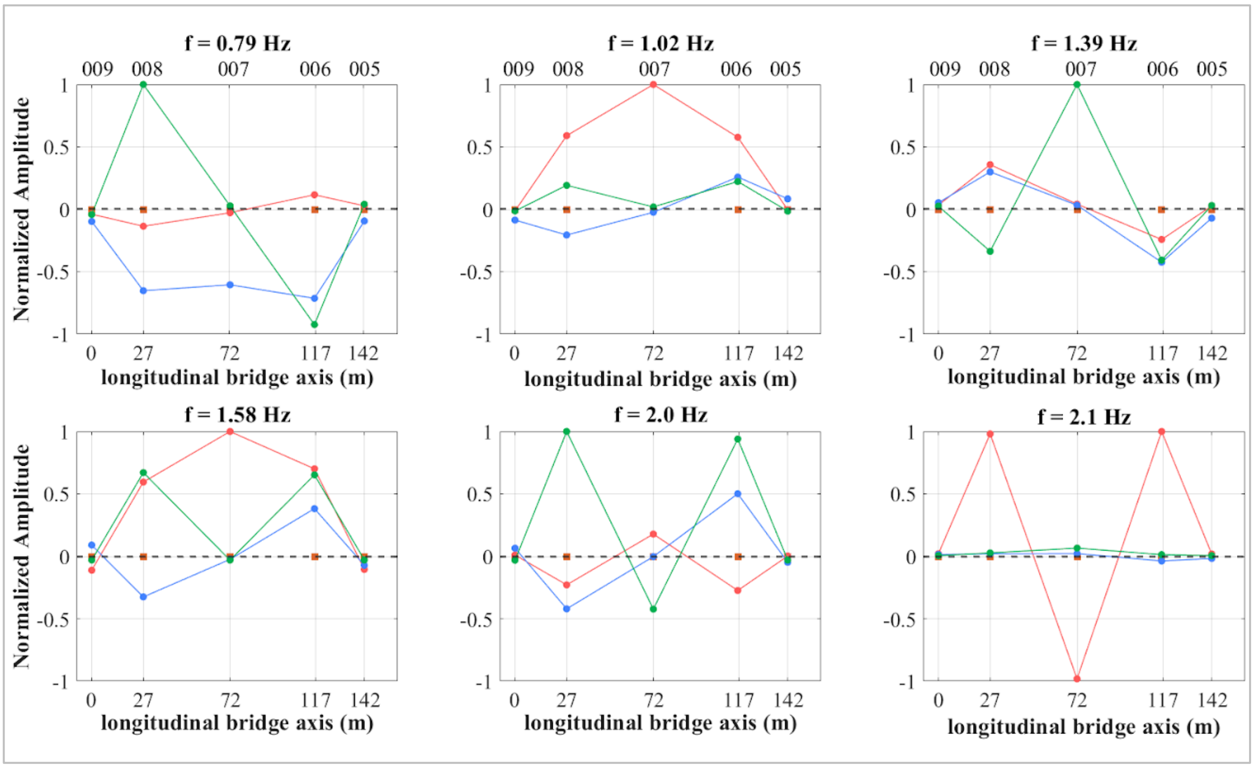

Fig. 4.20 Mode shapes corresponding to the six eigenfrequencies of the arch. Red, blue and green lines refer to the X (transverse), Y (longitudinal) and Z (vertical) directions, respectively; y-axis: for each mode the displacement values of the mode shape vector normalised by the component with the largest modulus.

Figure 4.21 shows the numerical mode shapes provided by ANAS for the first and third vertical modes (0.76 and 1.35 Hz, respectively). The experimental mode shapes of the Gravina Bridge are in good agreement with the numerical ones, giving the same results. The observed agreement between model and experimental results is interpreted as a consequence of the stationary dynamic behaviour the bridge.

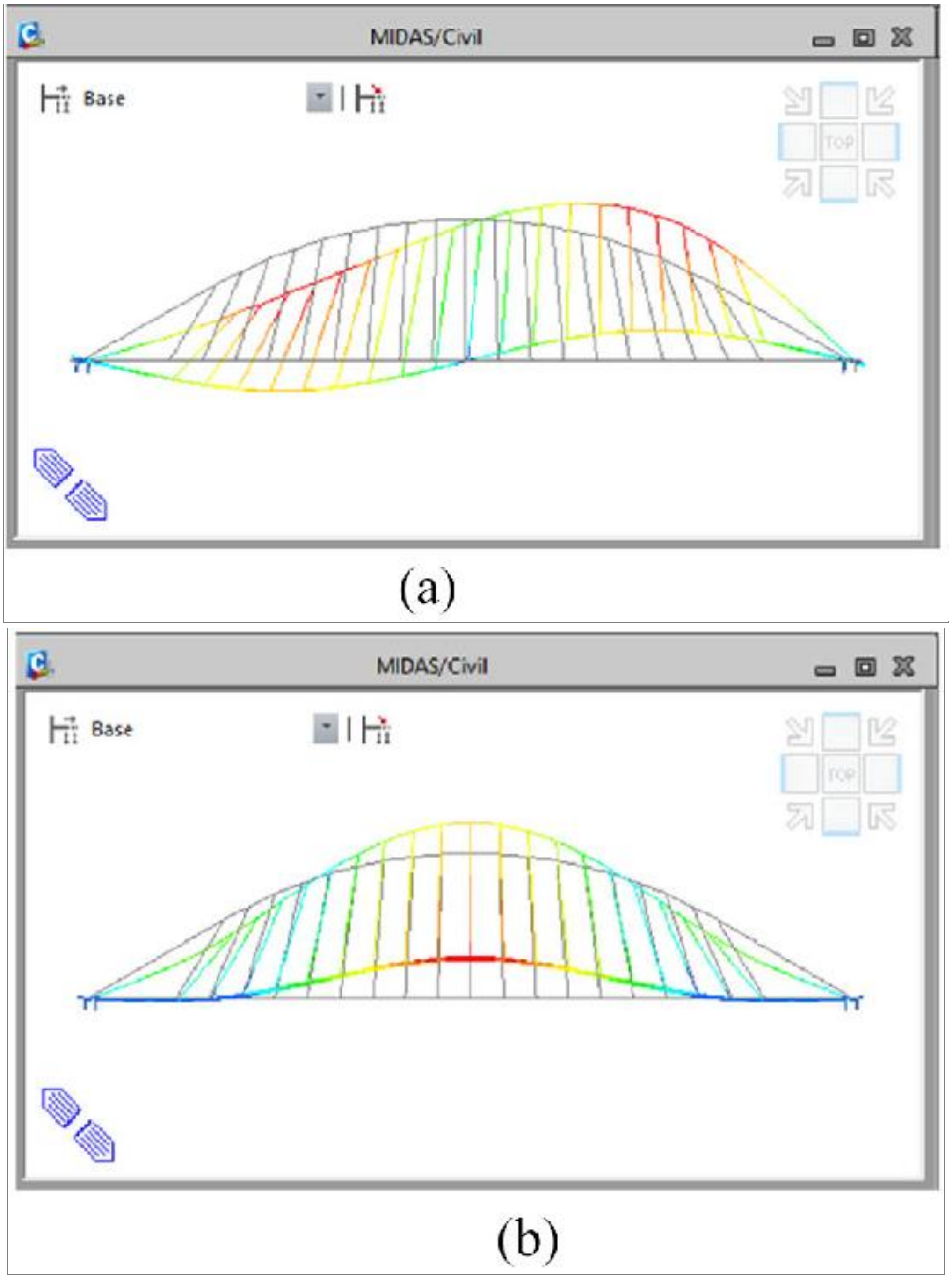

*Fig. 4.21 Numerical mode shapes of (a) the first mode of vibration and (b) the third mode of vibration (**Matildi et al., 2015**).*

4.4.8 Wave propagation velocity

In order to study the wave propagation through the Gravina Bridge, ANDI was applied using the same signals as for FDD, recorded in configuration 2a. The recorded data (88 minutes long) were divided equally into three parts (29 minutes in duration); then the method was applied to each trace. The deconvolution approach was carried out for the deck (Figure 4.22) for each of the three components of motion (red: transverse direction - X, blue: longitudinal direction -Y, green: vertical direction - Z). For configuration 2a, sensor 00 (located on the deck above the elastomeric isolator, Figure 4.22b) was chosen as a reference. However, considering sensor 04 on the other side of the deck as a reference gave very similar results, and thus, the IRFs are not shown here. First, common pre-processing of the signal (de-mean, de-trend, tapering, and bandpass) was performed in the same way for all three signals (29 minutes duration). Moving windows of 80-s duration were chosen, without overlapping and were stacked using the mean function. In order to identify the frequency range to be associated with the estimation of propagation velocities, I processed the recorded signal in three ranges using three bandpass filters: (i) 0.1 - 12 Hz, (ii) 0.1 - 5 Hz, and (iii) 7 - 13 Hz. The results obtained with ranges (i) and (iii) are very similar to each other, while they differ from the estimates in range (ii). Therefore, it turned out that probably the range in which it is correct to apply deconvolution interferomerty, in order to calculate the ambient noise wave propagation velocities in the infrastructure, is 7-13 Hz, since there is still significant energy content in this range and the deconvolved wave fields are more interpretable than those obtained by applying ANDI in the (ii) range (to which the modal frequencies of the bridge belong). Therefore, I chose analysis range (iii) by exclusion and only the results from this range are presented for the deck. I then applied the interferometric deconvolution technique to three equal parts (29 minutes long) into which I split the signal recorded in configurations 2a and 4a in order to obtain more robust results.

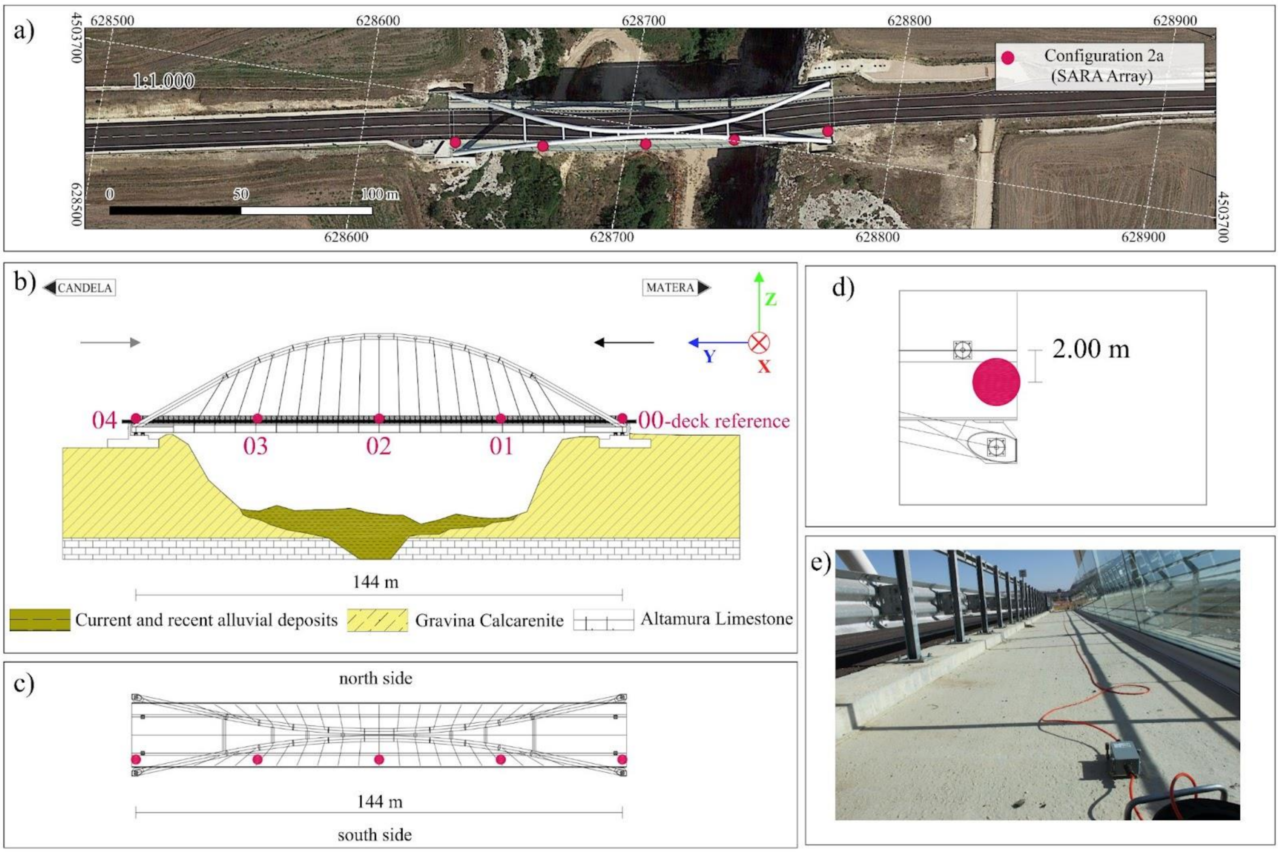

Fig. 4.22 (a) Configuration 2a: experimental setup, bridge top view; (b) Elevation: scheme of configuration 2a on the deck (red dots: SARA array), and sketch of foundation soil lithology; top-right: the acquisition reference system showing the three directions; grey arrow: direction of forward propagating wave; black arrow: direction of backward propagating wave; (c) scheme of the instrumental configuration 2a; (d) detailed information on position of the 00 SARA velocimeter, 2 m away from the elastomeric isolator under the main beam (type 1) and in axis with the elastomeric isolator (type 2) under the arch; (e) Photo of the velocimeter sensor 01 located at L4 Matera side of the structure south side in configuration 2a.

Figure 4.23 shows the deconvolved wavefields of the three components, (X - transverse: red line, Y - longitudinal: blue line and Z: green line) using the traces of about 29 minutes in length into which I divided the original 88 minutes long signal recorded on the deck in configuration 2a on 2019 July 12th. For each component and sensor, the waveforms of the three windows do not show significant variations. The IRFs of the deck are characterised by clear peaks of forward (from Matera to Candela, Figure 4.22b grey arrow) and backward propagating waves (from Matera to Candela, Fig. 4.22b black arrow), marked by dashed lines (Figure 4.23). It is possible to identify polarity changes of the main peaks of the IRFs of the Z component (Fig. 4.23), which can probably be related to the mode shape (positive and negative normalised amplitudes) of the fundamental mode of the deck at 0.76 Hz (Figure 4.20), although the deconvolution analysis was performed in the range of 7-13 Hz, i.e. in the range of the estimated eigenfrequencies of the bridge. Comparing the shape of the 1st deck mode (Figure 4.20) and the forward and backward propagating waves of the deconvolved waveforms in the Z direction (Figure 4.20), the polarity of the main peaks changes between sensors 00 and 01, 01 and 02, and 03 and 04 (Figure 4.23).

The interpretation of the deconvolved wavefields for the arch is much more difficult, given the greater complexity of this part of the structure. The results of the interferometric deconvolution of the ambient noise signal recorded in configuration 4a, which was 64 min long, and filtered in the range 0.1 - 12 Hz, are shown in Figure 4.24. For the arch, the polarity inversions observed for the main peaks of the IRFs of the Z component are likely due to the mode shape of the fundamental mode at 0.79 Hz in the Z and X directions (Figure 4.21). Moreover, especially in the IRFs of the arch, the X component of the deconvolved wavefields oscillates at a frequency of about 2.1 Hz (indicated by black dashed vertical lines), corresponding to the sixth mode of the arch. In this context, the waveforms polarities change between sensors 008 and 007, and 007 and 006, which is clearly visible in the transverse direction of the deconvolved wavefields (Figure 4.24) as already observed for the transverse mode shape of the sixth mode at f = 2.1 Hz of the arch (Figure 4.21). For the Y component of the arch, oscillation related to a higher mode can be seen at a frequency of about 5 Hz (Fig. 4.21). To investigate further, Fig. 4.25 shows the deconvolved wavefields of the three traces of about 23 minutes duration, where the signal recorded inside the arch on October 29, 2019 was also split and a bandpass filter of 7 - 13 was applied as in the case of the deck. Again, the three impulse response functions do not show pronounced variations; however, the difficulty of interpretation remains due to the complexity of this part of the structure, which is why the estimates of the propagation velocities are not shown here.

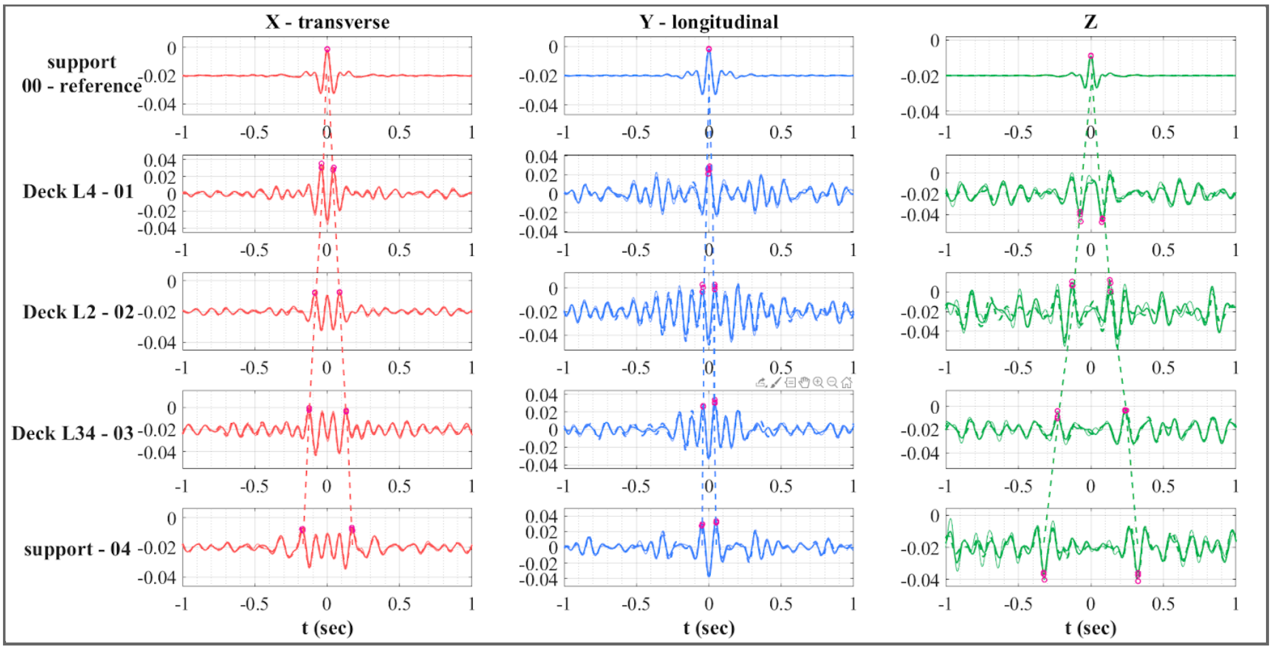

Fig. 4.23 Fig. 5 IRFs obtained for the Gravina bridge deck. The deconvolution was performed with respect to the sensor 00. The dashed lines indicate the forward and backward propagating waves and correspond to the wave propagation velocities estimated using the time lags between the pulses of forward and backward propagating waves. (X: red line, Y: blue line and Z: green line).

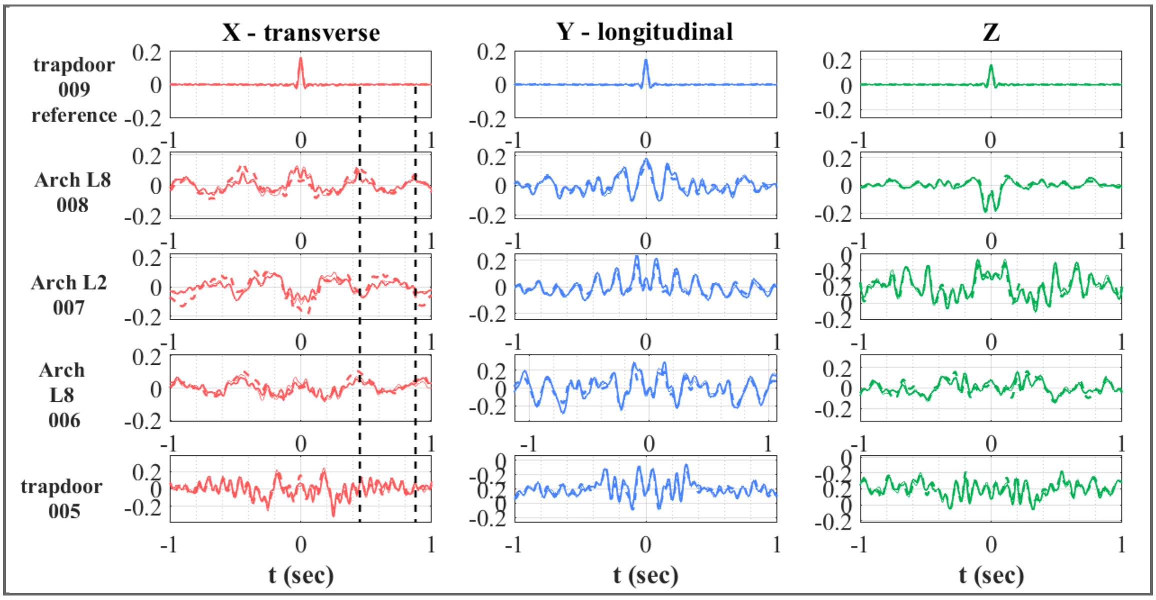

Fig. 4.24 Fig. 6 IRFs obtained for Gravina bridge arch. The deconvolution was performed with respect to the sensor GEO009. The dashed black lines correspond to the sixth mode of the arch at 2.1 Hz. In transverse direction of the deconvolved wavefields, the waveforms polarities change between sensors 008 and 007, and 007 and 006, (X: red line, Y: blue line and Z: green line).

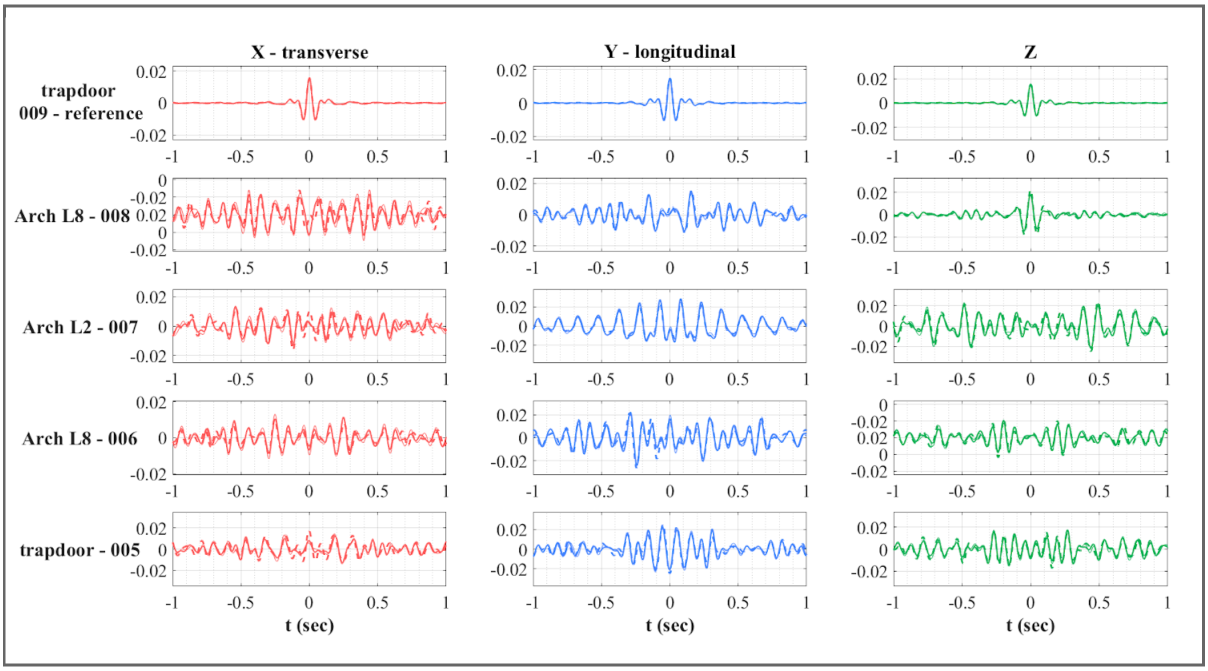

Fig. 4.25 Fig. 6 IRFs obtained for Gravina bridge arch. The deconvolution was performed with respect to the sensor GEO009. The three impulse response functions do not show pronounced variations; the difficulty of interpretation due to the complexity of this part of the structure did not allow it to recognise the forward and backward propagating waves. (X: red line, Y: blue line and Z: green line).

On the deck, for each trace with a duration of 29 minutes, the wave propagation velocities are estimated from the time lags between forward and backward propagating pulses in the deconvolved wavefileds and the distance of the locations of the sensors. Figure 4.26 shows the time lags (X: red circles, Y: blue circles, Z: green circles) for each sensor with respect to the distance of each sensor from the reference station (deck: sensor 00). The average velocities were estimated using a least squares fit which corresponds to the slope of the determined best fit line. The arithmetic mean of the three velocities and the standard deviation were calculated for each component (Figure 4.26). The lowest wave propagation velocity (about 450 m/s) was estimated in the vertical direction Z, which is associated with the least rigid component because the deck is most flexible in this direction. A wave propagation velocity of about 840 m/s was observed in the transverse direction X and the largest one in the longitudinal direction Y (about 2500 m/s), the most rigid direction. Small variations (less than 5%) in the forward and backward propagating wave velocities along the three components can be considered negligible. The average velocities of the forward and backward propagating waves show negligible differences (about 5%), which are related to the accuracy of the analysis and are probably not connected to degradation-related effects. The estimated velocities are in good agreement with those obtained for bridges by other authors (**Jian et al., 2020**; **Garcia – Macias and Ubertini, 2021**).

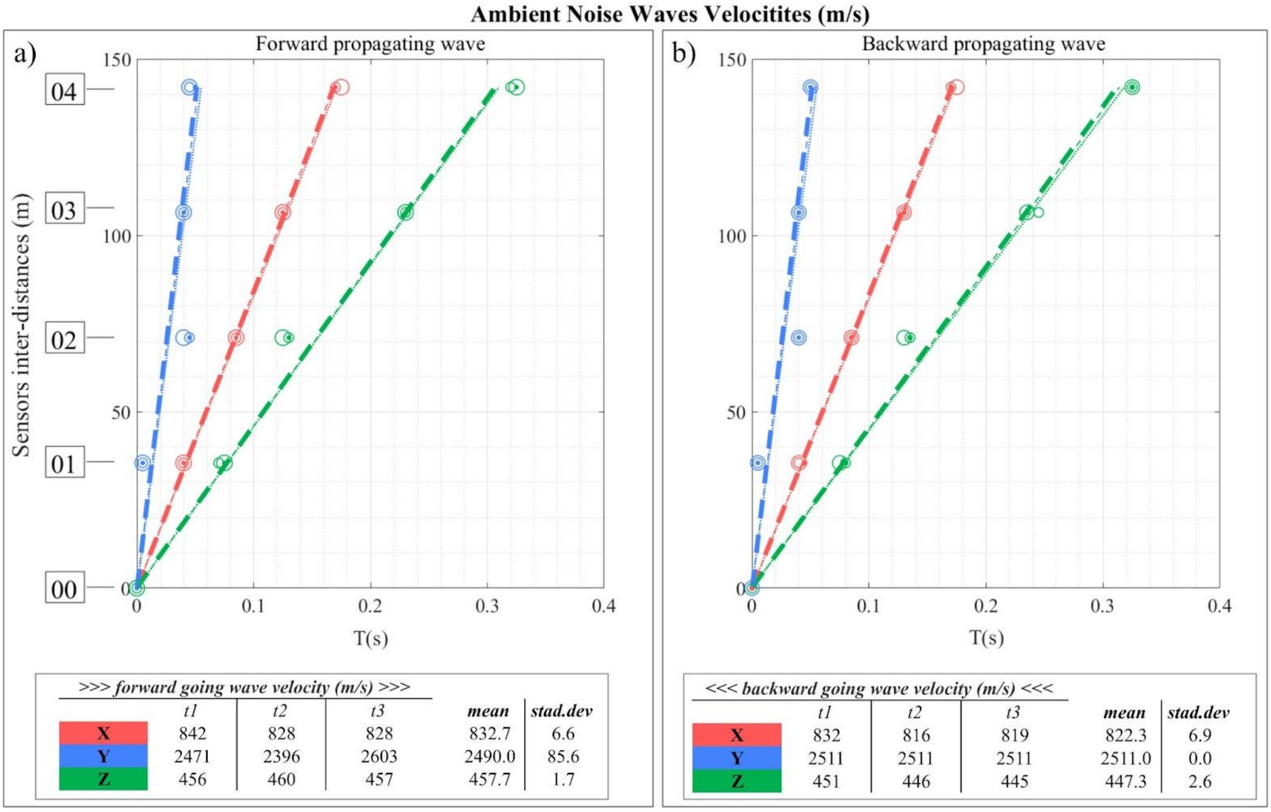

>>> forward going wave velocity (m/s) >>>

	t1	*t2*	*t3*	*mean*	*stad.dev*
🟥 **X**	842	828	828	832.7	6.6
🟦 **Y**	2471	2396	2603	2490.0	85.6
🟩 **Z**	456	460	457	457.7	1.7

<<< backward going wave velocity (m/s) <<<

	t1	*t2*	*t3*	*mean*	*stad.dev*
🟥 **X**	832	816	819	822.3	6.9
🟦 **Y**	2511	2511	2511	2511.0	0.0
🟩 **Z**	451	446	445	447.3	2.6

Fig. 4.26 Travel times between the pulses of forward (a) and backward (b) propagating waves at different points on the deck versus the distance of the considered sensor to the reference sensor (deck: 00). The slope of the best fit lines (thick dashed line for trace 1, thin dashed line for trace 2, and dotted line for trace 3 respectively) corresponds to the propagation velocities along the considered direction. Red: Transverse, X direction, Blue: longitudinal, Y direction, Green: vertical, Z direction. Bottom the average velocities estimated for each trace (t1, t2, and t3) in which the signal recorded in configuration 2a has been split, and the mean and standard deviation values are reported both for forward and backward propagating wave velocities.

Conclusion

The main scientific and technological objective of this research project was to develop a systemic approach based on the integration of unconventional, and non-invasive geophysical techniques for the diagnostic and monitoring of urban soil, overlapping buildings and infrastructures affected by natural risks, with reference to seismic risks. In this thesis work, several geophysical techniques have been applied for urban environment monitoring, aiming at the seismic characterization of the soil and buildings at urban scale, as well as the geophysical characterization of the modal parameters of a strategic infrastructure and its associated foundation soil. The first part of the thesis work focused on the urban area of Matera (southern Italy) which is of particular interest in terms of local seismic response. Despite the fact that some parts of the city are composed of hard Altamura limestone and Gravina calcarenite, the stratigraphic sequence in many parts of the city results in high amplification due to the strong impedance contrasts between a thick sand and clay layer overlying the Gravina calcarenites. Based on the availability of numerous pre-existing geological and geotechnical data, that provided a detailed knowledge of the geology of this area, 230 ambient noise measurements have been performed: 134 on the main lithologies and 96 on the most common building typologies. The Horizontal-to-Vertical Noise Spectral Ratio (HVNSR) method was used to analyse the seismic ambient noise recorded on the soils to estimate the soil fundamental frequencies and the relative amplitudes of the fundamental peaks of the soil throughout urban area which were then interpolated to obtain the soil iso-frequency and iso-amplitude maps. A good correlation was found between these maps and the detailed geology of Matera. The same analysis method was applied to 96 measurements on buildings which allowed to estimate the first eigenfrequencies, used to obtain the experimental period-height (T-H) relationship. Due to the availability of the heights of the entire building stock, it was possible to estimate the eigenfrequencies of the 4043 buildings using the T-H relationship. By comparing the vibration frequency ranges of all buildings with those of their foundation soils, the second objective of the thesis work was achieved, namely a double soil-building resonance map. The proposed innovative approach allowed to reconstruct a soil-building resonance map that represents the condition of the building stock in the linear-elastic domain. A severe resonance level was estimated for about 628 buildings (15.5%). The spatial information provided by the results of this study is undoubtedly crucial for identifying the most dangerous areas of the city, i.e., the parts of the city where the occurrence of the soil-building double resonance is likely to greatly increase the damage. In Italy, the built heritage represents an extremely important element in urban areas, therefore its interaction with the soil should be taken into account and implemented in microzonation studies, as this would allow for a more appropriate spatial planning and rational allocation of interventions. In this context, the dissemination of the results of the study to the scientific community and public administrations can play an important role. Therefore, for storing and sharing the data and results of this second objective of the thesis work, the interactive CLARA WebGIS was created, a useful tool developed with open-source software. CLARAWebGIS, accessible at https://smartcities-matera-clara.imaa.cnr.it/, is a user-friendly interface aimed at a wide range of end users (local administrations and planners, engineers and geologists, citizens, etc.). Through the platform, users can query and download following data:

- 319 geological and geotechnical surveys (Downholes, Mechanical Surveys, Calcarenite Sampling Stations, MASW, HVNSR, Seismic Refraction Surveys) from studies conducted between 1990 and 2010,
- 230 single-station seismic ambient noise measurements;
- geological and geomorphological maps, and a map of homogeneous microzones from a seismic perspective (MOPS);
- the estimated fundamental resonance frequencies for all urban soils;
- the estimated the main vibrational frequencies for 4043 overlying buildings;
- the resonance effect of each building in relation to the respective foundation soil.

It is hoped that this tool will be a starting point for the administration of all cities and that WebGis and a geodatabase similar to CLARA WebGIS can be built by combining existing and new geophysical data to characterise the soil and buildings.

In the next phase of this part of the thesis work, the data available in Clara WebGIS and related to masonry buildings were extracted from the database to compare the experimentally and the analytically estimated fundamental periods of historical URM buildings. The analytical fundamental periods were estimated with a simplified approach based on geological, geotechnical, and structural data. The experimental fundamental period of buildings founded on the soft clay was significantly higher than that of buildings founded on stiff calcarenite, given the number of storeys (e.g. 0.27 sec, 0.18 s). In addition, the thicker the clay layer, the higher was the fundamental period of the masonry building. These experimental observations indicate a clear influence of the soft foundation soil on the vibration frequency of the structure. This influence was studied by applying the simplified approach proposed by **Piro et al. (2020)** to seven masonry buildings. Since the approach proposed by **Piro et al. (2020)** takes into account the complexity of the soil-foundation compared to the traditional approaches from the literature, the analytically calculated frequencies are in good agreement with the experimental ones, providing a promising method for territorial-scale assessments of a large number of buildings.

Currently, another important topic in the field of disaster management is structural health monitoring (SHM) of strategic buildings and infrastructures to identify the dynamic characteristics and their changes over time. In this context, Operational Modal Analysis (OMA) and seismic interferometric methods play a key role. In the last part of the thesis work, the results of the structural characterisation of the Gravina Bridge through experimental monitoring are presented. The bridge was equipped with extensive instrumentation to record ambient vibrations. The collected dataset provides valuable results on structural properties, eigenfrequencies, mode shapes, and wave propagation velocities. Spectral analysis of the recordings from sensors installed along the deck and inside the arch identified the natural frequencies of the roadway infrastructure and played a key role in interpreting the mode shapes by evaluating their energy content. Six modes were identified by both frequency domain decomposition analyses and spectral amplitude variations using three-component recordings on the deck and on the arch. These results are in good agreement with those estimated by **Serlenga et al., (2021)**, but allow for expansion and clarification of some details, such as mode shapes identification. Six modes were identified for the deck by Frequency Domain decomposition, FDD have been evaluated: the 1st, 3rd and 6th are vertical blending modes, while the 2nd, 4th and 5th are likely vertical torsional modes. The FDD made it possible to estimate also six modes for the arch; however, this part of the bridge is more complex, and except for the 1st and 6th modes, which are mainly vertical and pure transverse modes, respectively, the 2nd, 3rd, 4th, and 5th modes include all components. Ambient wave propagation velocities were estimated for all three directions of the deck using Ambient Noise Deconvolution Interferometry (ANDI). Along the deck, average propagation velocities were estimated for the vertical, transverse, and longitudinal components at each measurement point on the Gravina bridge deck using a least squares fit. For the deck, the smallest wave propagation velocity (≈ 450 m/s) was observed along the vertical direction, which is probably related to the first flexural mode, i.e., the least rigid, since the deck is most flexible in this direction. An intermediate velocity (≈ 850 m/s) was observed in the transverse direction, and a maximum velocity in the longitudinal direction (≈ 2800 m/s) on the deck, which is the most rigid direction. The estimated velocities are in good agreement with those obtained for bridges by other authors in the literature. The average velocities of the forward and backward propagating waves show negligible differences (about 5%), which are related to the accuracy of the analysis and are probably not connected to degradation-related effects. Small percentage variations in the six eigenfrequencies were measured on the deck between two seasons (summer and autumn). The applied approach using standard spectral analysis, ANDI and standard OMA-based SHM, FDD allowed us to estimate the main structural parameters of the Gravina bridge by analysing short duration ambient noise signals (less than two hours). The latter were recorded by low-cost and non-invasive sensors, and by performing the dynamic tests without rerouting, blocking traffic flow, or interrupting the bridge use. The results of each applied method were used as a reference to better interpret and understand the results of the other applied techniques. In this way, an experimentally innovative and reproducible method has been developed to characterise the modal parameters not only of a complex infrastructure such as the bridge under study, but also of different structural typologies. Further studies will focus on new configurations with more sensors on the arch and deck of the Gravina bridge to explore the mode shape of the 3D structure in depth and to investigate the variations of eigenfrequencies with ageing, degradation and/or possible damage.

Acknowledgements

Prima di tutto vorrei ringraziare il mio supervisor Dr.ssa Maria Rosaria Gallipoli per aver creduto in me, per avermi incoraggiato e spronato fin dai primi passi nel mondo della ricerca e per avermi permesso di crescere come ricercatore. La ringrazio per avermi tramesso la sua esperienza e, attraverso il suo esempio, la passione per questo lavoro, per avermi insegnato il rigore nel metodo scientifico, per i suoi consigli, per essere stata la mia guida nel costruire questo percorso, per aver condiviso il suo tempo e fornito il supporto necessario durante questi anni in ogni momento, e per avermi dato la possibilità di collaborare con altri gruppi di ricerca, e di esplorare e conoscere il mondo della ricerca abbracciando ogni sfida come un'opportunità per crescere sia professionalemtne che dal punto di vista umano.

Ringrazio il Prof. Felice Carlo Ponzo, mio tutor universitario, per aver condiviso con me la sua conoscenza, per le sue utili osservazioni critiche, per avermi dato il suo tempo e per avermi permesso di costruire questo percorso e per i suoi saggi consigli scientifici.

Un particolare ringraziamento va al mio co-tutor Dr. Bojana Petrovic. Per tutto il tempo che mi ha costantemente dedicato nello studio e nella ricerca, dandomi preziose indicazioni, consigli scientifici, suggerimenti, modifiche, correzioni, per avermi spronato e condiviso la sua conoscenza, la sua esperienza, le sue intuizioni e le sue idee. Buona parte di questo lavoro di tesi non sarebbe quello che è se non fosse per il tuo costante supporto.

Il mio ringraziamento va anche al mio co-tutor Dr. Rocco Ditommaso per avermi guidato nella comprensione degli aspetti ingegneristici della mia ricerca, per il tempo che mi ha dedicato fornendomi consigli, indicazioni, interpretazioni preziose.

Un ringraziamento va ai revisori esterni Prof. Stefano Parolai e Prof. Matteo Picozzi per le loro utili osservazioni critiche e avermi dato gli spunti di riflessione per consolidare questo lavoro di tesi.

Un ringraziamento va al Prof. Francesco Silvestri e al suo gruppo di rcerca dell'Università di Napoli Federico II, Dr.ssa Annachiara Piro, Dr.ssa Filomena de Silva, e Prof. Fulvio Parisi per la collaborazione condotta durante questi anni. Spero potremo ancorsa lavorare insieme.

Un sincero ringrazimento va al Prof. Mattia Crespi e al suo team di ricerca della Sapienza Università di Roma, Dr.ssa Roberta Ravanelli, Dr.ssa Valeria Belloni, Dr. Lorenzo Lastilla per la proficua collaborazione che abbiamo avuto. Alla prossima!!

Un dovesoro ringraziamento va al Prof. Vincenzo Lapenna per aver creduto in me, per i suoi consigli, per essere stato un esempio sia dal punto di vista professionale che umano.

Con il cuore e la gratitudine che meritano ringrazio il Dr. Vincenzo Serlenga, il Dr. Giuseppe Calamita e la Dr.ssa Serena Panebianco per tutto il tempo che avete dedicato per aiutarmi a risolvere difficoltà e probelmatiche di carattere scientifico, e per il supporto continuo nelle diverse fasi di questo lavoro di tesi. Non potevo immaginare colleghi migliori.

Ringrazio tutti i co-autori dei lavori pubblicati durante questi anni di ricerca perché è anche grazie alle numerose discussioni scientifiche trascorse con loro che ho avuto la possibilità di sviluppare nuove competenze. In particolare, ringrazio i colleghi Dr.ssa Angela Perrone e Dr. Tony Alfredo Stabile per i preziosi consigli derivanti dalla loro esperienza professionale e i geologi Michele Lupo, Filippo Cristallo e Michele Vizziello per il supporto tecnico che mi hanno fornito durante alcune attività geologiche.

Un forte ringraziamento va al gruppo geoSDI per il supporto super professionale nella creazione di uno dei lavori pubblicati in questi anni di ricerca. Grazie davvero!!

Ringrazio tutto il gruppo geofisico del CNR-IMAA per avermi fatto sentire come a casa e accolto nella loro piccola grande famiglia per i quali riserverò i miei più cari ringraziamenti personalizzati in fase di stampa.

Infine, alla mia famiglia, faro della mia vita, supporto continuo e inesauribile, e a Valentina che ha preso un posto affianco a me in questo percorso e nella vita.

Bibliography

Akamatsu K., (1961). On microseisms in frequency range from 1c/s to 200c/s. Bull. Earthquake Res. Inst., Tokyo Univ., 39, 23-75.

Aki, K. (1957). Space and time spectra of stationary stochastic waves, with special reference to microtremors, Bull. Earthq. Res. Inst., 35, 415-456.

Aki K. Local site effect on ground motion. In:J.L. Von Thun (Editor), Earthquake Engineering and Soil Dynamics. It: Recent Advances in Ground-Motion Evaluation. Am. Sot. Civil Eng. Geotechnical Spec. Pub]., 20: 103-155 (1988)

Aki K., Larner K.L. (1970) Surface motion of a layered medium gaving an irregular interface due to incident plane SH waves. Jour. Geoph. Research, Vol. 70.

Al-Nimry, H., Resheidat, M., Al-Jamal, M., 2014. Ambient vibration testing of low and medium rise infilled RC frame buildings in Jordan. Soil Dyn. Earthq. Eng. 59, 21–29. https://doi.org/10.1016/J.SOILDYN.2014.01.002.

Albarello, D., Lunedei, E. (2010). Alternative interpretations of horizontal to vertical spectral ratios of ambient vibrations: New insights from theoretical modelling. Bulletin of Earthquake Engineering, 8(3), pp. 519–534

Albarello, D., Cesi, C., Eulilli, V., Guerrini, F., Lunedei, E., Paolucci, E., Pileggi, D., Puzzilli, L.M., 2011. The contribution of the ambient vibration prospecting in seismicì microzoning: an example from the area damaged by the 26th April 2009 l'Aquila (Italy) earthquake. Boll. Geofis. Teor. Appl. 52 (3), 513–538.

Albarello D, Lunedei E (2013) Combining horizontal ambient vibration components for H/V spectral ratio estimates. Geophys J Int 194(2):936–951

Ambraseys N.N. (1959) A note on the response of an elastic overburden of vaying rigidity to an arbitrary ground motion. Bull. Seism. Soc. Of America, Vol. 49.

Andrews, D.J. (1986). Objective Determination of Source Parameters and Similarity of Earthquakes of Different Size. In Earthquake Source Mechanics (eds S. Das, J. Boatwright and C.H. Scholz). https://doi.org/10.1029/GM037p0259

Arai, H., and K. Tokimatsu (1998). Evaluation of local site effects based on microtremor H/V spectra. Proceeding of the Second International Symposium on he Effects of Surface Geology on Seismic Motion. Yokohama, Japan. 2 673-680.

Asten M.W. (1978); Geological control of the three-component spectra of Rayleigh-wave microseisms, Bull. Seism. Soc. Am., 68-6, 1623-1636.

Asten M.W. e J.D. Henstridge (1984); Arrays estimators and the use of microseisms for reconnaissance of sedimentary basins, Geophysics, 49-11, 1828-1837.

Atzeni C, Bicci A, Dei D, et al. Remote survey of the leaning tower of Pisa by interferometric sensing. IEEE Geosci Remote Sens Lett 2010; 7(1): 185–189.

Augenti N, Parisi F (2019) Teoria e tecnica delle strutture in muratura. Hoepli, Milan, Italy

Aye, Z.C.; Sprague, T.; Cortes, V.J.; Prenger-Berninghoff, K.; Jaboyedoff, M.; Derron, M.-H. A collaborative (web-GIS) framework based on empirical data collected from three case studies in Europe for risk management of hydro-meteorological hazards. Int. J. Disaster Risk Reduct. 2016, 15, 10–23.

Aye, Z.C.; Jaboyedoff, M.; Derron, M.H.; Van Westen, C.J.; Hussin, H.Y.; Ciurean, R.L.; Frigerio, S.; Pasuto, A. An interactive web-GIS tool for risk analysis: A case study in the Fella River basin, Italy. Nat. Hazards Earth Syst. Sci. 2016, 16, 85–101.

Bakht B and Jaeger LG. Bridge testing—a surprise every time. J Struct Eng 1990; 116(5): 1370–1383.

Pierre-Yves Bard, Diffracted waves and displacement field over two-dimensional elevated topographies, Geophysical Journal International, Volume 71, Issue 3, December 1982, Pages 731–760, https://doi.org/10.1111/j.1365-246X.1982.tb02795.x

Bard P.Y. (1994) Effects of surface geology on ground motion: recent results and remaining issues. Proc. X Europena Conference on Earthquake Engineering, Vienna, Vol. 1.

Bard P.Y., Bouchon M. (1985) The two-dimensional resonance of sediment-filled valleys. Bull. Seism. Soc. Of America, Vol. 75.

Bard P.Y., Gabriel J.C. (1986) The seismic response of two-dimensional deposits with large vertical velocity gradients. Bull. Seism. Soc. Of America, Vol. 76.

Bard P.Y. e B.E. Tucker (1985); Underground and ridge site effects: a comparison of observation and theory, Bull. Seism. Soc. Am., 75, 4, 905-922.

Bard, P.Y., Gueguen, G., Wirgin, A., 1996. A note on the seismic wavefield radiated from large building structures into soft soils. In: Proceedings of 11th World Conference on Earthquake Engineering. 23-28 June, Paper N.1838.

Bard P.Y. (1998); Local effects on strong ground motion; basic physical phenomena and estimation methods for microzonation studies, Proc. of the Advanced Study Course on Seismic Risk “SERINA”, 21-27 September, Salonicco, Grecia, 229-299.

Bard, Pierre-Yves. (1999). Microtremor measurements: A tool for site effect estimation?. The effects of surface geology on seismic motion. 3. 1251-1279.

Barone, G., Marino, F., Pirrotta, A.: Low stiffness variation in structural systems: identification and localization. Struct. Control Health Monit. 15, 450–470 (2008)

Bedon, C., Dilena, M. & Morassi, A. Ambient vibration testing and structural identification of a cable-stayed bridge. Meccanica 51, 2777–2796 (2016). https://doi.org/10.1007/s11012-016-0430-2

Bendat, J.S. and Piersol, A.G. (2010). Data Analysis. In Random Data (eds J.S. Bendat and A.G. Piersol). https://doi.org/10.1002/9781118032428.ch11

Benedetti, L. et al. (2021). Multidisciplinary Investigations of a Steel–Concrete Composite Bridge. In: Rainieri, C., Fabbrocino, G., Caterino, N., Ceroni, F., Notarangelo, M.A. (eds) Civil Structural Health Monitoring. CSHM 2021. Lecture Notes in Civil Engineering, vol 156. Springer, Cham. https://doi.org/10.1007/978-3-030-74258-4_50

Benedettini F., Gentile C. Operational modal testing and FE model tuning of a cable-stayed bridge. Engineering Structures. vol 33, Issue 6, 2011, 2063-2073, ISSN 0141-0296, https://doi.org/10.1016/j.engstruct.2011.02.046.

Beneduce, P., Festa, V., Francioso, R., Schiattarella, M., Tropeano, M., 2004. Conflicting drainage patterns in the Matera Horst Area, southern Italy. Phys. Chem. Earth Parts A/B/C 29, 717–724. https://doi.org/10.1016/j.pce.2004.03.009.

Bertero, M. and P. Boccacci (1998). Introduction to inverse problems in imaging. Bristol:IOP Publishing.

Bindi D., Paolai S., Cara F., Di Giulio G., Ferretti G., Luzi L., Monachesi G., Pacor F., Rovelli A (2009). Site Amplifications Observed in the Gubbio Basin, Central Italy: Hints for Lateral Propagation Effects. Bulletin of the Seismological Society of America. 2009, 99(2A): 741 https://doi.org/10.1785/0120080238

Bindi, D., S. Parolai, M. Picozzi and A. Ansal (2010). Seismic input motion determined from a surface downhole pair of sensors: a constrained deconvolution approach. Bull. Seismol. Soc. Am., 100, no. 3, 1375 1380.

Bindi, D., Luzi, L., Parolai, S. et al. Site effects observed in alluvial basins: the case of Norcia (Central Italy). Bull Earthquake Eng 9, 1941–1959 (2011). https://doi.org/10.1007/s10518-011-9273-3

Bindi, D., Petrovic, B., Karapetrou, S., Manakou, M., Boxberger, T., Raptakis, D., Pitilakis, K.D., Parolai, S., 2015. Seismic response of an 8-story RC-building from ambient vibration analysis. Bull. Earthq. Eng. 13, 2095–2120. https://doi.org/10.1007/s10518-014-9713-y

Bivand, R., Pebesma, E.J., Gómez-Rubio, V., 2013. Applied Spatial Data Analysis with R. Springer.

Bokelmann GHR, Baisch S (1999) Nature of narrow-band signals at 2.083 Hz. Bull Seis Soc Am 89(1):156–164

Bonilla, L. F., Steidl, J. H., Lindley, G. T., Tumarkin, A. G., and Archuleta, R. J. (1997). Site amplification in the San Ferdinando Valley, California: variability of site effect estimation using S-wave, coda, and H/V methods. Bull. Seism. Soc. Am., 87, 710–730.

Bonnefoy-Claudet, S., Cornou, C., Kristek, J., Ohrnberger, M., Wathelet, Bard, P.-Y., Mozco, P., Fäh, D., Cotton, F. (2004). Simulation of seismic ambient noise: I. Results of H/V and array techniques on

Bonnefoy-Claudet, S., Cornou, C., Bard, P.-Y., Cotton, F., Moczo, P., Kristek, J., Fäh, D., 2006. H/V ratio: a tool for site effects evaluation. Results from 1-D noise simulations. Geophys. J. Int. 167, 827–837. https://doi.org/10.1111/j.1365-246X.2006.03154.x.

Bonnefoy-Claudet S, Baize S, Bonilla LF, Berge-Thierry C, Pasten C, Campos J, Volant P, Verdugo R (2009) Site effect evaluation in the basin of Santiago de Chile using ambient noise measurements. Geophys J Int 176(3):925–937

Borcherdt RD. Effects of local geology on ground motion near San Francisco bay. Bull Seismol Soc Am 1970; 60: 29–61.

Borlenghi, P., Gentile, C., Zonno, G. (2022). Monitoring Reinforced Concrete Arch Bridges with Operational Modal Analysis. In: Pellegrino, C., Faleschini, F., Zanini, M.A., Matos, J.C., Casas, J.R., Strauss, A. (eds) Proceedings of the 1st Conference of the European Association on Quality Control of Bridges and Structures. EUROSTRUCT 2021. Lecture Notes in Civil Engineering, vol 200. Springer, Cham. https://doi.org/10.1007/978-3-030-91877-4_42

Bormann, P., Wielandt, E. (2013): Seismic Signals and Noise. - In: Bormann, P. (Ed.), New Manual of Seismological Observatory Practice 2 (NMSOP2), Potsdam : Deutsches GeoForschungsZentrum GFZ, 1-62. https://doi.org/10.2312/GFZ.NMSOP-2_ch4

Bozzoni, F.; Famà, A.; Lai, C.G.; Mirfattah, S.A. Seismic risk assessment of seaports using GIS: The port of Gioia Tauro in Southern Italy. In Proceedings of the 33rd PIANC World Congress, San Francisco, CA, USA, 1–5 June 2014.

Brambati A, Faccioli E, Carulli GB, Cucchi F, Onofri R, Stefanini S, Ulcigrai F. Studio di microzonazione sismica dell’area di Tarcento (Friuli). Regione Autonomia Friuli-Venezia Giulia & Università degli Studi di Trieste con la collaborazione del Politecnico di Milano. Trieste (1980)

Brax, M., Causse, M. & Bard, PY. Ground motion prediction in Beirut: a multi-step procedure coupling empirical Green’s functions, ground motion prediction equations and instrumental transfer functions. Bull Earthquake Eng 14, 3317–3341 (2016). https://doi.org/10.1007/s10518-016-0004-7

Brax, M., Bard, P.-Y., Duval, A.-M., Bertrand, E., Rahhal, M.-E., Jomaa, R., Cornou, C., Voisin, C., Sursock, A., 2018. Towards a microzonation of the Greater Beirut area: an instrumental approach combining earthquake and ambient vibration recordings. Bull. Earthq. Eng. 16, 5735–5767. https://doi.org/10.1007/s10518-018-0438-1.

Brincker R, Zhang L, Andersen P. Modal Identification from Ambient Responses using Frequency Domain Decomposition. IMAC 18: Proceedings of the International Modal Analysis Conference (IMAC), San Antonio, Texas, USA, February 7-10, 2000; 625–630.

Brincker R., Zhang L., Andersen P. (2001) Modal identification of output-only systems using frequency domain decomposition Smart Mater. Struct. Vol. 10, 3, 441 DOI 10.1088/0964-1726/10/3/303

Brincker, R., Zhang, L., Andersen, P.: An overview of operational modal analysis: major development and issues. In: Proceedings of the 1st International Operational Modal Analysis Conference, Copenhagen, Denmark, 26–27 April 2005 (2005)

Brunton, S., & Kutz, J. (2019). Singular Value Decomposition (SVD). In Data-Driven Science and Engineering: Machine Learning, Dynamical Systems, and Control (pp. 3-46). Cambridge: Cambridge University Press. doi:10.1017/9781108380690.002

Cadet, H., Macau, A., Benjumea, B., Bellmunt, F., Figueras, S., 2011. From ambient noise recordings to site effect assessment: the case study of Barcelona microzonation. Soil Dyn. Earthq. Eng. 31, 271–281. https://doi.org/10.1016/J.SOILDYN.2010.07.005.

Castellaro, S., 2016. Soil and structure damping from single station measurements. Soil Dyn. Earthq. Eng. 90, 480–493.

Castellaro S, Mulargia F (2009b) The effect of velocity inversions on H/V. Pure Appl Geophys 166(4):567–592

Castellaro S, Mulargia F (2010) How far from a building does the ground-motion free-field start? The cases of three famous towers and a modern building. Bull Seis Soc Am 100(5A):2080–2094

Celebi M, Prince J, Dietel C, Onate M, Chavez G (1987) The Culprit in Mexico City—Amplification of Motions. Earthquake Spectra 3(2): 315-328. https://doi.org/10.1193/1.1585431.

Celebi, M. (1987) “Topographic and geological amplifications determined from strong-motion and aftershock records of the 3 March 1985 Chile earthquake”, Bull. Seism. Soc. Am. 77: 1147–1167

Çelebi M, Liu H-P. Before and after retrofit – response of a building during ambient and strong motions. Journal of Wind Engineering and Industrial Aerodynamics 1998; 77–78: 259–268.

Çelebi M, Ghahari SF, Taciroglu E. Responses of the odd couple Carquinez, CA, suspension bridge during the Mw6.0 south Napa earthquake of August 24, 2014. J Civil Struct Health Monit 2019; 9: 719–739.

Chatelain JL, Guillier B, Cara F et al (2008) Evaluation of the influence of experimental conditions on H/V results from ambient noise recordings. Bull Earthq Eng 6(1):33–74

Chatelain JL, Guillier B (2013) Reliable fundamental frequencies of soils and buildings down to 0.1 Hz obtained from ambient vibrations recordings with a 4.5-Hz sensor. Seism Res Lett 84(2):199–209. https://doi.org/10.1785/0220120003

Chávez-García F.J., Cuenca J., Lermo J. e H. Mijares (1995); Seismic microzonation of the city of Puebla, Mexico, Proc. of the Third International Conference on Recent Advances in Geotechnical Earthquake Engineering and Soil Dynamics, St Louis, Missouri, April, 2, 545-548.

Chávez-García, F. J., Sanchez, L.R., and Hatzfeld, D. (1996) “Topographic site effects and HVSR. A comparison between observations and theory”, Bull. of Seis. Society of America, 86: 1559-1575

Chavez-Garcia, F. J., Rodriguez, M., Field, E. H., and Hatzfeld, D. (1997) “Topographic site effects. A comparison of two non-reference methods”, Bul.of the Seismological Society of America, 87: 1667-1673

Chávez-García, F.J., Cárdenas, M., 2002. The contribution of the built environment to the ‘free-field’ ground motion in Mexico City. Soil Dyn. Earthq. Eng. 22, 773–780. https://doi.org/10.1016/S0267-7261(02)00098-2.

Chiauzzi, L., Masi, A., Mucciarelli, M., Cassidy, J.F., Kutyn, K., Traber, J., Ventura, C., Yao, F., 2012. Estimate of fundamental period of reinforced concrete buildings: code provisions vs. experimental measures in Victoria and Vancouver (BC, Canada). In: Proceedings of 15 WCEE, Lisboa 2012, Paper Number 3033.

Chopra AK. Dynamics of Structures (Prentice-hall International Series I Civil Engineering and Engineering Mechanics) 5th Edition (1995)

Chouet, B., De Luca, G., Milana, G., Dawson, P., Martini, M., Scarpa, R. (1998). Shallow velocity of Stromboli volcano, Italy, derived from small-aperture array measurements of Strombolian tremor. Bull. Seism. Soc. Am., 88-3, 653-666.

Clough RW and Penzien J. Dynamics of Structures. Computers and Structures, Incorporated, 2003 – 739 (2003)

Commissione Tecnica MS3907, 2014. Microzonazione sismica. Standard di rappresentazione e archiviazione informatica, versione 4.0, giugno 2015, Roma. http:// protezionecivile.gov.it/jcms/it/commissione_opcm_3907.wp.

Commissione Tecnica MS3907, 2015a. Commissione Tecnica per la Microzonazione Sismica, Microzonazione Sismica, Statistiche, dicembre 2014, Roma. http://protezionecivile.gov.it/jcms/it/commissione_opcm_3907.wp.

Commissione Tecnica MS3907, 2015b. Commissione Tecnica per la Microzonazione Sismica, Linee guida per la gestione del territorio in aree interessate da faglie Attive e Capaci (FAC). http://protezionecivile.gov.it/jcms/it/commissione_opcm_3907.wp.

Commissione Tecnica MS3907, 2015c. Commissione Tecnica per la Microzonazione Sismica, Linee guida per la gestione del territorio in aree interessate da liquefazione (LQ). http://protezionecivile.gov.it/jcms/it/commissione_opcm_3907.wp.

Comune di Matera. Piano Strutturale Comunale. Available online: https://www.comune.matera.it/piano strutturale-comunale (accessed on 31 March 2021).

Conti R, Morigi M, Viggiani MB. Filtering effect induced by rigid massless embedded foundations. Bull Earthq Eng 15:1019–1035 (2016)

Cooley, J.W., and J.W. Tukey (1965). An algorithm for the machine calculation of complex Fourier series. Math. Comput., 19, 297–301.

Cornou, C. (2002). Traitement d'antenne et imagerie sismique dans l'agglomération grenobloise (Alpes françaises): implications pour les effets de site (In french). Université Joseph Fourier, 260.

Cornou C, Guéguen P, Bard P-Y, Hagshenas E (2004) Ambient noise energy bursts observation and modeling: trapping of structure-soil harmonic induced-waves in a topmost sedimentary layer. J Seismolog 8(4):507–524
Coutant, O., Programme de simulation numerique Axitra (version 1 and 2), Rapport LGIT, 1989

Cox BR, Cheng T, Vantassel JP, Manuel L (2020) A statistical representation and frequency-domain window-rejection algorithm for single-station HVSR measurements. Geophys J Int 221(3):2170–2183. https://doi.org/10.1093/gji/ggaa119

Cross EJ, Koo KY, Brownjohn JMW, et al. Long-term monitoring and data analysis of the Tamar Bridge. Mechanical Systems and Signal Processing 2013; 35: 16–34.

D‟Amico V., Picozzi M., Albarello D., Naso G. e Tropenscovino S. (2004). Quick estimate of soft sediments thickness from ambient noise horizontal to vertical spectral ratios: a case study in southern Italy. J. Earthq. Engineering, 8, 6, 895-908.

D’Amico V, Picozzi M, Baliva F, Albarello D (2008) Ambient noise measurements for preliminary site-effects characterization in the Urban area of Florence, Italy. Bull Seis Soc Am 98:1373–1388

Darragh R.B., Shakal A.F. (1991). The site response of two rock and soil station pairs to strong and weak ground motion. Bulletin of the Seismological Society of America. 81 (5): 1885–1899. doi: https://doi.org/10.1785/BSSA0810051885.

Davis, L.L., West, L.R., 1973. Observed effects of topography on ground motion. Bull. Seismol. Soc. Am. 63 (1), 283–298.

Decreto ministeriale numero 493 del 03/12/2021 | mit, https://www.mit.gov.it/normativa/decretoministeriale-numero-493-del-03122021 (accessed 27 June 2022).

Delgado J, López Casado C, Estévez A, Giner J, Cuenca A, Molina S (2000) Mapping soft soils in the Segura river valley (SE Spain): a case study of microtremors as an exploration tool. J Appl Geophys 45:19–32

Di Felice, P.; Spadoni, M. MAHA: A comprehensive system for the storage and visualization of subsoil data for seismic microzonation. Comput. Geosci. 2013, 54, 113–121.

G. Di Giulio, M. Ercoli, M. Vassallo, M. Porreca, Investigation of the Norcia basin (Central Italy) through ambient vibration measurements and geological surveys, Engineering Geology, Volume 267, 2020, 105501, ISSN 0013-7952, https://doi.org/10.1016/j.enggeo.2020.105501

Ditommaso R, Mucciarelli M and Ponzo FC. Analysis of nonstationary structural systems by using a band-variable filter. Bull Earthq Eng 2012; 10: 895–911.

Ditommaso, R., Vona, M., Gallipoli, M. R., and Mucciarelli, M.: Evaluation and considerations about fundamental periods of damaged reinforced concrete buildings, Nat. Hazards Earth Syst. Sci., 13, 1903–1912, https://doi.org/10.5194/nhess-13-1903-2013, 2013.

Ditommaso R, Ponzo FC and Auletta G. Damage detection on framed structures: modal curvature evaluation using stockwell transform under seismic excitation. Earthq Eng Eng Vib 2015; 14: 265–274.

Ditommaso R, Iacovino C, Auletta G, et al. Damage Detection and Localization on Real Structures Subjected to Strong Motion Earthquakes Using the Curvature Evolution Method: The Navelli (Italy) Case Study. Applied Sciences 2021; 11: 6496.

Ditommaso R and Ponzo FC. Automatic evaluation of the fundamental frequency variations and related damping factor of reinforced concrete framed structures using the short time impulse response function (STIRF). Eng Struct 2015; 82: 104–112.

Dravinski M., G. Ding e K.L. Wen (1996); Analysis of spectral ratios for estimating ground motion in deep basins, Bull.Seism.Soc.Am., 86, 3, 646-654.

Dobry R., Whitman R.V., Roesset J.M. (1971) Soil properties and the one-dimensional theory of arthquake amplififcation. Research Report R71-18, dep. Civ. Eng. MIT, Cambbridge Mass. (USA)

Douze, E. J. Rayleigh waves in short-period seismic noise. Bulletin of the Seismological Society of America 1964; 54 (4): 1197–1212. doi: https://doi.org/10.1785/BSSA0540041197

Douze,E. J. Short-period seismic noise. Bulletin of the Seismological Society of America 1967; 57 (1): 55–81. doi: https://doi.org/10.1785/BSSA0570010055

Duval, AM., Vidal, S., Méneroud, JP. et al. Caracas, Venezuela, Site Effect Determination with Microtremors. Pure appl. geophys. 158, 2513–2523 (2001). https://doi.org/10.1007/PL00001183

Elsabee F, Murray JP. Dynamic Behavior of Embedded Foundations. R77-33 (1977)

European Comission. The Urban Agenda for the EU—Regional Policy—European Commission. Available online: https://ec.europa.eu/regional_policy/en/policy/themes/urban-development/agenda/ (accessed on 31 March 2021).

Fabozzi, S., Albarello, D., Pagliaroli, A. et al. The possible use of equivalent homogeneous subsoil models for 1D seismic response analyses in seismic microzonation studies. Bull Earthquake Eng 20, 2259–2281 (2022). https://doi.org/10.1007/s10518-021-01273-z.

Faccioli, E. (1991) “Seismic amplification in the presence of geological and topographic irregularities”, Proc. of 2nd Intern. Conf. on Recent Advances in Geotechnical Earthq. Engrg., 1779-1797

Fago, P.; Pignatelli, C.; Piscitelli, A.; Milella, M.; Venerito, M.; Sansò, P.; Mastronuzzi, G. WebGIS for Italian tsunami: A useful tool for coastal planners. Mar. Geol. 2014, 355, 369–376. [CrossRef]

Fäh, D., Kind, F., and Giardini, D. (2001). A theoretical investigation of average H/V ratios. Geophys. J. Int. 145, 535-549.

Falcone G., Acunzo G., Mendicelli A., Mori F., Naso G., Peronace E., Porchia A., Romagnoli G., Tarquini E., Moscatelli, M. (2021). Seismic amplification maps of Italy based on site-specific microzonation dataset and one-dimensional numerical approach. Engineering Geology, 289, art. no. 106170. doi: 10.1016/j.enggeo.2021.106170.

Farrar CR, Duffey TA, Cornwell PJ, et al. Excitation methods for bridge structures. In: Proceedings of the 17th international modal analysis conference, Kissimmee, FL, 1 February 1997, pp. 1063–1068. Bethel, CT: Society for Experimental Mechanics, Inc.

Ferrari R., Pioldi F., Rizzi E., Gentile C., Chatzi E., Klis R., Serantoni E., Wieser A. Heterogeneous sensor fusion for reducing uncertainty in structural health monitoring. UNCECOMP 2015 - 1st ECCOMAS Themat. Conf. Uncertain. Quantif. Comput. Sci. Eng. (2015) 511–528 doi:10.7712/120215.4289.821.

Ferrari, R.; Pioldi, F.; Rizzi, E.; Gentile, C.; Chatzi, E.; Serantoni, E.; Wieser, A. Fusion of wireless and non contact technologies for the dynamic testing of a historic RC bridge. Meas. Sci. Technol. 2016, 27, 124014.

Ferrari R., Froio D., Rizzi E., Gentile C., Chatzi N.E., Model updating of a historic concrete bridge by sensitivity- and global optimization-based Latin Hypercube Sampling, Engineering Structures, Volume 179, 2019, Pages 139-160, ISSN 0141-0296, https://doi.org/10.1016/j.engstruct.2018.08.004.

Ferrari G., Albarello D. e Martinelli G., 2000 - Tromometric measurements as a tool for crustal deformation interpretation. Seism. Res. Lett., 71, 5, 562-569

Fiamingo A., Bosco M., Massimino M.R. (2018). The role of soil in structure response of a building damaged by the 26 December 2018 earthquake in Italy, Journal of Rock Mechanics and Geotechnical Engineering, https://doi.org/10.1016/j.jrmge.2022.06.010

Field, E. H. e Jacob, K. (1993); The theoretical response of sedimentary layers to ambient seismic noise, Geophys. Res. Lett., 20, 2925–2928.

Field E.H. e K.H. Jacob (1995); A comparison and test of various site-response estimation techniques, including three that are not reference-site dependent, Bull. Seism. Soc. Am., 85, 4, 1127-1143.

Finn, W. D. L. (1991) “Geotechnical engineering aspects of seismic microzonation”, Proc. 4th Intern. Conf. Seismic Zonation, August 25-29, Stanford, California, E.E.R.I. (editor), Oakland CA, 1: 199-250.

Foti, D., Ivorra, S., Bru, D., and Dimaggio, G. (2012). “Dynamic identification of a pedestrian bridge using operational modal analysis,” in Proceedings Eleventh International Conference on Computational Structures Technology (Dubrovnik), 4–7.

Foti, S., Hollender, F., Garofalo, F. et al. Guidelines for the good practice of surface wave analysis: a product of the InterPACIFIC project. Bull Earthquake Eng 16, 2367–2420 (2018). https://doi.org/10.1007/s10518-017-0206-7

Francini, M.; Artese, S.; Gaudio, S.; Palermo, A.; Viapiana, M.F. To support urban emergency planning: A GIS instrument for the choice of optimal routes based on seismic hazards. Int. J. Disaster Risk Reduct. 2018, 31, 121–134.

Frankel A. (1994) New developments in estimating basin response effects on ground motions. Proc. Of the Seminar on New Developments in Earthquake Ground Motion Estimation and Implications for Engineering Design Practic, Applied Technology Council, ATC 35-1.

Frigerio, S.; VanWesten, C.J. RiskCity andWebRiskCity: Data Collection, Display, and Dissemination in a Multi-Risk Training Package. Cartogr. Geogr. Inf. Sci. 2010, 37, 119–135. [CrossRef]

Frigerio, S.; Kappes, M.; Blah ° ut, J.; Skupinski, G. The use of geo-information and modern visualization tools for risk communication. In Advances in Natural and Technological Hazards Research; Springer: Berlin/Heidelberg, Germany, 2014; Volume 34, pp. 383–407.

Gallipoli M.R., Mucciarelli M., Castro R.R., Monachesi G. e P. Contri (2004); Structure, soil-structure response and effects of damage based on observations of horizontal-to-vertical spectral ratio of microtremors, Soil Dynamics and Earthquake Engineering, 24, 6, 487-495.

Gallipoli, M.R., Mucciarelli, M., Ponzo, F., Dolce, M., D'Alema, E., Maistrello, M., 2006. Buildings as a seismic source: analysis of a release test at Bagnoli, Italy. Bull. Seismol. Soc. Am. 96, 2457–2464. https://doi.org/10.1785/0120060015.

Gallipoli, M.R., Mucciarelli, M. and Vona, M. (2009), Empirical estimate of fundamental frequencies and damping for Italian buildings. Earthquake Engng. Struct. Dyn., 38: 973-988. https://doi.org/10.1002/eqe.878

Gallipoli, M.R., Mucciarelli, M., Šket-Motnikar, B., Zupanćić, P., Gosar, A., Prevolnik, S., Herak, M., Stipčević, J., Herak, D., Milutinović, Z., Olumćeva, T., 2010. Empirical estimates of dynamic parameters on a large set of European buildings. Bull. Earthq. Eng. 8, 593–607. https://doi.org/10.1007/s10518-009-9133-6.

Gallipoli, M.R., Albarello, D., Mucciarelli, M., Bianca, M., 2011. Ambient noise measurements to support emergency seismic microzonation: the Abruzzo 2009 earthquake experience. Boll. Geofis. Teor. Appl. 52 (3), 539–559.

Gallipoli, M.R., Lupo, M., 2012. Caratterizzazione dei terreni e risposta sismica locale dell'area urbana di Matera. Tecniche speditive per la stima dell'amplificazione sismica e della dinamica degli edifici Studi teorici ed applicazioni professionali a cura di Marco Mucciarelli, ARACNE editrice S.r.l. ISBN 978–88–548–4495–7. ARACNE editrice S.r.l., pp. 323–342.

Gallipoli MR, Bianca M, Mucciarelli M, Parolai S, Picozzi M. Topographic versus stratigraphic amplification: mismatch between code provisions and observations during the L'Aquila (Italy 2009) sequence. - Bulletin of Earthquake Engineering, 11, 5, 1325-1336 DOI: 10.1007/s10518-013-9446-3 (2013)

Gallipoli MR, Stabile TA, Gueguen P, et al. Fundamental period elongation of a RC building during the Pollino seismic swarm sequence. Case Stud Struct Eng 2016; 6: 45–52.

Gallipoli MR, Calamita G, Tragni N, Pisapia D, Lupo M, Mucciarelli M, Stabile TA, Perrone A, Amato L, Izzi F, La Scaleia G, Maio D, Salvia V (2019) Evaluation of soil-building resonance effect in the urban area of the city of Matera (Italy). Eng Geol 272:105645

Gallipoli MR, Stabile TA, Massolino G, et al. Structural health monitoring of the Ferrara University before and after the 2012 Emilia (Italy) earthquake, and after the damage repairs. Structural Health Monitoring 2020; 19: 838–853.

Gallipoli, M.R., Petrovic, B., Calamita, G. et al. Towards specific T–H relationships: FRIBAS database for better characterization of RC and URM buildings. Bull Earthquake Eng (2023). https://doi.org/10.1007/s10518-022-01594-7

García-Macías E, Ubertini F. Seismic interferometry for earthquake-induced damage identification in historic masonry towers. Mechanical Systems and Signal Processing 2019; 132: 380–404.

García-Macías E, Ubertini F. Structural assessment of bridges through ambient noise deconvolution interferometry: application to the lateral dynamic behaviour of a RC multi-span viaduct. ArchivCivMechEng 2021; 21: 123.

Gazetas G. Vibrational characteristics of soil deposits with variable wave velocity. Int. Journ. For Numerical and Anlytical Methods in Geomechanics, Vol. 6 (1982)

Gazetas G. Analysis of machine foundation vibrations: State of the art. Int J Soil Dyn Earthq Eng 2:2–42. https://doi.org/10.1016/0261-7277(83)90025-6 (1983)

Gazetas G., Dakoulas P. (1992) Seismic analysis and design of rockfill dams: state of-the-art. Soil Dynamics and Earthquake Engineering, Vol. 11, Elsevier.

Geli L., Bard P.Y., Jullien B. (1988) The effect of topography on earthquake ground motion: a review and new results. Bull. Seism. Soc. Of America, Vol. 78. No. 1

Gentile C. Application of microwave remote sensing to dynamic testing of stay-cables. Remote Sens 2010; 2(1): 36–51.

Gentile C and Saisi A. Ambient vibration testing and condition assessment of the Paderno iron arch bridge. Constr Build Mater 2011; 25(9): 3709–3720.

Gentile, C., Saisi, A. Continuous dynamic monitoring of a centenary iron bridge for structural modification assessment. Front. Struct. Civ. Eng. 9, 26–41 (2015). https://doi.org/10.1007/s11709-014-0284-4

Givens MJ, Mylonakis G, Stewart JP. Modular analytical solutions for foundation damping in soil-structure interaction applications. Earthq Spectra. (2016)

Gjorgjeska I., Sheshov V., Stojmanovska M., Bojadjieva J., Dojchinovski D., Edip K., Poposka M. (2022). Multi-method approach for seismic site characterization. Proceedings of the 3rd European Conference on Earthquake Engineering and Seismology (3ECEES), Bucharest, Romania, September 4-9, 2022; 2175-2184.

Goel, R.K., Chopra, A.K., 1997. Period formulas for moment-resisting frame buildings, Structural Engineering Division ASCE; 123:1454-1461.

Gosar, A. Determination of masonry building fundamental frequencies in five Slovenian towns by microtremor excitation and implications for seismic risk assessment. Nat Hazards 62, 1059–1079 (2012). https://doi.org/10.1007/s11069-012-0138-0

Green MF. Modal test methods for bridges: a review. In: Proceedings of the 13th international modal analysis conference, Nashville, TN, 13-16 February 1995.

Grelle, G., Bonito, L., Rosalba, M. et al. Topographic effects observed at Amatrice hill during the 2016–2017 Central Italy seismic sequence. Earthq. Eng. Eng. Vib. 20, 63–78. https://doi.org/10.1007/s11803-021-2005-z (2021)

Gueguen, P., Bard, P.-Y., Oliveira, C.S., 2000. Experimental and Numerical Analysis of Soil Motions Caused by Free Vibrations of a Building Model. Bull. Seismol. Soc. Am. 90, 1464–1479. https://doi.org/10.1785/0119990072.

Gueguen, P., Bard, P.-Y., Chávez-García, F.J., 2002. Site-city seismic interaction in Mexico City-like environments: an analytical study. Bull. Seismol. Soc. Am. 92, 794–811. https://doi.org/10.1785/0120000306.

Guler, K., Yuksel, E., Kocak, A., 2008. Estimation of the fundamental vibration period of existing RC buildings in Turkey Utilizing Ambient Vibration Records. J. Earthq. Eng. 12, 140–150. https://doi.org/10.1080/13632460802013909.

Gutenberg B. (1958); Microseisms, Advan. Geophys., 5, 53-92.

Horike, M. (1985). Inversion of phase velocity of long period microtremors to the S-wave-velocity structure down to the basement in urbanized areas. J. Phys. Earth, 33, 59-96.

Huang, J.; Huang, R.; Ju, N.; Xu, Q.; He, C. 3DWebGIS-based platform for debris flow early warning: A case study. Eng. Geol. 2015, 197, 57–66. [CrossRef]

Iacovino C, Ditommaso R, Ponzo FC, et al. The interpolation evolution method for damage localization in structures under seismic excitation. Earthq Eng Struct 2018; 47: 2117–2136.

Ibrahim S R and Milkulcik E C 1976 The experimental determination of vibration test parameters from time responses Shock Vib. Bull. 46 187–96

Idriss IM. Influence of local site conditions on earthquake ground motions, Proc. of Fourth U.S. Nat. Conf. on Earthquake Engineering, Palm Springs, California, 1, 55-57 (1990)

Idriss I.M., Seed H.B. (1968) Seismic response of horizontal soil layers. Journal of Soil Mechanics and Foundation Division, ASCE, Vol. 94, No. SM4

Ilhan O., Zulfikar C. (2022). Simulation-based Site Amplification Factors for Medium Stiff-to-Stiff Sites in Southern Coast of Izmir City. Proceedings of the 3rd European Conference on Earthquake Engineering and Seismology (3ECEES), Bucharest, Romania, September 4-9, 2022; 2185-2192.

Imposa, S.; Lombardo, G.; Panzera, F.; Grassi, S. Ambient Vibrations Measurements and 1D Site Response Modelling as a Tool for Soil and Building Properties Investigation. Geosciences 2018, 8, 87. https://doi.org/10.3390/geosciences8030087

Italian National Institute of Statistics, ISTAT, 2018. Territorial bases and census variables. (Original name in italian: Basi territoriali e variabili censuarie). https://www.istat.it/it/archivio/104317 (Accessed January 2020). Italian National Institute of Statistics.

Jian J, Snieder R, Nakata N. Extracting the Response of the Bay Bridge, California, from the Application of Multichannel Deconvolution to Earthquake-Induced Shaking. Bulletin of the Seismological Society of America 2020; 110: 556–564.

Jibson, R. (1987) Summary of research on the effects of topographic amplification of earthquake shaking on slope stability, Open-File Report 87-268, U.S. Geological Survey, Menlo Park, Cal.

Jongmans D., Campillo M. (1993). The response of the Ubaye valley (France) for incident SH and SV waves: comparison between measurements and modeling. Bull. Seism. Soc. Of America, Vol. 83, No. 3

Jornet-Monteverde, J.A.; Galiana-Merino, J.J.; Soler-Llorens, J.L. Design and Implementation of a Wireless Recorder System for Seismic Noise Array Measurements. Sensors 2022, 22, 8103. https://doi.org/10.3390/s22218103

Juang J-N and Pappa R S 1985 An eigensystem realization algorithm for modal parameter identification and modal reduction J. Guidance, Control Dynam. 8 620–7

Kanai, K., Tanaka, T., Oada, K. (1954). Measurement of the Microtremor. Bulletin of Earthquake Research Institute, University of Tokyo, 32, 199-209.

Kanai K, Tanaka T (1961) On microtremors VIII. Bull Earthq Res Inst 39:97–114

Kanai K., Yoshizawa S. On the period and the damping of vibration in actual buildings. Bulletin of the earthquake research institute. Vol. 39 (1961), pp. 477-489.

Kanamori, H., Mori, J., Anderson, D.L., Heaton, T.H., 1991. Seismic excitation by the space shuttle Columbia. Nature. 349, 781–782. https://doi.org/10.1038/349781a0.

Karapetrou S, Manakou M, Bindi D, et al. "Time-building specific" seismic vulnerability assessment of a hospital RC building using field monitoring data. Engineering Structures 2016; 112: 114–132.

Karbhari VM and Lee LS. Service life estimation and extension of civil engineering structures. Cambridge: Woodhead Publishing, 2010.

Kausel E. Early history of soil-structure interaction. Soil Dyn Earthq Eng 30:822–832. https://doi.org/10.1016/j.soildyn.2009.11.001 (2010)

Kawase, J. and Aki, K. (1990) "Topography Effect at the Critical SV-Wave Incidence: Possible Explanation of Damage Pattern by the Whittier Narrows,California, Earthquake of 1 October 1987." Bulletin of the Seismological Society of America, 80(1): 1-22

Kham, M., Semblat, J.F., Bard, P.Y., Dangla, P., 2006. Seismic site-city interaction: main governing phenomena through simplified numerical models. Bull. Seism. Soc. Am. 96, 1934–1951.

Kim S, Stewart JP. Kinematic soil-structure interaction from strong motion recordings. J Geotech Geoenviron Eng 129:323–335 (2003)

Kokusho, T.; Ishizawa, T. Site Amplification during Strong Earthquakes Investigated by Vertical Array Records. Geosciences 2021, 11, 510. https://doi.org/10.3390/geosciences11120510

Koller, M. G., Chatelain, J. L., Guillier, B., Duval, A. M., Atakan, K., Lacave, C., Bard, P. Y. (2004, August). Practical user guidelines and software for the implementation of the H/V ratio technique: measuring conditions, processing method and results interpretation. In Proceedings of the 13th World Conference on Earthquake Engineering, Vancouver, Canada

Konno, K. and Ohmachi, T.: Ground-motion characteristics estimated from spectral ratio between horizontal and vertical components of microtremor, Bull. Seism. Soc. Am., 88(1), 228–241, 1998.

Kramer SL. Geotechnical earthquake engineering. Prentice-Hall, New Jersey (1996)

Kudo, K. (1995). Practical estimates of site response. State-of-art report. Proceedings of the fifth Internationnal Conference on Seismic Zonation. Nice, France.

Kudu FN, Bayraktar A, Pakir PG, et al. Ambient vibration testing of Berta Highway Bridge with post-tension tendons. Steel Compos Struct 2014; 16(1). DOI:10.12989/scs.2014.16.1.021

Lacanna G, Ripepe M, Coli M, et al. Full structural dynamic response from ambient vibration of Giotto's bell tower in Firenze (Italy), using modal analysis and seismic interferometry. NDT & E International 2019; 102: 9–15.

Lai, C.G. (1998). Simultaneous inversion of Rayleigh phase velocity and attenuation for near-surface site characterization. PhD Diss., Georgia Inst. of Techn., Atlanta (Georgia, USA)

Lanzo G, Silvestri F. Risposta Sismica Locale. Hevelius Edizioni (1999)

Laurenzano, G., Priolo, E., Gallipoli, M.R., Mucciarelli, M., Ponzo, F.C., 2010. Effect of vibrating buildings on free-field motion and on adjacent structures: the Bonefro (Italy) case history. Bull. Seism. Soc. Am. 100 (2), 802–818.

LeBrun, B., Hatzfel, D., and Bard, P.-Y. (1999) "Experimental study of ground motion on a large scale topography". J. of Seismology, 3(1): 1-15

Lermo J. e F.J. Chavez-Garcia (1994); Are microtremor useful in site response evaluation?, Bull. Seim. Soc. Am., 84, 5, 1350-1364.

Li, T. M. C., Ferguson, J. F., Herrin, E., D. H. B. (1984). High-frequency seismic noise at Lajitas, Texas. Bull. Seism. Soc. Am., 74-5, 2015-2033.

Lunedei E., Albarello D. (2009). On the seismic noise wavefield in a weakly dissipative layered Earth. Geophys. J. Int. (2009) 177, 1001–1014, doi: 10.1111/j.1365-246X.2008.04062.x

Lunedei, E., Albarello, D. (2010) Theoretical HVSR curves from full wavefield modelling of ambient vibrations in a weakly dissipative layered Earth (2010) Geophysical Journal International, 181 (2), pp. 1093-1108. Cited 95 times. doi: 10.1111/j.1365-246X.2010.04560.x

Macıas E.G., Castro-Triguero R., Gallego R., Carretero J., G´omez-Casero M. Operational Modal Analysis and Detection of Non-linear structural behavior of bowstring Arch bridge., in: International Operational Modal Analysis Conference, 2015

Magalhães F., Cunha A., Caetano E. Vibration based structural health monitoring of an arch bridge: From automated OMA to damage detection. Mechanical Systems and Signal Processing, Vol. 28, 2012, pp. 212-228, ISSN 0888-3270, https://doi.org/10.1016/j.ymssp.2011.06.011.

Makra K, Raptakis D, Ch´avez-Garc´ıa FJ, Pitilakis K (2001) Site effects and design provisions: the case of Euroseistest, PAGEOPH 158, 2349–2367

Makra, K., Raptakis, D., Chávez-García, F.J., Pitilakis, K. (2002). Site Effects and Design Provisions: The Case of Euroseistest. In: Roca, A., Oliveira, C. (eds) Earthquake Microzoning. Pageoph Topical Volumes. Birkhäuser, Basel. https://doi.org/10.1007/978-3-0348-8177-7_5

Malagnini L., Tricarico P., Rovelli A., Herrmann R.B., Opice S., Biella G. e R. de Franco (1996); Explosion, earthquake, and ambient noise recording in a Pliocene sediment-filled valley: Inferences on seismic response properties by reference- and non-reference-site techniques, Bull. Seism. Soc. Am., 86, 3, 670-682.

Mallet, R. (1862). Great Neapolitan Earthquake of 1857, London, 2 vols.

Manna, P.; Bonfante, A.; Colandrea, M.; Di Vaio, C.; Langella, G.; Marotta, L.; Mileti, F.A.; Minieri, L.; Terribile, F.; Vingiani, S.; et al. A geospatial decision support system to assist olive growing at the landscape scale. Comput. Electron. Agric. 2020, 168, 105143. [CrossRef]

Maravas A, Mylonakis G, Karabalis LD. Simplified discrete systems for dynamic analysis of structures on footings and piles. Soil Dyn Earthq Eng 61–62:29–39 (2014)

Mascandola, C., Barani, S., Massa, M. et al. Clustering analysis of probabilistic seismic hazard for the selection of ground motion time histories in vast areas. Bull Earthquake Eng 18, 2985–3004 (2020). https://doi.org/10.1007/s10518-020-00819-x.

Matildi IG, Raccagni IM, Isani IS, et al. IL PONTE AD ARCO “GRAVINA” DI MATERA SULLA S.S.655 “BRADANICA”. 2015; 8.

Meixedo, A., Ribeiro, D., Santos, J. et al. Progressive numerical model validation of a bowstring-arch railway bridge based on a structural health monitoring system. J Civil Struct Health Monit 11, 421–449 (2021). https://doi.org/10.1007/s13349-020-00461-w

Michel, C., Guéguen, P., Lestuzzi, P., Bard, P.-Y., 2010. Comparison between seismic vulnerability models and experimental dynamic properties of existing buildings in France. Bull. Earthq. Eng. 8, 1295–1307. https://doi.org/10.1007/s10518-010-9185-7.

Mihaylov D, El Naggar MH, Dineva S (2016) Separation of high-and low-level ambient noise for HVSR: application in city conditions for Greater Toronto area. Bull Seis Soc Am 106(5):2177–2184

MIT (2018) Norme Tecniche per le Costruzioni. DM 17/1/2018, Italian Ministry of Infrastructure and Transportation, Rome, Italy (in Italian)

Mobarki M., Talbi A., Djadia L. (2022). Site effects analysis in Algiers city using simulated accelerograms. Proceedings of the 3rd European Conference on Earthquake Engineering and Seismology (3ECEES), Bucharest, Romania, September 4-9, 2022; 2175-2184.

Molnar S, Assaf J, Sirohey A, Adhikari S (2020) Overview of local site effects and seismic microzonation mapping in Metropolitan Vancouver, British Columbia. Canada Eng Geol 270:105568. https://doi.org/10.1016/j.enggeo.2020.105568

Molnar, S., Sirohey, A., Assaf, J. et al. A review of the microtremor horizontal-to-vertical spectral ratio (MHVSR) method. J Seismol 26, 653–685 (2022). https://doi.org/10.1007/s10950-021-10062-9

Moore M, Phares BM, Graybeal B, et al. Reliability of Visual Inspection for Highway Bridges, Volume I: Final Report. FHWA-RD-01-105, https://rosap.ntl.bts.gov/view/dot/33883 (1 June 2001, accessed 24 June 2022).

Mori F, Mendicelli A, Moscatelli M, Romagnoli G, Peronace E, Naso G. A new Vs30 map for Italy based on the seismic microzonation dataset. Eng Geol 2020;275:105745. https://doi.org/10.1016/j.enggeo.2020.105745.

Moscatelli M, Albarello D, Scarascia Mugnozza G, Dolce M (2020) The Italian approach to seismic microzonation. Bull Earthq Eng 18:5425–5440

Mucciarelli M. Reliability and applicability of Nakamura’s technique using microtremors: an experimental approach. J Earthq Eng 1998; 2(4): 625–638.

Mucciarelli, M., and M. R. Gallipoli. 2001. “A critical review of 10 yearsof microtremor HVSR technique.” Boll. Di Geofisica Teorica EdApplicata 42 (3–4): 255–266

Mucciarelli, M., Contri, P., Monachesi, G., Calvano, G., Gallipoli, M. An empirical method to assess the seismic vulnerability of existing buildings using the HVSR technique (2001) Pure and Applied Geophysics, 158 (12), pp. 2635-2647. doi:10.1007/PL00001189

Mucciarelli M, Gallipoli MR (2004) The HVSR Technique from Microtremor to Strong Motion: Empiricaland Statistical Consideration. In: 13th World Conference on Earthquake Engineering Canada

Mucciarelli, M., Masi, A., Gallipoli, M.R., Harabaglia, P., Vona, M., Ponzo, F., Dolce, M., 2004. Analysis of RC building dynamic response and soil-building resonance based on data recorded during a damaging earthquake (Molise, Italy, 2002). Bull. Seismol. Soc. Am. 94, 1943–1953. https://doi.org/10.1785/012003186.

Mucciarelli, M., Gallipoli, M.R., Di Giacomo, D., Di Nota, F. and Nino, E. (2005), The influence of wind on measurements of seismic noise. Geophysical Journal International, 161: 303-308. https://doi.org/10.1111/j.1365-246X.2004.02561.x

Mucciarelli, M., Bianca, M., Ditommaso, R., Gallipoli, M.R., Masi, A., Milkereit, C., Parolai, S., Picozzi, M., Vona, M., 2011. Far field damage on RC buildings: the case study of Navelli during the L’Aquila (Italy) seismic sequence, 2009. Bull. Earthq. Eng. 9, 263–283. https://doi.org/10.1007/s10518-010-9201-y.

Müller, M.; Vorogushyn, S.; Maier, P.; Thieken, A.H.; Petrow, T.; Kron, A.; Büchele, B.; Wächter, J. CEDIM Risk Explorer—A map server solution in the project “Risk Map Germany”. Nat. Hazards Earth Syst. Sci. 2006, 6, 711–720. [CrossRef]

Mylonakis G, Gazetas G. Seismic soil-structure interaction: beneficial or detrimental? Journal of Earthquake Engineering, 4:3, 277-301, DOI: 10.1080/13632460009350372 (2000)

Nakamura Y. A method for dynamic characteristics estimation of subsurface using microtremor on the ground surface. Quart Rep Railway Tech Res Inst (RTRI) 1989; 3025-33.

Nakamura, Y. (1996). Real-time information systems for hazards mitigation. Proceedings of the 11th World Conference on Earthquake Engineering. Acapulco, Mexico.

Nakamura Y. (2000); Clear identification of fundamental idea of Nakamura's technique and its applications, Proc. Of 12th World Conference on Earthquake Engineering, New Zeland.

Navarro, M., Vidal, F., Enomoto, T., Alcalá, F.J., Sánchez, F.J., Abeki, N., 2007. Analysis of site effects weightiness on RC building seismic response. The Adra (SE Spain) example. Earthq. Eng. Struct. Dyn. 36, 1363–1383.

NEHRP. Consultants Joint Venture. Soil-Structure Interaction for Building Structures (2012)

Nogoshi, M., & Igarashi, T. (1970). On the Propagation Characteristics of Microtremor. Journal of the Seismological Society of Japan, 23, 264-280.

Nogoshi, M. and Igarashi, T. (1971), "On the Amplitude Characteristics of Microtremor (Part 2) (in Japanese with English abstract)", Jour. Seism. Soc. Japan, 24, 26-40.

Ogawa Y., Shimizu K., Joji E. e D. Maejima (1998); Estimation of peak horizontal ground velocity based on microtremors, Proceedings of the 11th European Conference on Earthquake Engineering.Paris, France.

Ohmachi T., Nakamura Y. e T. Toshinawa (1991); Ground motion characteristics of the San Francisco bay area detected by microtremor measurements, Second International Conference on Recent Advances in Geotechnical Earthquake Engineering and Soil Dynamics, St Louis, 2, 1643-1648.

Ohori M, Nobata A and Wakamatsu K. A comparison of ESAC and Fk methods of estimating phase velocity using arbitrarily shaped microtremor arrays. Bull Seismol Soc Am 2002; 92(6): 2323–2332.

Okada H. The microtremor survey method. Geophysical Monograph Series SEG. Tulsa, OK: Soc Explor Geophys, 2003, p. 12.

Okada, H. (2003). The microtremor survey method. Geophys. Monograph Series, Vol. 12, Society of Exploration Geohysicists, 129 pp.

Oliveira, C.S., Navarro, M. Fundamental periods of vibration of RC buildings in Portugal from in-situ experimental and numerical techniques. Bull Earthquake Eng 8, 609–642 (2010). https://doi.org/10.1007/s10518-009-9162-1

Oppikofer, T.; Nordahl, B.; Bunkholt, H.; Nicolaisen, M.; Jarna, A.; Iversen, S.; Hermanns, R.L.; Böhme, M.; Molina, F.X.Y. Database and online map service on unstable rock slopes in Norway—From data perpetuation to public information. Geomorphology 2015, 249, 69–81. [CrossRef]

Orcesi AD and Frangopol DM. Optimization of bridge maintenance strategies based on structural health monitoring information. Struct Saf 2011; 33(1): 26–41.

Overschee P., Moor B. Subspace Identification for Linear Systems. Theory — Implementation — Applications. Springer New York, NY. Kluwer Academic Publishers 1996. ISBN 978-1-4613-8061-0, ed. 1, pp. 272. https://doi.org/10.1007/978-1-4613-0465-4

Pan, T.-C., Goh, K.S., Megawati, K., 2014. Empirical relationships between natural vibration period and height of buildings in Singapore. Earthq. Eng. Struct. Dyn. 43, 449–465. https://doi.org/10.1002/eqe.2356.

Paolucci, E., Albarello, D., D'Amico, S., Lunedei, E., Martelli, L., Mucciarelli, M., Pileggi, D., 2015. A large scale ambient vibration survey in the area damaged by May–June 2012 seismic sequence in Emilia Romagna, Italy. Bull. Earthq. Eng. 13, 3187–3206. https://doi.org/10.1007/s10518-015-9767-5.

Parolai, S., Bindi, D., and Augliera, P. (2000). Application of the Generalized Inversion Technique (GIT) to a microzonation study: numerical simulations and comparison with different site-estimation techniques. Bull. Seism. Soc. Am., 90, no. 2, 286–297.

Parolai, S., Bindi, D., and Troiani, L. (2001a). Site response for the RSM seismic network and source parameters in the Central Apennines (Italy). Pure Appl. Geophys., 158, 695–715.

Parolai S., Bormann P., Milkereit C. (2001b). Assessment of the natural frequency of the sedimentary cover in the Cologne area (Germany) using noise measurements.Journal of Earthquake Engineering, 5:4, 541-564, DOI: 10.1080/13632460109350405

Parolai, S., and Richwalski, S. M. (2004). The importance of converted waves in comparing H/V and RSM site responses. Bull. Seism. Soc. Am., 94, 304–313.

Parolai S, Facke A, Richwalski S, et al. Assessing the vibrational frequencies of the Holweide Hospital in the city of Cologne (Germany) by means of ambient seismic noise analysis and FE modelling. Nat Hazards 2005; 34:217–230.

Parolai, S., and Galiana-Merino, J. J. (2006): Effect of transient seismic noise on estimates of H/V spectral ratios. Bull. Seism. Soc. Am., 96, 1, 228-236.

Parolai S, Picozzi M, Strollo A, Pilz M, Di Giacomo D, Liss B, Bindi D (2009) Are transients carrying useful information for estimating H/V spectral ratios? Increasing Seismic Safety by Combining Engineering Technologies and Seismological Data. Springer, Dordrecht, pp 17–31

Parolai S., Orunbaev S., Bindi D., Strollo A., Usupaev S., Picozzi M., Di Giacomo Di., Augliera P., D'Alema E., Milkereit C., Moldobekov B., Zschau J.; Site Effects Assessment in Bishkek (Kyrgyzstan) Using Earthquake and Noise Recording Data. Bulletin of the Seismological Society of America 2010; 100 (6): 3068–3082. doi: https://doi.org/10.1785/0120100044

Parolai, S. (2012): Investigation of site response in urban areas by using earthquake data and seismic noise. - In: Bormann, P. (Ed.), New Manual of Seismological Observatory Practice 2 (NMSOP-2), Potsdam: Deutsches GeoForschungsZentrum GFZ, 1-38. https://doi.org/10.2312/GFZ.NMSOP-2_ch14

Pedersen H., Le Brun B., Hatzfeld D., Campillo M., Bard P.-Y.; Ground-motion amplitude across ridges. Bulletin of the Seismological Society of America 1994;; 84 (6): 1786–1800. doi: https://doi.org/10.1785/BSSA0840061786

Peeters B, Ventura CE. Comparative study of modal analysis techniques for bridge dynamic characteristics. Mechanical Systems and Signal Processing 2003; 17: 965–988.

Perret, D. (2015). Single station H/V technique. In Shear wave velocity measurement guidelines for Canadian seismic site characterization in soil and rock, (ed.) J.A. Hunter and H.L. Crow; Natural Resources Canada, Earth Sciences Sector, Information Product 110 (English and French), 78–84; 90–93

Peruzzi, G., Albarello, D., Baglione, M. et al. Assessing 1D litho-stratigraphical amplification factor for microzoning studies in Italy. Bull Earthquake Eng 14, 373–389 (2016). https://doi.org/10.1007/s10518-015-9841-z

Pessina, V.; Meroni, F. AWebGis tool for seismic hazard scenarios and risk analysis. Soil Dyn. Earthq. Eng. 2009, 29, 1274–1281. [CrossRef]

Peterson, J. (1993), Observations and modelling of seismic background noise. US geological Survey, open-file report 93–322.

Petrovic B, Bindi D, Pilz M, et al. Building monitoring in Bishkek and Dushanbe by the use of ambient vibration analysis. Annals of Geophysics; 58. Epub ahead of print 24 April 2015. DOI: 10.4401/ag- 6679.

Petrovic, B., Parolai, S., 2016. Joint deconvolution of building and downhole strongmotion recordings: evidence for the seismic wavefield being radiated back into the shallow geological layers. Bull. Seismol. Soc. Am. 106, 1720–1732. https://doi.org/10.1785/0120150326.

Petrovic B, Dikmen SU, Parolai S. Real data and numerical simulations-based approaches for estimating the dynamic characteristics of a tunnel formwork building. Bull Earthquake Eng 2018; 16:1633–1656.

Petrovic, B., Parolai, S., Pianese, G., Dikmen, S.U., Moldobekov, B., Orunbaev, S., Paolucci, R., 2018. Joint deconvolution of building and downhole seismic recordings: an application to three test cases. Bull. Earthq. Eng. 16, 613–641. https://doi.org/10.1007/s10518-017-0215-6.

Pianese G, Petrovic B, Parolai S, et al. Identification of the nonlinear seismic response of buildings by a combined Stockwell Transform and deconvolution interferometry approach. Bull Earthquake Eng 2018; 16: 3103–3126.

Picozzi M, Parolai S, Albarello D (2005) Statistical analysis of noise horizontal-to-vertical spectral ratios (HVSR). Bull Seis Soc Am 95(5):1779–1786

Picozzi M, Strollo A, Parolai S, Durukal E, Ozel O, Karabulut S, Zschau J, Erdik M. Site characterization by seismic noise in Istanbul, Turkey. Soil Dynam Earthq Eng 2009;29(3):469–82.

Picozzi M, Ditommaso R, Parolai S, et al. Real time monitoring of structures in task force missions: the example of the Mw = 6.3 Central Italy Earthquake, April 6, 2009. Nat Hazards 2010; 52: 253–256.

Picozzi M, Parolai S, Mucciarelli M, et al. Interferometric Analysis of Strong Ground Motion for Structural Health Monitoring: The Example of the L'Aquila, Italy, Seismic Sequence of 2009. Bulletin of the Seismological Society of America 2011; 101: 635–651.

Pieraccini M, Fratini M, Parrini F, et al. Interferometric radar vs. Accelerometer for dynamic monitoring of large structures: an experimental comparison. NDT E Int 2008; 41(4): 258–264.

Pilz M, Parolai S, Leyton F, Campos J, Zschau J. A comparison of site response techniques using earthquake data and ambient seismic noise analysis in the large urban areas of Santiago de Chile. Geophys J Int 2009;178(2):713–28.

Pilz, M., Parolai, S., Picozzi, M., Wang, R., Leyton, F., Campos, J. and Zschau, J. (2010), Shear wave velocity model of the Santiago de Chile basin derived from ambient noise measurements: a comparison of proxies for seismic site conditions and amplification. Geophysical Journal International, 182: 355-367. https://doi.org/10.1111/j.1365-246X.2010.04613.x

Pinzón, L.A., Pujades, L.G., Macau, A., Figueras, S., 2019. Increased seismic hazard in Barcelona (Spain) due to soil-building resonance effects. Soil Dyn. Earthq. Eng. 117, 245–250. https://doi.org/10.1016/J.SOILDYN.2018.11.022.

Piro A., de Silva F., Parisi F., Scotto di Santolo A., Silvestri F. Effects of soil foundation structure interaction on fundamental frequency and radiation damping ratio of historical masonry building sub structures. Bulletin of E arthquake Eng ineering 1 8, 1187 1212. https://doi.org/10.1007/s10518 019 00748 4 (2020)

Piro A., Tragni N., de Silva F., Calamita G., Cristallo F.M., Gallipoli M.R., Silvestri F. (2022). Uno studio sperimentale e analitico sugli effetti dell'interazione terreno struttura in un quartiere di Matera. Incontro Annuale dei Ricercatori di Geotecnica 2022 – IARG2022 Caserta, 7-8-9 settembre.

Pitarka A., Irikura K., Iwata T. (1996). Was the basin edge geometry responsible for the ground motion amplification in the disaster belt-like zone during January 17, 1995, Kobe (Hyogo-ken Nambu), Japan earthquake? Proceedings of the International Workshop on Site Response subjected to Strong Earthquake Motions, January 16-17, Yokosuka, Japan.

K. PITILAKIS , D. RAPTAKIS , K. LONTZETIDIS , TH. TIKA-VASSILIKOU & D. JONGMANS (1999) GEOTECHNICAL AND GEOPHYSICAL DESCRIPTION OF EURO-SEISTEST, USING FIELD, LABORATORY TESTS AND MODERATE STRONG MOTION RECORDINGS, Journal of Earthquake Engineering, 3:3, 381-409, DOI:10.1080/13632469909350352

Pitilakis, Kyriazis & Makra, Konstantia & Raptakis, Dimitrios. (2001). 2D vs 1D site effects with potential applications to seismic norms: The cases of EUROSEISTEST and Thessaloniki. August 2001 Conference: XV ICSMGE TC4 Satellite Conference on "Lessons Learned from Recent Strong Earthquakes", pp. 123-133.At: Istanbul, Turkey, Volume: Invited Lecture.

Pitilakis, K. (2004). Site Effects. In: Ansal, A. (eds) Recent Advances in Earthquake Geotechnical Engineering and Microzonation. Geotechnical, Geological, and Earthquake Engineering, vol 1. Springer, Dordrecht. https://doi.org/10.1007/1-4020-2528-9_6

Ponzo FC, Ditommaso R, Auletta G, et al. A fast method for structural health monitoring of Italian strategic reinforced concrete buildings. Bull Earthq Eng 2010; 8: 1421–1434.

Priestley, MB., (1981). Spectral analysis and time series. New York: Academic Press.

Primofiore I, Baron J, Klin P, Laurenzano G, Muraro C, Capotorti F, Amanti M, Vessia G. 3D numerical modelling for interpreting topographic effects in rocky hills for Seismic Microzonation: the case study of Arquata del Tronto hamlet. Eng. Geol. 279, 1–22. https://doi.org/10.1016/j.enggeo.2020.105868 (2020)

Puglia R, Albarello D, Gorini A, Luzi L, Marcucci S, Pacor F (2011) Extensive characterization of Italian accelerometric stations from single-station ambient-vibration measurements. Bulletin Earthquake Engineering 9:1821–1838

Rainieri C, Fabbrocino G. Operational Modal Analysis of Civil Engineering Structures. New York, NY: Springer New York. Epub ahead of print 2014. DOI: 10.1007/978-1-4939-0767-0.

Raptakis D., Chávez-García F.J., Makra K., Pitilakis K. (2000) Site effects at Euroseistest—I. Determination of the valley structure and confrontation of observations with 1D analysis. Soil Dynamics and Earthquake

Engineering, Vol. 19, Issue 1, 2000, pp. 1-22, ISSN 0267-7261, https://doi.org/10.1016/S0267-7261(99)00025-1

Raptakis, D., N. Theodulidis & K. Pitilakis 1998a. Data analysis of the Euroseistest strong motion array in Volvi (Greece): standard and horizontal to vertical ratio techniques. Earthquake Spectra, 14:203-224.

Raptakis, D., F.J. Chávez-García, K. Makra & K. Pitilakis 1998b. Site effects at Euroseistest — I: Determintation of the valley structure and confrontation of observations with 1D analysis. Soil Dyn. Earthq. Eng.

Raptakis, D., Makra, K., Anastasiadis, A. et al. Complex Site Effects in Thessaloniki (Greece): I. Soil Structure and Comparison of Observations with 1D Analysis. Bull Earthquake Eng 2, 271–290 (2004). https://doi.org/10.1007/s10518-004-3799-6

Raptakis, D., Makra, K., Anastasiadis, A. et al. Complex Site Effects in Thessaloniki (Greece): II. 2D SH Modelling and Engineering Insights. Bull Earthquake Eng 2, 301–327 (2004). https://doi.org/10.1007/s10518-004-3803-1

Riepl, J., Bard, P.-Y., Hatzfeld, D., Papaioannou, C., and Nechtschein, S. (1998). Detailed evaluation of site response estimation methods across and along the sedimentary valley of Volvi (EURO-SEISTEST). Bull. Seism. Soc. Am., 88, no. 2, 488–502.

Rippa F, Vinale F. Effetti del terremoto del 23 novembre 1980 sul patrimonio edilizio di Napoli. Atti XV Convegno Italiano di Geotecnica, Spoleto. AGI, Roma (1983)

Roädelsperger S, Laa¨ ufer G, Gerstenecker C, et al. Monitoring of displacements with ground-based microwave interferometry: IBIS-S and IBIS-L. J Appl Geod 2010; 4(1): 41–54.

Roca A, Oliveira C (2001). Introduction. Pure Appl Geophys. 158(12), 2291–2294. https://doi.org/10.1007/PL00001170

Roesset J. Fundamentals of soil amplification. Seismic Design for Nuclear Power Plants. ed. R.J. Hansen. The M.I.T. Press (1970)

Roselli, I., Malena, M., Mongelli, M. et al. Health assessment and ambient vibration testing of the “Ponte delle Torri” of Spoleto during the 2016–2017 Central Italy seismic sequence. J Civil Struct Health Monit 8, 199–216 (2018). https://doi.org/10.1007/s13349-018-0268-5

Rovithis, E.; Makra, K.; Kirtas, E.; Manesis, C.; Bliziotis, D.; Konstantinidou, K. Field Monitoring of Strong Ground Motion in Urban Areas: The Kalochori Accelerometric Network (KAN), Database andWeb-GIS Portal. Earthq. Spectra 2018, 34, 471–501. [CrossRef]

Sakaji, K. (1998). Temporal variation of the power spectra of microtremors observed at soil and rock sites. Graduation thesis, Hokkaido University (in Japanese).

Salameh, C., Guillier, B., Harb, J., Cornou, C., Bard, P.-Y., Voisin, C., Mariscal, A., 2016. Seismic response of Beirut (Lebanon) buildings: instrumental results from ambient vibrations. Bull. Earthq. Eng. 14, 2705–2730. https://doi.org/10.1007/s10518-016- 9920-9.

Salawu OS and Williams C. Review of full-scale dynamic testing of bridge structures. Eng Struct 1995; 17(2):113–121.

Salvati, P.; Balducci, V.; Bianchi, C.; Guzzetti, F.; Tonelli, G. AWebGIS for the dissemination of information on historical landslides and floods in Umbria, Italy. GeoInformatica 2009, 13, 305–322. [CrossRef]

Salvermoser J, Hadziioannou C, Stähler SC. Structural monitoring of a highway bridge using passive noise recordings from street traffic. J Acoust Soc Am 2015; 138: 3864–3872.

Sánchez-Sesma FJ. Diffraction of elastic SH waves by wedges. Bulletin of the Seismological Society of America; 75 (5): 1435–1446. doi: https://doi.org/10.1785/BSSA0750051435 (1985)

Sanchez-Sesma FJ. Elementary solutions for the response of a wedge-shaped medium to incident SH and SV waves, Bull. Seism. Soc. Am., 80, 737-742 (1990)

Schmidt, R.O. (1981). A Signal Subspace Approach to Multiple Emitter Location and Spectral Estimation, PhD thesis Stanford University, Stanford, CA.

Scibek, J. Multidisciplinary database of permeability of fault zones and surrounding protolith rocks at world wide sites. Sci. Data 2020, 7, 1–14. [CrossRef]

Seed H.B., Murarka R., Lysmer J. e I.M. Idriss. Relationships of maxima acceleration, maximum velocity, distance from source, and local site conditions for moderately strong earthquakes, Bull. Seism. Soc. Am., 66, 1323-1342 (1976)

Seed H.B., Dickenson S.E., Idriss I.M. (1991). Principal geotechnical aspects of the 1989 Loma Prieta earthquake. Soils and Foundations, Vol. 31. No. 1. https://doi.org/10.3208/sandf1972.31.1.

Semblat, J.F., Kham, M., Bard, P.Y., Gueguen, P., 2004. Could “site-city interaction” modify site effects in urban areas? In: Proceeding of the 13th World Conference on Earthquake Engineering Vancouver, BC, Canada.

Serlenga V, Gallipoli MR, Ditommaso R, et al. An integrated approach for structural behavior characterization of the Gravina Bridge (Matera, Southern Italy). Structural Health Monitoring. 2021;20(6):3371-3391. doi:10.1177/1475921720987544

SESAME European project. (2003). Nature of noise wavefield. Final Report WP08. http://sesame-fp5.obs.ujf-grenoble.fr/Delivrables/D13.08_finalreport.pdf

SESAME European project (2004). Nature of noise wavefield. Final Report WP08. http://sesame-fp5.obs.ujf-grenoble.fr/Delivrables/D13.08_finalreport.pdf

Sextos A., De Risi R., Pagliaroli A., Foti S., Passeri F. ,Ausilio E., Cairo R., Capatti M., Chiabrando F., Chiaradonna A., Dashti S., De Silva F., Dezi F., Durante M.G., Giallini S., Lanzo G., Sica S., Simonelli A.L.,

Sgattoni G, Castellaro S (2020) Detecting 1-D and 2-D ground resonances with a single-station approach. Geophys J Int 223(1):471–487

Shi, X.; Yang, G.; Yu, D.; Xu, S.; Warner, E.D.; Petersen, G.W.; Sun, W.; Zhao, Y.; Easterling, W.E.; Wang, H. A WebGIS system for relating genetic soil classification of China to soil taxonomy. Comput. Geosci. 2010, 36, 768–775. [CrossRef]

SM Working Group (2015) Guidelines for seismic microzonation, conference of regions and autonomous Provinces of Italy—Civil Protection Department, Rome, http://www.protezionecivile.gov.it/httpdocs/cms/attach_extra/ GuidelinesForSeismicMicrozonation.pdf. Last Accessed April 2020 (Original Italian Edition: Gruppo di lavoro MS, Indirizzi e criteri per la microzonazione sismica, Conferenza delle Regioni e delle Province autonome—Dipartimento della protezione civile, Roma, 2008, 3 vol. e Dvd).

Snieder R, Şafak E. Extracting the Building Response Using Seismic Interferometry: Theory and Application to the Millikan Library in Pasadena, California. Bulletin of the Seismological Society of America 2006; 96: 586–598.

Snieder R, Hubbard S, Haney M, et al. Advanced Noninvasive Geophysical Monitoring Techniques. Annu Rev Earth Planet Sci 2007; 35: 653–683.

Snieder R, Miyazawa M, Slob E, et al. A Comparison of Strategies for Seismic Interferometry. Surv Geophys 2009; 30: 503–523.

Stabile TA, Giocoli A, Perrone A, et al. A new joint application of non-invasive remote sensing techniques for structural health monitoring. J Geophys Eng 2012; 9(4): S53–S63.

Stabile TA, Perrone A, Gallipoli MR, et al. Dynamic Survey of the Musmeci Bridge by Joint Application of Ground-Based Microwave Radar Interferometry and Ambient Noise Standard Spectral Ratio Techniques. IEEE Geoscience and Remote Sensing Letters 2013; 10: 870–874.

Stanko D., Markušić S., Strelec S., Gazdek M. HVSR analysis of seismic site effects and soil-structure resonance in Varaždin city (North Croatia) Soil Dyn. Earthq. Eng., 92 (2017), pp. 666-677, 10.1016/j.soildyn.2016.10.022

Steidl, J.H., A.G. Tumarkin & R.J. Archuleta 1996. What is a reference site? Bull. Seism. Soc. Am., 86:1733-1748.

Stockwell RG, Mansinha L and Lowe RP. Localization of complex spectrum: the S transform. IEE Trans Signal Process 1996; 44(4): 9981001.

Strollo, A., Bindi, D., Parolai, S., Jäckel, K.-H. (2008): On the suitability of 1 s geophone for ambient noise measurements in the 0.1–20Hz frequency range: experimental outcomes. - Bulletin of Earthquake Engineering, 6, 1, 141-147

Sun M, Alamdari MM, Kalhori H. Automated Operational Modal Analysis of a Cable-Stayed Bridge. Epub ahead of print 2017. DOI: 10.1061/(ASCE)BE.1943-5592.0001141.

Sunahara, Y. (1981). Stochastic system theory, vol. 1. Asakura Press (in Japanese).

Thiebes, B.; Bell, R.; Glade, T.; Jäger, S.; Anderson, M.; Holcombe, L. A WebGIS decision-support system for slope stability based on limit-equilibrium modelling. Eng. Geol. 2013, 158, 109–118. [CrossRef]

Tikhonov, A.N. and V.Y. Arsenin (1977). Solution of ill-posed problems. Washington: Wiston/Wiley.

Todorovska MI, Trifunac MD. Earthquake damage detection in the Imperial County Services Building III: Analysis of wave travel times via impulse response functions. Soil Dynamics and Earthquake Engineering 2008; 28:387-404

Todorovska MI, Niu B, Lin G, et al. A new full-scale testbed for structural health monitoring and soil– structure interaction studies: Kunming 48-story office building in Yunnan province, China. Structural Control and Health Monitoring 2020; 27: e2545.

Tokimatsu, K. (1997). Geotechnical site characterization using surface waves. Earthquake Geotechnical Engineering, Ishihara (ed.), Balkema, Rotterdam, 1333-1368.

Toksöz, M.N., and Lacoss, R.T. (1968). Microseisms – Mode structure and sources. Science, 159,872-873.

Tragni N., Gallipoli M.R., Lupo M., Massolino G., Mucciarelli M., Rebez A., Stabile T.A., Sandron D. (2019). Utilizzo di rumore sismico per la caratterizzazione rapida degli edifici. Bollettino di Geofisica Teorica ed Applicata. Vol. 60, supplemento 2, pp. s148-s153; dicembre 2019

Tragni, N.; Calamita, G.; Lastilla, L.; Belloni, V.; Ravanelli, R.; Lupo, M.; Salvia, V.; Gallipoli, M.R. Sharing Soil and Building Geophysical Data for Seismic Characterization of Cities Using CLARA WebGIS: A Case Study of Matera (Southern Italy). Appl. Sci. 2021, 11, 4254. https://doi.org/10.3390/app11094254

Tragni, N.; Petrovic, B.; Serlenga V.; Ponzo F.C.; Ditommaso R; Gallipoli M.R. Structural characterization of an arch bridge in Italy using wave propagation analysis. Extended Abstract. 3rd European Conference on Earthquake Engineering & Seismology Bucharest, Romania, 2022.

Triantafyllidis, P., Hatzidimitriou, P. M., Theodulidis, M., Suhadolc, P., Papazachos, C., Raptakis, D., and Lontzetidis, K. (1999). Site effects in the city of Thessaloniki (Greece) estimated from acceleration data and 1D local soil profiles. Bull. Seism. Soc. Am., 89, 521–537.

Tropeano, M., Marino, M., Pieri, P., 1994. Evidenze di tettonica distensiva Plio–Pleistocenica al margine orientale della Fossa bradanica: l'Horst di Zagarella. Il Quaternario. 7, 597–606.

Tropeano M and Sabato L. Response of Plio-Pleistocene mixed bioclastic-lithoclastic temperate-water carbonate systems to forced regressions: the Calcarenite di Gravina Formation, Puglia, SE Italy. In: Hunt D and Gawthorpe RL (eds) Sedimentary Responses to Forced Regressions. Volume. 172, London: Geological Society, Spec Publ, 2000, pp. 217–243.

Tsogka, C., Wirgin, A., 2003. Simulation of seismic response in an idealized city. Soil Dyn. Earthq. Eng. 23, 391–402. https://doi.org/10.1016/S0267-7261(03)00017-4.

Türker T., Bayraktar A. Structural safety assessment of bowstring type RC arch bridges using ambient vibration testing and finite element model calibration. Measurement, Vol. 58, 2014, pp. 33-45, ISSN 0263-2241, https://doi.org/10.1016/j.measurement.2014.08.002.

Udwadia F. E. and M. D. Trifunac (1973). Comparison of earthquake and microtremor ground motions in El Centro, California. Bull. Seism. Soc. Am., 63-4, 1227-1253.

Vallianatos F, Hloupis G (2009) HVSR technique improvement using redundant wavelet transform. Increasing Seismic Safety by Combining Engineering Technologies and Seismological Data. Springer, Dordrecht, pp 117–137

Van Overschee P and De Moor B 1996 Subspace Identification for Linear Systems (Dordrecht: Kluwer)
Veletsos A and Meek JW. Dynamic behavior of building-foundation systems. Earthq Eng Struct Dyn 3:121–138 (1974)

Varone, C., Lenti, L., Martino, S., Bozzano, F., Semblat, J.F., 2019. Modelling of seismic urban wavefield in highly heterogeneous Site-City configurations. In: Silvestri, Moraci (Eds.), Earthquake Geotechnical Engineering for Protection and Development of Environment and Constructions. Associazione Geotecnica Italiana, Rome, Italy, pp. 5506–5512 ISBN 978-0-367-14328-2.

Veletsos AS, Meek JW (1974) Dynamic behaviour of building-foundation systems. Earthq Eng Struct Dyn. https://doi.org/10.1002/eqe.4290030203

Vessia, G., Parise, M., Tromba, G., 2013. A strategy to address the task of seismic microzoning in landslide-prone areas. Adv. Geosci. https://doi.org/10.5194/adgeo-35-23-2013.

Vessia, G., Pisano, L., Tromba, G., Parise, M., 2016. Seismically induced slope instability maps validated at an urban scale by site numerical simulations. Bull. Eng. Geol. Environ. https://doi.org/10.1007/s10064-016-0940-0.

Viggiani G and Atkinson JH. Stiffness of fine-grained soil at very small strains. Gdotechnique 45, No. 2, 249-265 (1995)

Vinale F and Simonelli AL. L’eterogeneità dei terreni nei fenomeni di amplificazione locale, XV Convegno Nazionale di Geotecnica, Spoleto, Book of Abstract, 1, 221-230. (1983)

Vold H, Kundrat J, Rocklin G T and Russel R 1982 A multi-input modal estimation algorithm for minicomputer (SAE Technical Paper Series, No 820194)

Whelan, M., Salas Zamudio, N. & Kernicky, T. Structural identification of a tied arch bridge using parallel genetic algorithms and ambient vibration monitoring with a wireless sensor network. J Civil Struct Health Monit 8, 315–330 (2018). https://doi.org/10.1007/s13349-017-0266-z

Wiggins RW, Clayton RA. (1976) Source shape estimation and deconvolution of teleseismic bodywaves. Geophysical Journal of the Royal Astronomical Society; 47: 151-177

Wirgin A., Bard P.Y. (1996). Effects of building on the duration and amplitude of ground motion in Mexico City, Bull. Seism. Soc. Am., 86, 914-920.

Wolf J. Dynamic soil-structure interaction. Prentice Hall, Englewood Cliff (1985)

Yaglom, A.M. (1962). An introduction to the theory of stationary random functions (translated and edited by R.A. Silverman). Dover Publications Inc.

Yamamoto, H. (2000). Estimation of shallow S-wave velocity structures from phase velocities of love- and Rayleigh- waves in microtremors. Proceedings of the 12th World Conference on Earthquake Engineering. Auckland, New Zealand.

Yamanaka, H., Takemura, M., Ishida, H, Niwa, M. (1994). Characteristics of long-period microtremors and their applicability in exploration of deep sedimentary layers. Bull. Seism. Soc. Am., 84, 1831-1841.

Zonno, G., Gentile, C. (2021). Assessment of Similar Reinforced Concrete Arch Bridges by Operational Modal Analysis and Model Updating. In: Rainieri, C., Fabbrocino, G., Caterino, N., Ceroni, F., Notarangelo, M.A. (eds) Civil Structural Health Monitoring. CSHM 2021. Lecture Notes in Civil Engineering, vol 156. Springer, Cham. https://doi.org/10.1007/978-3-030-74258-4_54

Zordan T., Briseghella B., Liu T. Finite element model updating of a tied-arch bridge using Douglas-Reid method and Rosenbrock optimization algorithm. Journal of Traffic and Transportation Engineering (English Edition), Volu. 1, Issue 4,2014, pp. 280-292, ISSN 2095-7564, https://doi.org/10.1016/S2095-7564(15)30273-7.